Investigation of Cavity Flow Aerodynamics Using Computational Fluid Dynamics

Jason Henderson, B.Eng

Thesis submitted to the Faculty of Engineering,
University of Glasgow, for the Degree of Doctor of Philosophy

University of Glasgow
Department of Aerospace Engineering

August 2001

ALL MISSING PAGES ARE BLANK

IN

ORIGINAL

Dedicated to my father, James, my mother,
Norah, and my wife, Kirsty.

Abstract

The acoustic environment of a bomb bay or cavity causes large pressure oscillations and the severity of them is a problem that has intrigued researchers for years [68]. Many suppression techniques have been applied with varying degrees of success. Despite this, the understanding of why the pressure oscillations exist or how the suppression methods work have not been investigated as thoroughly. Advances in CFD permits modelling of the cavity environment to be performed and to reveal details about the flow which is difficult to obtain from experiments. The contribution of this thesis is to investigate the flow physics for cavity flows and use the CFD results synergistically with experimental and theroretical information to enhance the understanding of the problem.

The realism of the computational aerodynamics method is substantially validated before any investigation of the flow features is performed, which is the motivation of this work. The verification of the approach is discussed with regards to the problem of grid discretisation for cavity flows. The approach is validated against experimental data for open, transitional-open, transtional-closed, and closed cavity flow from Mach 0.6 to Mach 1.35. For open cavity flow pressure traces taken on the floor of the cavity agree well with those obtained from experiment. Other characteristics of the flow agree well with experimental data and the validation instils confidence that the flow physics simulated.

Open cavity flow is that of most interest to researchers. The flow is typical to that found to exist in the bomb bay of the F-111 and is characterised by intense acoustic levels. A review of the work of previous experimental researchers is included for comparison with the findings of the present thesis. The flow physics indicate that

a series of vortices travel downstream in the cavity and are driven by vorticity generated at the upstream lip of the cavity. When strengthened the downstream moving vortex influences the mass addition and expulsion at the trailing edge initiating a pressure wave which propagates upstream and sustains the process by completing the feedback lopp. These features are elucidated upon in the present thesis. The flow at Mach 0.85 and Mach 1.19 is analysed with only differences in the external stream being apparent for the higher Mach number case.

The suppression of the acoustic environment is investigated by sloping the aft wall of the cavity. The results of the CFD study are used to examine why sloping of the aft cavity wall is successful. It is shown that the flow tends towards a steady state and the results are compared to the hypothesis of Heller and Bliss. This hypothesis is substantiated by the present simulations and in doing so the work demonstrates the ability of CFD to be used as a tool in conjunction with experimental methods to enhance the understanding of cavity flows.

An area of cavity flows for which information is sparse is for the transitional cavity flows. a review of the literature shows that the 4 types of cavity flow exist at supersonic speeds and these are identified by the CFD. The results of the computational study are used to examine when the impingement and exit shocks, characteristic of closed cavity flow, collapse to form a single shock wave. This point is defined as L/D_{crit} and occurs when the vertices of the seperation and recompression wakes merge. It represents the boundary between transitional-closed flow and closed flow and the CFD predictions are compared to Prandtl-Meyer theory when investigating the position of L/D_{crit}.

Similar cavity flows for subsonic speeds are examined. Previously only one type of transitional flow was believed to exist. The CFD study shows that transitional flow can be further classified as transitional-open and transitional-closed flow at subsonic Mach numbers. A previous experimental study was extremely useful in terms of providing the pressure distributions used to classify cavity flows today. However it was not too instructive about the flow features occurring in the transitional

cavities. CFD is used to investigate the flows and indicates erroneous conclusions derived from the experimental results due to a lack of pressure tappings. Once this is identified, other characteristics of the the flow are examined as possible indicators to the type of flow occurring. The value of CFD to be used synergistically with experimental information is clearly demonstrated and is a theme that runs through this thesis.

Acknowledgements

I would like to express my sincere gratitude to my supervisors Dr. Ken Badcock and Prof. Bryan Richards. Their continual assistance and encouragement and relentess enthusiasm have been greatly appreciated. Thanks also to the other members of the CFD group, especially Mark Woodgate, for all their help over the past three years. Special thanks is extended to John Ross from DERA Bedford for generously providing experimental data and fruitful discussions during the course of the study I would also like to express my gratitude to Ian Wrisdale at the Defence Evaluation and Research Agency, Bedford for his advice and practical assistance.

This work is supported by sponsorship from DERA Bedford.

Contents

List of Figures

Nomenclature

a	speed of sound
$\mathbf{A}$	mean Jacobian matrix
c	speed of sound
$d()$	diffusion term
$d\mathbf{x}$	vector of gridpoint displacement
D	cavity depth
e	energy
E	total energy per unit mass
E_t	total energy per unit volume
$\mathbf{F}, \mathbf{G}$	flux vector components
f	frequency
h_{aux}	auxiliary cell area
H	total enthalpy
$\mathbf{I}$	unit matrix
J	Jacobian matrix
k_v	Emperical constant = 0.57
l	cavity length
L	cavity length
M	Mach number
m	mode number

p	pressure
p_{rms}	root mean square pressure
$\mathbf{P}$	vector of primitive variables
Pr	Prandtl number
q	Dynamic pressure
q_x, q_y	heat flux vector components
$\mathbf{R}$	residual
$\mathbf{R}$	matrix of right eigenvectors
$\mathbf{R^{-1}}$	matrix of left eigenvectors
$\mathbf{R}^*$	unsteady residual
Re	Reynolds number
Re_l	Reynolds number based on cavity length
S	separation point
S	Strouhal number
t	time
t^*	pseudo time
T	time period
T	static temperature
T_0	reference temperature, 288.16[K]
u, v	velocity components
U, V	contravariant velocity components
$\mathbf{U}$	vector of state variables
$\mathbf{W}$	vector of conserved variables
x, y	cartesian co-ordinates
α	Emperical Constant = 0.25
β	shock angle

γ	specific heat ratio
δ	non-dimensional longitudinal distance in a cavity
δ	deflection angle
ξ, η	curvilinear co-ordinates
ϵ_r	entropy fix coefficient
λ	eigenvalue
Λ	matrix of eigenvalues
μ	laminar viscosity
ρ	density
τ	stress
i	inviscid
m	pseudo time level
n	time level
v	viscous
$+$	right hand side state
$-$	left hand side state
$*$	dimensional quantities
$\hat{}$	values in general curvilinear form

Subscripts

m	frequency corresponding to mode m
min	minimum
max	maximum
$mean$	mean
n	normal component
t	turbulent component

r	radial component
R	right hand side
t	tangential component
T	values for turbulent flows
x, y, z	components in x,y,z directions
x, y, z	partial differentiation with respect to x,y,z
∞	freestream values

Acronyms

BILU	Block Incomplete Lower-Upper factorisation
CFD	Computational Fluid Dynamics
DERA	Defence Evaluation and Research Agency
GCL	Geometric Conservation Law
GSG	Conjugate Gradient Method
MUSCL	Monotone Upstream-Centred Schemes for Conservation Laws
NATO	North Atlantic Treaty Organisation
PMB2D	Parallel Multi-Block Two-Dimensional
PSI	Pounds per Square Inch
PTT	Pseudo Time Tolerance
RANS	Reynolds Averaged Navier-Stokes
RMS	Root Mean Square
SPL	Sound Pressure Level

Chapter 1

Introduction

Since the 1950's the flow phenomena in aircraft wheel wells and weapon bays has intrigued many researchers. With the USA favouring internal store carriage in current and future generations of fighter aircraft, cavity aerodynamics has received much recent interest. The nature of the pressure fluctuations in a cavity were first investigated in 1955 [52] [68]. About 10 years later the advent of high speed computers saw the development of Computational Fluid Dynamics (CFD). Today the sophisticated computational methods that have been developed have established CFD as a complement to experimental and theoretical aerodynamics. The work of this thesis will use CFD to enhance the explanations of cavity flow physics obtained from experimental work.

The problems associated with cavities in aircraft arose from an apparent lack of foresight by aircraft designers and this does not appear to have changed. Charles Epstein, an expert in the field of carriage and release of stores in tactical military aircraft, recently asked the leading NATO nations how they were planning to carry weapons on the aircraft. Each answered that they would design and test the aircraft first then think about store separation problems. Such an approach then leaves many problems that are often not recognised until the first flight test, which by that time means solutions to the problems can be restricted. The current US defence policies also favour B-2 bombers serving as a vanguard to the military effort. The B-2 bomber is riding a wave of acclaim following its success in Kosovo in 1999, and

a plan to reopen the production line to build 40 more of the bombers is one proposal awaiting a decision in the Pentagon [23]. It is therefore seen that the problems associated with cavities are a current and future challenge.

Some of the problems associated with aircraft cavities are shown by the movies included in the CD accompanying this thesis, which was released by Charles Epstein [28]. The film concerns aircraft-stores compatibility testing and shows conventional weapons release from a B-2 bomber, similar to that represented in Figure 1.1. From the film the store release is far from successful and there is significant downward pitching of the stores, particularly those closest to the cavity rear wall. When you consider that 28 rows of 3 stores, making a total of 84, are being released it is apparent how big a problem cavity aerodynamics is. Indeed footage inside the cavity shows just how small the clearance of each store is and also gives a feel for the turbulent nature of the problem. When the Boeing Company took the film it is said that the pilots would never have considered another mission had they seen the footage. The film confirms the importance of finding ways to alleviate the problems in cavities. Footage of store release from an F-111 (open cavity flow is typical to this type of aircraft cavity) shows successful release of bluff bombs at supersonic speeds. However while the store release was successful it was found that the acoustic environment was so severe parts of the aircraft also fell out the bomb bay with the store! Again the severely turbulent nature of the flow is evident from the film. It is therefore not suprising that researchers are still striving to fully understand the problem and devise methods to suppress the pressure oscillations in a cavity.

The work in this thesis will investigate the flow physics occurring in specific types of cavities. The four types of cavity that have previously been identified can be characterised as open flow, transitional-open flow, transitional-closed flow and closed flow. The type of flow occurring is dependant on the length/depth (L/D) ratio of the cavity. The terminology *closed* and *open* flow first appears in the paper by Charwat et al [21]. Intuition suggest that the terms may be better suited if swapped around. Charwat offers no explanation for the choice of terms so the reason for them is open to conjecture. There may be a connection to the engineering case of a heat engine with a closed cycle. For this the working substance is continuously circulated

Figure 1.1: B-2 bomber releasing stores

and does not need replenished - a situation that is similar to what happens for the separation and recompression wakes familiar to closed flow. The separation and recompression regions are closed, while for the smaller L/D ratios mass addition and expulsion occur justifying the open flow terminology.

Open flow generally occurs when the cavity is deep (L/D$\leq$8), as found in bomb bays typical of the F-111. For this case the flow essentially bridges the cavity with a shear layer forming over the cavity. Despite the flow being highly complex a nearly uniform longitudinal static pressure distribution is produced and good store separation is generally not difficult to achieve. However the problem with open cavity flow concerns the acoustic environment. Resonant tones occur in the cavity and the pressure fluctuations in the cavity can cause acoustic levels between 160 and 180 db. These levels, similar to a jet engine exhaust at 20 feet or a booster rocket, can cause early structural failure and damage to store avionics. Open cavity flow will be investigated in chapter 3 while chapter 4 investigates the effect of a rear wall sloping as a device to alleviate the acoustic environment. The second type of cavity flow is for shallow cavities and is termed closed cavity flow. This cavity configuration is

typical of the bomb bays of a B1 bomber. Closed cavity flow generally occurs for L/D≥13. In closed cavity flow, the flow separates at the forward face of the cavity, reattaches at some point along the cavity floor, and separates again before reaching the rear cavity bulkhead. For shallow cavities where the flow is of the closed type, acoustic tones are not present; however, the flow produces an adverse static pressure gradient that can cause the separating store to experience large nose-into-the-cavity pitching moments. Closed cavity flow will be investigated in chapters 5 and 6. The third and fourth mean cavity flow types occur for cavities with values of L/D that fall between closed cavity flow and open cavity flow and are slight variations of these defined flows. There is very little understanding of the transitional cavity flows which are considered in Chapters 5 and 6.

Cavity aeroacoustics and the associated problems have been investigated experimentally since 1955 [52] [68] yet there are many questions still unanswered. Indeed one of the most renowned researchers in the field, H Heller, recently published a paper [42] detailing experimental results similar to those he first published in 1975 [41], albeit using a different experimental technique. There are still many questions relating to what is the driving mechanism of cavity flows. In this respect it is arguable that the understanding of cavity flow mechanisms is no further on than it was 40 years ago. Part of the problem is attributable to the fact that experiments can be limited with regards to what they can reveal about cavity flowfields, especially at supersonic speeds. Another significant factor contributing to this lack of understanding is the approach many researchers appear to have taken when investigating cavity flows. The main practical problem of interest is the severe acoustics experienced in the cavity. Much of the previous research documented in the literature is intent on solving the problem rather than understanding exactly what causes it. So while the experimental work reached a plateau with regards to understanding the problem, methods of suppressing the flow and the development of ingenious palliative devices went into overdrive. Undeniably there has been success in suppressing cavity tones but much of this is attributable to the sheer volume of ad-hoc methods that have been investigated.

This work will use CFD to enhance understanding of the physical phenomena in cavity flows. With the information obtained from the simulations for open cavity flow the suppression of cavity pressure oscillations and the effectiveness of sloping of rear cavity walls can be evaluated more methodically. Industry is continually embracing the idea of CFD being of use in the design process thus offering another avenue to the methods of experiment and pure theory. One early success was the experimental NASA aircraft called HiMAT (Highly Manoeuvrable Aircraft Technology), *designed to test concepts of high manoeuvrability for the next generation of flight planes. Wind tunnel tests of preliminary design for HiMAT showed it would have unacceptable drag at speeds near the speed of sound; if built that way the plane would be unable to provide any useful data. The cost of redesigning it in further wind tunnel tests would have been around $150,000 and would have unacceptably delayed the project. Instead, the wing was redesigned by a computer at a cost of $6,000.*[19] Boeing also used CFD substantially in designing the 777. This is not to suggest that CFD is infallible as consideration must be given to discretisation error, turbulence models, convergence and linearisation errors. However as long as you are aware of the limitations in the numerical techniques, even if you can not quantify them in a particular solution, the results can still be interpreted successfully. Similarly many experiments of real life engineering problems are made with assumptions in them i.e. not Reynolds number matched, wrong flow boundary conditions. This is often required as it is not possible to run the correct experiment within a reasonable budget/timescale. Therefore, like CFD, care has to be exercised in interpreting the results and drawing conclusions. Generally subscale experiments have to be validated in the real device which may not be possible until the first production unit is in place. In these cases and more specifically cavity aerodynamics, CFD can provide a coplementary avenue of investigation. Cavity tests are prohibitively expensive. One method of aircraft-stores compatibility testing is drop model testing. An F-111 model will be constructed for a wind tunnel and to drop a store from the bomb bay the heavy scaling laws are used to build the model of the store. This often means that expensive materials, such as gold, are required for the model. Also if a $100,000 experimental test is conducted and a few weeks later you detect something unexpected in the data or that you needed more instrumentation it is often difficult

to re-run the test programme. The advantage with CFD is that the solution can be investigated whenever and wherever in the space that is of interest. However there still exists the problem of validating the CFD data. The primary impetus of this thesis is to show that experiments and CFD can be used in tandem to elucidate what is known about cavity flows. The aim is to use CFD in areas that experiments have yet to address and thus provide further information concerning cavity flow phenomena. Consideration of the information previously known will then be used with the CFD information in an attempt to enhance what is known about open, transitional and closed cavity flows - and which is a main objective of this thesis.

In chapter 2 wind tunnel data will be used to validate the CFD results. The realism of the results is important and the simulation is substantially validated. The frequencies and amplitudes of the discrete tones and Sound Pressure Levels (SPLs) are considered. Direct comparisons of pressure history traces in the cavity are shown for the experimental and CFD data. Verification of the method is discussed and issues of turbulence modelling and discretisation (grid included error) as well as the approach to solving the Reynolds Averaged Navier Stokes equations are considered.

In chapter 3 CFD is used to enhance the understanding of cavity flows obtained from wind tunnel analysis. A review of the findings from the main experimental works is presented. The flow phenomena in the cavity are described for Mach 0.85 flow over an open cavity. The detailed flowfield is shown to be characterised by a series of vortices convecting downstream while pressure waves emanating from the trailing edge propagate upstream. The effect of Mach number is considered. The CFD simulations are used to elucidate the earlier explanations derived from experimental studies. An understanding of the flow features by CFD allows the suppression of cavity tones to be investigated in the subsequent chapter methodically. Using the jigsaw analogy the puzzle is known and can now be solved.

Chapter 4 concerns the effect of sloping the rear cavity wall as a device to suppress cavity pressure oscillations. It is obvious that CFD can be used in the initial winnowing of possible suppression devices. Heller & Bliss [41] and Franke & Carr

[32] experimentally investigated the effect of many suppression devices. Several of the concepts did not reduce oscillatory amplitudes, and on occasion caused higher levels than observed in the basic cavity. The sloped rear wall cavities simulated have already been investigated experimentally with regards to the extent of the suppression achieved. The current simulations allow a description of how the sloped aft wall suppresses cavity pressure oscillations.

Chapters 5 and 6 concerns the use of CFD to investigate cavity flows for which very little information has been documented in the literature. The understanding of transitional cavity flow phenomena is relatively sparse compared to that for open and closed cavity flow. The general method to classify cavity flows is consideration of the pressure distributions along the cavity floor. This indicator is used in chapter 5 to identify the types of flow occurring for cavities with L/D ratios from 10 to 20. By considering theoretical fluid dynamics the flow over a closed cavity is analysed in detail. This is an area that CFD can be used to investigate the physical phenomena occurring which may be influenced by experimental procedures. At supersonic speeds the experiment gradually increased or decreased the cavity L/D ratio during the experiment via a sliding block facility. The L/D ratios were not investigated individually and so a hysteresis region is found to exist depending on whether the L/D ratio is increasing or decreasing. The CFD results will not have this uncertainty and this can be viewed as a model situation where the experimental study is limited and CFD has a potential role to play. The detail obtained from the CFD study enables identification of the flow features not previously detected by experiments.

Chapter 6 extends the analysis of transitional cavity flow phenomena from supersonic speeds to subsonic regimes. In particular the boundaries where the cavity flow changes from open to transitional and from transitional to closed cavity flow are defined. These boundaries were defined by interpretation of the pressure distributions along the cavity floor from experiments. CFD effectively allows more data sample points than compared to experiment and the present results show interesting trends in the data that can be used to elucidate the classification of cavity flows, specifically those in the transitional regime. These trends are related to the flow

behaviour and the description of the flow phenomena for transitional cavity flow completes the cavity set. Finally, comparisons are drawn between subsonic results and the supersonic ones from the preceding chapter.

The important results from the thesis are summarised in the Chapter 7. The aim of the work to use CFD to complement both experimental and theoretical fluid dynamics in the solution and analysis of cavity aerodynamic problems will be reviewed. Recommendations for future work are suggested.

Chapter 2

Simulation details

2.1 Overview

This chapter considers the simulation details and presents a validation and verification study to evaluate the realism of the solutions obtained. The chapter starts with a discussion of the modelling options available and then moves on to consider the turbulence modelling issue. Next, the RANS simulation results for the three types of flow considered in detail in the following chapters, are assessed for numerical accuracy and physical realism.

2.2 Mathematical Models

Several factors dictated the choice of mathematical models used in the present study. Intuitively the numerical approach must be time accurate to model the unsteady flow features. The unsteady shear layer that traverses the cavity opening, typical of high Reynolds number flow, must be resolved spatially which necessitates grid clustering along wall boundaries to capture the boundary layer. Since the flows over a cavity involve strong viscous-inviscid interactions with large separated flow regions, the results in this thesis are obtained by solution of the Navier-Stokes equations. These equations are derived by considering the conservation of mass, momentum and energy and result in a system of non-linear partial differential equations. Although a three-dimensional analysis is possible previous experimental and

computational studies [80] [64] [61] [88] have shown that even for three-dimensional cavities the fundamental flow behaviour, particularly along the cavity centreline is predominantly two-dimensional in nature. The present results are also compared with the case of a cavity with the bay doors at 90°. The likely effect of the doors is to channel the flow down the cavity, preventing leakage in the spanwise direction. It is therefore suggested that the case with doors vertically up is likely to be more two-dimensional than when the doors are off. The two-dimensional Navier-Stokes equations are given in Appendix B

To account for the turbulent characteristics of the flow it is normal to employ a time averaging. The resulting equations are called the Reynolds Averaged Navier-Stokes equations (RANS). The RANS form of the equations consists of a time averaged component and a turbulent fluctuating component giving the following terms, for example for density, pressure and velocity components, to replace the instantaneous components:

$$u = \bar{u} + u', \qquad v = \bar{v} + v', \qquad \rho = \bar{\rho} + \rho', \qquad p = \bar{p} + p'$$

An alternative method to Reynolds averaging the NS equations over a suitable time scale is to solve the NS equations on a grid with the spacing resolution small enough to capture the smallest turbulent length scales. An extremely fine grid would be required and such an approach is impractical in terms of cost and time. For RANs the effective viscosity is taken as the sum of the molecular and turbulent viscosities where the turbulent viscosity, μ_T is calculated by means of the $k - \omega$ turbulence model. For the high Reynolds number flows typical to cavities the upstream boundary layer is turbulent.

2.3 Turbulence Influences for Cavity Flows

There have been two main types of turbulence modelling used for the cavity flow simulations described in the literature. The first is in the class of algebraic models, the most prominent example being Baldwin-Lomax. The second is the family of two equation turbulent kinetic energy based models, amongst which are $k - \omega$ and $k - \epsilon$.

2.3.1 Algebraic based studies

A modified form of Baldwin-Lomax was used in [64]. For points outside the cavity the usual form of the Baldwin-Lomax model is used. Inside the cavity a relaxation approach is used to provide a sense of history to the development of the turbulence. The eddy-viscosity applied is an average of the top corner and locally calculated values, weighted by the distance from the upstream wall. The example considered had $M_\infty = 1.5$ and $Re = 1.09$ million. The mean flow equations were solved by a predictor-corrector method using a reduced time step of 0.00073, with sampling between reduced times of 4.27 and 23.23. The grid used for half the cavity span had 43.5k points in the cavity and 110.25k points outside. No time step or grid refinement was presented.

A two-dimensional version of this case was examined in ref [46] with the Beam-Warming factorisation used for the time stepping. A grid of only 5.5k points was claimed to be adequate. No grid or time step refinement results were presented. The turbulence model was again based on a relaxed version of the Baldwin-Lomax model.

A relaxed version of the Deiwert mixing length model was used in ref [95]. Again the relaxation was applied in the cavity based on the upstream corner value of the eddy viscosity. The example used was at $M_\infty = 1.5$, $Re = 1.35$ million and L/D=3. Explicit two step differencing was used and no time or grid refinement presented.

A relaxed version of the Cebeci-Smith model was used in ref [50]. A supersonic open case was examined at $M_\infty = 1.5$, a Reynolds' number of 2 million and L/D=6. The time marching was by the explicit predictor-corrector method and time histories were judged to have settled at a reduced time of 30. The grid only had 3700 points. No grid or time step convergence was presented.

In ref [14] the modified Baldwin-Lomax model was used to compute cavity flow at $M_\infty = 0.95$, a Reynolds' number of 8 million and L/D=4.5. The grid used had 18875 points and no refinement study was shown. The Beam-Warming approximate factorisation was used for the time stepping and significant differences between first

and second order time accuracy was observed. No time step refinement was shown and sampling was made between times 5 and 85.

Finally, a comparison of the influence of different forms of the Baldwin-Lomax model was made [85]. An LU decomposition with sub-iterations was used for the time stepping and the case considered had $M_\infty = 2.0$, $Re = 0.369$ million and L/D=2.0. A grid with 15.18k points was used and it was stated that a grid with double the number of points in each direction gave results which were only marginally different. However, no results were shown to support this claim. Sampling was carried out over 71 characteristic times but no time step refinement was shown. The models compared were four versions of the Baldwin-Lomax model, including the upstream relaxation model and two versions of a laminar description, first laminar everywhere and alternatively laminar in and above the cavity. All of the models give similar qualitative results with the standard Baldwin-Lomax model giving levels about 10dB lower than the other models.

2.3.2 Two equation kinetic energy based studies

In ref [76], Chen's 2-equation turbulence model was used with Nichol's compressibility and strain corrections. The Beam-Warming approximate factorisation was used to solve the equations in 64k time steps up to a characteristic time of 16. No time step refinement was presented. The case computed was identical to the one of [64] described above. The grid used had 11500 points but no refinement study was presented. Similar results to those obtained for a two-dimensional simulation using the relaxed Baldwin-Lomax model were obtained.

In ref [98] the $k - \omega$ model was used, modified for compressibility effects. A reduced time step of 0.01 was used to compute the case considered in [95] (described above) to a characteristic time of 600. No time step refinement was presented. Two grids were tested for the turbulent simulations and a time trace of pressure at one location in the cavity over the early development of the flow was shown to be similar on the two grids. The SPL results seem to be inconsistent with those in ref [95].

2.3.3 Summary of RANS Modelling

With the exception of the systematic study of ref [85] it is difficult to draw conclusions on the influence of the turbulence modelling, despite similar cases being studied by several authors. There is very little evaluation of the influences of numerical accuracy, making direct comparisons of little value. The evidence from the study of [85] suggests that the unmodified Baldwin-Lomax model results in turbulence values which are too high, leading to lower pressure fluctuations than observed in experiment. There is no evidence of a clear cut advantage in using the two-equation turbulence models as opposed to the relaxed version of a mixing length model. The laminar results given in [85] agree to within 5dB with the relaxed turbulent results.

2.3.4 Validity of RANS

The time averaging used to derive the RANS equations means that these can only be used to model unsteady flows when there is a clear frequency gap between time scales of the mean flow resolved on the grid and the turbulence which is described by the turbulence model. Given the high frequency components present in the cavity flow it seems doubtful whether this is the case for this situation. When no gap is present the minimum level of modelling necessary for a rigorous analysis is Large Eddy Simulation (LES) where part of the turbulent spectrum is resolved on the grid and influence of the sub-grid eddies is modelled. The cost of LES at large Reynolds numbers is very large to allow resolution of the spectrum down to inertial scales. There are no published LES results for cavity flows at conditions approaching the Mach and Reynolds numbers of interest for the current work.

Some recent work has considered a hybrid RANS-LES approach for cavity flows. The company CRAFT has developed two approaches [78] [77]. The first is based on using a coarse grid LES, termed VLES [78], to resolve only the largest eddies on the grid and to model the sub-grid scale eddies using the Smagorinski model. The approach was seen to give better agreement with measurements than the Baldwin-Lomax model but no assessment of the predictions as the grid is refined was made. A second approach is a hybrid of RANS-LES and involves matching a near-wall

RANS solution with an outer LES solution. Again no detailed evaluation of the performance of the approach was made.

A second approach followed by the company Metacomp involves using a scaling of the eddy viscosity to remove the contribution of turbulence which has already been resolved on the grid [13]. The technique, termed LNS, showed some differences in the level of fluctuations observed for a cavity test case but no real evaluation was presented. However, the approach is rationally based.

For cavity simulations the choice is therefore seen to be between RANS which is theoretically doubtful or other LES inspired approaches which are either unproven or too costly. The approach taken in this thesis is to use the RANS predictions in conjunction with all available experimental data. It is hoped that the credibility of the simulation results can therefore be established and then used to provide extra information. It is however anticipated that numerical problems will be encountered with, for example, obtaining a grid independent solution.

2.4 Numerical Method and Data Analysis

2.4.1 Numerical Method

The PMB2D code was used for the calculations presented in this thesis. This is a generic CFD code developed at the University of Glasgow and has been used to successfully model steady and unsteady flows including aerofoils [25], wings, rearward facing steps [38], jets [39], in subsonic, transonic and more recently hypersonic flows. The predominant features of the code are described in [11] and are summarised here. A cell-centred finite volume discretisation method is employed to solve the RANS equations. The current formulation employs Osher's flux approximation scheme and MUSCL variable interpolation for the discretisation of the convective terms occurring in the governing equations. Central differencing is used to discretise the diffusive terms. A steady state calculation proceeds in two phases, where the freestream starting solution is initially smoothed using an explicit scheme and then an implicit scheme is used to obtain rapid convergence. The linear system

arising at each implicit time step is solved using a Generalised Conjugate Gradient method and a BILU factorisation is used as a preconditioner. The code employs a structured multi-block grid system. An important feature of the code is the use of approximate Jacobian matrices for the left hand side of the linear system. The k-ω turbulent model is implemented to describe the influence of turbulence. The unsteady part of the code employs an implicit unfactored dual-time method. Here, the rate of convergence between two consecutive real-time steps is monitored by the so-called Pseudo Time Tolerance (PTT), which is defined as

$$\frac{||\mathbf{w}^{n+1,m+1} - \mathbf{w}^{n+1,m}||_2}{||\mathbf{w}^{n+1,m+1} - \mathbf{w}^{n}||_2}$$

where $\mathbf{w} = (\rho, \rho u, \rho v, \rho E)$ is the vector of conserved variables and $\mathbf{w}^{n,m}$ denotes the m-th pseudo time iterate at the n-th real time level. The detailed formulation is described in Appendix B

2.4.2 Data Analysis

A comparison of the CFD pressure traces with a section taken from experiment is shown in Figures 2.1 and 2.2. As will be seen in RMS spectra plots, the CFD data is more sinusoidal in nature than the experimental data. However, as is evident in Figure 2.1, the comparison of the CFD data with a portion from experiment is very good indeed. The pressure is plotted in Pounds per square inch (PSI) and the time is in seconds. The agreement is quite remarkable and has never been shown to such an extent by other researchers. Numerous works have analysed the flow features but only show comparison with power spectral densities and sound pressure levels in the cavity. Even then the comparisons are not astounding. To date this is the only study to show a direct comparison of the pressure traces. The acoustic streamwise pressure distributions along the cavity floor are represented as the Root Mean Square (RMS) pressures and the overall sound pressure level, SPL. The RMS pressure values are a measure of the statistical standard deviation of the signal and as such provide the magnitude of the fluctuating component around the mean value. The RMS of the

pressure is calculated as follows:

$$P_{rms} = \sqrt{\left(\frac{\sum(P - P_{mean})^2}{n}\right)}$$

The SPL in decibels (dB) is defined as:

$$SPL(dB) = 20\, log_{10}\left(P_{rms}/2\, x\, 10^{-5} Pa\right)$$

where $2\, x\, 10^{-5} Pa$ is the standard reference pressure [57]. In addition to the results being presented in terms of the logarithmic decibel scale, they will also be shown in terms of P_{rms}/q.

It is probably better to use a cumulative distribution function over RMS pressure analysis in that frequency resolution problems and window sizes cease to be an issue. However the present analysis intends only to identify frequencies and compare the effects of suppression in later chapters and therefore RMS pressure analysis will suffice. Also power spectral density (PSD) representation is more suited to broad band pressure spectra rather than the narrow band which is typical of cavity modes. So it is more appropriate to use power spectrum when looking at the current data.

For the experimental data the sample is over 3 seconds long with a time increment of 0.0001667 seconds. The sampling rate is 6000Hz and the frequency resolution is 10Hz for 600 samples per window. Figure 2.3 shows an acoustic spectra along the cavity floor. The computational data is for a sample of a much shorter time of 0.1016 s. The time increment is 0.0000339 s and the resolution is 12Hz. The associated spectra are shown in Figure 2.4. The discrete frequencies of interest are predicted reasonably well, with the dominant second tone of 413 Hz from CFD comparing to the 381 Hz predicted experimentally. This is well within the 10 % tolerance from the Rossiter [69] and Smith [79] empirical formula. The 1st and 3rd tones are also picked up by the simulations and again compare reasonably well. However the RMS pressure levels are over-predicted by CFD and for some locations are double the amplitude for the corresponding experimental frequencies. This leads to an over-prediction of the overall sound pressure levels (SPL's) by CFD in the cavity. This can be seen in Figure 2.13. The CFD results do not capture the noise which is

clearly present in the experiment. From the pressure history traces (Figures 2.1 and 2.2) the experimental data is more random in nature than the CFD data which is sinusoidal for all locations apart from X/L= 0.25, X/L=0.65 and X/L=0.75. The background noise has the effect of adding to the overall SPLs so that it is closer to the CFD predictions than it would be without the noise.

2.5 Open Subsonic and Supersonic Flow

2.5.1 Description of Experimental Test Cases

Experimental Data

Comparisons of predictions by the current method are made with experimental data provided by John Ross of Defence and Evaluation Research Agency, Bedford [72]. Test were carried out in the Aircraft Research Association Ltd 9ft x 8ft (2.74m x 2.44m) transonic wind tunnel at Mach numbers of 0.6, 0.8, 0.85, 0.9, 0.98, 1.1, 1.19 and 1.35. Tunnel total pressure in all cases was atmospheric. The rectangular cavity tested has a length-to-depth (L/D) ratio of 5 and a width to depth (W/D) ratio of 1. The cavity houses a one tenth scale AMRAM missile which is sting mounted at the centre line. It is felt the carriage of the missile will not significantly effect the overall flow physics of the cavity environment. This is supported by the similarity in measured pressure fluctuations on the cavity floor between cases with the missile at different vertical heights. The selected test cases are shown in table 6.1.

Pressure time histories were measured along a line at one quarter span on the floor of the cavity. The tests were carried out with bay doors at various angles. Large differences were observed between the pressure fluctuations obtained with doors vertically up and doors off, as shown in figure 2.10. The width to length ratio of the cavity suggests that three dimensional effects will be significant. The likely effect of the doors is to channel the flow down the cavity, preventing leakage in the spanwise direction. It is therefore suggested that the case with doors vertically up is likely to be more two-dimensional than when the doors are off. Comparisons are made in this section between the calculations on the coarse grid described in the previous

Mach Number	Re(per unit length)	L/D
0.4*	4.126e6	5
0.6	5.630e6	5
0.85	6.783e6	5
0.98	7.149e6	5
1.19	7.348e6	5

Table 2.1: Summary of Test Cases; * no experimental data at Mach 0.4

section and the experimental data. The SPL distributions are shown in figure 2.13 and show excellent qualitative and quantitive agreement, providing some support for the contention that the data set obtained with vertical doors is the most appropriate for the validation of a two-dimensional simulation.

2.5.2 Verification

A detailed evaluation of the influences of the simulation parameters for the M=0.85 case is made. The parameters of interest are time step, grid density, pseudo time convergence level, settling time and far field boundary conditions. Two grids were generated for these investigations. The dimensions and extent of the coarse grid are shown in figures 2.5 and 2.6. A coarse grid was extracted from the fine one by taking every second point. The fine grid has a total of 63266 points and the coarse grid 20301. Results in this section are shown in terms of the time averaged pressure fluctuation distributions along the cavity floor in terms of root mean squared (RMS) or sound pressure level (SPL) values.

Boundary Conditions

The boundary conditions used are solid wall on the plates and cavity walls, symmetry conditions ahead and after the plates and far field conditions. For supersonic cases it is possible to curtail the computational domain on the plates before and after the cavity by imposing a boundary layer profile upstream and extrapolating variables downstream [8]. However, for subsonic freestreams, this treatment does not allow the

unsteadiness due to the cavity to propagate correctly out of the domain. Numerical tests on a laminar case at M=0.6, L/D=5 suggested that a far field distance of 5L was adequate to remove significant dependence of the solutions on domain size [8].

Time Accuracy

Non-dimensional time steps of 0.005 and 0.02 were used to calculate the evolution of the flow on the coarse grid. These give respectively 560 and 140 time steps for the dominant frequency in the flow and a resolution of about 50 and 12 steps for the fourth mode. The distribution for these two time steps is shown in figure 2.7 and shows excellent agreement, suggesting that a time step of 0.02 is adequate on this grid. The calculation on the fine grid at this time step however shows a different behaviour with the first main frequency from the coarse solution absent. The use of a smaller time step, 0.005, on the fine grid results in the reappearance of the first frequency. Since the calculation at the smaller time step took 3 weeks of CPU time it was not possible to demonstrate temporal convergence on the fine grid. However it is noted that a smaller time step is required on the fine grid than the coarse.

Grid Refinement

The comparison of the distributions obtained on the coarse and fine grids is shown in figure 2.8. The two sets of results are not close, either qualitatively or quantitatively. Tests at higher Mach numbers have shown that the solution is sensitive to refinement across the cavity, but not in the streamwise direction. It is noticeable in the literature that no comprehensive grid refinement study has been published and from communications with engineers at BAE SYSTEMS, this sensitivity has been observed using Fluent [10]. Further communications with researchers at University of Illinois have highlighted similar problems.

A possible explanation for the observed behaviour is that the RANS modelling is not appropriate, as discussed above. The implication of this for grid refinement is that more layers of vortical structures would be resolved on the finer grids. A set of laminar calculations was used to investigate this on a sequence of grids which included an extra fine level. The instantaneous flow visualisation on these three

grids showed the resolution of extra layers of complexity in the vortical structures as suggested. When using RANS, the effect of turbulent eddies is modelled through the turbulence model. If the eddies are also resolved on the grid, then a form of double accounting is taking place. In this case, no grid converged solutions would be obtained using RANS.

Settling

The irregular nature of the time histories means that some care has to be taken when calculating time averaged pressure fluctuations. The comparison of the distributions obtained on the coarse grid for two time intervals, 10-21 and 10-57, is shown in figure 2.9 and shows that the interval 10-21 is adequate.

Pseudo Time Convergence Level

The influence of the convergence level is significant. Using the measure defined in the equation, the influence was tested for levels of 0.005 and 0.001 (i.e. ratio of latest pseudo time update to real time update was 0.5% and 0.1% respectively). The distributions obtained are identical. However, when a value of 0.05 is used the pressure fluctuations damp out and the flow reaches a steady state.

2.5.3 Validation

Frequencies

The frequencies of the discrete tones measured in the computations are compared with those predicted by the empirical formula developed by Rossiter [69] and modified by Smith [79] to give

$$f_m = \frac{U_\infty}{L} \frac{m - \alpha}{\frac{M_\infty}{\sqrt{1+[(\gamma-1)/2]M_\infty^2}} + \frac{1}{k_v}}$$

where γ is the ratio of specific heats; M_∞ and U_∞ are the freestream Mach number and flow speed, respectively; and f_m is the resonant frequency corresponding to the mth mode. Heller and Bliss determined from their experiments that the constants α and k_v are 0.25 and 0.57, respectively[41]. Heller [40] estimated that for cavities with a L/D ratio of 4 or greater , the difference between the Rossiter formula and

experiments should be within 10%

Figure 2.11 shows the variation of the Strouhal numbers between Mach 0.4 and Mach 1.19 for a cavity with L/D=5. The lines represent the Strouhal number predicted by the above equation for the first four modes. The symbols, depicting the computational predictions, show that the measured frequencies are well within desired accuracy. This agreement is generally attained for simulated results. The real challenge for a simulation is to predict fluctuation levels realistically.

SPL at Mach 0.85

First consider the results at a freestream Mach number of 0.85. A comparison of the simulated SPL distribution along the cavity floor is made with experiment in figure 2.13. The non-dimensionalised root mean square pressure distribution is shown in figure 2.12. From both comparisons the qualitative and quantitative trends of the computational predictions closely adhere to those obtained by experiment:

- There is a drop in the SPL between the front bulkhead and 1/4 length position.
- This is followed by an increase in SPL till a plateau is reached near the centre of the cavity
- A second decrease in SPL is then seen to occur before, as expected, the SPL rises significantly as the rear bulkhead is approached.

The main discrepancies between the results are seen near the rear bulkhead where the computational results over-predict the SPL by about 2dB.

SPL at Mach 1.19

Comparisons of experimental and computed data for the SPL at a freestream Mach number of 1.19 are shown in figure 2.14. The difference between calculation and the experimental data ranges from 1 to 10dB. However, the shape of the distribution is well represented by the calculation The major differences are seen to occur at X/L = 0.25 and $0.6 \leq X/L \leq 0.8$. At most the difference is 10dB occurring at the 0.25 location. It will be discussed in chapter 3 that at these locations significant

interactions between waves and vortices occur. The prediction of the SPL near the rear bulkhead is again seen to be within 2dB of the experimental data. For the purposes of understanding cavity flow mechanisms the excellent qualitative agreement is significant.

Mach 0.4 to Mach 1.19

The variation of the SPL with Mach number for selected cavity probe positions is shown in Figure 2.15. Data is presented at X/L locations of 0.55 and 0.95. No particular emphasis is placed on these locations given since they were the only positions for which data was available over the range of Mach numbers. No experimental data was available for Mach 0.4. From the figure it is seen that the simulation predicts the SPL levels well at these locations throughout the Mach number range.

2.6 Transitional Supersonic Flow

2.6.1 Verification

The Mach 1.35 freestream flow over a cavity with L/D=10 is considered. This flow is steady and is called transitional as will be discussed in chapter 5. The distributions of pressure and skin friction along the cavity floor are shown in figures 2.17 (a) and (b) are very similar. The grid dimensions are as for the subsonic open cavity flow cases.

2.6.2 Validation

The pressure distribution along the cavity floor is shown in figure 2.16.The experimental data taken from Kaufman [48] for similar conditions is included for comparison. Agreement is seen to be good both qualitatively and quantitatively. This is the only experimental data available for validation.

2.7 Subsonic Transitional Flow

2.7.1 Verification

As the length to depth ratio is increased the flow type changes from open flow which is characterised by strong unsteadiness to closed flow which is steady. There is a region where the flow is termed transitional and this will be investigated in chapter 6.

The solution for the L/D=12 cavity at Mach 0.85, which is transitional closed flow, converges to a steady state. The fine grid has around 64,000 points with over 20,000 being in the cavity. A coarse grid has a total near 16,000 points with just over 10,000 being in the cavity. The pressure and skin friction distributions on the floor of the cavity are shown in figures 2.18 (a) and (b) and indicate a grid independent solution. The streamlines obtained on the coarse and fine grids are shown in figures 2.19 and 2.20 and very similar features are observed.

The verification for the open-transitional case at L/D=8 and a freestream Mach number of 0.9 yielded identical conclusions to those given above for the L/D=5 cavity.

2.7.2 Validation

The transitional-open results for L/D=8 were compared with the experimental results of references [61] and [88]. The experimental data was obtained for cavities with varying W/D from 1 to 4. The data obtained with W/D=4 is used here as the three-dimensional effects are likely to be minimised.

The predicted sound pressure levels from a pressure trace in the cavity is shown in figure 2.21 for the M=0.9 transitional flow case. The experimental frequencies detected by Tracy [88] are shown by the vertical dashed lines and these agree well with the tones predicted numerically. The frequency content is highlighted for the dominant mode (mode 2) at 400Hz and the value of 148 dB agrees very well with the experimental level, as is evident from figure 2.21.

The pressure distribution along the cavity floor for the same case is shown in figure 2.22(a). The comparison of the prediction with the static pressures measured in the experiment is very good both qualitatively and quantitatively. The cavity aft wall pressures are compared with experiment in figure 2.22(b). The experimental setup allowed only for a limited number of pressure ports on the aft wall and these are shown by the four symbols. Again agreement is good. Further discussion of the aft wall pressures will be presented later.

2.8 Closed Supersonic Cavity Flow

In the closed cavity flow computation, no significant flow fluctuations were detected after the initial transient is purged, Figure 2.23. The small amplitude oscillations observed in the pressure history plot are thought to be associated with the expected unsteadiness from the shear layer separation. Figure 2.23 shows the monitored pressure trace at selected positions within the cavity. It is seen, as expected, that differences between pressure at the front and rear of the cavity do exist.

The computed skin friction coefficient distribution over the cavity floor is shown in Figure 2.25 and helps identify the flow separation and reattachment points. It can be seen that the skin friction is negative in the areas dominated by the two vortices; the larger vortex formed at the front wall occupies the area between $0.0 \leq X/L \leq 0.2$, whilst the smaller vortex at the rear wall occupies $0.8 \leq X/L \leq 1.0$. The shear layer impingement location after the initial separation is seen to occur at X/L=0.2. The separation location before the rear wall occurs at X/L=0.75. The present computed skin friction coeffiecient distribution shows good qualitative agreement with that of Kim [49].

Considering the Cp distributions, shown in Figure 2.24, the computation underpredicts the pressures near the forward wall and over predicts the pressures near the rear wall. The source of this discrepancy is thought to be attributable to 3-dimensional effects [49]. For closed cavities it is thought that the cavity width in the experiments contributes to the shear layer expanding more freely in to the cav-

ity. This would cause a greater flow deflection at the front wall hence producing lower pressures in this location. The stronger expansion of the flow inevitably leads to the cavity flow being faster than in purely 2-dimensional flow. Intuitively, this flow, with the increased velocity, would produce a stronger exit shock which in turn causes the higher pressure rise close to the rear wall. Overall the results show good qualitative agreement with the experimental values. In addition the present computation, in agreement with experiment, shows the pressure coefficient on the rear face to decrease as the top of the cavity is approached. This was not predicted in the computations of Kim.

2.9 Conclusions

The evaluation of the numerical scheme carried out in this chapter for open flow has shown the following:

- convergence with respect to the time step was achieved, although the time step required was dependent on the grid
- the pseudo time convergence level needs to be tight, otherwise the pressure histories were damped
- far field boundary conditions are needed for subsonic freestreams, whereas the domain can be truncated using a boundary later profile on the upstream plate and variable extrapolation downstream, for supersonic flow
- the coarse grid results show excellent agreement with experiment over a range of Mach numbers
- this agreement is lost on grid refinement
- the behaviour observed from grid refinement is consistent with the suggestion that RANS is inappropriate for these flows due to mean flow-turbulence interaction

A satisfactory simulation must have demonstrated grid convergence. However, it has been argued that it is not possible to achieve this using RANS modelling. Since

LES is unproven at the Reynolds' numbers of interest here it was decided to exploit the excellent agreement with experiment on the coarse grid to analyse flow mechanisms. The viscous element to a cavity flow comes from the generation of vorticity involving the shear layer. Various sources of diffusion are present in the simulation, namely modelling of molecular and turbulent, and numerical. It is possible that the balance between these elements on the coarse grid gives a level which is realistic, even though the elements are not in the correct proportions. Careful evaluation of the flow field with all available information from other sources is required to put this study on as sure a footing as possible due to the absence of grid convergence. Developments in LES will provide a future check on the conclusions of the present study. A better understanding of the flow mechanisms is important to help design control approaches. The ultimate test of these is made experimentally. Hence, in the absence of a satisfactory alternative, it was felt that analysing the coarse grid RANS solutions could give useful information and this is done below in chapter 3.

For the steady solutions obtained for shallower cavities grid independent solutions have been demonstrated and good agreement with the limited experimental data achieved. This provides a good basis to examine the mechanisms involved with the transition from open to closed flow for the supersonic and subsonic cases.

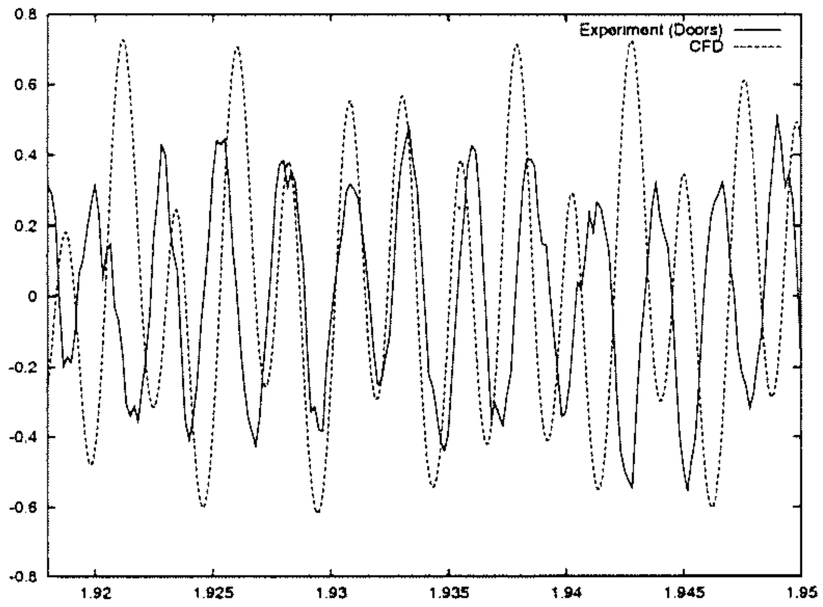

(a) X/L=0.05

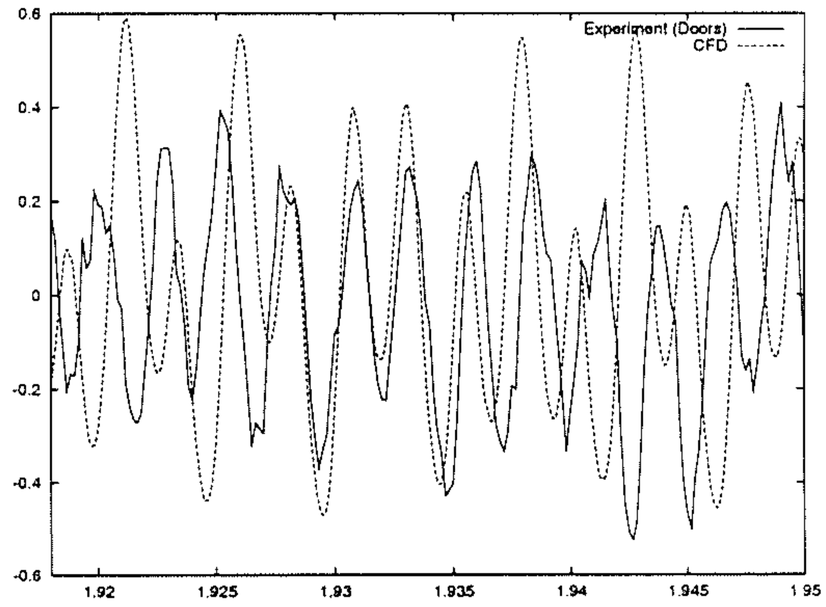

(b) X/L=0.15

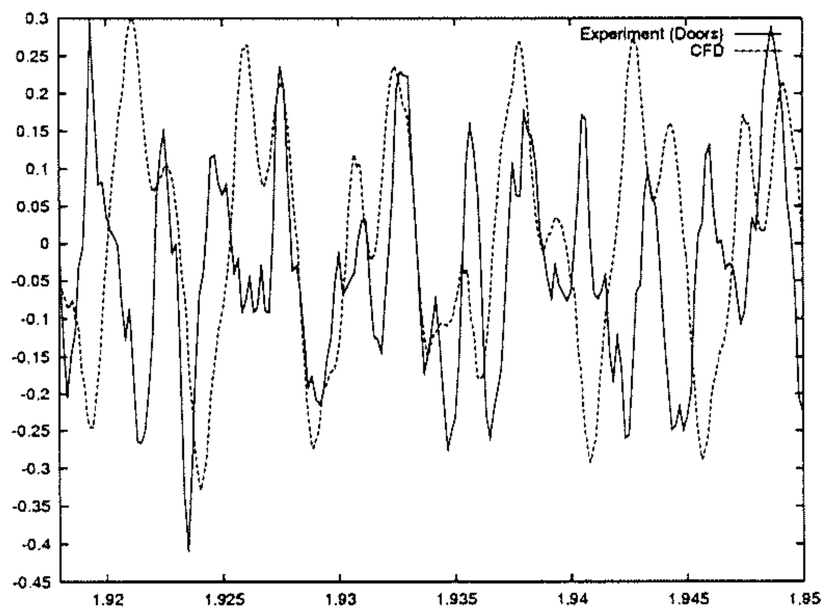

(c) X/L=0.25

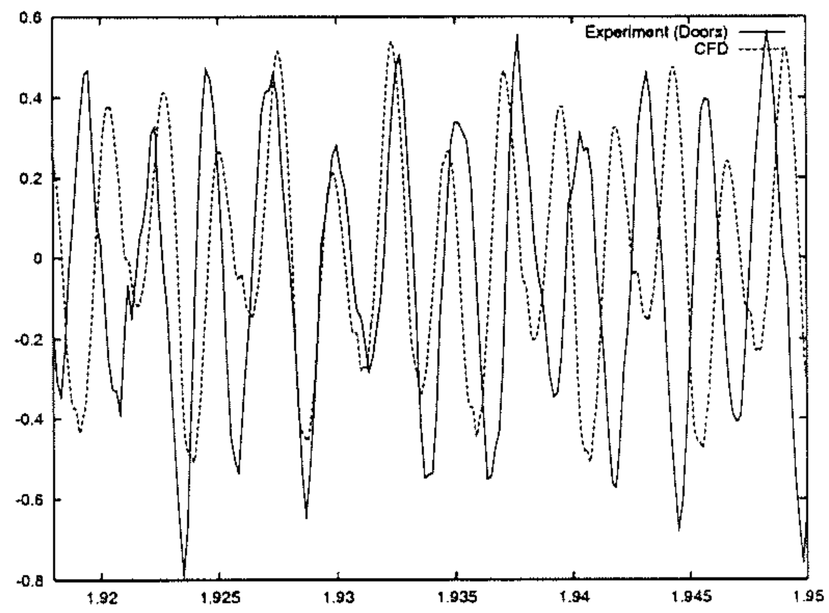

(d) X/L=0.35

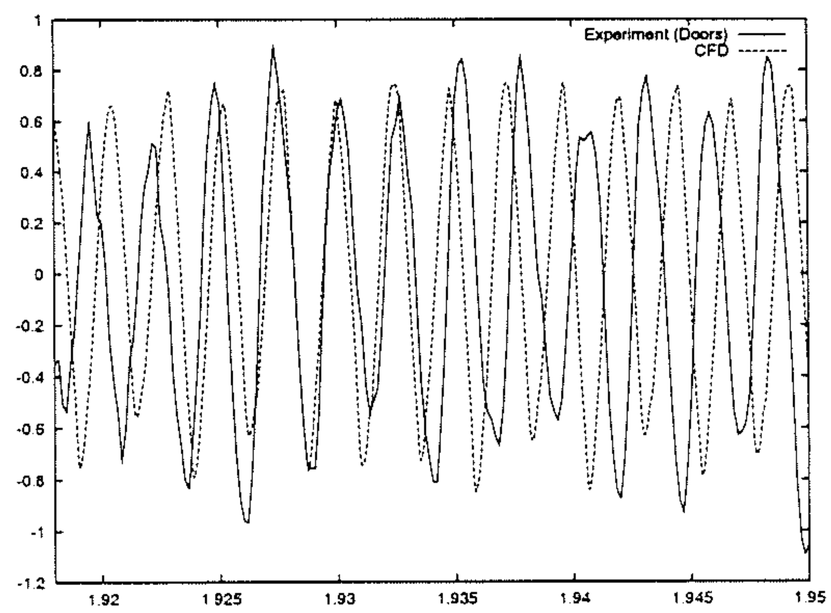

(e) X/L=0.45

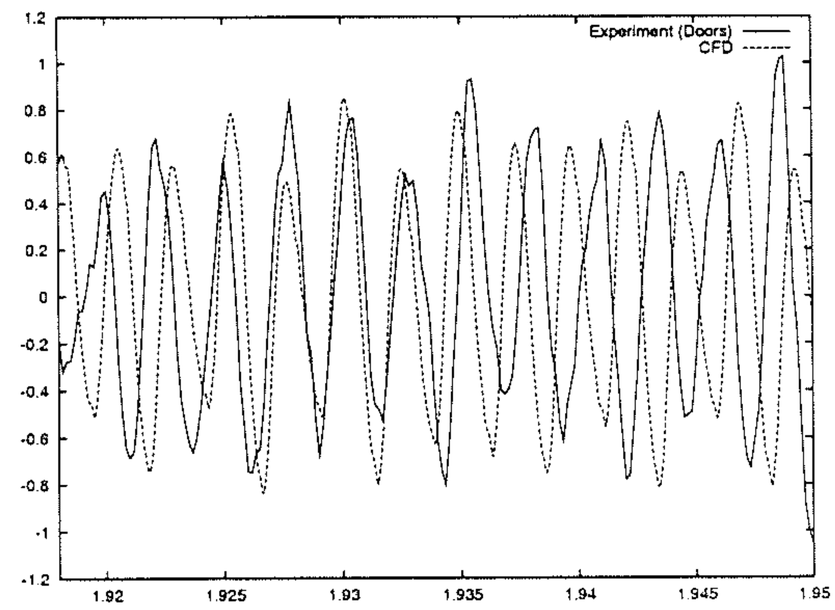

(f) X/L=0.55

Figure 2.1: Comparison of CFD Pressure Histories with Experiment

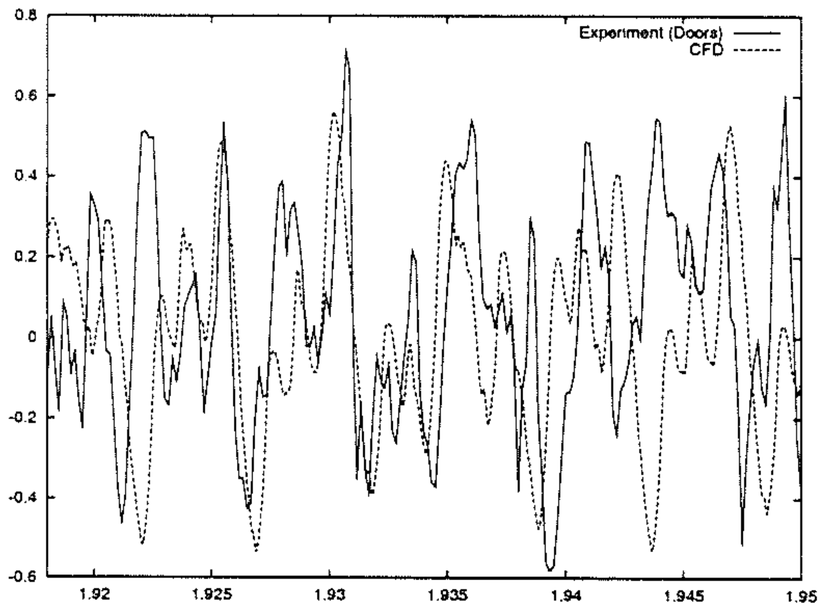

(a) X/L=0.65

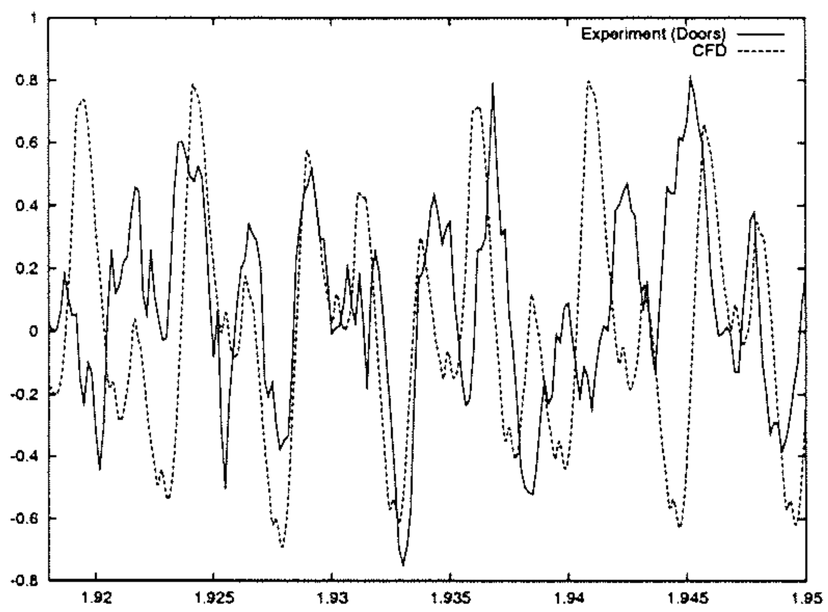

(b) X/L=0.75

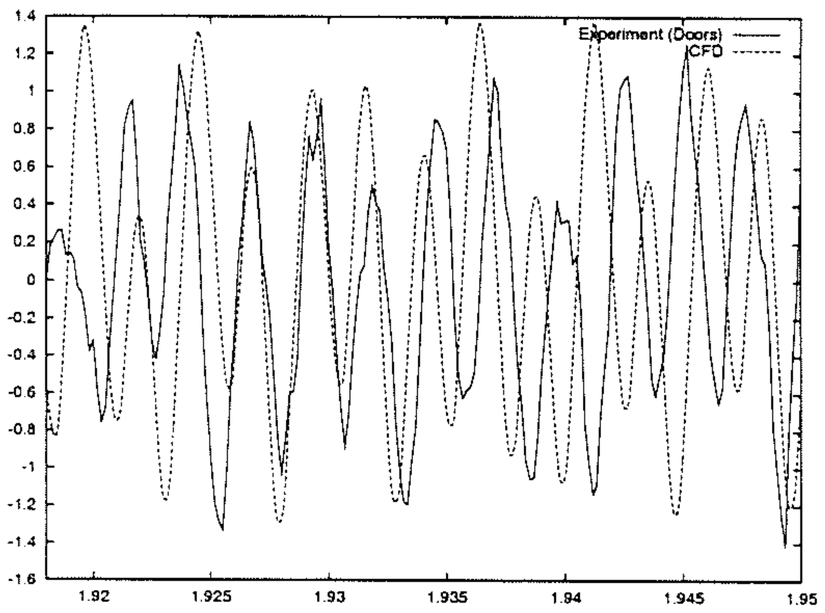

(c) X/L=0.85

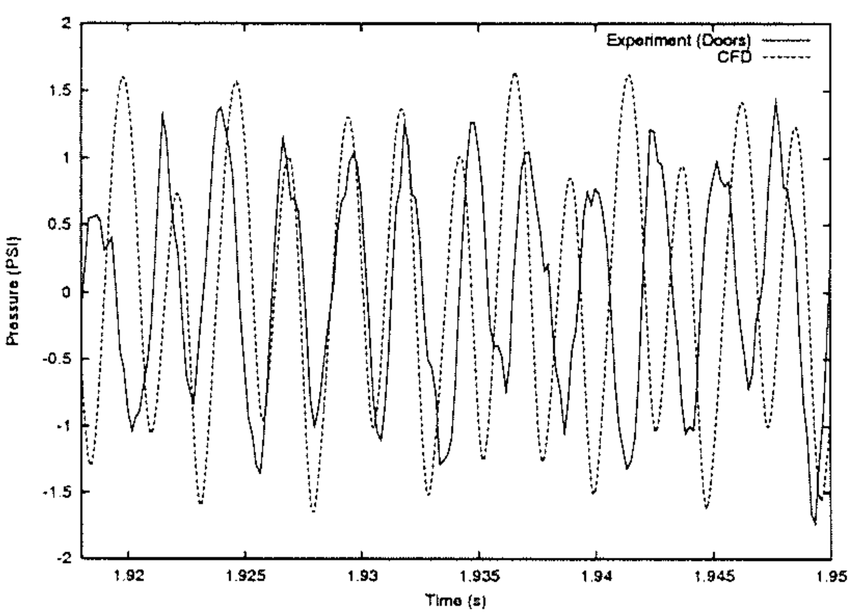

(d) X/L=0.95

Figure 2.2: Comparison of CFD Pressure Histories with Experiment

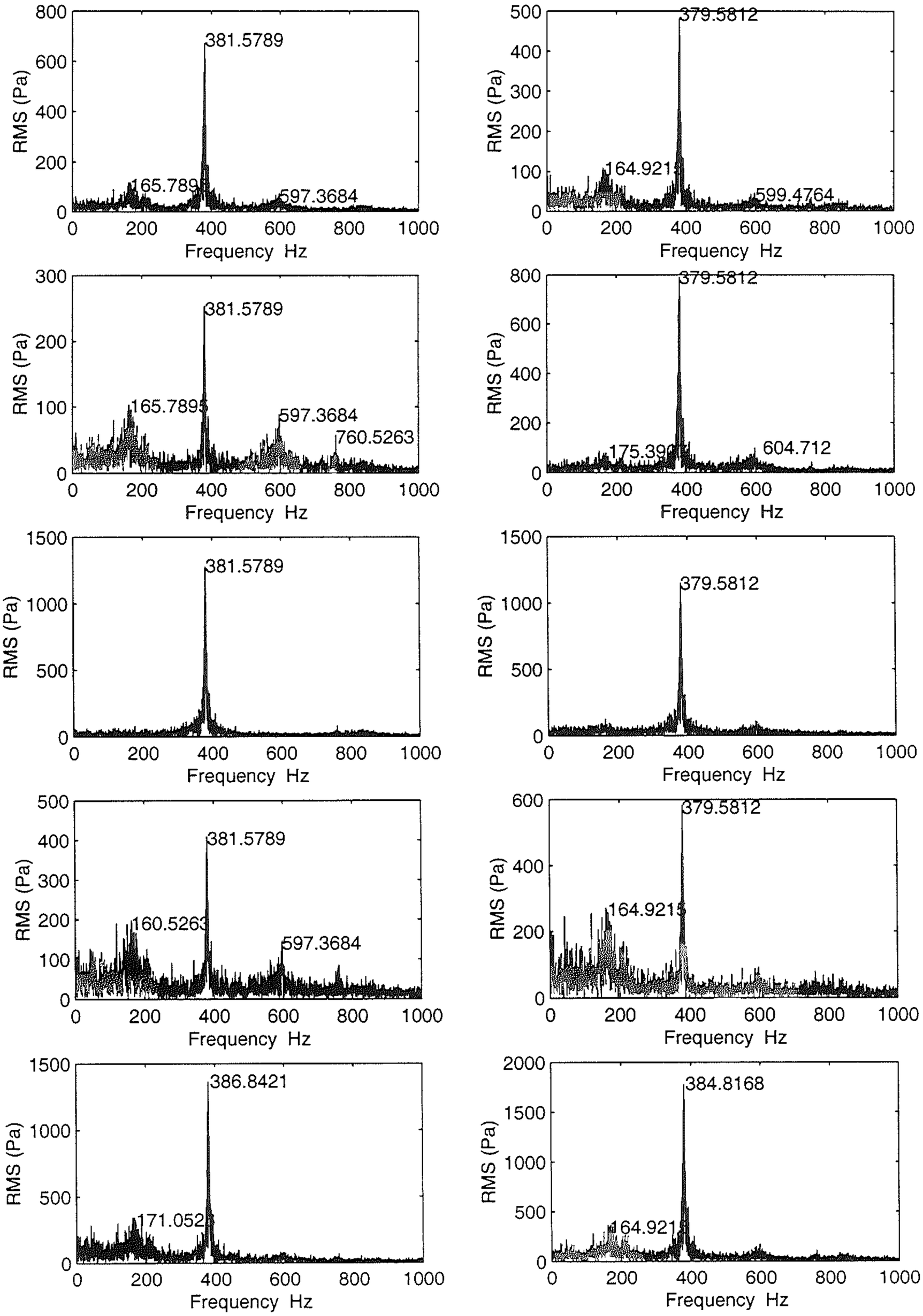

Figure 2.3: Experimental RMS Pressures along Cavity Floor. From left to right, top to bottom: X/L= 0.5, 0.15, 0.25, 0.35, 0.45, 0.55, 0.65, 0.75, 0.85, 0.95

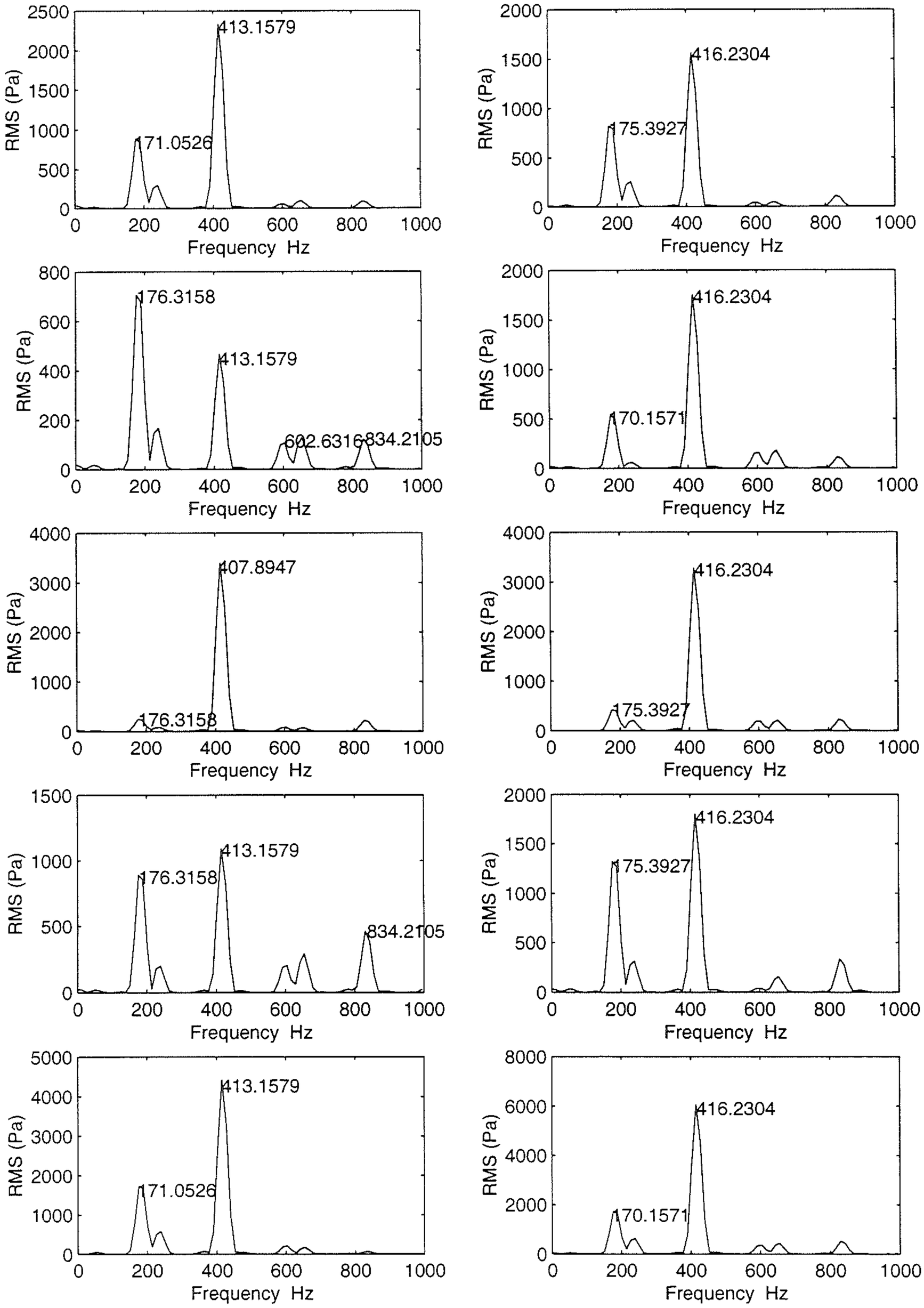

Figure 2.4: CFD RMS Pressures along Cavity Floor for Clean Cavity Mach 0.85. From left to right, top to bottom: X/L= 0.5, 0.15, 0.25, 0.35, 0.45, 0.55, 0.65, 0.75, 0.85, 0.95

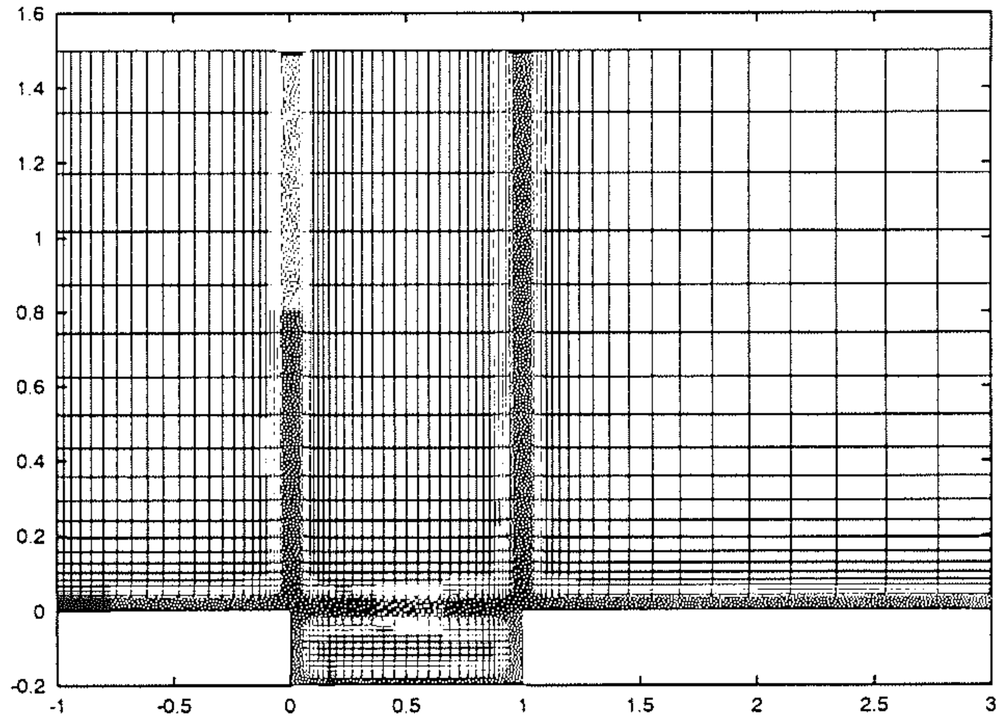

Figure 2.5: Dimensions and Extent of Coarse Grid

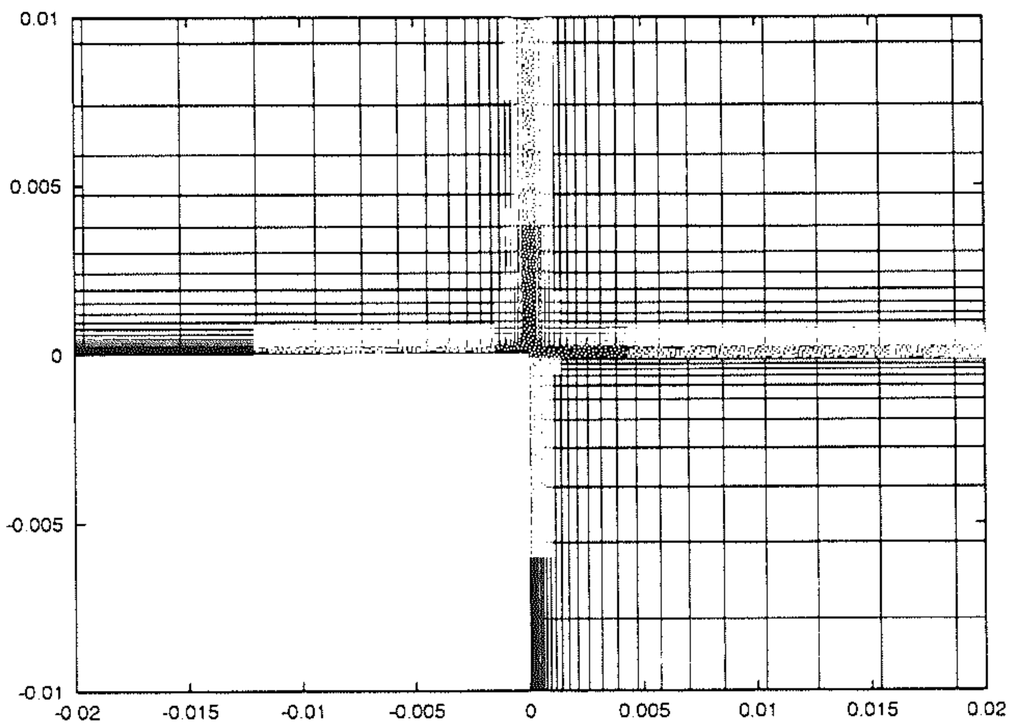

Figure 2.6: Boundary Layer clustering for Coarse Grid

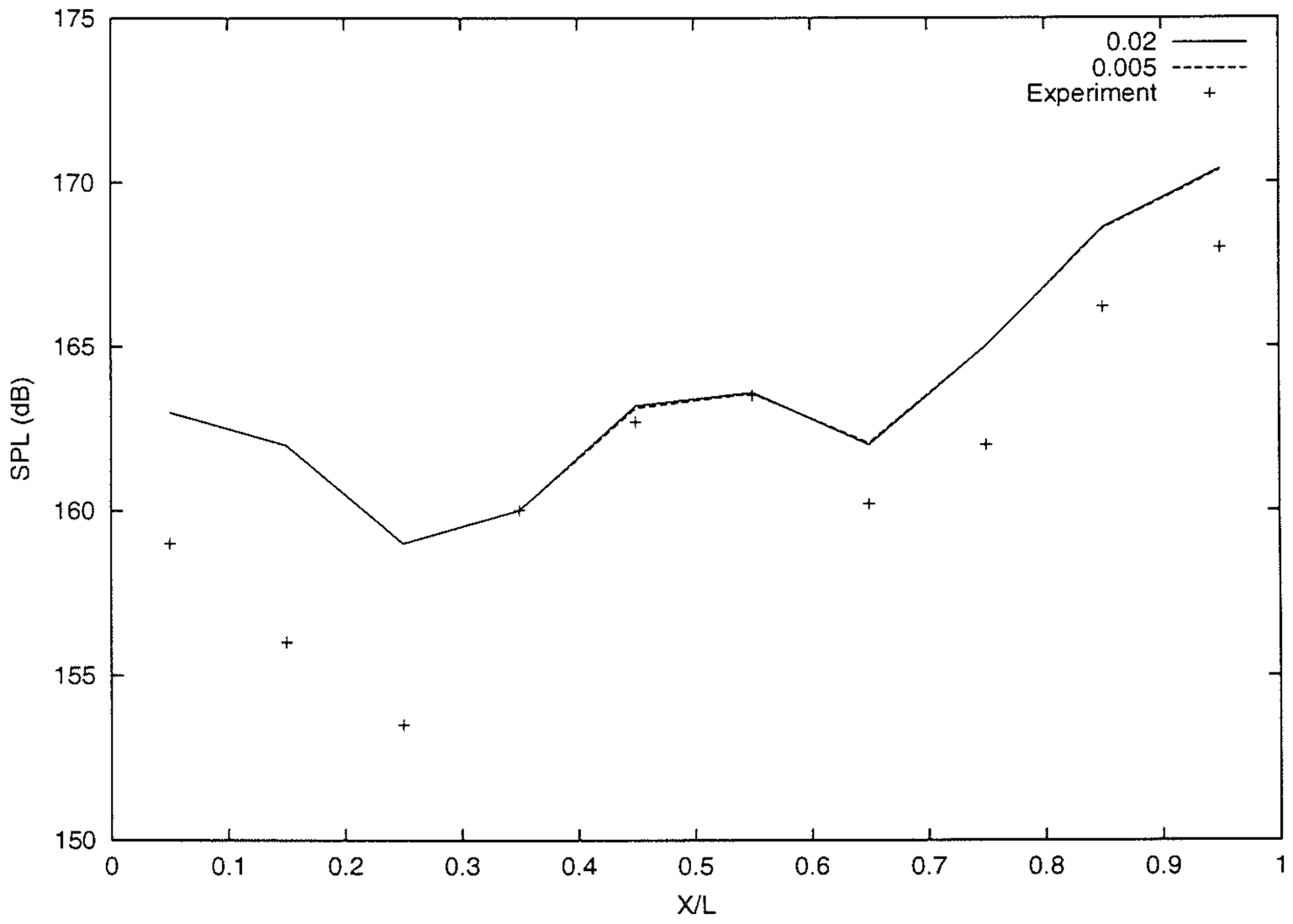

Figure 2.7: Comparison of distributions for time steps of 0.02 and 0.005 on coarse grid

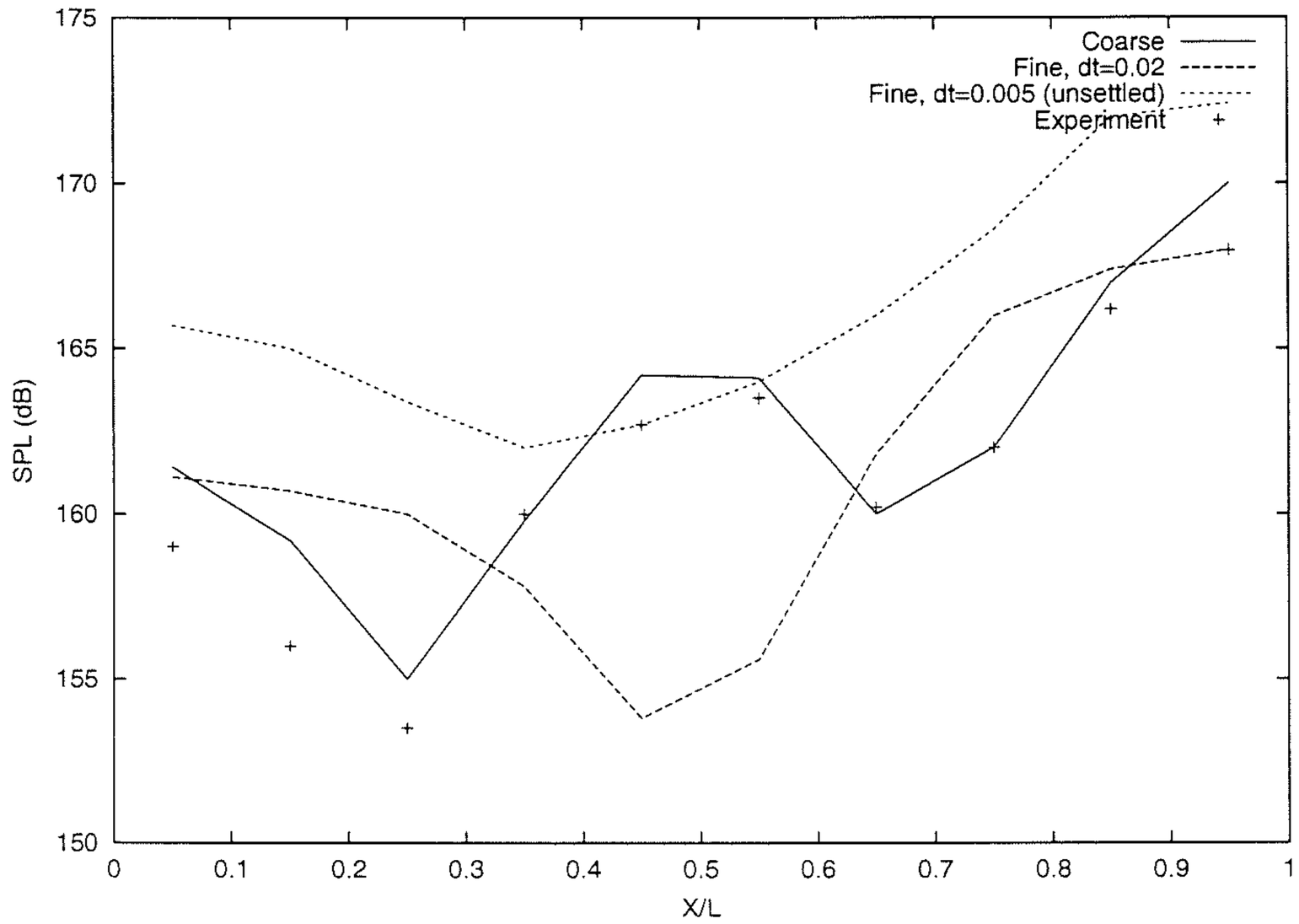

Figure 2.8: Comparison of distributions on coarse and fine grids

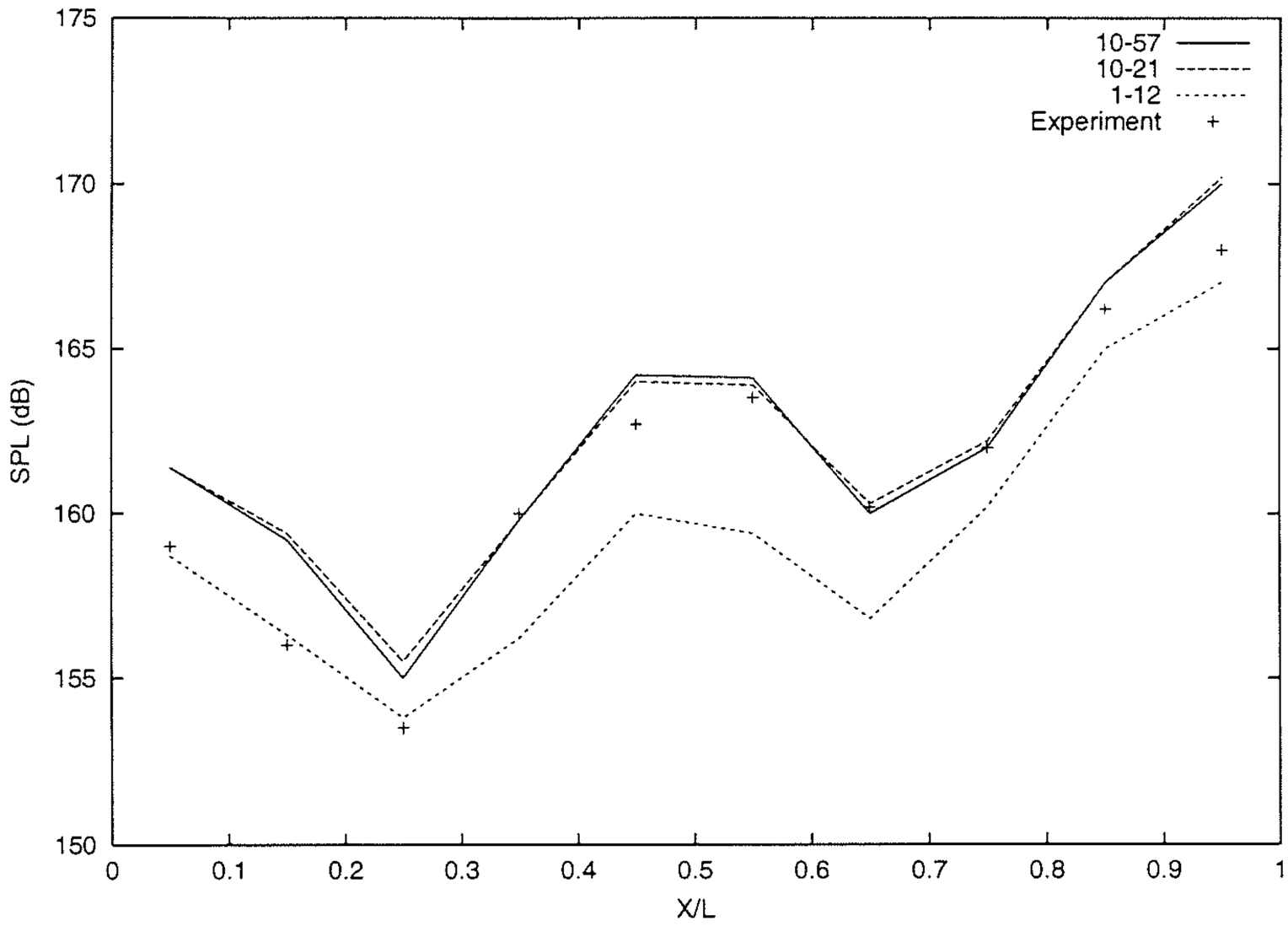

Figure 2.9: Evaluation of Settling Interval

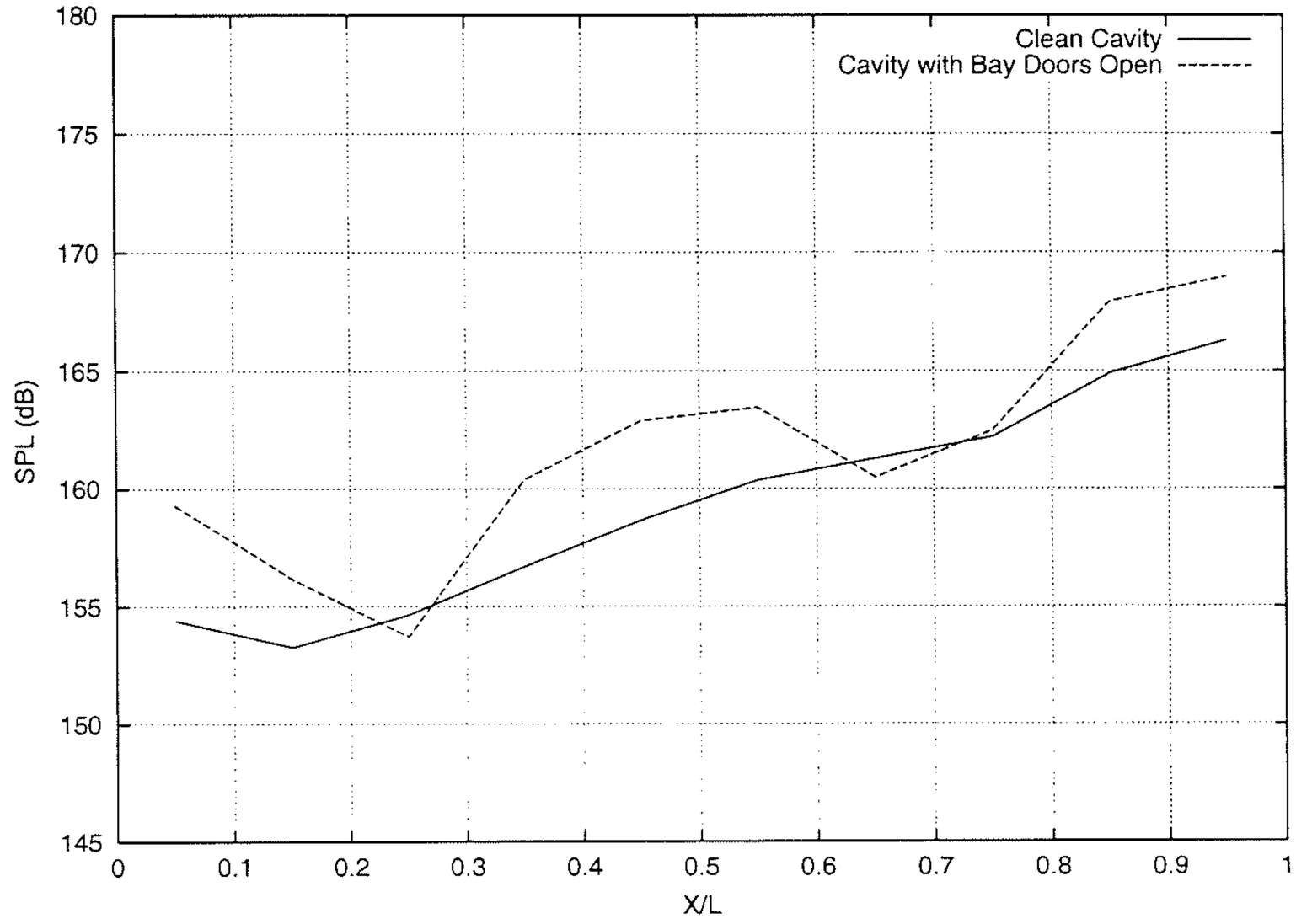

Figure 2.10: Experimental SPL distribution for clean and cavity with doors cases (M=0.85 and L/D=5)

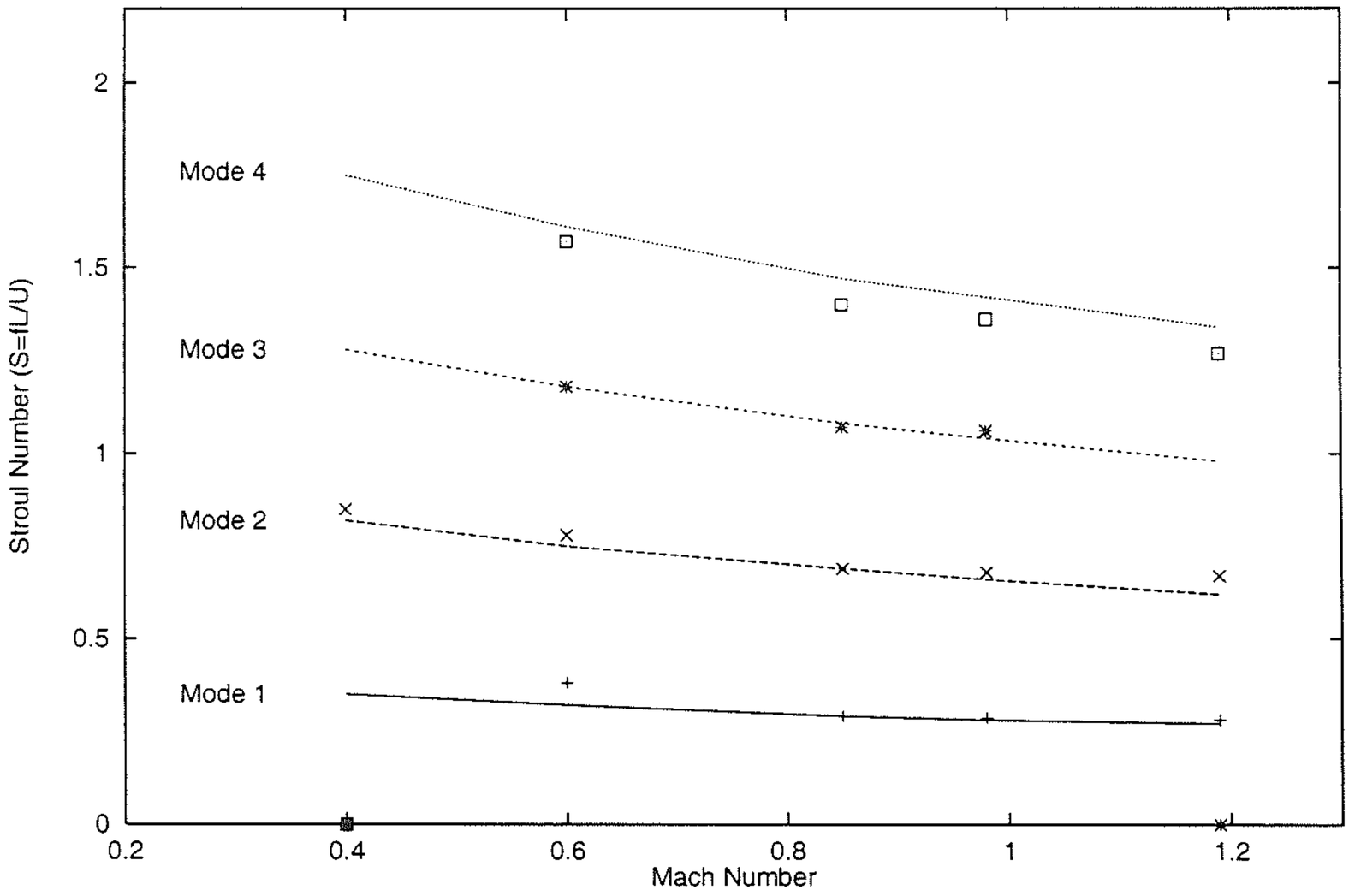

Figure 2.11: Variation of Strouhal Number with Mach Number for L/D=5

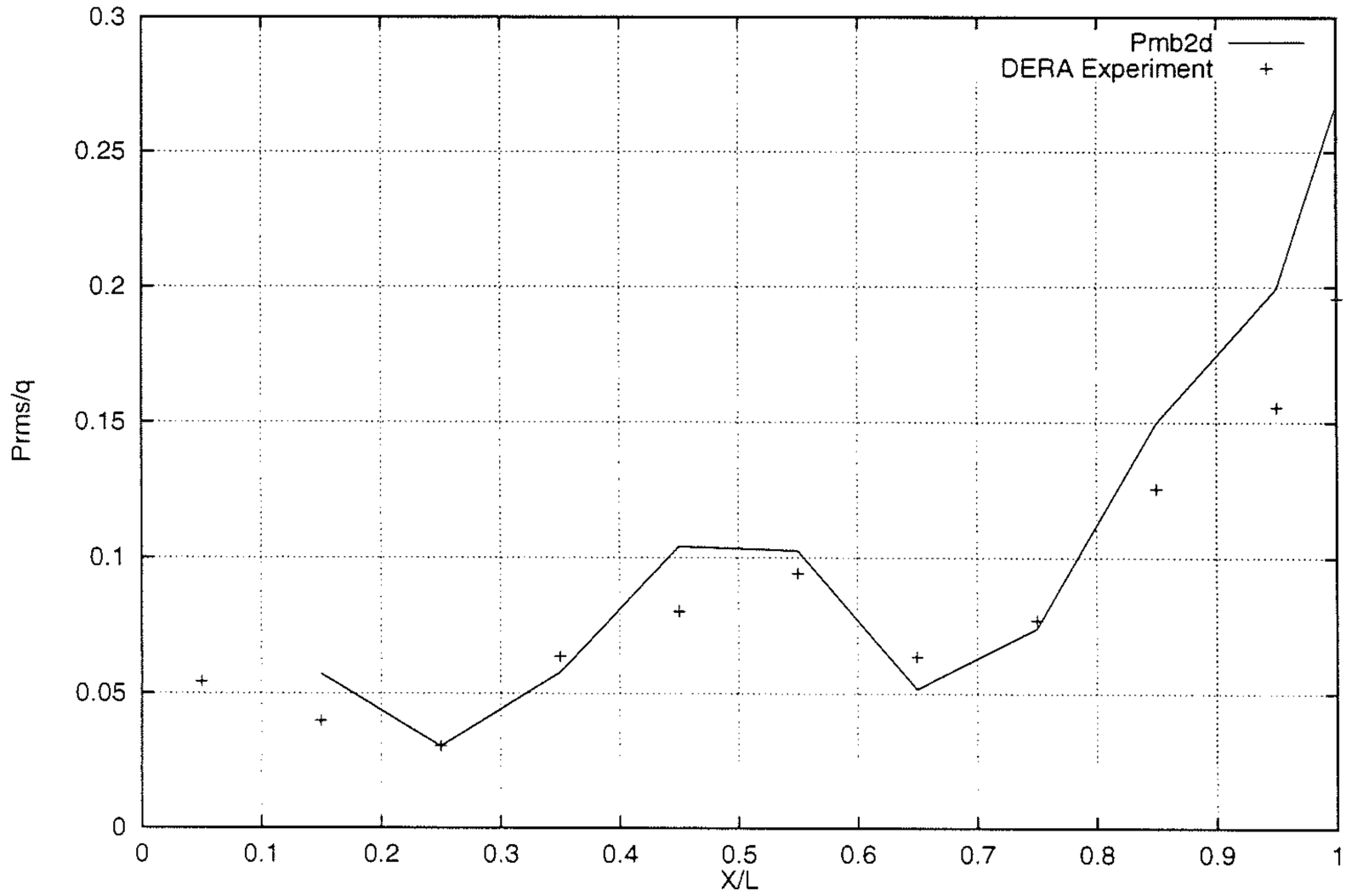

Figure 2.12: Variation of Prms/q along cavity floor for M=0.85, L/D=5

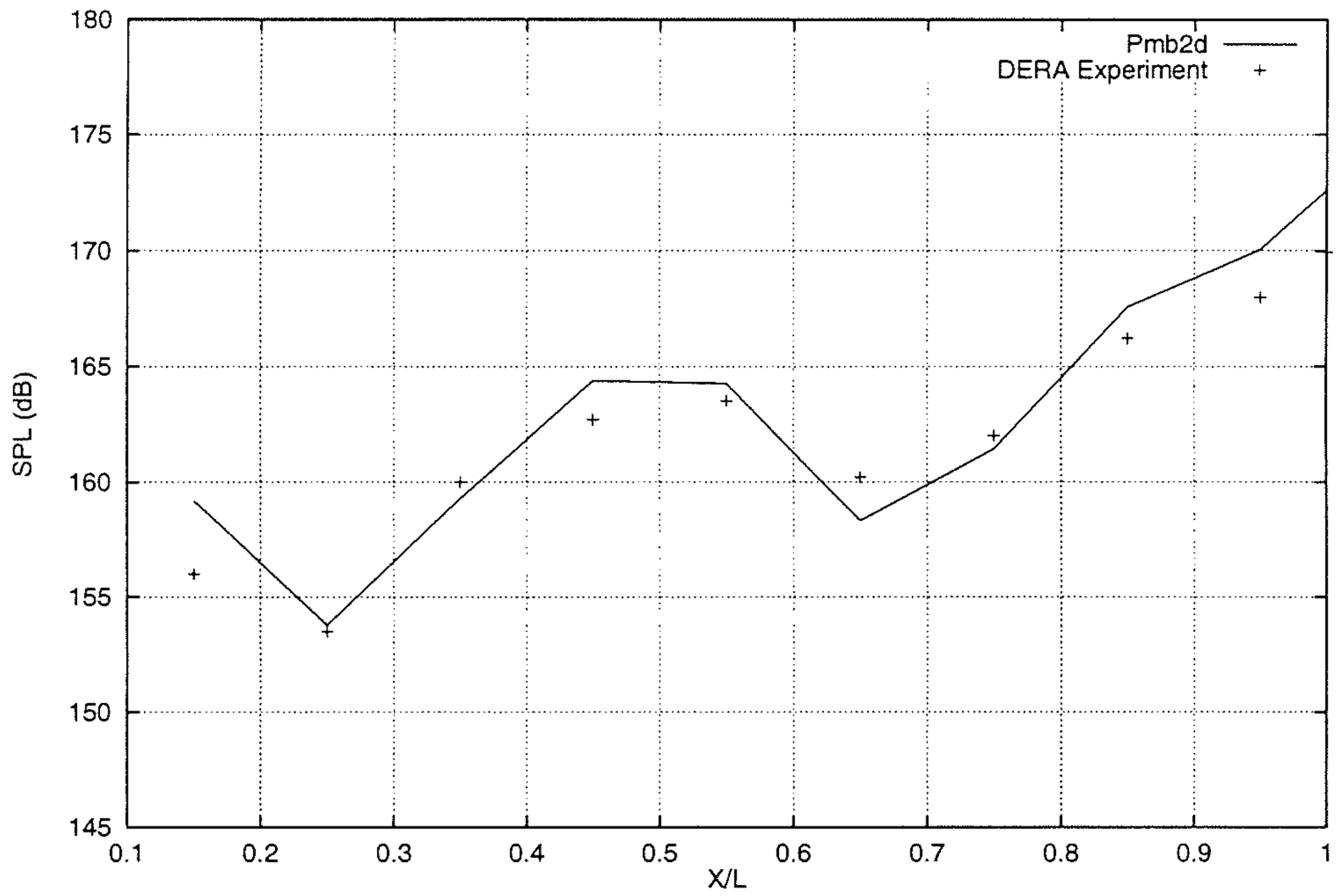

Figure 2.13: Variation of SPL along cavity floor for M=0.85, L/D=5

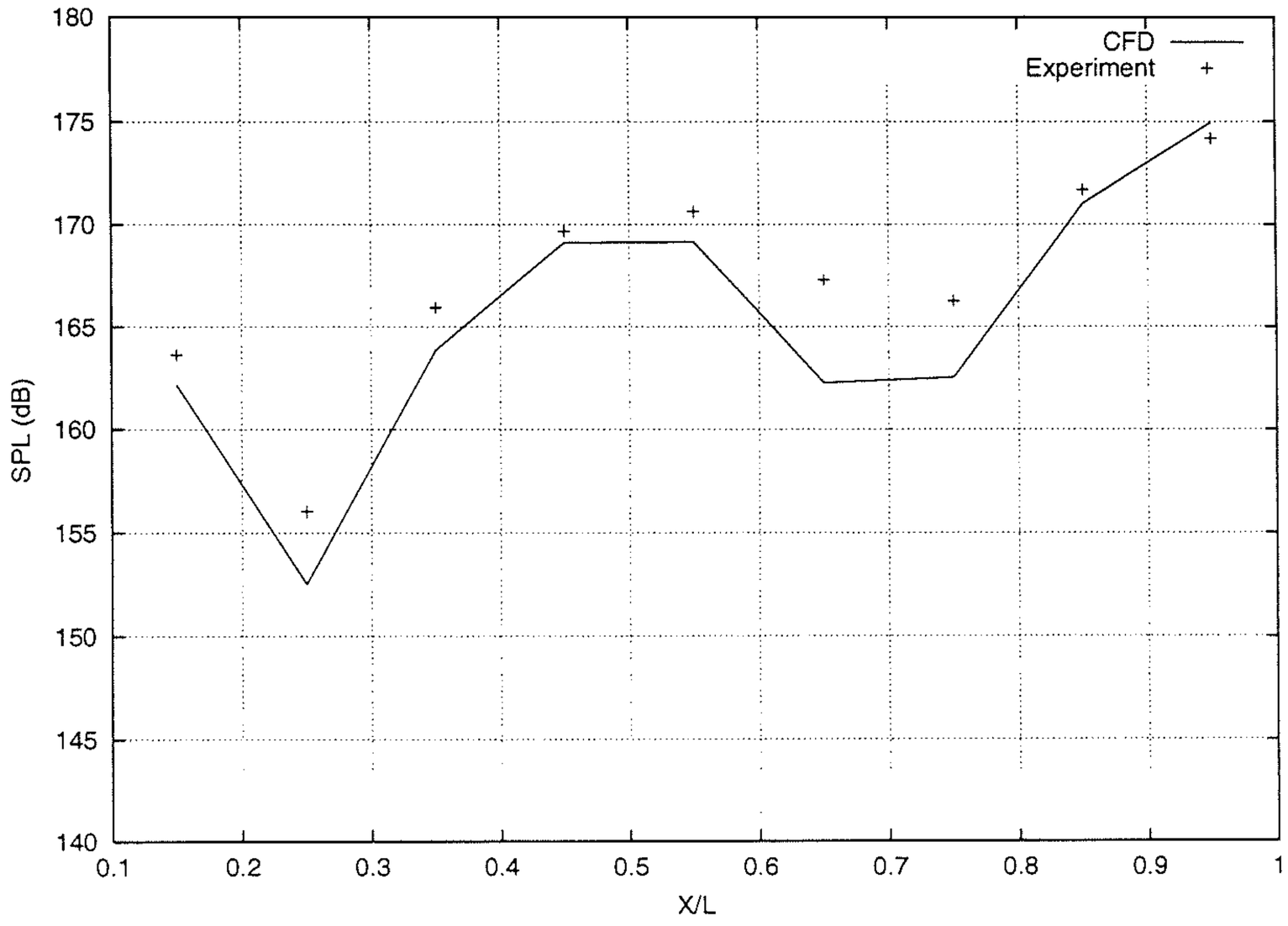

Figure 2.14: Variation of SPL along cavity floor for M=1.19, L/D=5

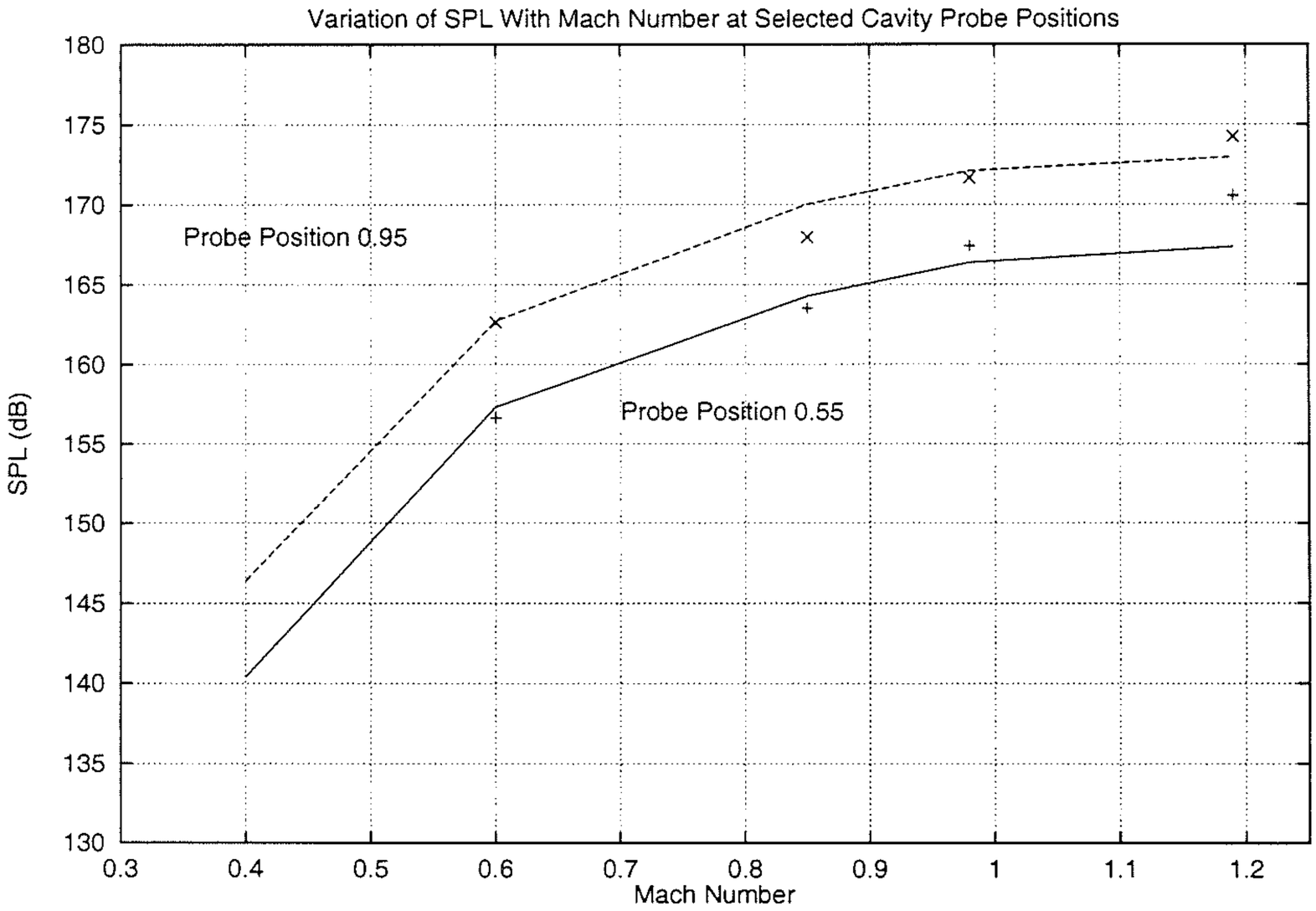

Figure 2.15: Variation of SPL with Mach Number at Selected Probe Positions on the cavity floor.

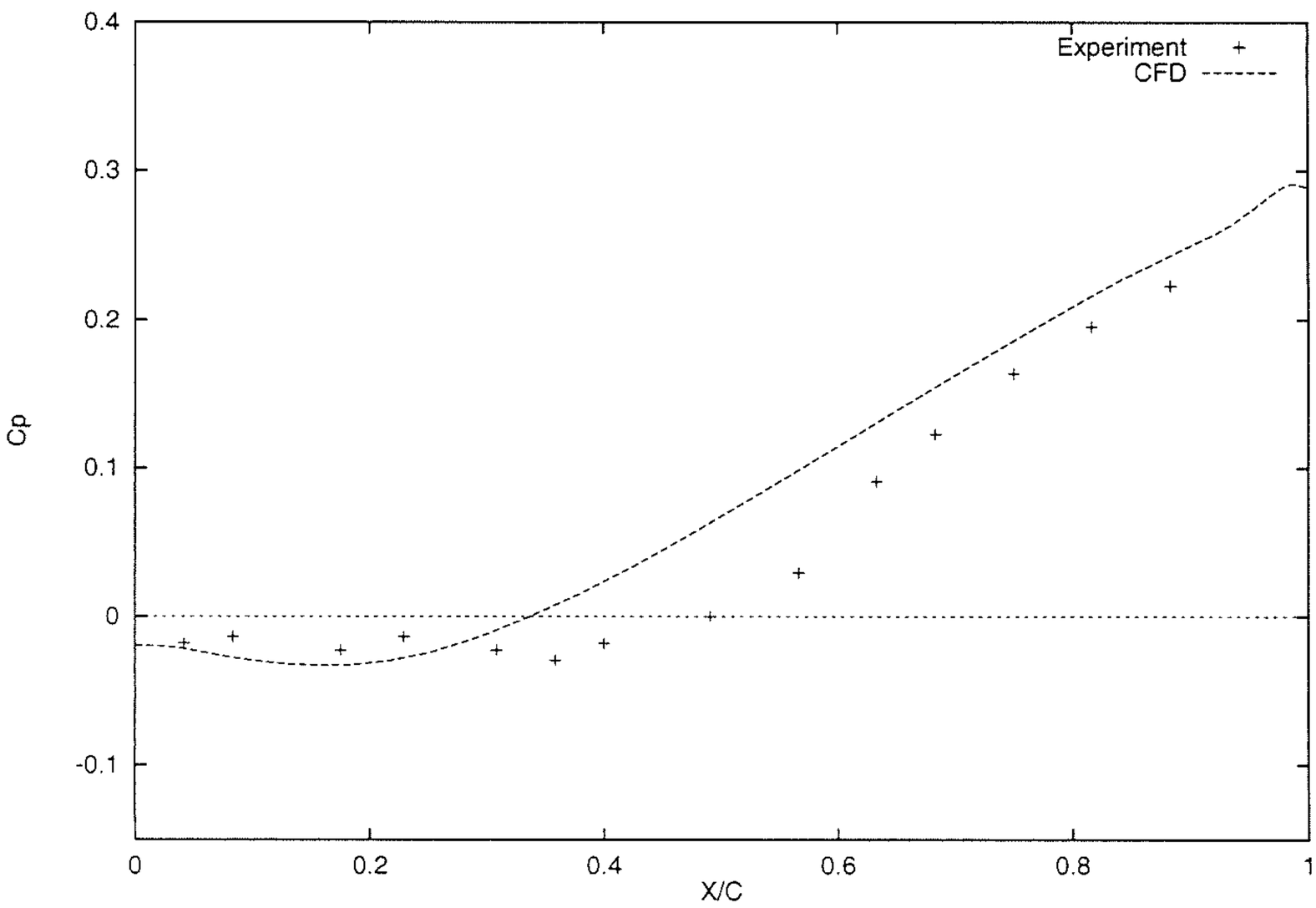

Figure 2.16: Pressure Distribution Along Cavity Floor for L/D=10, Mach 1.35

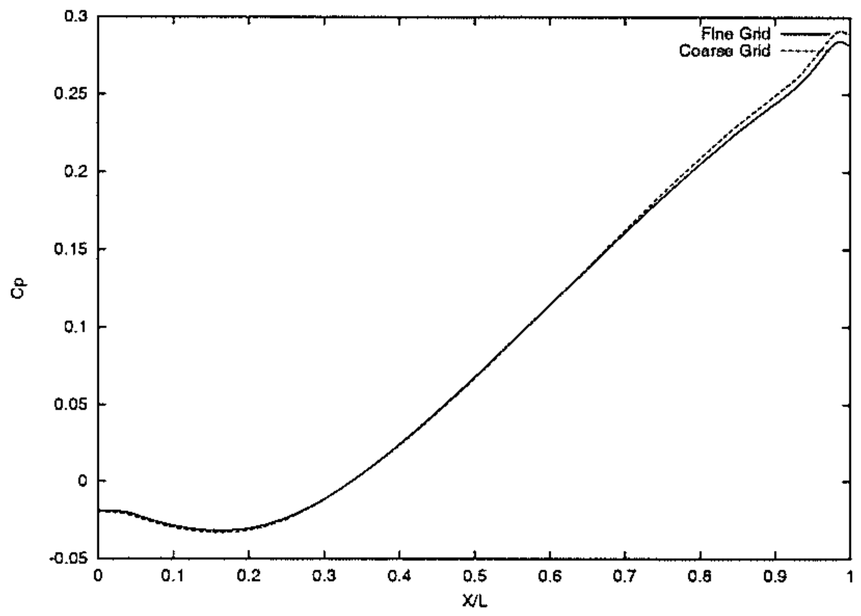

(a) Cp Distribution

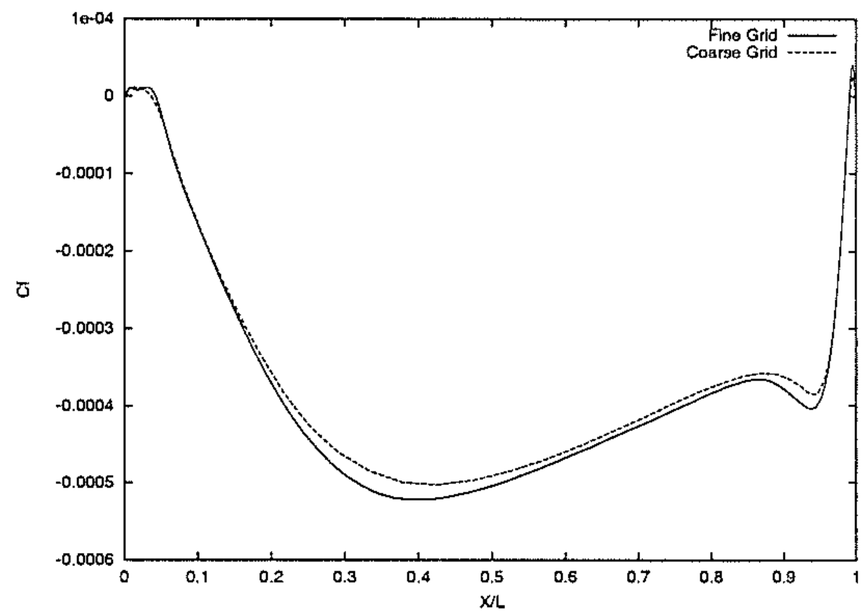

(b) Skin Friction Distribution

Figure 2.17: L/D=10, Mach 1.35: Grid Refinement

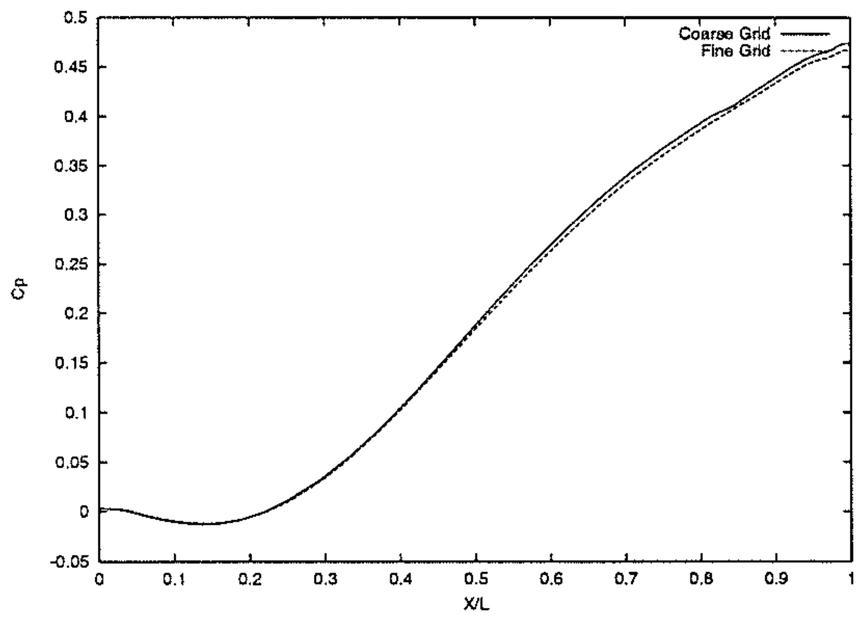

(a) Cp Distribution

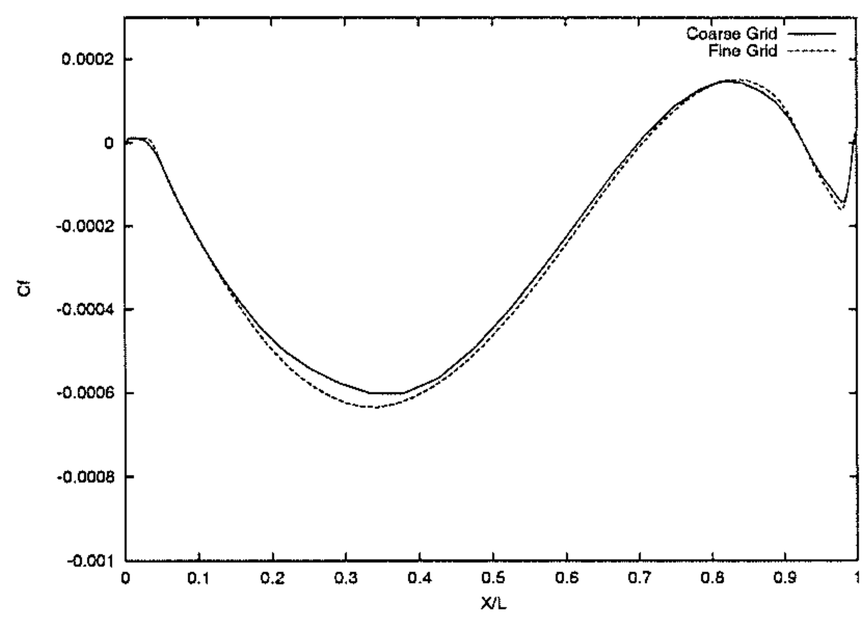

(b) Skin Friction Distribution

Figure 2.18: L/D=10, Mach 0.85: Grid Refinement

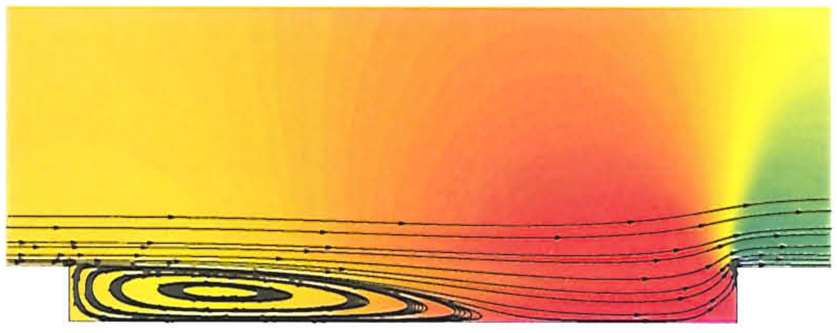

Figure 2.19: Instantaneous Flowfield for L/D=12, Mach 0.85: Coarse Grid

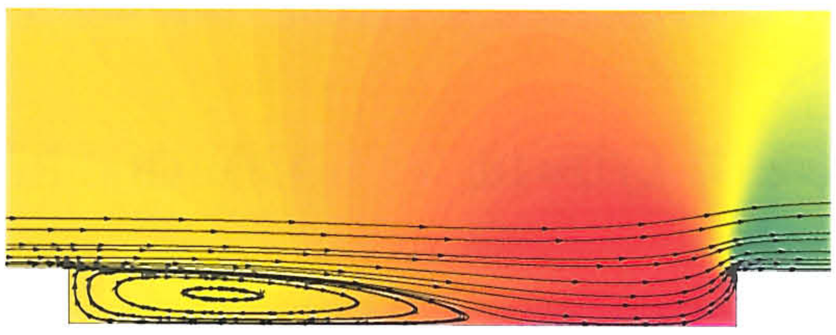

Figure 2.20: Instantaneous Flowfield for L/D=12, Mach 0.85: Fine Grid

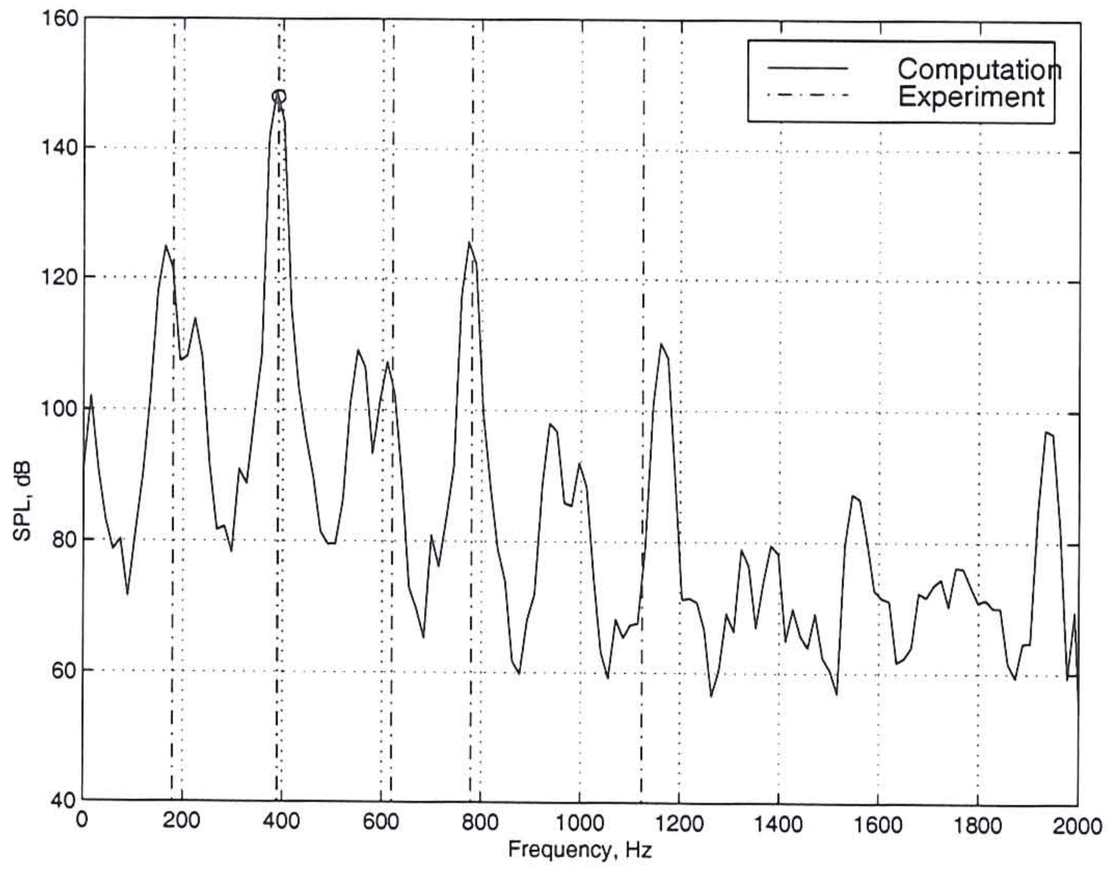

Figure 2.21: Mach 0.9, L/D=8: Pressure Spectra on Cavity Floor

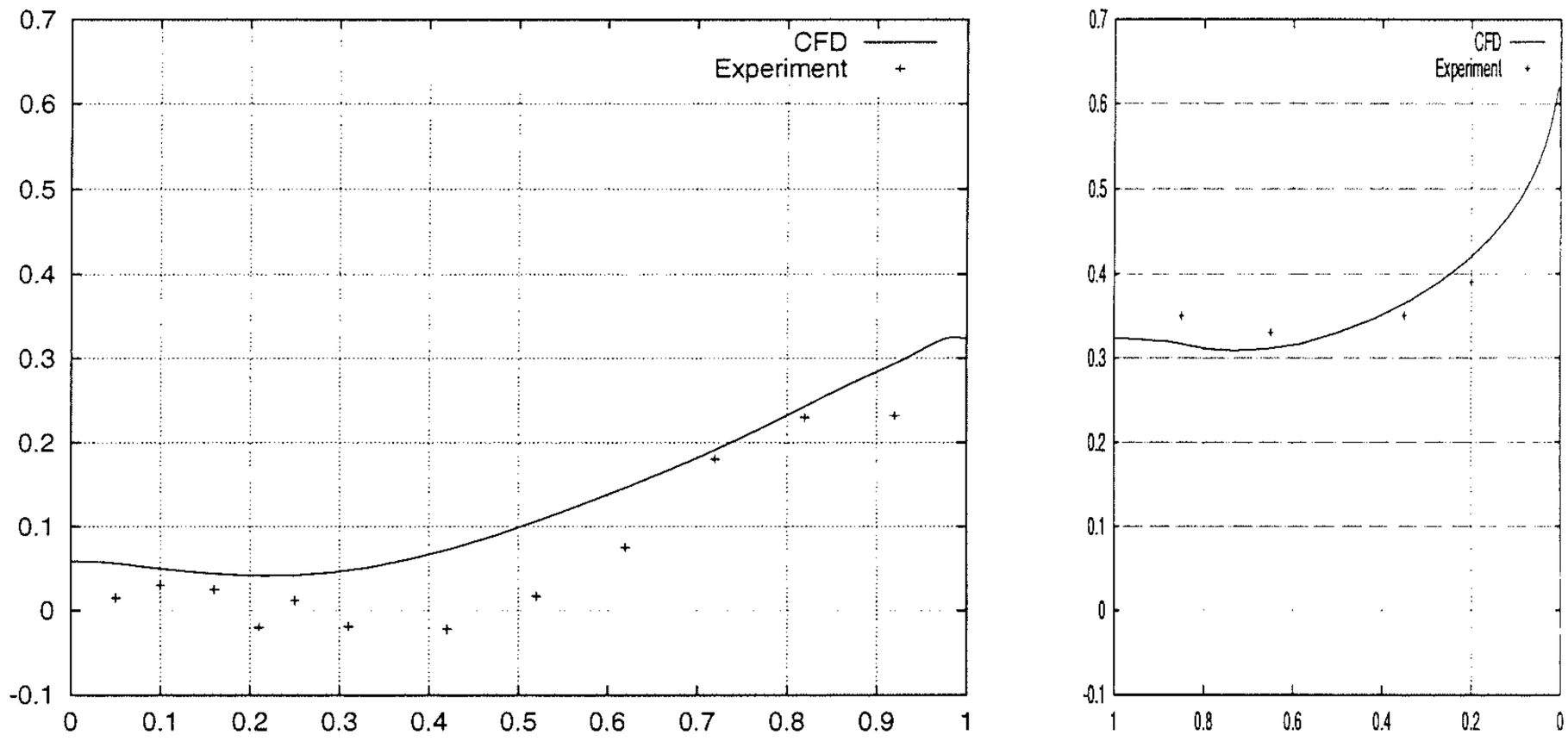

(a) Cavity Floor (b) Cavity Aft Wall

Figure 2.22: L/D=8 Mach 0.9: Pressure Distribution for Transitional Cavity Flow.

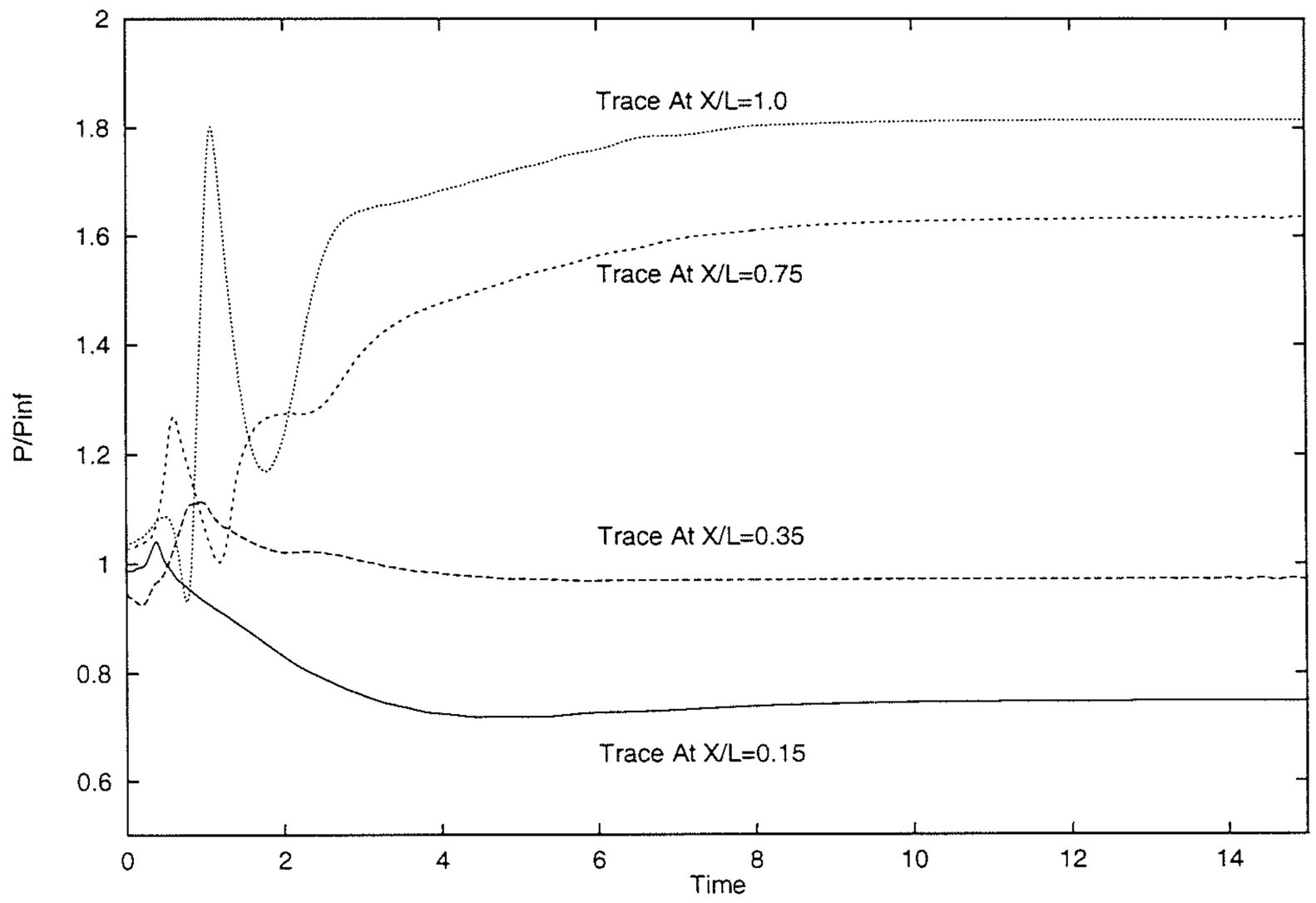

Figure 2.23: Monitored Pressure History on Cavity Floor for L/D=20

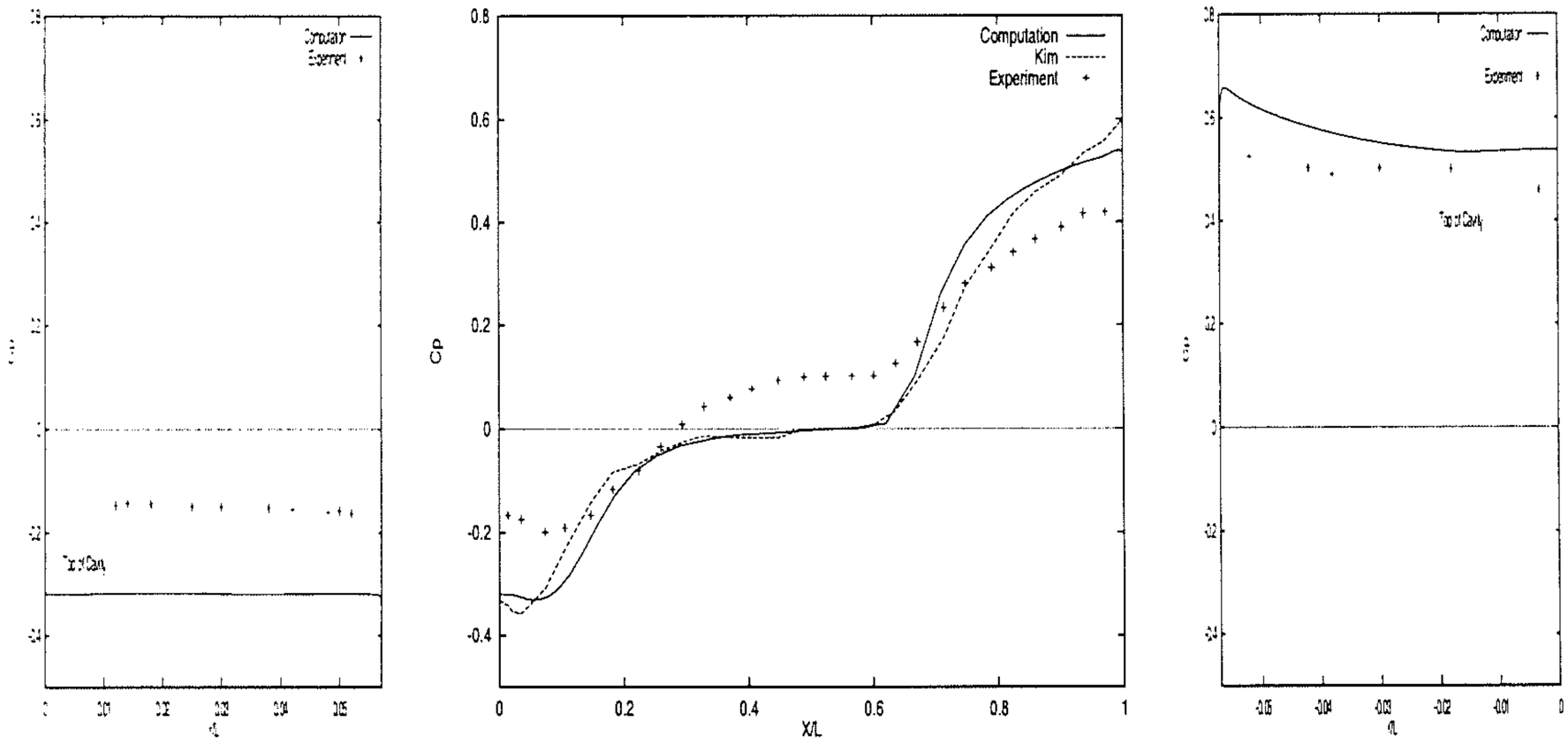

(a) Front Face (b) Distribution on Cavity Floor (c) Rear Face

Figure 2.24: Cavity Pressure Distribution for Closed Cavity Flow

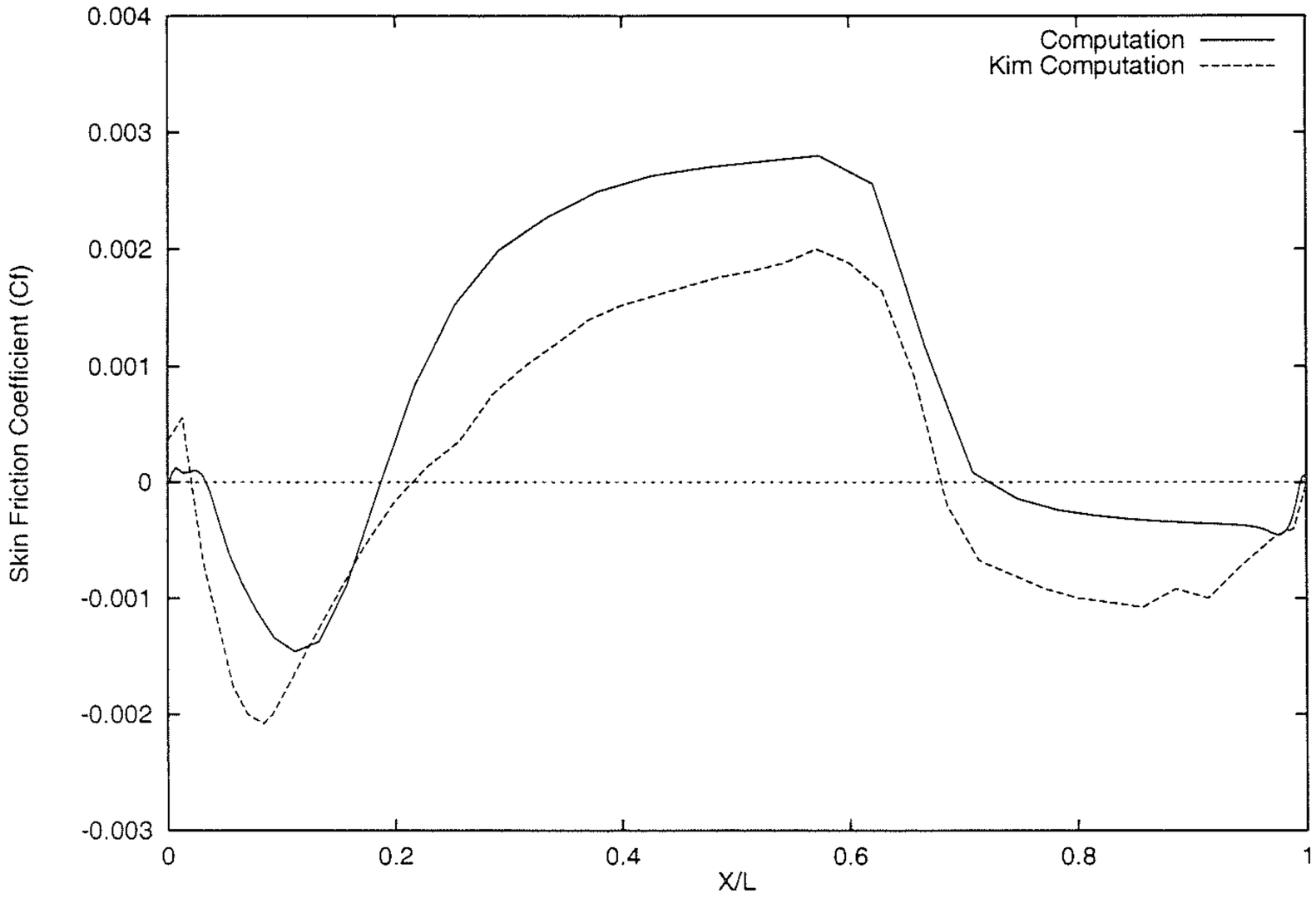

Figure 2.25: Skin Friction Coefficient Distribution on Cavity Floor for L/D=20 Cavity

Chapter 3

Investigation of Flow Phenomena for Open Cavity Flow

3.1 Overview

Open cavity flows arise at small length to depth ratios ($L/D \leq 7$) and are characterised by intense acoustic levels. The use of internally carried stores makes an understanding of the flow mechanisms important since control of the fluctuations is necessary to protect the integrity of the aircraft structure and electronic equipment housed in the cavity. Experimental studies date back to 1955 and have been the principal source of evidence. However, the difficulty in obtaining flow field visualisation due to the high frequency of the significant events has meant that at best the information obtained was either time averaged or unsteady values at the wall. The advent of high speed computers and modern CFD has allowed a number of simulation based investigations to be carried out.

The current chapter aims to use the detailed results obtained from a solution of the Reynolds' Averaged Navier-Stokes equations to describe the flow mechanisms for transonic open cavity flow. The chapter starts with a review of the theories derived from experimental and computational studies. Then, a detailed analysis of the flow field obtained for the M=0.85, L/D=5 case is presented. The influence of Mach number on this solution is discussed by considering results from the case with

M=1.19. Finally, the mechanisms of the flow are summarised.

3.2 Theories from Experiments

Krishnamurty published his pioneering work on the generation of acoustic pressure oscillations by flow over a cavity in 1955 [52]. This work was motivated by the need to understand the flow field in bomb bays used for the internal carriage of weapons. Schlieren pictures showed that the cavity emits strong acoustic radiation. Three parameters that influence the acoustic field were identified, namely dimensions, Mach number and upstream boundary layer development. The main findings were:

- a laminar boundary layer upstream provided a clear and well-defined acoustic field, while the field obtained from a turbulent boundary layer was weak and diffused

- the radiation was found to become more intense and directional as the Mach number is increased.

- a minimum length was required for an acoustic field to occur.

- as the L/D ratio of the cavity was increased (from L/D = 1), the intensity of the acoustic radiation was observed to increase at first before it gradually diminished

- the wavelength of the acoustic radiation increased with the cavity length

Although the study was primarily exploratory, Krishnamurty recognised that the oscillating shear layer impinging on the aft wall of the cavity was a key element in the production of the acoustic radiation. Although the Schlieren pictures did not indicate the presence of vortices in the cavity, Krishnamurty did state that vortex motion may be an essential feature driving the flow. The Schlieren photograph for Mach 0.804 and L/D=4, which is close to the configuration analysed below, is shown in figure 3.1. The pressure field obtained from a CFD analysis is shown in figure 3.2. The acoustic radiation is evident above the cavity in both figures. The low pressure regions in figure 3.2 (lighter shade in the cavity) represent the vortex cores.

Figure 3.1: Schlieren image by Krisnamurty, L/D=5 Mach 0.804

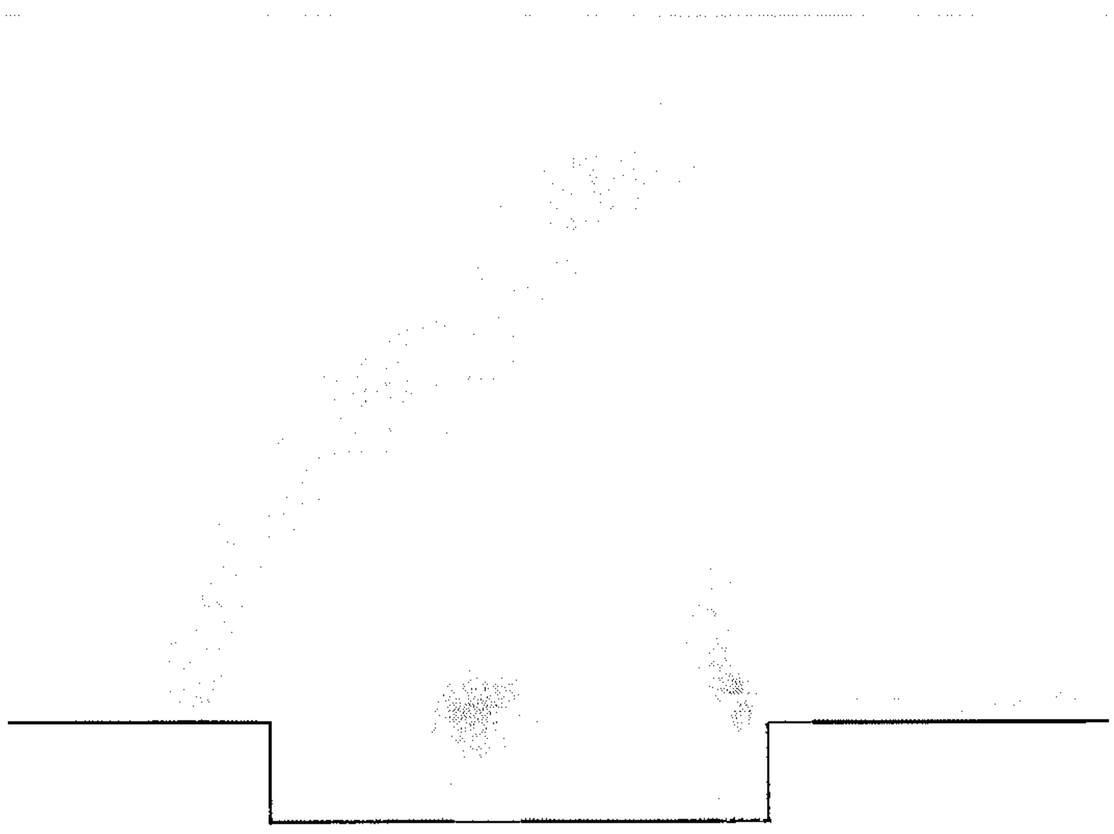

Figure 3.2: Pressure field from RANS simulation, L/D=5 Mach 0.85

It was also shown that the Strouhal number S varies with Mach number, with S defined as

$$S = \frac{fL}{U_\infty}$$

where f is the frequency, L the cavity length and U_∞ the freestream velocity. The variation of S with Mach number for a turbulent boundary layer is shown in Figure 3.3. The dependence of the Strouhal number on the cavity length was not investigated. Krishnamurty recorded two frequencies of equal magnitude with the *high* frequency almost double the *low* frequency. The detection of these two frequencies stimulated studies which would develop predictive methods.

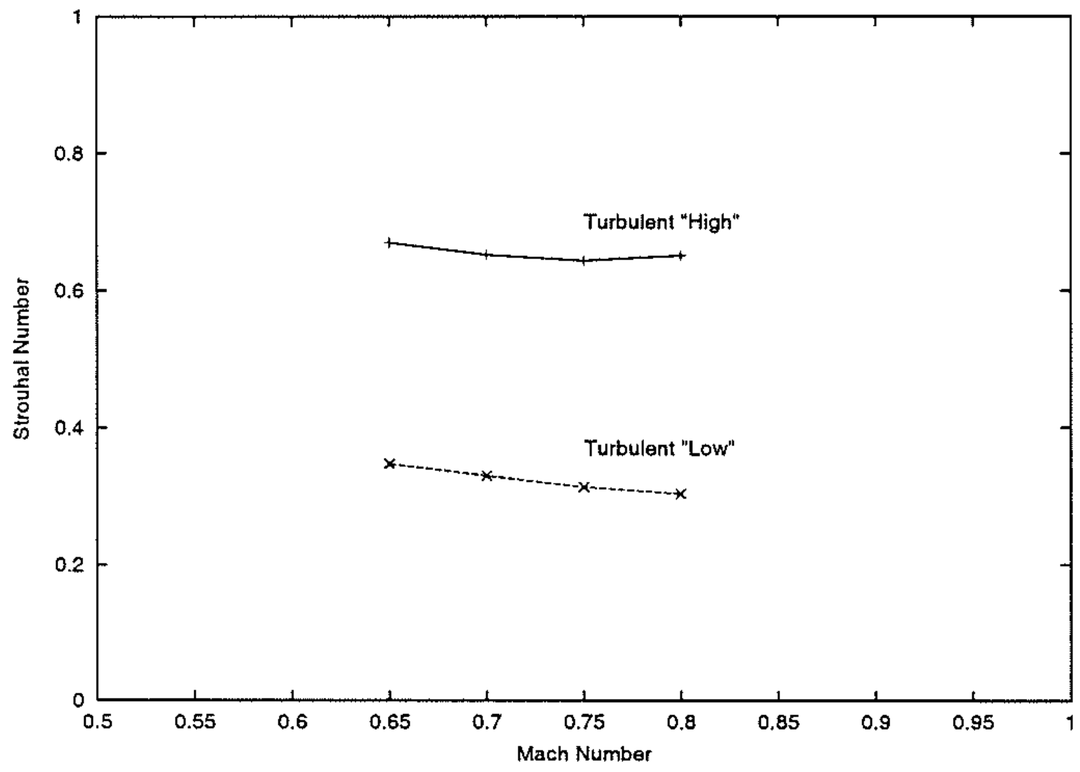

Figure 3.3: Variation of Strouhal Number with Mach Number (Krishnamurty)

In 1964, Rossiter advanced on the findings of Krishnamurty [69]. More than two frequencies were observed for a case with L/D=4. He suggested that these frequencies indicated a feedback mechanism. A formula was suggested which shows the variation of the Strouhal number with Mach number. The pressure fluctuations that were measured produced distinct peaks in the pressure spectra. This indicated that periodic pressure variations were superimposed on a background of a random nature. The random component was shown to be predominant in shallower cavities, while the periodic component (due to acoustic resonance in the cavity) was more significant in deeper cavities. The amplitude spectra for deeper cavities shows that the fluctuating pressures, which are of a periodic nature, are composed of a dominant frequency with a smaller contribution at other frequencies. These frequencies

lie on curves similar to those found by Krishnamurty (shown in figure 3.3). For a particular Mach number at a given L/D ratio, up to 4 modes were identified.

A semi-empirical formula was proposed for predicting the discrete tones detected in the experiments. Rossiter proposed that vortices which are shed from the cavity leading edge are convected downstream until they interact with the aft cavity wall, generating acoustic pulses. These acoustic pulses propagate upstream in the cavity eventually reaching the front cavity wall. At this time they induce separation of the shear layer which results in the shedding of another vortex, completing the feedback loop. Based on this description a formula was proposed to predict the frequencies, given by

$$f_m = \frac{U_\infty}{L} \frac{m - \gamma}{M_\infty + \frac{1}{\kappa}}$$

where m is an integer index for the frequency of interest (m=1,2,3....), γ is a constant for a fixed L/D and κ represents the ratio of the speed of the vortices to the freestream speed. The parameter γ accounts for the time lag that occurs between a vortex being shed from the front of the cavity and an acoustic disturbance being generated at the aft wall. It is assumed that the acoustic radiation initiates vortex shedding at the leading edge, whilst the impact of the vortices on the aft cavity wall is the generating mechanism for new acoustic waves. Values of γ and κ are determined by curve fitting the measured data.

The agreement for a range of Mach numbers between the frequencies predicted and measured by Rossiter is shown to be close in figure 3.4. There is normally more disagreement with the experimental measurements of others but the performance of the formula is still good, and is generally accepted.

The derivation of Rossiter's equation was built on an hypothesised flow behaviour. The important feature observed by Rossiter from shadowgraphs was vortex shedding from the front cavity wall. As noted earlier, this was not detected in the Schlieren pictures of Krishnamurty. Later Heller et al[40] provided evidence of the flow structure using woollen tufts placed inside the cavity, suggesting that the mean cavity flow

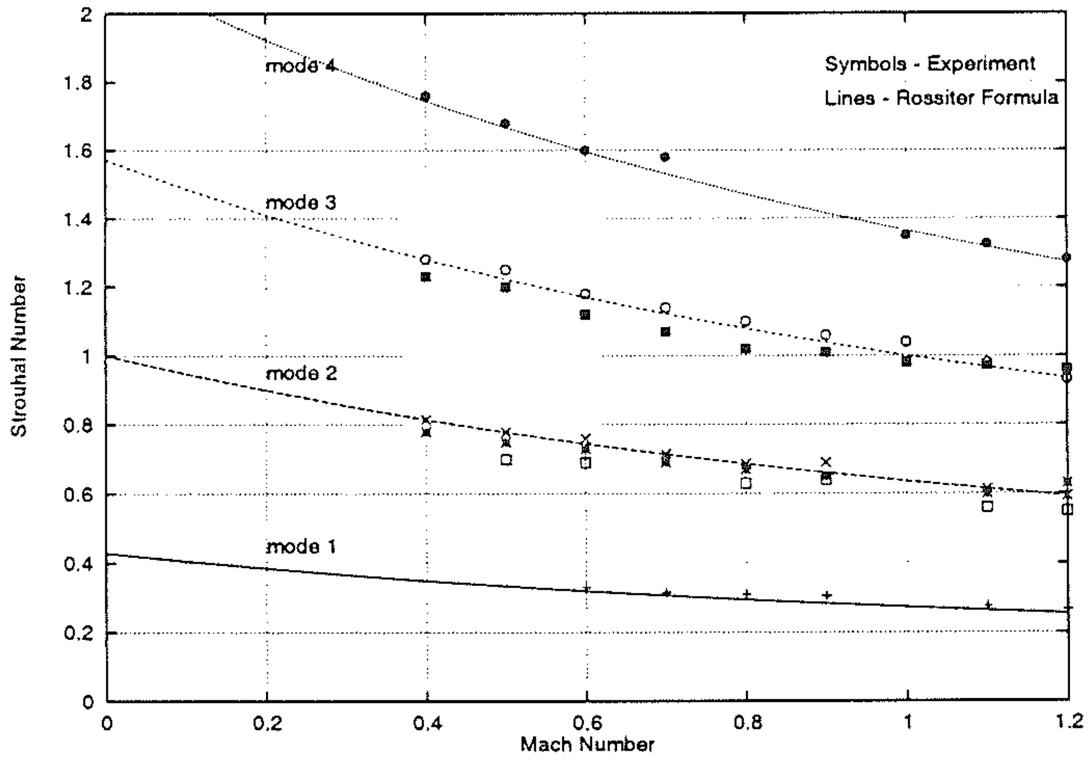

Figure 3.4: Variation of Strouhal Number with Mach Number (Rossiter)

consists of a single vortex driven by the freestream flow. Further work by Heller[41] found no vortex shedding to occur when water table visualisation techniques were used. Tam and Block[17] concluded that that accumulated evidence suggests that the vortex shedding from the front cavity wall may not be as important as Rossiter believed it to be. However, the work of Heller and co-workers indicated that the empirical model of Rossiter was qualitatively correct in proposing an acoustic source at the cavity trailing edge. Rossiter also showed that the variation of the unsteady pressures along the floor of the cavity, plotted in terms of root mean square (rms) values, increase in intensity with distance from the leading edge and approach a maximum at the aft cavity wall.

Bilanin and Covert [16] improved Rossiter's description of the events that sustain the discrete frequency oscillations. Although Rossiter highlighted the existence of an acoustic source, he neither explained how these acoustic disturbances were generated nor how they excited the shear layer at the cavity leading edge to initiate the shedding of another vortex. Bilanin and Covert attributed the cavity oscillations to an instability in the free shear layer [16]. This description was based on events similar to those proposed by Rossiter. The shear layer was assumed to be periodically disturbed at the upstream cavity wall, exciting an instability. The shear layer disturbance caused mass addition and expulsion at the aft cavity wall. The generation of the acoustic pulses at the trailing edge was attributed to this rather

than the impact of downstream moving vortices. Once the acoustic disturbances are created it was suggested that they propagate upstream to the front cavity wall, completing the feedback loop. Bilanin and Covert modelled these events using a line source at the aft cavity wall. This pulsated periodically to represent the generation of an acoustic pulse due to the action of the fluctuating shear layer. Likewise the excitation of the shear layer at the front wall by the upstream propagation of the acoustic disturbances was modelled by a line pressure force. This model was free from empirical constants and showed reasonable agreement with experimental data for high supersonic Mach numbers. For high subsonic and low supersonic speeds agreement was worse. There is also a fundamental problem with their model at very high supersonic speeds, according to Tam and Block [17]. They idealised the shear layer as a thin vortex sheet however Miles shows that for a thin vortex sheet the flow becomes stable for $M \geq 2^{1.5}$. If this is the case then the reliance of the Bilanin and Covert model on the instability of the shear layer means there are no driving mechanisms for the flow. This is contrary to what experimental results show. No account was given of how the discrete frequencies were sustained and the acoustic disturbances interacted with the flowfield or excited the shear layer at the upstream lip.

A description of the events occurring in an open cavity which was based on wave propagation was put forward by Heller and Bliss in 1975 [41]. The experimental study recorded information about frequencies, mode shapes and acoustic levels for different L/D ratios and Mach numbers. Palliative devices were also investigated. Despite basing the description on acoustic wave propagation, use was made of the equation developed by Rossiter. The tones detected in the experiments fell on the curves that are associated with the resonant modes, as defined by the Rossiter equation, modified to account for the higher sound speed in the cavity as

$$f_m = \frac{U_\infty}{L} \frac{m - \alpha}{\frac{M_\infty}{\sqrt{1+[(\gamma-1)/2]M_\infty^2}} + \frac{1}{\kappa}}$$

where γ is the ratio of specific heats and f_m is the modified resonant frequency corresponding to the mth mode. Heller and Bliss determined from their experiments that the constants α and κ are 0.25 and 0.57, respectively. It was previously esti-

mated that for cavities with a L/D ratio of 4 or greater, the difference between the unmodified Rossiter formula and experiments should be within 10% [40].

Although the derivation of the Rossiter equation was based on vortex shedding, Heller and Bliss did not consider this for their modified equation and instead focussed on wave propagation. Figure 3.5-1 indicates a pressure wave moving downstream and approaching the trailing wall. This wave produces an outward deflection of the shear layer that allows fluid to leave the cavity at the trailing edge. Upstream, a pressure wave, which previously had been travelling upstream, is reflected from the forward wall and now also moves downstream. In Figure 3.5-2, the upstream wave continues to travel downstream. The downstream wave, however, has reflected from the aft wall and propagates upstream through the relatively inactive fluid within the cavity. This wave moves supersonically with respect to the freestream and so a compression wave is generated in the external flow. At the rear bulkhead, the shear layer lies below the cavity lip, resulting in mass addition to the cavity. The forward and rearward propagating waves intersect near the centre of the cavity and, after interacting, maintain their respective directions as shown in Figure 3.5-3. At the aft bulkhead, the shear layer continues to inject fluid into the cavity, thus creating a recirculating flow. In Figure 3.5-4, the aft wave is seen to lift the shear layer above the downstream lip, resulting in mass removal, while the forward wave is about to impact the front bulkhead and complete the oscillation cycle that began with the situation depicted in Figure 3.5-1.

3.3 Theories from Simulations

Several computational studies have been published since 1988. None of these studies constitute a completely rigorous investigation but they provide detailed information on what the flowfield might look like. We therefore review several of these studies in the light of experimental theories summarised in the previous section. All of the studies are for supersonic freestreams, possibly because this makes applying far field boundary conditions simpler.

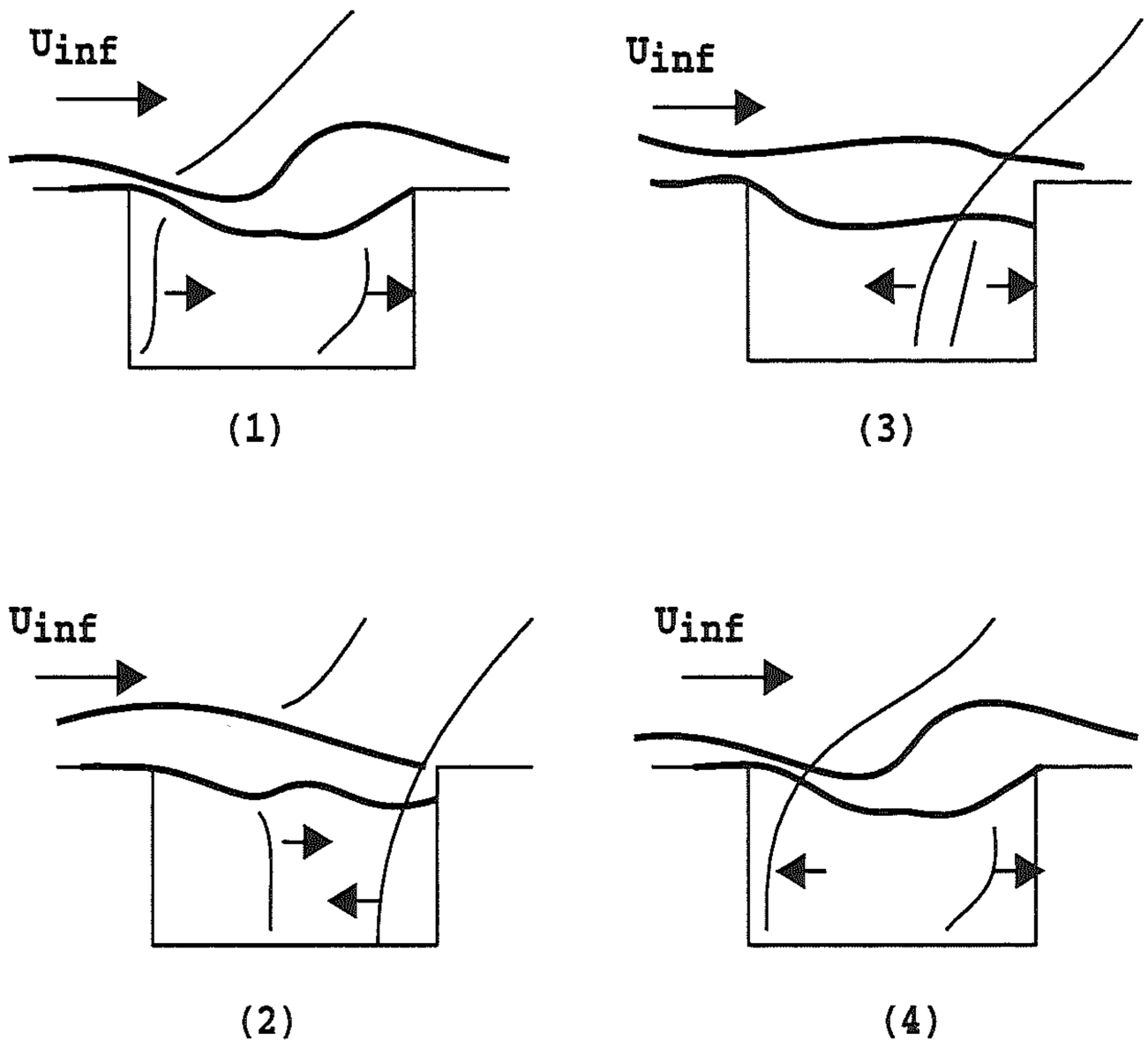

Figure 3.5: Schematic Representation of Cavity Oscillation Cycle

The first published study was by Rizzetta in 1988 [64]. This showed vortex shedding from the front lip and wave propagation outside the cavity.

Evidence of mass addition and expulsion was shown by Hamed and co-workers [76]. A compression wave originated from shear layer impingement on the rear cavity wall. Vortex shedding from the front lip was also evident.

Two studies by Zhang [95] [98] showed considerable detail about the flow field. Compression waves were evident outside the cavity and these originated from the impingement of the shear layer on the rear cavity wall. Mass addition and expulsion cycles were a prominent feature as the shear layer oscillated. The existence of vortical structures in the cavity was described in detail in [98]. A vortex shed at the leading edge was shown to move downstream until it mixed with a vortex at the trailing edge. The strength of the trailing edge vortex varied during the expulsion and addition.

A detailed description of a simulated result is given in reference [84]. The motion of waves and vortices was tracked and contrasted with the theory of Heller. In particular, downstream moving waves appeared to dissipate rather than reflect from the rear wall. In addition, the vorticity shed at the leading edge does not appear to generate the waves by impinging on the trailing edge.

3.4 Analysis of Flow Physics for L/D=5,M=0.85 Case

In this section the simulation results for the M=0.85, L/D=5 case are examined to identify the flow mechanisms. The events are examined at twelve times between 21.32 and 22.92, labelled by letters (a) to (l), corresponding to 2.415×10^{-3} seconds. The flow involves the interaction of vortices in the cavity, which play a major role in the feedback mechanism. There are usually two vortices present in the cavity, though one is seen to dominate, as shown in the streamline plots in Figures 3.6. Between times (a) and (c) a second vortex is formed resulting from the elongation of the original vortex. This new vortex is strengthened from vorticity generated at the upstream lip of the cavity and convects downstream, as shown by the vorticity contours in Figure 3.7 & Figure 3.10. The high level of vorticity at the leading edge of the cavity is evident. The pressure waves propagating upstream are clearly visible in Figure 3.8. Pressure history traces for locations on the cavity floor and aft cavity wall are shown in Figures 3.15. The locations of the vortex cores and pressure waves have been tracked from the solutions and are plotted in Figures 3.12 to 3.14.

The flow is characterised by a series of vortices whose cores travel smoothly down the cavity from 0.2L to 0.9L mainly at a height of 0.6 to 0.7 above the cavity floor, which can be seen in Figure 3.6. The vortices are formed and are driven mainly from the vorticity growth at the upstream lip of the cavity, which is seen to grow from time (a) to (g) in Figure 3.7. The shear layer above the cavity takes a wavy shape with a peak occurring directly above the core of the moving vortices. This peak lies above the cavity rim, as is evident in Figure 3.6. The pressure is also locally low in the vicinity of the vortices, as shown in Figure 3.11 which superim-

poses the pressure contours and streamlines at time instant (c). The lower pressure regions are represented in green, with red representing higher pressure regions. The troughs of the shear layer lie roughly half way between the moving vortex cores and are below the cavity rim. The pressure is locally high in this region between the troughs. Although for most of the time there are two vortices present (and hence two shear layer peaks), there is at any one time only one dominant vortex. For about 10 percent of the time there is one sole vortex whose core is at around 0.7L.

The history of a particular vortex involves its inception at position (0.2L,0.5D). Figures 3.6 (a) to (c) show the initial formation of the vortex; involving its splitting from the preceding vortex, which has at the time been stretched to fill the whole cavity (and thus is the only vortex present) with its core lying between 0.65L and 0.75L. The vortex strengthens from the leading edge vorticity (Figure 3.10) and the remnants of the vortex from the previous cycle, which is absorbed as it approaches the aft wall at time (a). As it moves towards the aft wall the core moves up, signalling the onset of mass expulsion. The trajectory of the vortex cores is shown in figures 3.12 and 3.14. By the time the core of the vortex approaches the aft of the cavity it is weakened by the expulsion of some mass over the rear cavity wall (Figures 3.6 (e) to (g)). This happens because the motion of the vortex eventually causes the shear layer to detach from the aft wall at time (f). With the shear layer separating from the aft wall the resultant pressure decrease causes the vortex to split, with flow in the upper part of the vortex (the crest of the shear layer above the vortex core), escaping downstream of the trailing edge, weakening the vortex. The flow from the upper part of the vortex (which lies above the cavity rim) escapes and convects downstream from the cavity leaving the weakened vortex, shown in Figure 3.6 (h). The pressure at the aft wall decreases due to the detachment of the shear layer, which causes a release from the relatively high pressures caused at flow attachment regions. Whilst this is occurring the new vortex has moved downstream and its presence causes the now weakened trailing edge vortex to move down towards the cavity floor (Figure 3.6 (h)-(i)). This motion causes the shear layer to reattach to the aft wall of the cavity, containing the weakened vortex. This signals the end of the mass expulsion process and the start of mass addition. The flow again stagnates on the aft wall of the cavity again increasing the pressure locally. The pressure rise can be seen from time 21.72

in Figure 3.15(j) and is evident in the pressure contours from Figures 3.8 (h) to (j). The new vortex is seen to ride below and to the front of the deflected shear layer and therefore force the upward motion of the shear layer after X/L=0.3. (Figures 3.6 (f)-(h) The vortices are therefore responsible for the upward (and downward) deflection of the shear layer. It is evident that as the vortex moves downstream it controls the deflection of the shear layer. While the shear layer is deflected up near the leading edge it is deflected downwards at the cavity trailing edge. Again, this downward deflection may be attributed to the motion of the downstream moving vortex. From Figures 3.6 (a)-(c) at the front of the vortex its downward momentum causes the shear layer to deflect into the cavity. As it does there is an interaction with the smaller vortex residing near the trailing edge of the cavity. The two then merge and are forced to the top of the cavity initiating mass expulsion from the cavity. Returning to the trapped vortex - it is slowly squeezed towards the lower aft corner of the cavity, which is seen at times (g) and (h) in Figure 3.6. During this time the new vortex has gained by feeding on the vorticity generated at the upstream cavity lip. The new vortex also feeds off the remnants of the weakened vortex and when the new core has reached 0.5L to 0.55L (time (j) in Figure 3.6) this vortex absorbs the weakened vortex trapped in the corner, now nearly stationary at (0.9L, 0.4D), assisted by the lower pressure between the vortices. This results in a single vortex in the cavity. It is strengthened by the entrained fluid during the mass addition part of the cycle. Fluid is pulled in to the cavity and turns down the rear wall and then back along the bottom wall. The single vortex becomes elongated due to the additional mass from the absorbed vortex, stretching towards the front of the cavity where a lobe is formed at time (j). The shear layer deflects into the cavity, with its shear force in the streamwise direction. The upstream vortex also gains momentum in the opposite direction from the absorbed vortex that is downstream in the cavity. These effects combine to cause the lobe to split and create a new vortex, as shown at times (l), (a), (b), (c), (d), completing the cycle. This event completes one oscillation cycle. The average convection speed of the vortex core is estimated from Figure 3.13 over the middle 60 percent of the cavity length is 38 percent of the freestream speed, which is Mach 0.323.

At the aft wall of the cavity, the pressure reaches a maximum soon after the shear

layer impingement, increasing from time (j). The maximum here is the highest value in the flow field and is 35 percent above the freestream static pressure. By comparison if the freestream stagnated it would be around 60 percent above the static pressure. This pressurisation continues for about 0.2T of the cycle and triggers a strong pressure wave, aligned at roughly 45^o to the oncoming flow, to propagate forward and upward from the region of the cavity. The pressure wave is first evident at time (j) and can be followed in Figure 3.8 as it propagates towards the front of the cavity in the equivalent time that a vortex core is convected down the cavity, thus connecting it to the dominant 2nd tone. Pressure waves from previous cycles can also be seen. Following the pressure wave upstream a suction wave is in turn propagated with the same alignment and direction, caused by the escape of fluid lowering the pressure at the rear of the cavity. This again covers the cavity length in the equivalent time to a vortex core convecting down the cavity. These observations provide the evidence that the unsteadiness is caused by a feedback mechanism from the shear layer attachment and detachment from the rear wall of the cavity. The average propagation speed of the upstream waves, derived from Figure 3.12, is approximately 50 percent of the freestream speed.

These upstream travelling waves (associated with pressure increases for pressure waves and decreases for suction waves) meet the downstream travelling vortex cores (associated with pressure decreases) and the zones between the cores (associated with pressure increases) and create the characteristic wall pressure traces (Figure 3.15) and the resulting 'W' shape of the SPL along the cavity floor, shown in Figure 2.13. The upstream travelling pressure wave meets the vortex cores in the vicinity of 0.35L and of 0.7L causing the pressure fluctuations to be smaller and also enhancing the higher frequency tones. Figure 3.11 shows the vortex core meeting a pressure wave at X/L=0.7. Figure 3.15 (g) shows the level of the oscillations to be lower though the frequency of them increases. Figure 2.4 shows that the 1st tone in the cavity is enhanced at X/L=0.75. The same behaviour is evident when the pressure waves meet the vortex cores at X/L=0.35.

The upstream travelling suction wave meets the vortex cores between 0.55L and 0.2L, as shown in Figure 3.8 between times (i) and (j). This is where the sound pressure levels are large and the second tone is more prominent. Although not necessarily

important to the analysis, the formation of a vortex, at (0.2L, 0.5D) coincides with the passing of the upstream suction wave at this point and is coincident with the passing of the upstream pressure wave with the sole downstream vortex at around 0.7L. Also, the merging of vortices occurs at the coincidence of the vortex with the upstream travelling pressure wave at (0.9L, 0.7D) and of the dominating upstream vortex with the passing of a suction wave at (0.5L, 0.6D).

Away and above the cavity the acoustic field generated is shaped by the pressure and suction waves generated upstream at about 45 degrees to the freestream and the suction and pressure waves moving downstream and generated from the vortex cores and the high pressure regions between them. Thus where the pressure waves and suction waves enhance each other there lie patches of high and low pressures respectively. Since the streamwise travelling waves are weaker by about 1L away from the cavity the counter streamwise waves become predominant. It is when the pressure waves pass over the leading edge of the cavity that the feedback loop is completed. Figure 3.9 shows the flowfield at Time=22.02 just as a pressure wave passes over the leading edge of the cavity. Figure 3.10 shows the flowfield slightly later (T=22.12) when the leading edge vortex feeds from the growth of vorticity caused by the pressure wave passing over the leading edge. The vorticity at the leading edge is seen to be smaller before the pressure wave passes over the leading edge (Time=21.92, Figure 3.7 (f)).

3.5 Influence of Mach Number

Between Mach 0.85 and Mach 1.19 there is a significant rise in the unsteady pressure level within the cavity for the experimental results (compare Figures 2.13 and 2.14) The CFD results are seen to exhibit a similar trend. At Mach 1.19 the SPL distribution along the cavity floor is similar to that for Mach 0.85 flow, with the exception of a slight plateau in the distribution between X/L =0.65 and X/L=0.75. This would suggest that the flow physics in the cavity will tend to be similar. Ross [70] also found that there was evidence of a cyclic variation of the acoustic disturbances which is evident from the present work. Figure 3.16 shows the discrete tones predicted at Mach 1.19. The tones measured are seen to increase in amplitude with

the third and fourth tones especially becoming more apparent even if their contribution may not be significant. For a L/D=6.5 cavity, Ross [70] found the dominant tone to be at 340Hz with other tones that agreed with the Rossiter predictions for 133Hz, 574Hz, and 795Hz - not too disimilar to the present predictions. Ross found, in agreement with the present results, that *maximum amplitude is found for the second tone and is very much higher than those found for the other tones.* No information was obtained about the flow features from the study of Ross which is an area that the present work addresses.

As expected the features inside the cavity for transonic open cavity flow are similar to those exhibited for subsonic cavity flow. Pressure fluctuations exist which are caused by the oscillating shear layer which in turn drives the vortex interaction and pressure wave propagation, as previously discussed for the subsonic case. The similar vortex interaction to the subsonic cavity flow is evident from Figure 3.19, which shows streamlines superimposed on the Mach contours. In transonic and supersonic flow experiments, discrete vortices are not usually seen so there is nothing with which to compare the present streamline plots. In addition few experimental works have provided flow visualisation about supersonic or transonic open cavities for the external flow either. However research recently published by H. Heller & J. Delfs [42] has provided information about the external flow-field for transonic cavity flow. The experiments were conducted in an effort to provide a clearer understanding of the physical mechanisms prevalent in the external flow-field. The findings will be compared to the results from the simulations.

An arbitrary point has been chosen for the start of the oscillation cycle. The cycle is analysed between the non-dimensional times of 41.62 and 43.12. Figure 3.19 shows the Mach contour plots at different time instances in the cycle. Shown in Figure 3.18 are the pressure distributions on the cavity rear wall. From the animations it is seen that the pressure waves move outward into the external flow-field as well as forward. Heller and Delfs report that the external wave front moves out into the external medium as it is no longer attached to an internal pressure wave propagating upstream inside the cavity. They suggest that the internal wave reflects off the front cavity wall and moves downstream and is no longer capable of supporting an external

wave front. These claims supported earlier work with water table simulations [41]. It is important to mention that the water table simulations correspond to the first mode of oscillation. It has been shown in the current work, and is freely admitted by Heller, that the second mode dominates (though higher modes are rarely seen in water table experiments).

The sketches for the leading edge flow are shown in Figure 3.17 (a) for the work of Heller and Bliss and Heller and Delfs [41] [42]. Rossiter's explanation, Figure 3.17 (b) favours a theory of discrete vortices. He proposes that the shear layer rolls up and periodically sheds vortices from the cavity leading edge. Rossiter explains that a newly formed vortex moves above the cavity rim and slows the external flow to such an extent that a bow wave is produced at the leading edge. As the vortex is convected downstream it produces pressure waves which propagate upstream, as shown in the figures. At first it seems that the two explanations are at odds with one another. However the present results suggest they are in-fact different perspectives of the same event.

In Figure 3.19 (a) it is seen that at the very leading edge of the cavity the shear layer is deflected upward which results in the formation of a compression shock. This feature is present in the Schlieren optical spark photographs of Heller [42] and shown schematically in Figure 3.17 (a). The compression shock is quasi-steady, so when the the shear layer starts to deflect downward the formation of an expansion wave will cause it to disappear. This shock will therefore appear and disappear in one oscillation cycle. In Figure 3.19 (c) the leading shock is already weakened as the shear layer starts to deflect down into the cavity but reforms in Figure 3.19 (g) when the shear layer is deflected upwards, completing one oscillation cycle. It is difficult to establish the Mach angle of the leading edge shock because of its quasi-steady nature. However an approximate value of 59° compares very well to the 57.17° predicted by the Mach angle formula from oblique shock theory [2] for compressible flow, $\mu = sin^{-1}\frac{1}{M}$. In addition to the quasi-steady compression shock at the leading edge it is evident that pressure waves are travelling from the cavity trailing edge towards the front of the cavity. The wavefront, which has been marked for clarity, is seen moving forward in Figures 3.19 (b), (c) and (d). The angle of inclination at the leading edge is clearly less than that for the quasi-steady compression wave. This

can be explained by the fact that the pressure wave is moving against the freestream flow. The freestream Mach number is 1.19 which means that the wavefront is moving at a Mach number greater than 1.19. From the Mach angle formula the angle of inclination will therefore be less. It is seen in Figure 3.19 (d) that as the external front reaches the leading edge of the cavity a new vortex is forming. Its formation follows the description given for the subsonic case. The wave in the external flow can be seen to move off into the farfield in Figures 3.19(d) - (h), as is suggested by Heller et al. It is also suggested by Heller that the internal wave supporting this front will reflect off the front cavity wall and move downstream (Figure 3.17 (a)). Figures 3.19(d) through to (h) show a new vortex in the cavity traveling downstream.

Figures 3.19 show a wavefront moving upstream and when it moves into the free medium a vortex is seen at the leading edge. The CFD results show features common to Figures 3.17 (a) & (b), hence linking the theories. Rossiter proposed that the growth of this new vortex is responsible for the bow wave at the leading edge, which has previously been referred to as the quasi-steady compression shock. Heller's explanation is similar, attributing the quasi-steady compression shock to the deflection of the shear layer. Figure 3.19(d) shows that when the vortex is formed the shear layer is deflected downward at the cavity leading edge, thus is not capable of supporting the compression shock. The vortex grows and moves towards the top of the cavity (position similar to that for Mach 0.85 flow in Figure 3.14). This causes an upward deflection of the shear layer which in turn causes the formation of the leading edge compression wave seen in Figure 3.19(h). It is seen that the explanations given by Heller et al and Rossiter can be related once again.

While the events at the front of the cavity have been related to a reasonable extent, those occurring at the cavity trailing edge are more difficult to connect. Rossiter investigated Mach 1.2 flow over a cavity of L/D=2 while Heller obtained similar conditions by accelerating Mach 0.73 over an aerofoil section thus obtaining Mach 1.22 flow over a cavity of L/D=2. The present results are for Mach 1.19 flow over a cavity of L/D=5 so differences in the flow features are to be expected. From shadowgraphs, Rossiter believed that three pressure waves existed at the trailing edge. There is a breakdown shock wave in the periodic mass outflow from the cavity. Rossiter believes that waves D and C appear before vortex A has reached

the trailing edge but only propagate upstream once vortex A (Figure 3.17 (b))is expelled from the cavity. Rossiter mentions that wave D is not tangential to the Mach line. This feature has already been detected in the present results which, in agreement with Heller, shows the wave to propagate upstream *before* the vortex reaches the trailing edge. The wave D can only move upstream if it is trailing a pressure wave in the cavity also moving upstream. The wave moves into the free medium when it detaches from this internal cavity wave. This occurs when the internal wave reflects off the front wall. It has already been shown that the *reflected wave* from the Heller study coincides with the *vortex* from the Rossiter study. This means that wave D must move upstream *before* the vortex reaches the trailing edge. Of course the present results are for a cavity of L/D=5 while Rossiter investigated L/D=2. His results effectively allowed one vortex and one acoustic wave to exist at any time. It is therefore slightly more difficult to interpret the chain of events. The present case shows two vortices to exist in the cavity and a pressure wave to be emitted each time a vortex approaches the trailing edge. Indeed, when Rossiter develops his empirical formula to determine the phase relation between vortices and pressure waves the description of the events are similar to those seen by the CFD results. One of the fundamental assumptions in the development of the empirical relationship is that the frequency of the vortex is equal to the frequency of acoustic radiation. This has previously been shown to be the case for subsonic flow (Figure 3.12) and is also true for the present results of Mach 1.19 flow. An important fact from the development of the relationship is that Rossiter shows that a vortex is responsible for the acoustic radiation which in turn initiates a new vortex at the leading edge. The present results show that it is not the leading edge vortex but another one in the cavity that is responsible for the acoustic radiation. The leading edge vortex will eventually become this *second* vortex and ultimately be responsible for the acoustic radiation.

Figure 3.18 shows the pressure on the aft wall to be approaching a minimum at T=42.62. This represents the mass expulsion process as can be seen in Figures 3.19(d)-(f) (pressure trace is slightly down the aft wall so there is a lag in the trace compared to the events shown in Figures 3.19). The outflow has been described as a *plume* by Rossiter which is recognisable in Figure 3.19 (d). A feature detected by

Heller during the mass expulsion process was a compression wave after the trailing edge which occurs as the shear layer re-attaches at the trailing edge. Although not as prominent as the one witnessed by Heller there is a slight compression region at the trailing edge evident in Figures 3.19(e) & (f). A possible reason why it may not be as strong as the compression wave witnessed by Heller is that the cavity in the present study is L/D=5. Figure 3.19(e) shows a saddle point between the two vortices which means the flow riding on the vortex crest at the trailing edge has not expanded as much as it would have otherwise. The subsequent compression will be weaker relative to the case where no saddle point existed. It is probably the case that two vortices never co-existed for the L/D=2 case in the Heller experiments, hence the stronger compression wave. The compression wave is, as to be expected, tangential to the Mach angle. The same can be said for the quasi-steady bow shock wave highlighted in Figure 3.19(b). Whereas the compression shock at the leading edge occurs when the shear layer is deflected upward, the bow shock at the trailing edge occurs when the shear layer deflects down into the cavity leaving the aft wall exposed to the freestream. Heller attributed the formation of the compression wave to an *outward/inward* bulk [42]. Previously explained in reference [44], the simulations show that when the shear layer deflects into the cavity at the trailing edge (Figure 3.19 (b)) the boundary layer after the trailing edge develops at the top corner of the aft wall. The boundary layer flow is by it's nature slower than the flow being expelled from the cavity. The quasi-steady bow shock aids the natural development of the boundary layer by compressing the flow before the trailing edge. However when the shear layer starts to lift above the cavity the boundary layer is no longer *protected* and has an impact on the fast moving flow riding on the crest above the trailing edge vortex, Figure 3.19 (e). The flow in the boundary layer is effectively trapped - bounded by the wall below it and the freestream flow above it. Eventually over-expanded flow on the shear layer crest encounters the slower moving boundary layer flow and the result is the formation of the compression wave. An explanation is given by Rona [67] describing the flow being ejected to be circumvented by the supersonic flow. The wall then turns the circumventing flow on itself creating the compression shock. Rona did not connect the event to the behaviour of the trailing edge vortex.

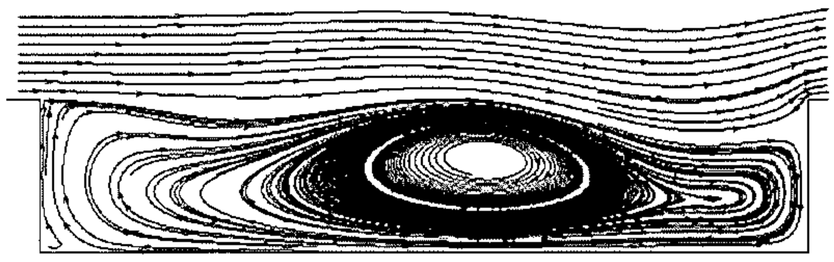

(a) Time=21.32

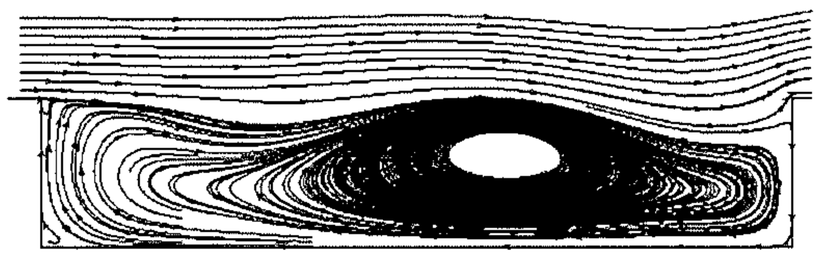

(b) Time=21.42

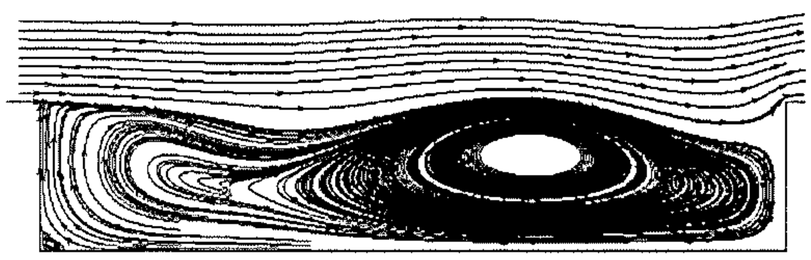

(c) Time=21.52

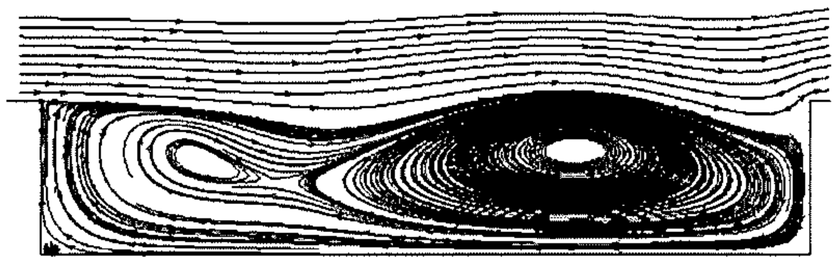

(d) Time=21.62

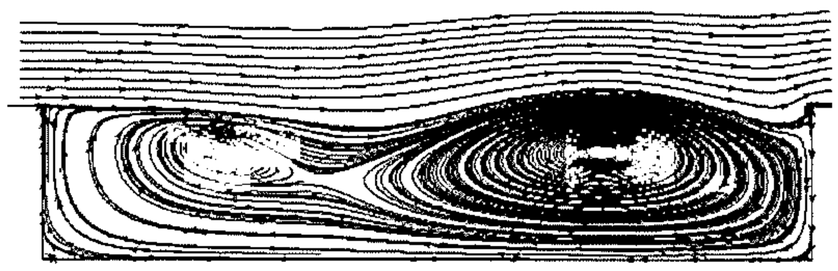

(e) Time=21.72

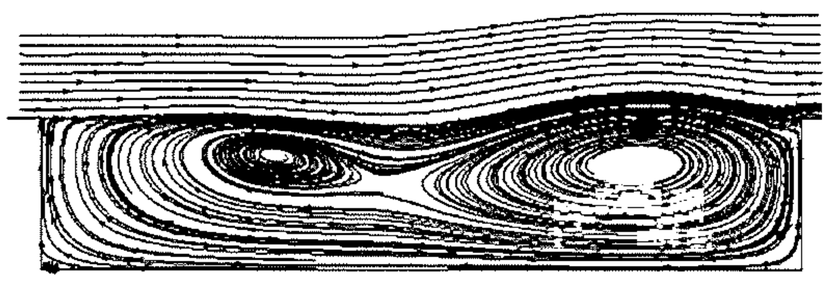

(f) Time=21.92

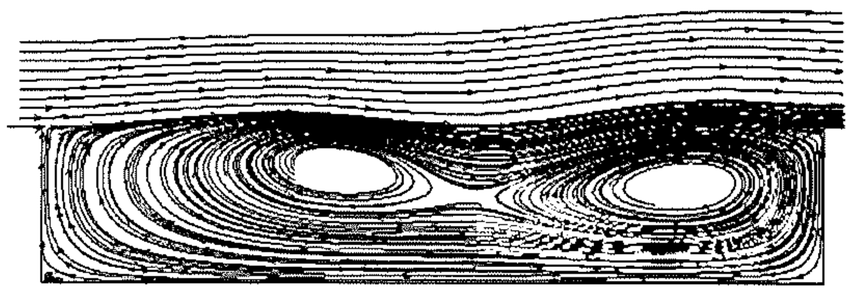

(g) Time=22.12

(h) Time=22.32

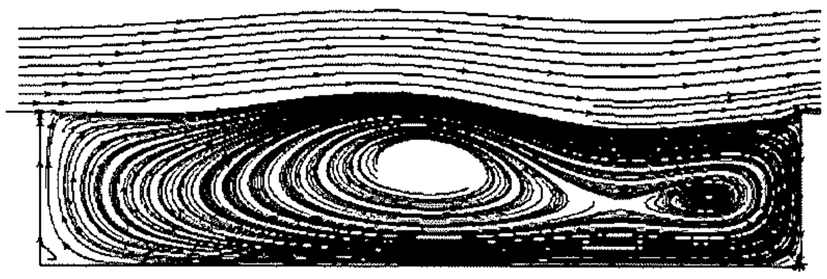

(i) Time=22.52

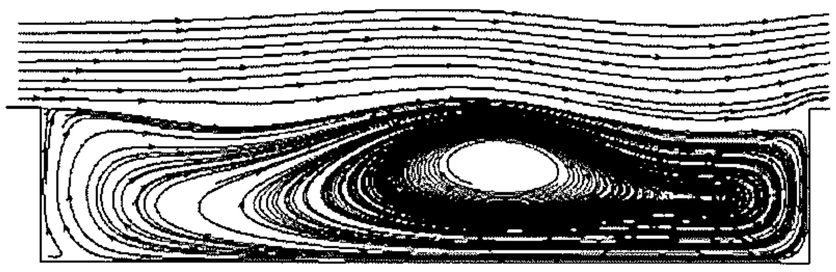

(j) Time=22.72

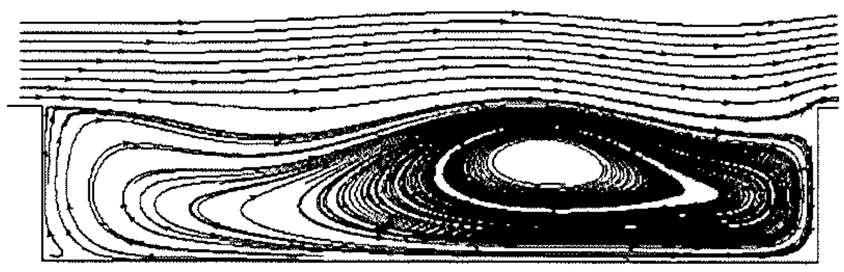

(k) Time=22.82

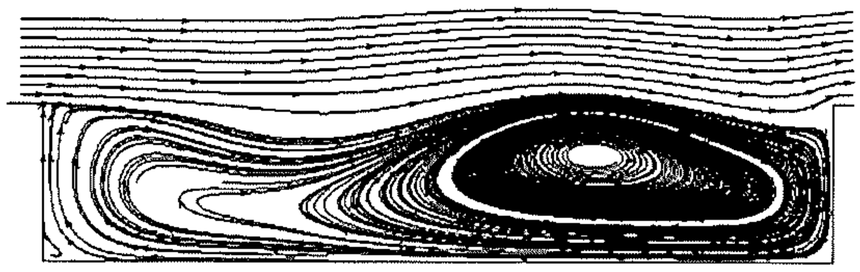

(l) Time=22.92

Figure 3.6: Streamlines for L/D=5, Mach 0.85

(a) Time=21.32 (b) Time=21.42 (c) Time=21.52

(d) Time=21.62 (e) Time=21.72 (f) Time=21.92

(g) Time=22.12 (h) Time=22.32 (i) Time=22.52

(j) Time=22.72 (k) Time=22.82 (l) Time=22.92

Figure 3.7: Vorticity Contours for L/D=5, Mach 0.85 (Red - high vorticity, blue - low vorticity))

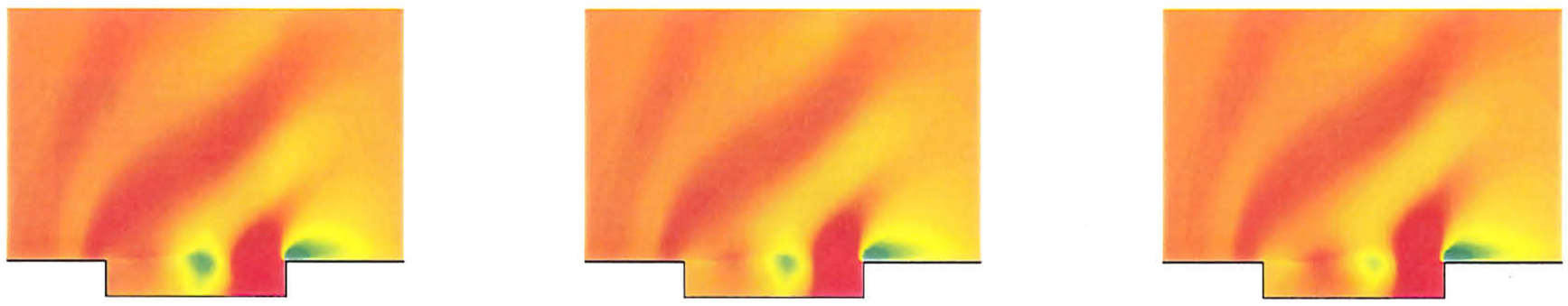

(a) Time=21.32 (b) Time=21.42 (c) Time=21.52

(d) Time=21.62 (e) Time=21.72 (f) Time=21.92

(g) Time=22.12 (h) Time=22.32 (i) Time=22.52

(j) Time=22.72 (k) Time=22.82 (l) Time=22.92

Figure 3.8: Pressure Contours for L/D=5, Mach 0.85 (Red - higher pressure, green/yellow - lower pressure)

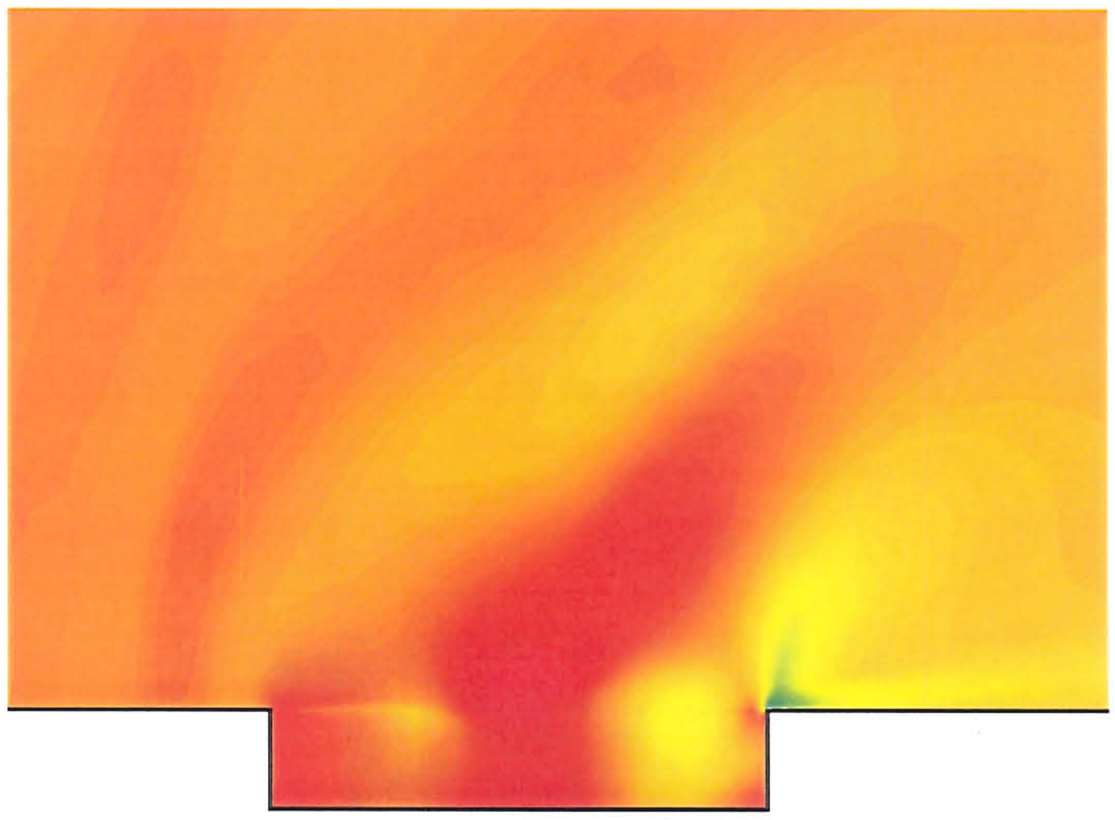

Figure 3.9: Instantaneous Pressure Contours at T=22.02.

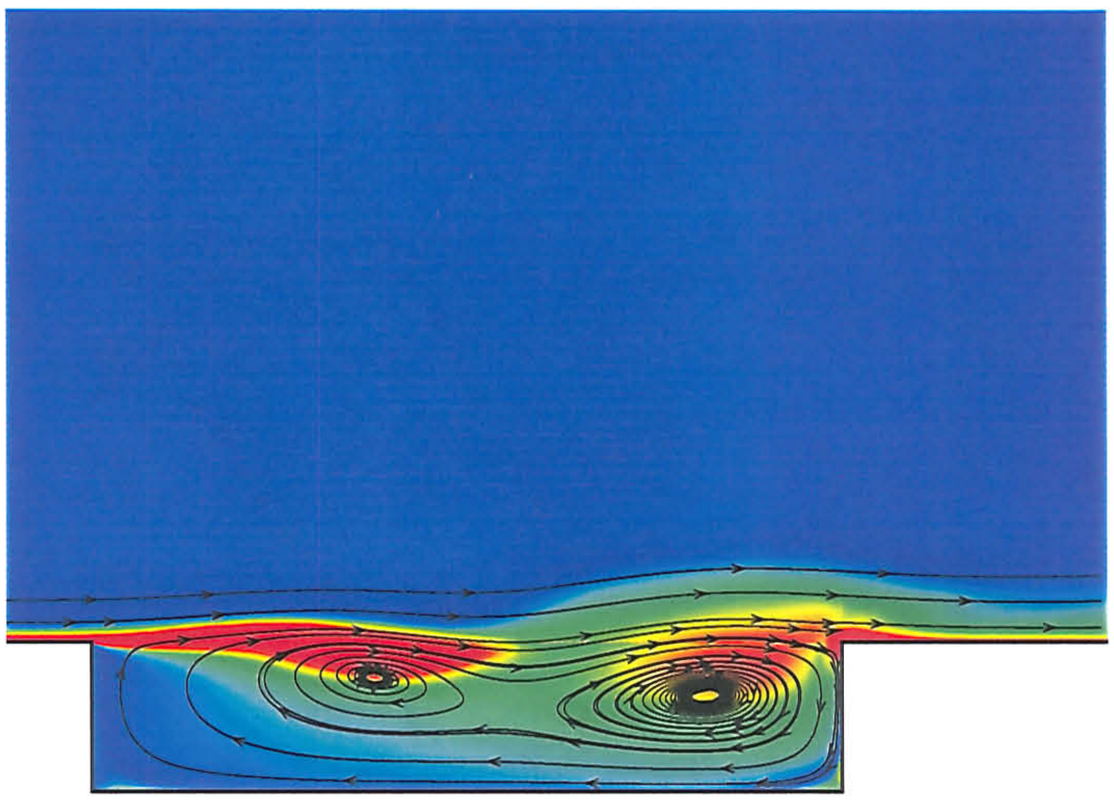

Figure 3.10: Vorticity Contours and Streamlines at T=22.12

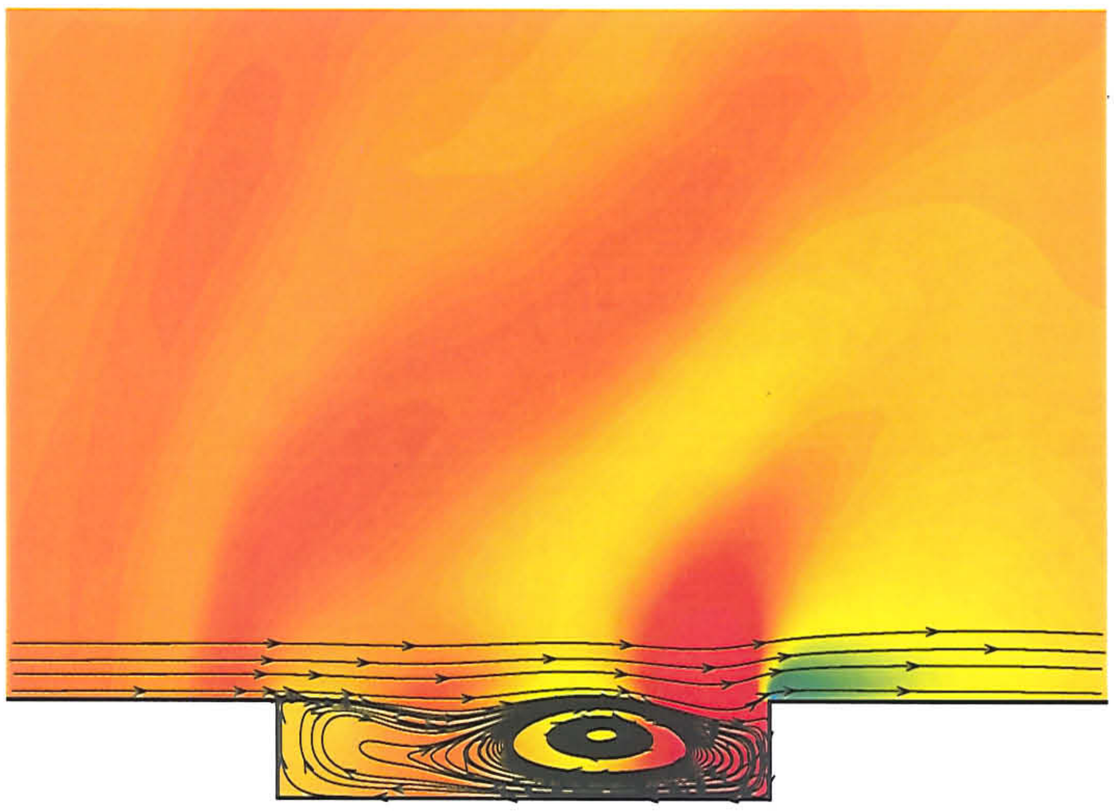

Figure 3.11: Streamlines superimposed on Pressure Contours at T=21.52

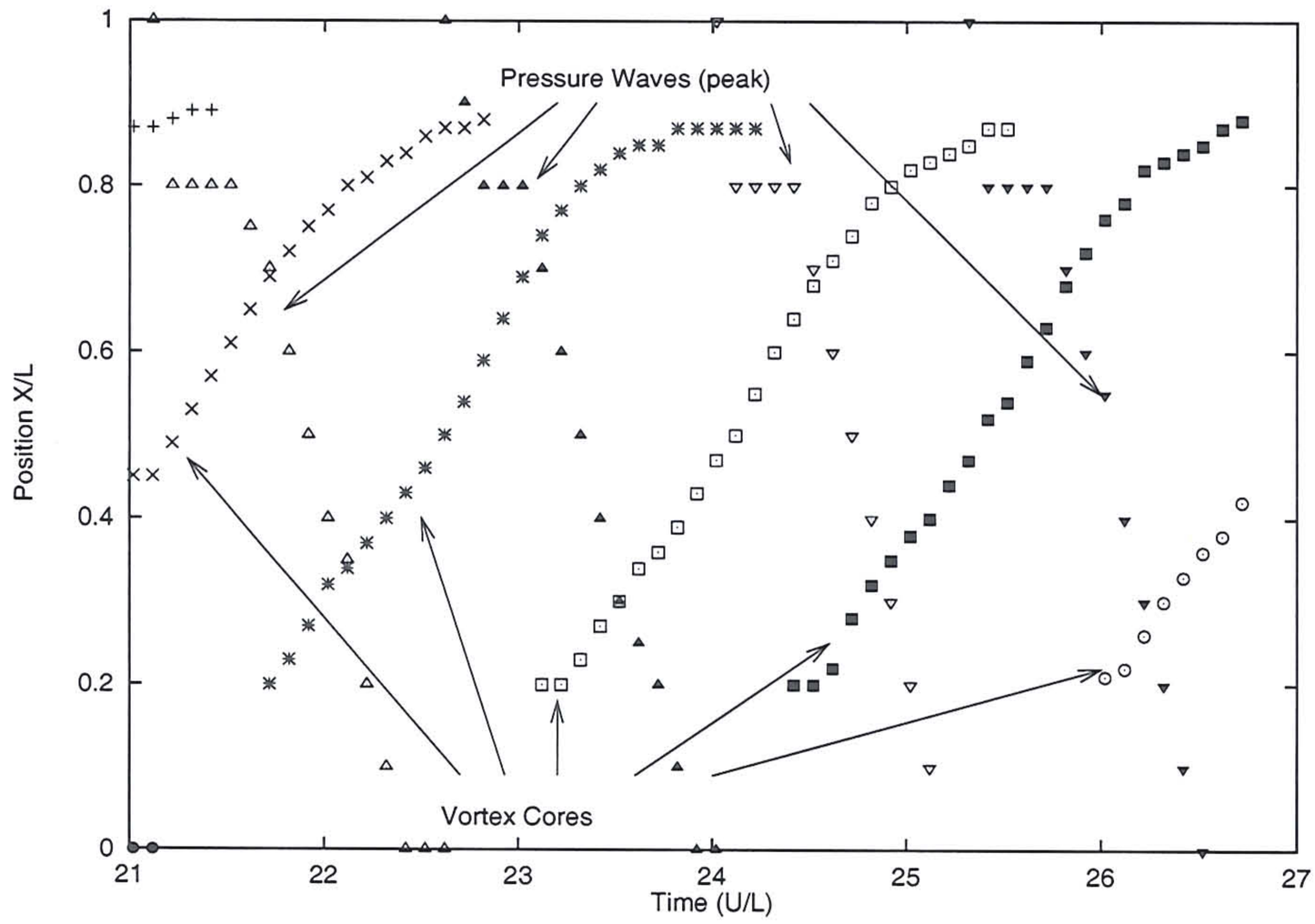

Figure 3.12: Tracking of Vortex Cores and Waves

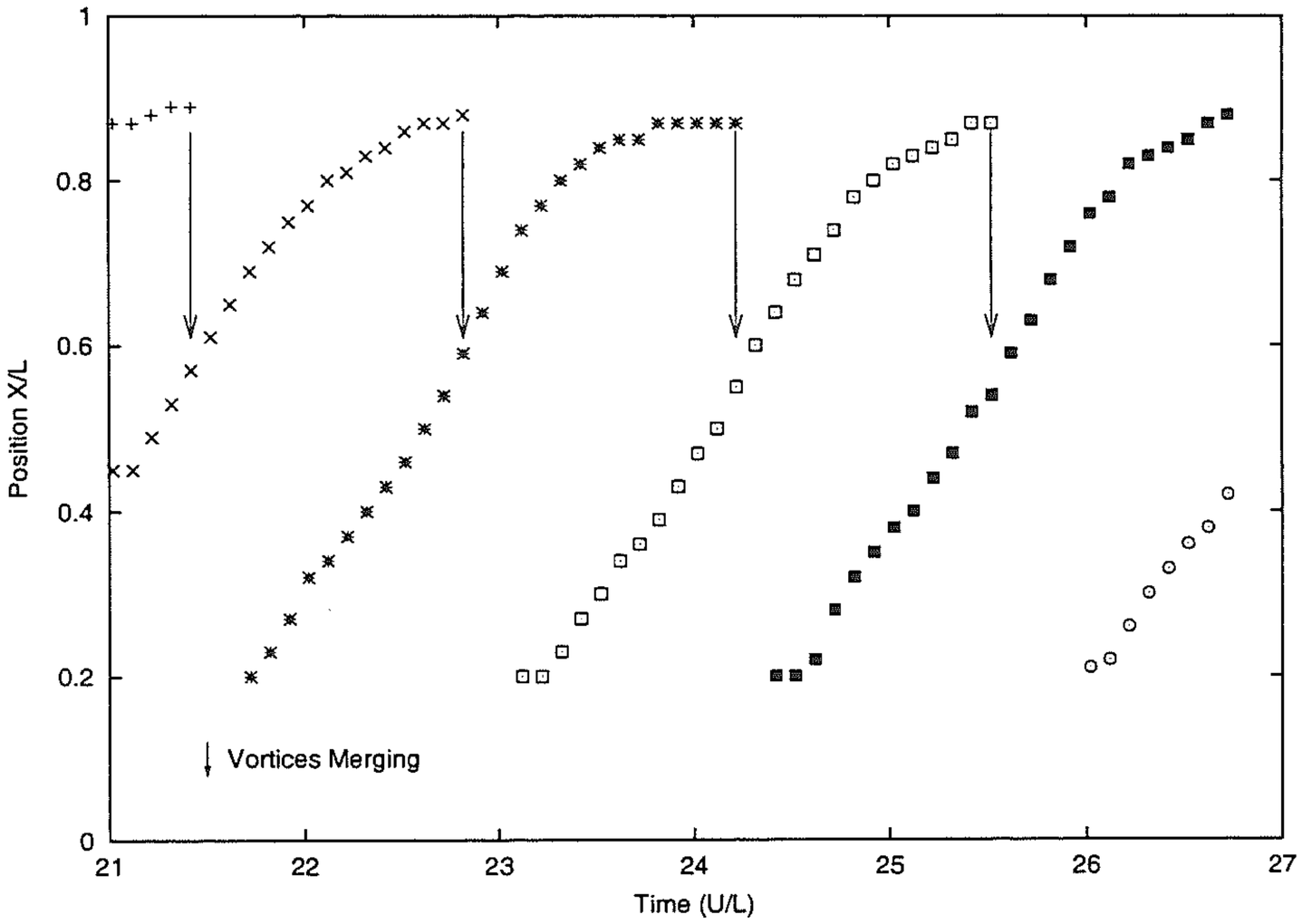

Figure 3.13: Horizontal Tracking of Vortex Cores

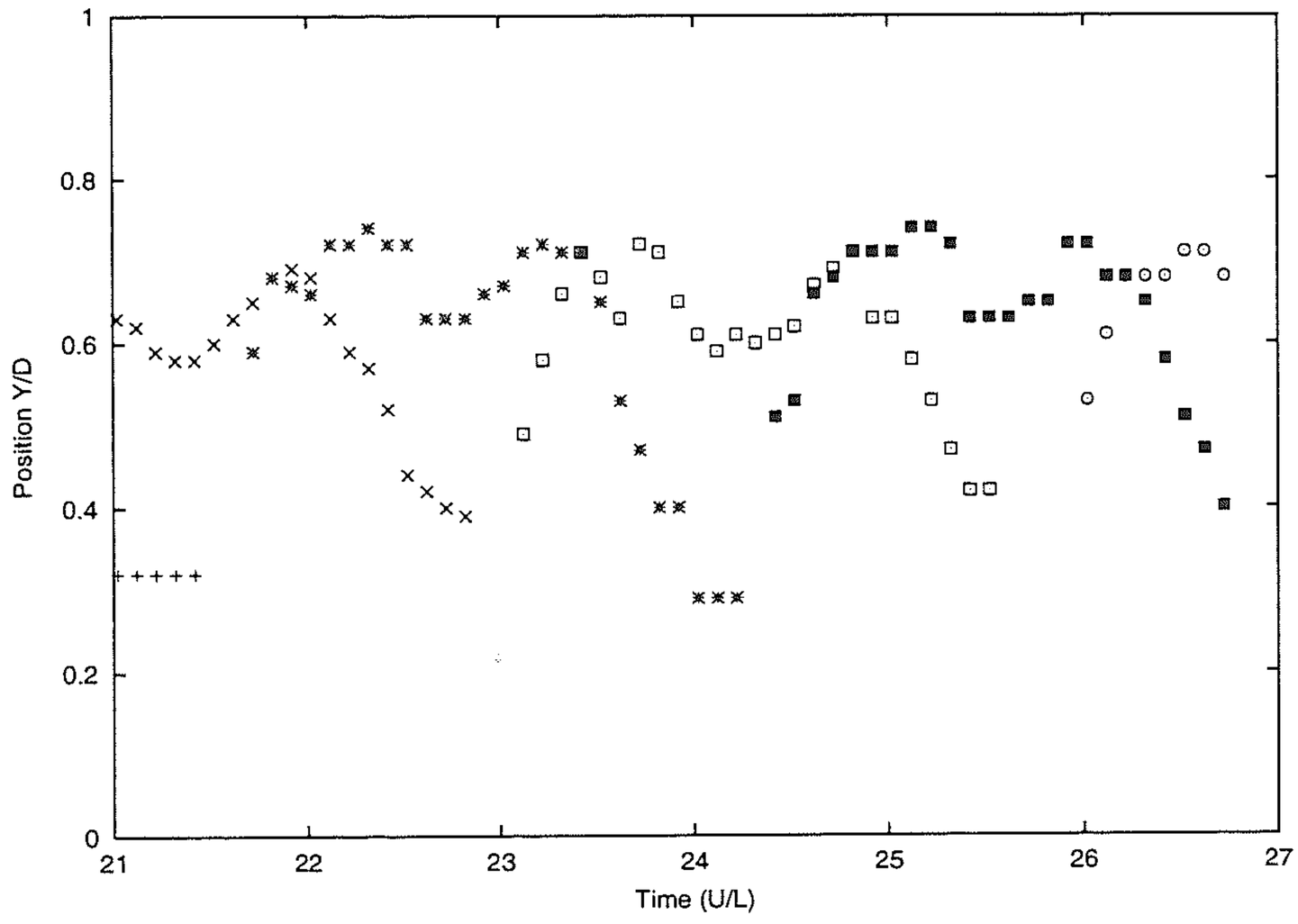

Figure 3.14: Vertical Tracking of Vortex Cores

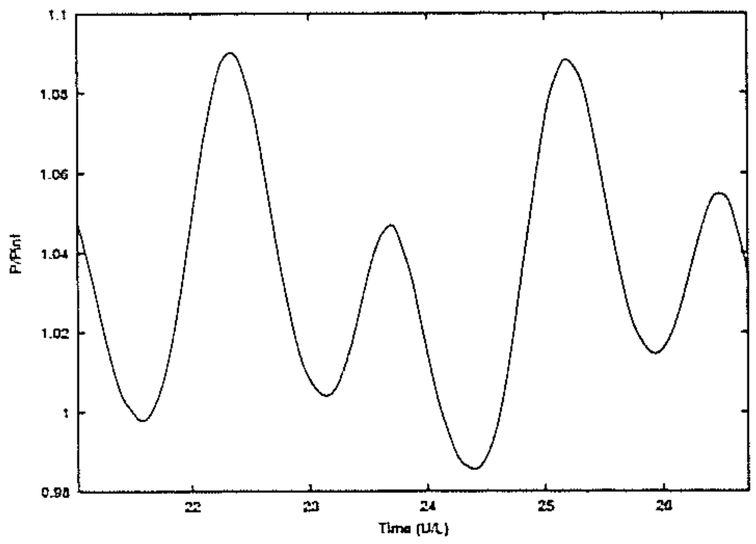

(a) X/L=0.15

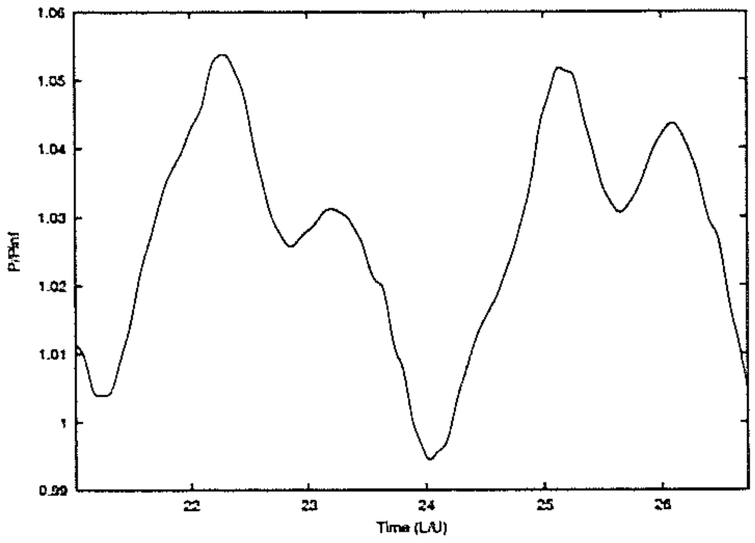

(b) X/L=0.25

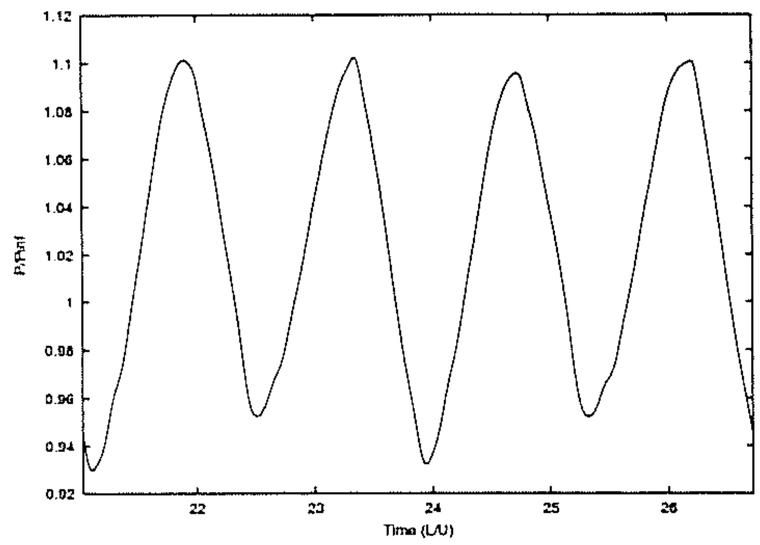

(c) X/L=0.45

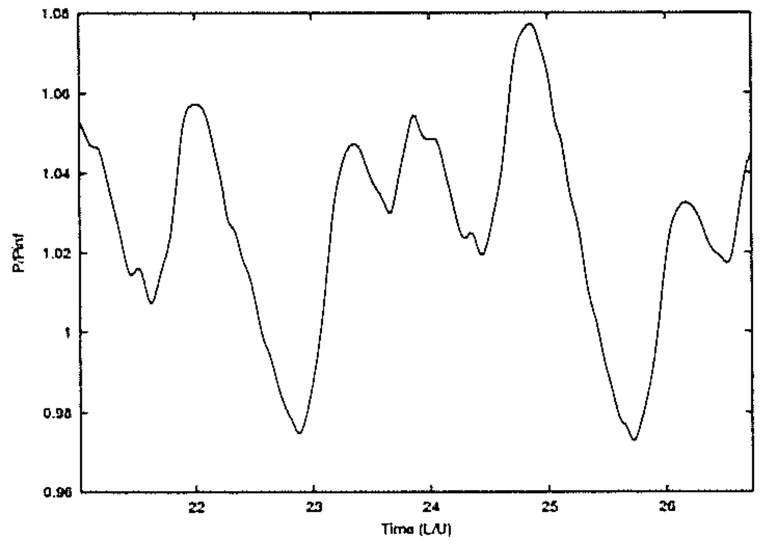

(d) X/L=0.65

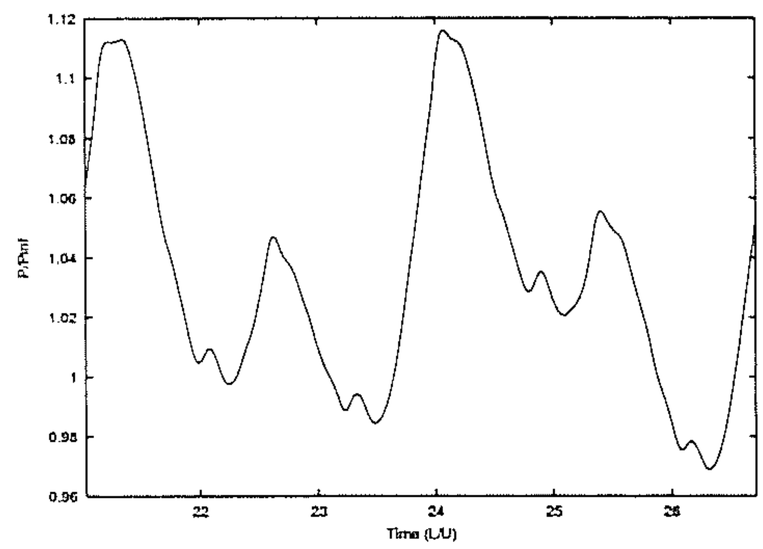

(e) X/L=0.75

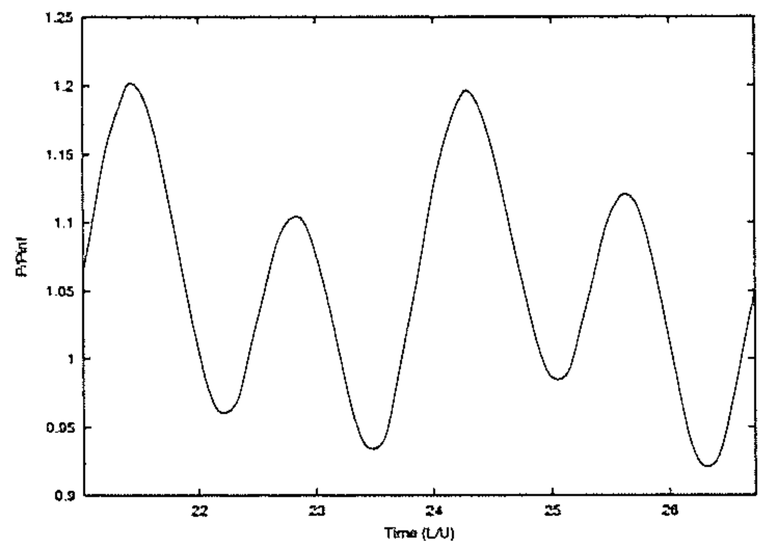

(f) X/L=0.85

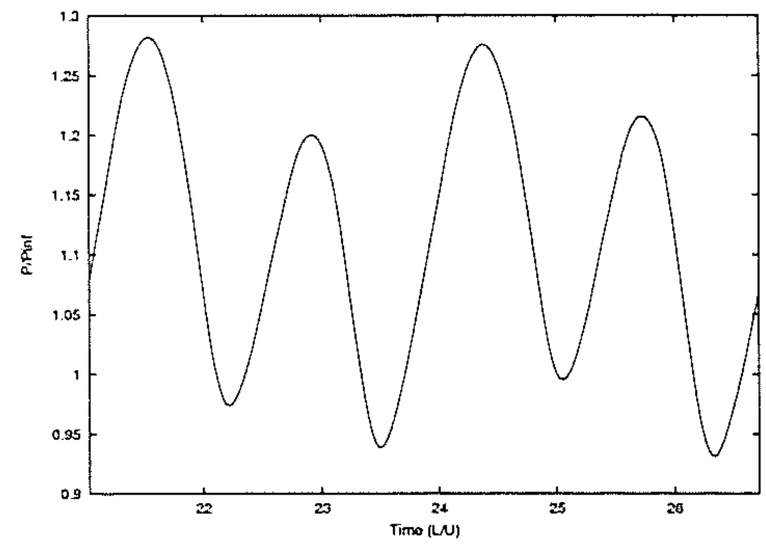

(g) X/L=0.95

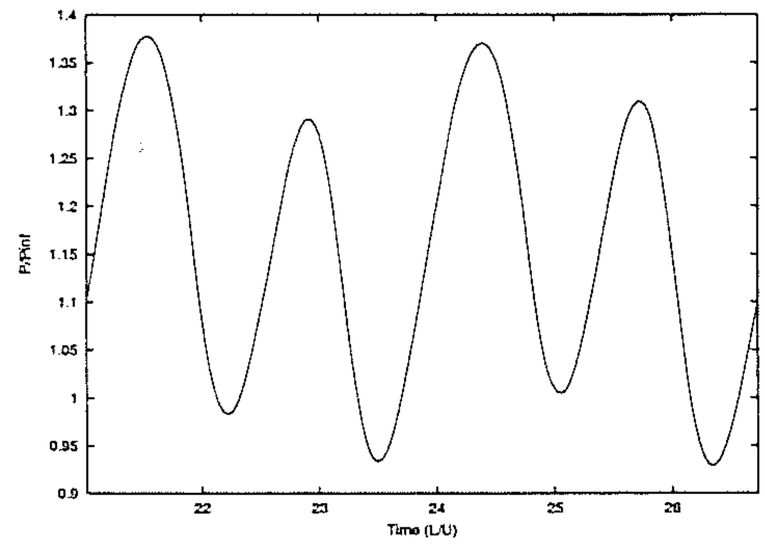

(h) Rear Wall

Figure 3.15: Monitored Pressure History at Selected Locations on the cavity floor

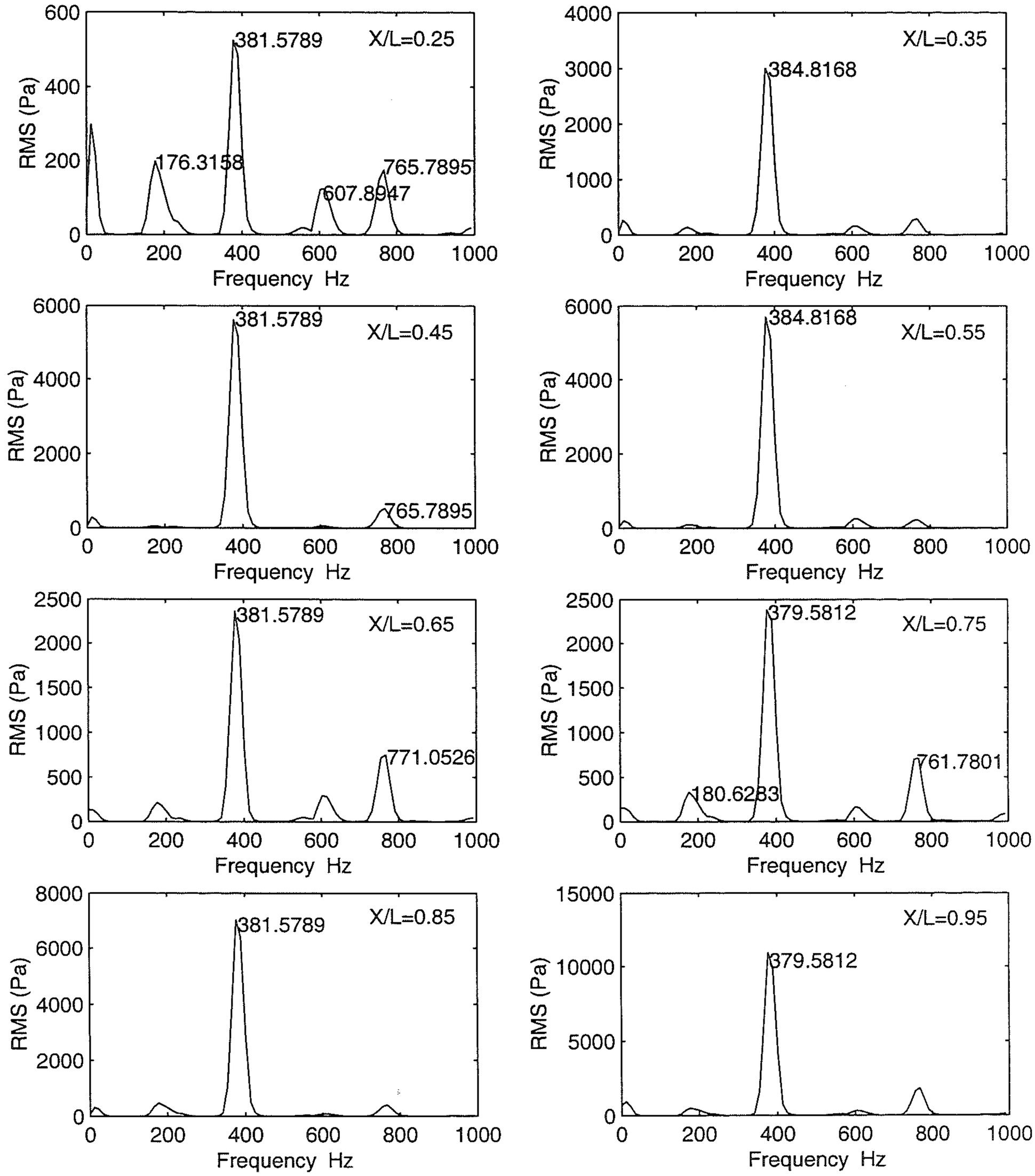

Figure 3.16: CFD RMS Pressures along Cavity Floor for Clean Cavity Mach 1.19

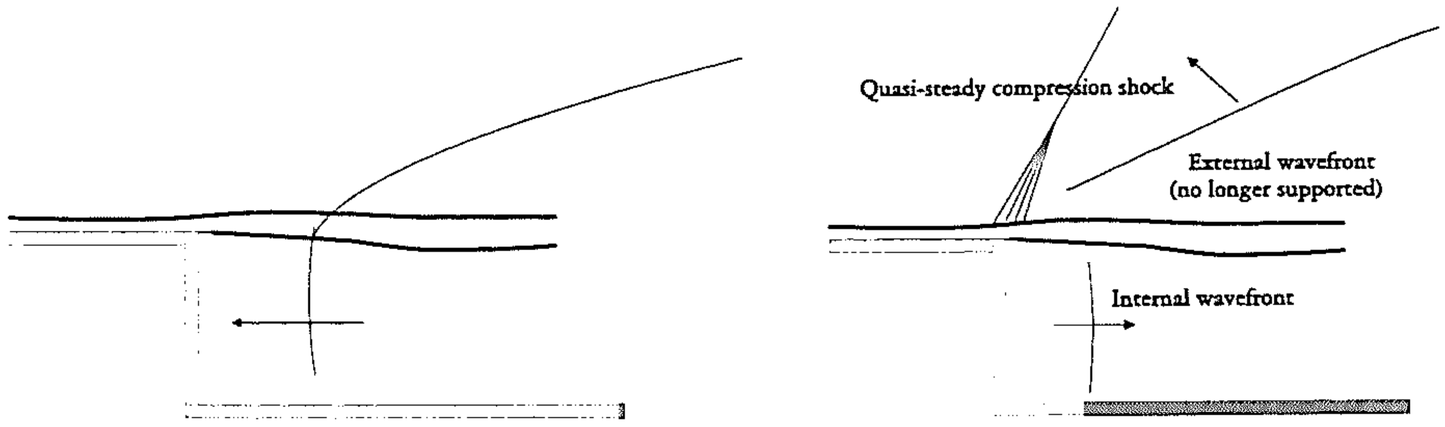

(a) Heller interpretation of events

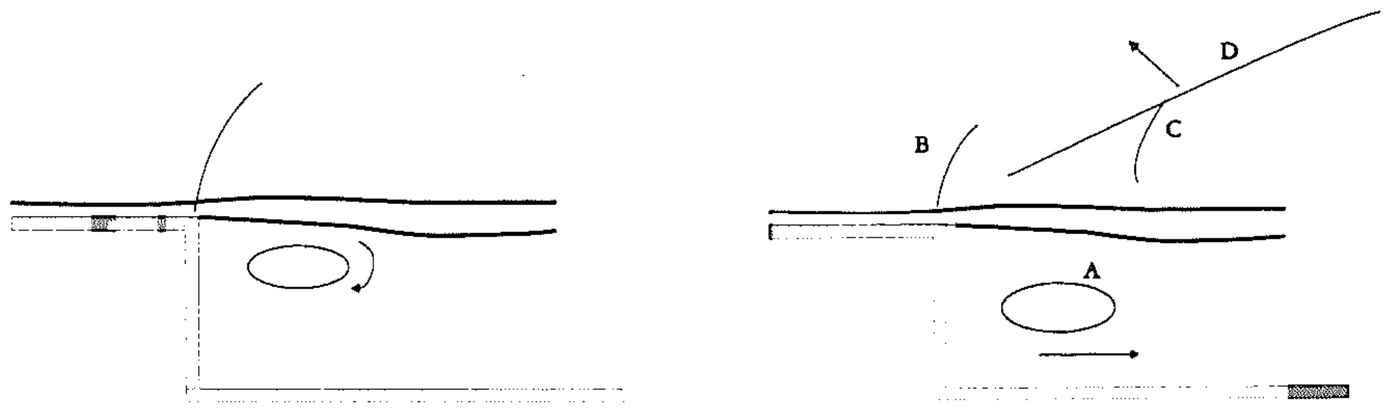

(b) Rossiter interpretation of events

Figure 3.17: Interpretation of internal flowfield for supersonic external flow

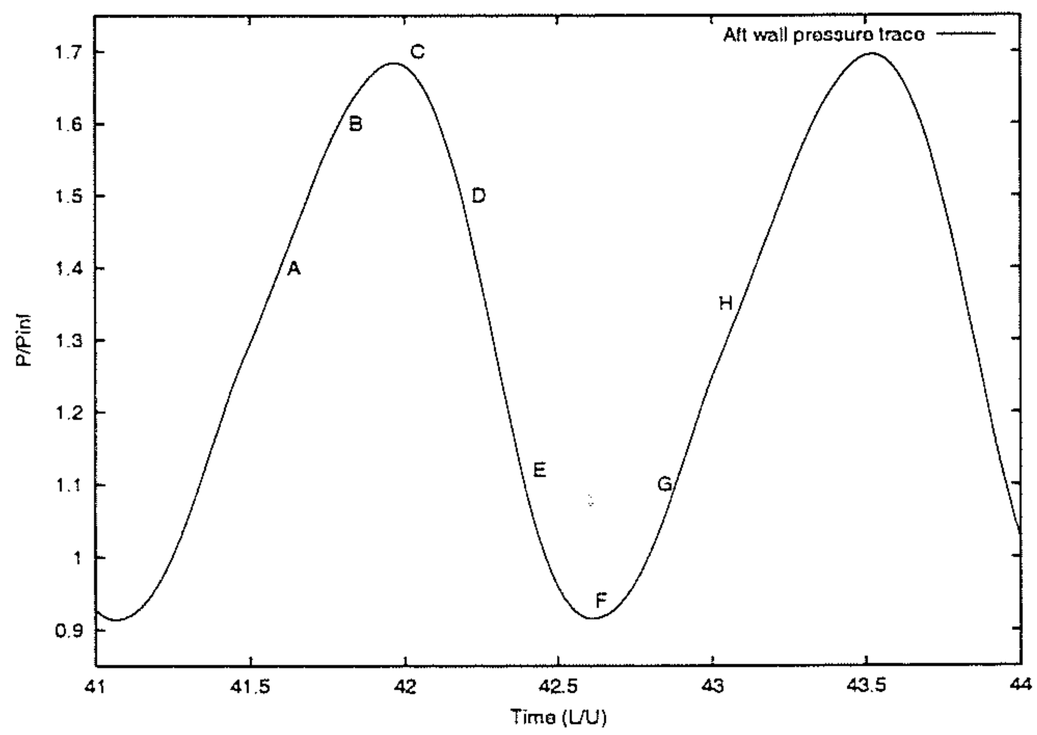

Figure 3.18: Pressure trace from aft cavity wall

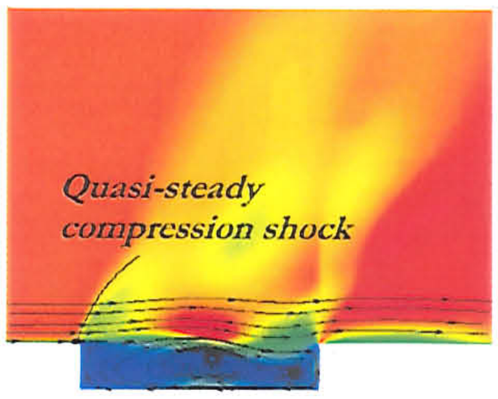

(a) T=41.62

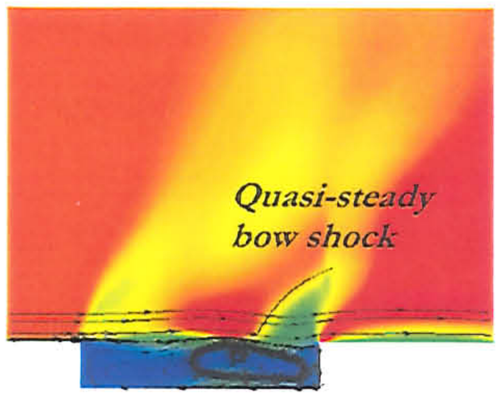

(b) T=41.82

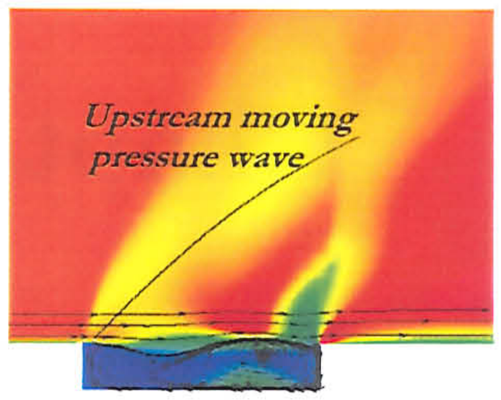

(c) T=42.02

(d) T=42.22

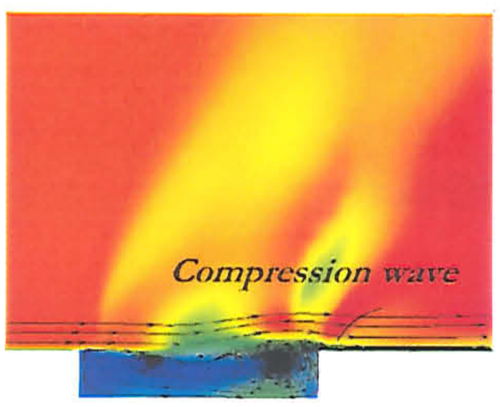

(e) T=42.42

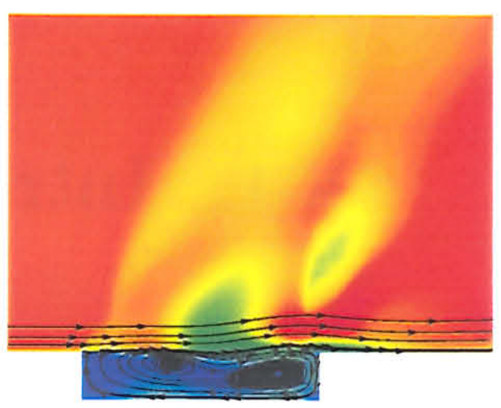

(f) T=42.62

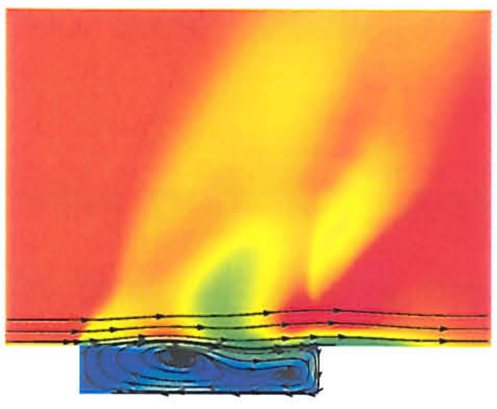

(g) T=42.82

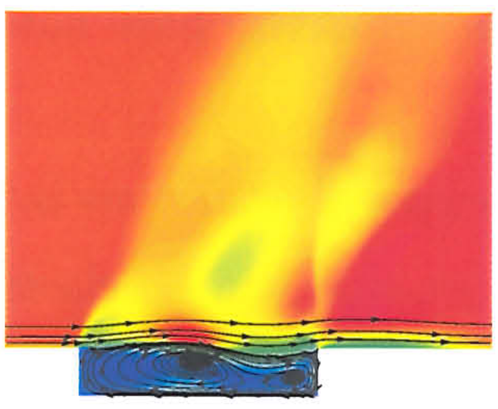

(h)T=43.12

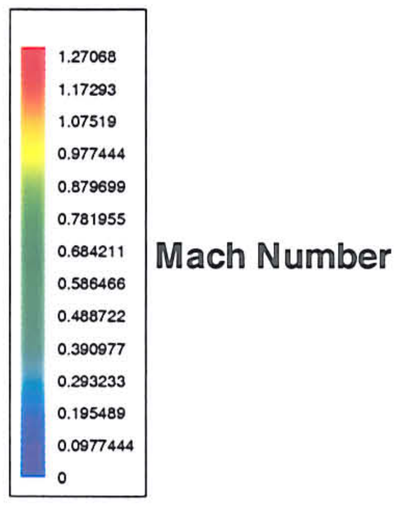

Figure 3.19: Mach number contours for Mach 1.19 Flow

Chapter 4

Suppressing Cavity Pressure Oscillations by Aft Wall Sloping

4.1 Introduction

As reported anecdotically by Ffowcs-Williams [31] it has been calculated that the first generation of the Boeing 707 aircraft at take-off produced as much sound as the world population shouting in phase together! A Boeing 767 of 30 years later (with four times as much thrust per engine) produced as much sound as the city of New York shouting in phase. Unfortunately advances in the suppression of the acoustic environment of a bomb bay or cavity have not been as impressive as this.

For the suppression of pressure fluctuations in a cavity many techniques have been applied. Methods of suppression can be classified into two groups: active control and passive control. Both seek to suppress the amplitude of the oscillations by manipulating the shear layer across the cavity. Active control is interesting because it has the potential to be optimised for various flow conditions. Techniques include pulsed injection [74] [75], sweeping jets [63], and injected flow through slots parallel to the leading edge [94]. These methods create small disturbances, which perturb the shear layer near the dominant Rossiter modes. These examples have shown reductions in the region of 6 to 10 dB in the acoustic environment using low frequency forcing. However, suppression is usually observed only for some of the tones. The

suppression achieved is similar to the levels expected from passive devices employed in aircraft. Typical industrial statements [83] concerned with the level of suppression required are *the more the better* but *as long as it doesn't cost anything.* This cautionary statement suggests that the use of passive control devices are desirable. Indeed investigation is still being conducted in this area, including the comprehensive study of Ross [72], which provides the background to this chapter.

The effectiveness of two passive control devices used in tandem was described by Clark [22] for suppressing cavity oscillations in the F-111 aircraft. In this work a spoiler device mounted at the front of the cavity and 45° sloping of the aft wall produced the most effective suppression. An important consideration allied to the effectiveness of passive devices is the ease and simplicity with which they can be fitted into existing cavity systems. A solution that requires substantial redesign of the aircraft is not practical. This gives a reason why passive devices are still favoured over active ones. Another consideration is that the device should not have significant adverse effects on the aircraft performance. To this end a slanted rear wall reduces the capacity of the weapons bay. This restricts the angle of inclination of the rear wall. With a leading edge spoiler the excrescent drag is a problem. The drag has been found to increase by up to 50 % in some cases [41]. The current chapter looks at the sloping of the rear cavity wall. The flow is thought to be stabilised [41] for sloped cavity walls and so produces an aerodynamically cleaner flow than is experienced for a cavity with a leading edge spoiler. The benchmark case discussed in Chapter 3 allows a detailed evaluation to be made.

4.2 Control Devices

Stanek et al [83] have recently investigated the control of cavity resonance through very high frequency forcing. Fluid dynamic actuators with characteristic operating frequencies of several kHz have been used to dramatically reduce the acoustic level in the cavity. Unlike other active control methods which induce low frequency perturbations, these actuators produce disturbances at frequencies far higher than the Rossiter modes. High frequency forcing invokes different physical mechanisms

in the flow which drains energy from the lower Rossiter frequencies, suppressing the oscillations.

Heller and Bliss [41] were the first investigators to thoroughly consider passive control devices in the cavity. In order to lessen the severity of the oscillation amplitudes they attempted to stabilise the shear layer by altering the periodic mass addition process occurring at the trailing edge. Stabilisation of the shear layer was attempted by the use of palliative devices. Vortex generators such as spoilers were used upstream to generate vorticity in the shear layer. Sloped rear walls were used to stabilise the flow at the cavity trailing edge by suppression of the feedback mechanism. These were found to be effective at subsonic and supersonic speeds reducing the discrete tone levels. In particular the 45° slope was found to produce the greatest suppression. An interesting aside is that Heller and Bliss, although concerned with passive control devices, suggested forcing of the shear layer at higher frequencies.

Franke and Carr [32] attempted to eliminate the cavity pressure oscillations by varying the cavity geometry. Many configurations were selected based on the results of the Heller and Bliss experiments. They showed that leading edge sloping was also effective when used in tandem with rear wall sloping. This double ramp was only effective when flow separation occurred near the beginning of the inlet ramp, which was not always the case. Franke and Carr showed that the dominant second mode was suppressed when using sloped walls.

It is worthwhile to pause and consider the reason why rear wall sloping may be effective in the suppression of cavity resonance. It has been shown that cavity flows are dominated by vortical flow structures created upstream in the cavity that then propagate downstream to the aft cavity wall, impinge on it and send pressure disturbances upstream to complete the feedback loop. The feedback mechanism sustains the coherent pressure fluctuations so it is reasonable to assume that modification of the aft wall will have a marked effect on the pressure oscillations in the cavity. Pereira and Sousa [60] used visualisation techniques to investigate the attenuation of the flow oscillations from modified rear walls. This showed that the use of a curved

rear wall attenuated the fluctuation peak magnitudes. In addition, the experiments indicated why this particular rear wall shape was successful. The attenuation was a direct consequence of the most frequent escape of the separated shear-layer vortices approaching the impingement edge. Chapter 3 showed that for clean open flow the vortex was only partially clipped and expelled from the cavity. Pereira and Sousa [60] showed that for a curved wall "complete escape" of the approaching shear-layer vortex occurs.

Zhang, Rona and Edwards [96] studied the effect of trailing edge geometry for supersonic (Mach 1.5) cavities driven by a thick shear layer. The trailing edge of the cavity was modified using wedges and ramps, producing reductions of up to 11.6 dB in the rms value along the cavity floor. The time averaged pressure drag was also significantly reduced. The main cause of the pressure drag reduction is the elimination or reduction of the high-pressure area near the downstream corner of the cavity due to the presence of a vortex [96]. Apart from the observation that mass ejection is easier at the cavity trailing edge no explanation was given as to why the pressure oscillations are reduced. Zhang, Chen, Edwards and Rona [97] also looked at attenuating cavity oscillations through leading edge passive devices for Mach 1.5 flow. The devices, similar to those tested by Heller and Bliss [41] and Franke and Carr [32], included compression ramps and expansion surfaces. It is known that leading edge pressure disturbances are significant in sustaining the feedback loop and so creating the high oscillations experienced in the cavity. Zhang hoped that by altering the flow past the leading edge significant reductions in the SPL would be achieved.

4.3 Experimental Results and Background

The current study intends to provide a clearer understanding of why the sloping of the rear wall is successful in attenuating the pressure oscillations. The investigation will follow the experimental tests conducted by J Ross [72], which investigated a

number of passive control techniques [71], including sloped cavity entry and exit and saw-tooth spoilers at the cavity leading edge. Contrary to the computational simulations of Zhang [97], which showed an expansion surface (sloped leading edge) produced a near stable environment in the cavity, the experiments of Ross and Peto [71] found that the unsteady pressure levels experienced in the cavity actually increased.

The test configuration is similar to that for the open flow case studied in Chapter 2, with the weapon's bay doors deployed at the fully open position. The current study is made with a cavity that stores an AMRAAM missile at a position of two store diameters inside the cavity. However the results are typical of the missile being 4 diameters outside the cavity. The details and experimental conditions are shown in Figure 4.1. When the rear wall is sloped the cavity ceiling length is kept constant, which causes an increase in the cavity volume. With this in mind a trade off between attenuation of the SPL and increase in cavity volume would be sought. In the experiments [72], rear wall slopes of 76° and 63.4° were investigated as viable options. A slope of 53.1° was also tested though it was felt that the increase in cavity volume made this option unfeasible. Indeed when the second part of the experiments aimed to enhance the attenuation effects of a rear wall slope (by chamfering the exit slope), a 63.4° slope was selected for further testing.

The total rms sound pressure level variation along the cavity floor for the experiments is shown in Figure 4.2 for rear wall slopes of 76.0°, 63.4° and 53.1° at Mach 0.85. The clean case is shown for comparison purposes. The effect of rear wall sloping is clearly evident in terms of the reductions experienced in the unsteady pressure levels for slopes of 63.4° and 53.1°, which produce similar results. A slope of 76° is not nearly as effective. The unsteady pressure levels are lessened significantly along the cavity floor. However on the aft cavity wall the reductions are not as pronounced. Nonetheless, the 5.1 dB reduction at the aft wall is equivalent to a reduction in amplitude by a factor of 1.8. Ross [72] found that the maximum reductions were experienced at X/L=0.95, where the unsteady pressure levels were reduced by 12.8 dB (a factor of 4.4). From Figure 4.2 it was concluded by Ross [72] that the effectiveness of the rear wall slope approaches a limit at some angle between

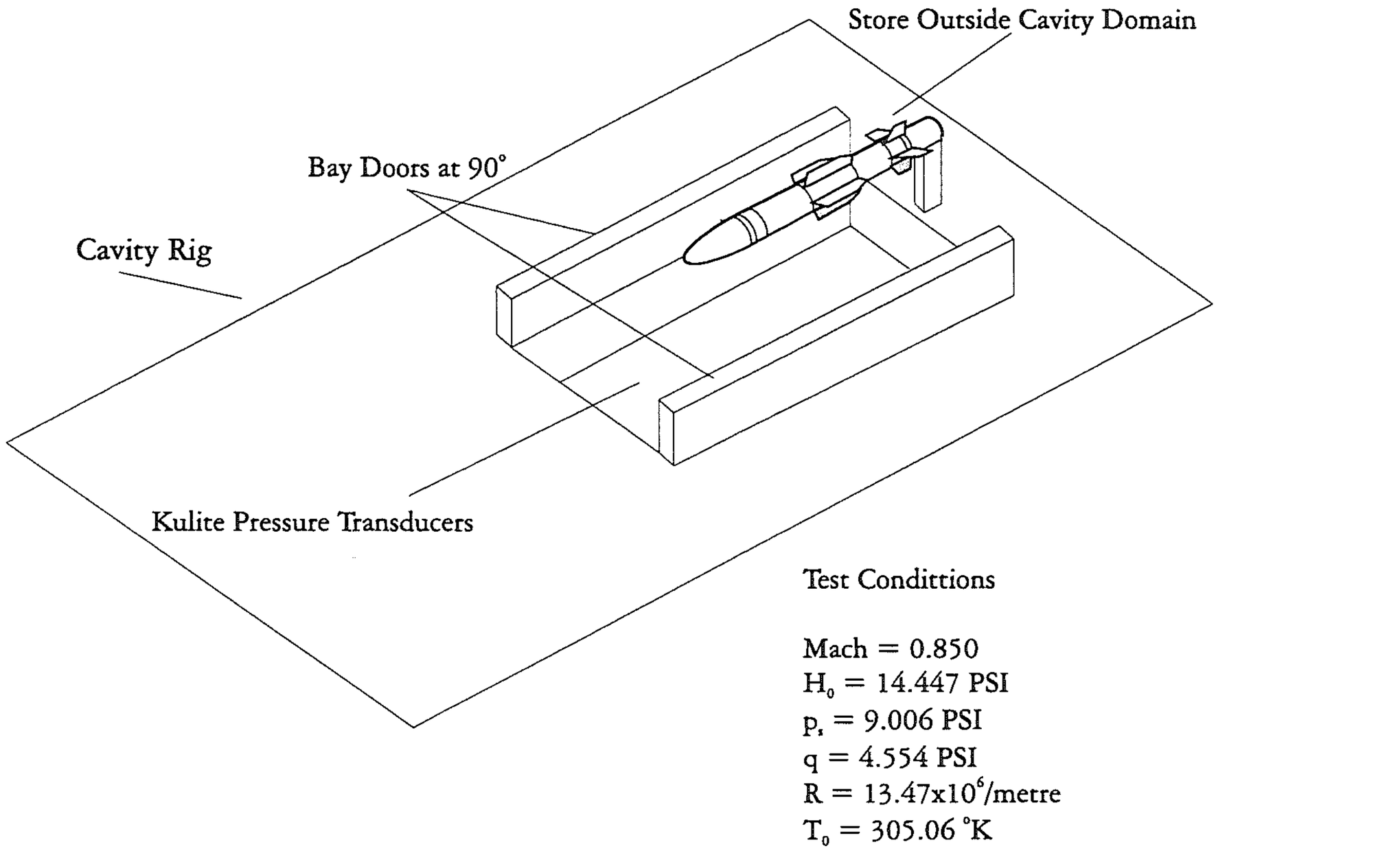

Figure 4.1: Cavity rig showing details of weapon bay doors and store

76° and 63.4°. One of the objectives of the present study is to investigate this. It was demonstrated (though not shown here) that the reduction in the unsteady pressure levels was attributable to a reduction in the energy in the predominant 2nd tone (380Hz), leaving no single tone dominant.

The influence of 76.0° and 63.4° slopes at various Mach numbers is shown in Figure 4.3. These are shown for a probe location of X/L=0.55 in the cavity but are indicative of the trends experienced at other locations in the cavity. The results at X/L=0.95 for the steepest slope are included to illustrate this. Figure 4.3 shows that for a clean cavity there is a gradual increase in the SPL as the Mach number increases from Mach 0.8 to Mach 1.19. This is followed by a slight decrease between Mach 1.19 and Mach 1.35. A similar trend is exhibited for a rear wall slope of 76.0°, suggesting that the flow physics for this degree of sloping are similar to those for the clean cavity. When the 63.4° slope is utilised the pattern is different. There is an increase in the SPL for Mach Numbers between 0.85 and 0.95 followed by a substantial decrease for Mach numbers between 0.95 and 1.19 (which is opposed to

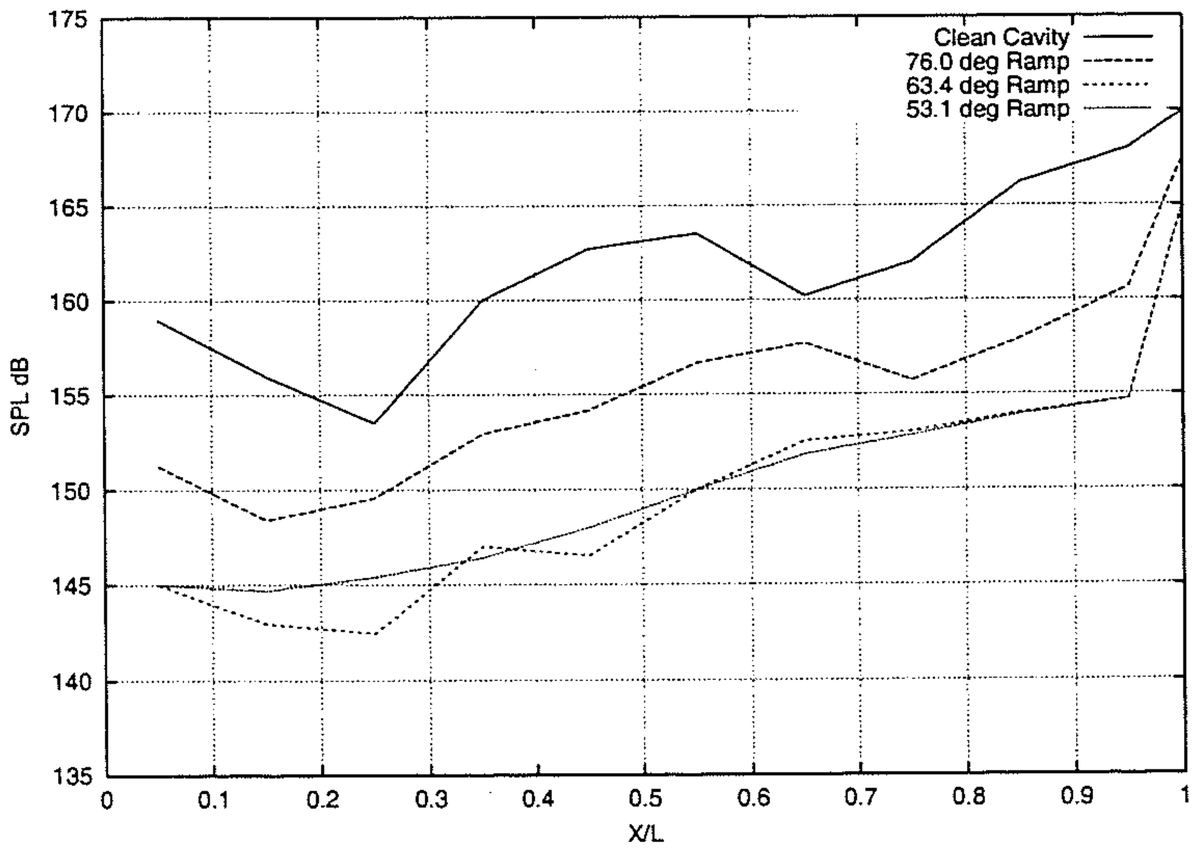

Figure 4.2: Effect of Rear Wall Sloping on Unsteady Pressure Level along Cavity Floor [72]

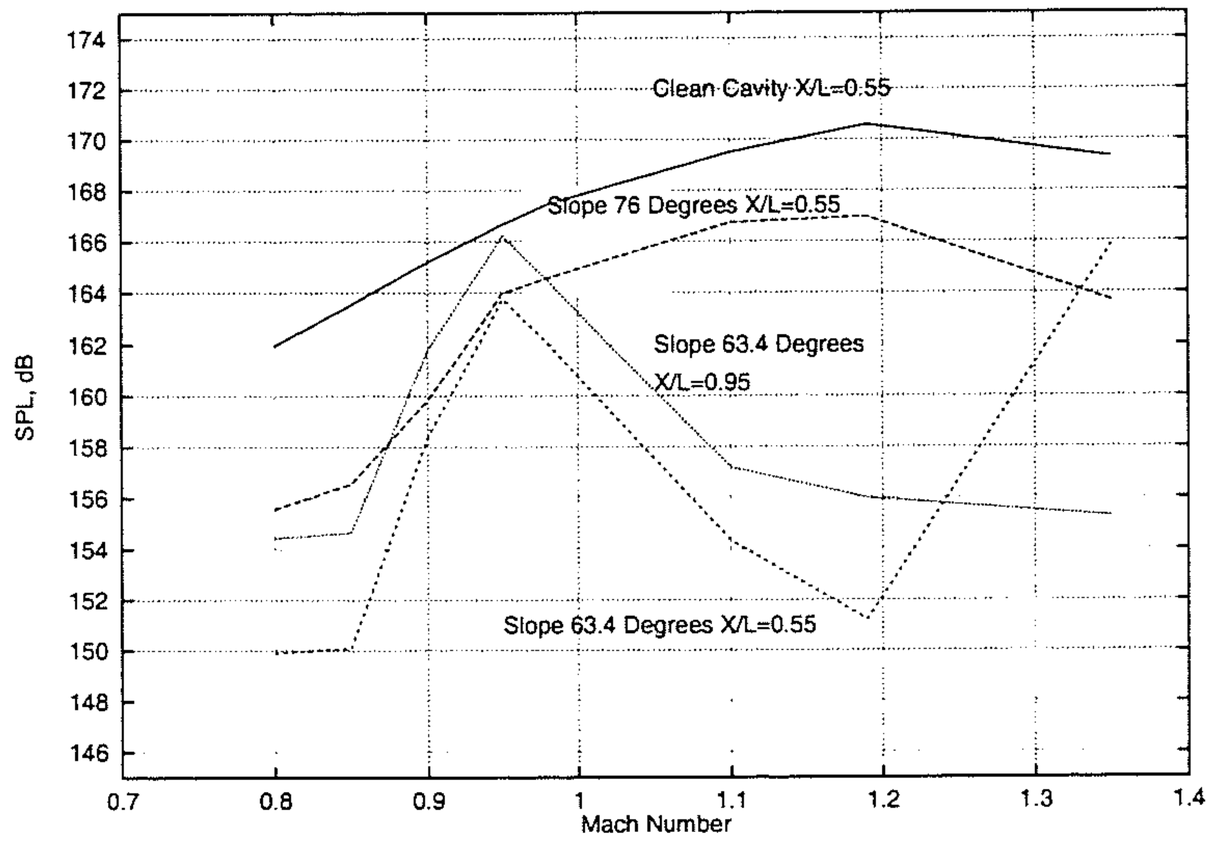

Figure 4.3: Effect of Rear Wall Sloping on Unsteady Pressure Level along Cavity Floor; Mach Number Variation [72]

the decrease seen for the clean and 76.0°). This pattern is similar for a slope of 53.1°, although is not shown here. It is therefore reasonable to assume that at 63.4° the flow physics is distinctively different from the clean cavity and for a slope of 76.0°. Intuition suggests that somewhere between 76.0° and 63.4° a value will exist where the flow makes the transition from the type corresponding to *clean* flow to that which is representative of *suppressed* flow. We consider the results between

Mach 0.95 and Mach 1.19 to investigate the behaviour (Figure 4.4). For the clean and 76.0° case the SPL increases between these limits, while it decreases for a slope of 63.4°. If the assumption of a transition region existing between 76.0° and 63.4° is true, then it is to be expected that there will be slope angle that will produce a level distribution between these limits. The expected result is as indicated in Figure 4.4 and is investigated in the following section. If a critical angle is found to exist then this will helpful in constructing a hypothesis as to why a certain amount of rear sloping is successful. This chapter will investigate the behaviour of sloping rear walls in the transonic region to determine if the expected trend in Figure 4.4 exists. The main differences between the clean cavity and that with a slope of 63.4° at Mach 0.85 will be shown. It is also possible that the reduction in the SPLs is a gradual progression as the rear wall is sloped to a lesser inclination. Therefore the proposed transtion will then represent the region after which the differences in the flow fields become more noticable.

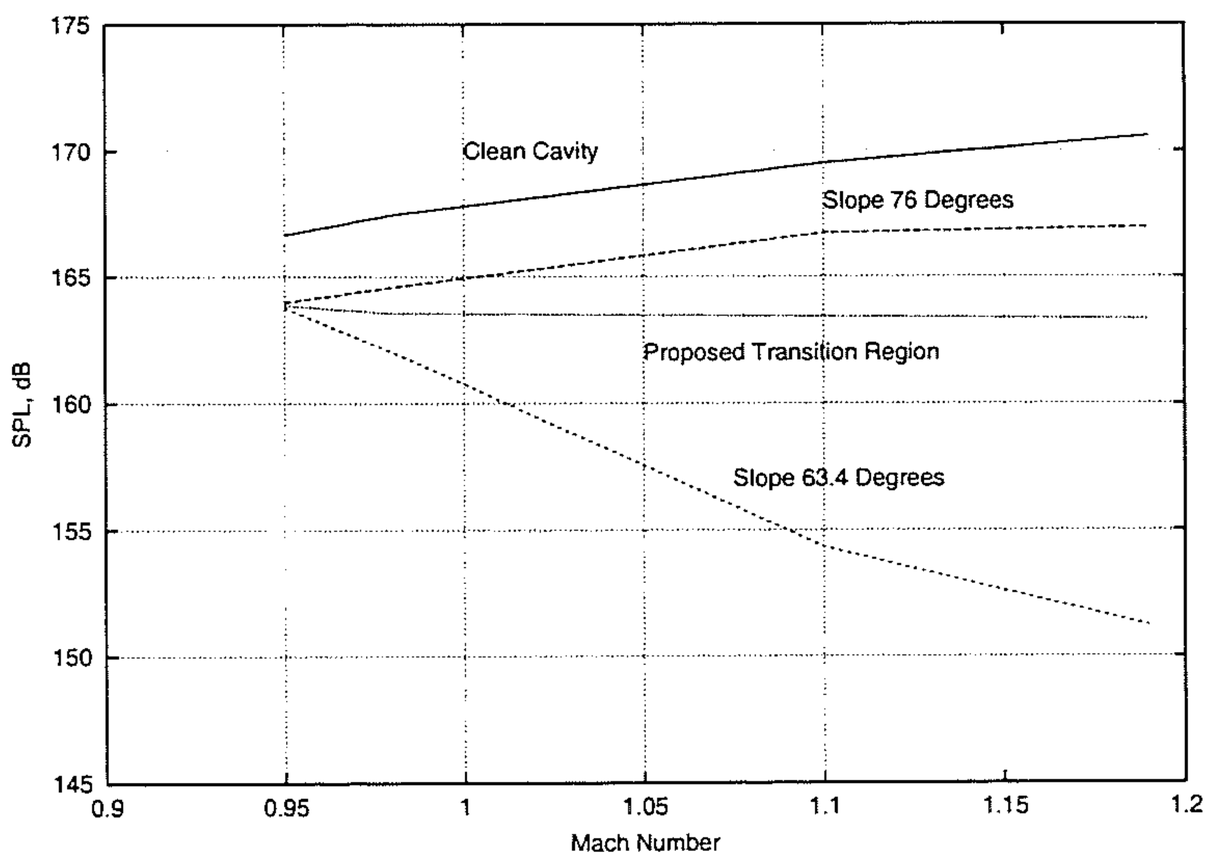

Figure 4.4: Effect of Rear Wall Sloping on Unsteady Pressure Level along Cavity Floor; Predicted behaviour

4.4 Validation

The details of the calculations follow those previously presented for the clean case. Comparing the CFD data in Figure 4.5 with the experimental data shown in Fig-

ure 4.2 the similarities are easily recognisable. The effectiveness of the rear slope increases as the slope angle decreases. On the aft wall of the cavity the SPL levels are still high for both the experimental and CFD results. The location of the 2nd trough is seen to move from $X/L = 0.65$, for the clean cavity, to $X/L = 0.75$ for the 76.0° case. This trend is seen in both experimental and CFD results. This trough is shown to be levelled in the experiments for the 63.4° case but is still present for the CFD data. In the experiments a limit is approached at around 63.4°. For the CFD results the limit shown is for a slope of 63.4°. A slightly shallower slope showed there are no significant reductions in the SPL levels. A direct comparison of the experimental and CFD data is shown in Figure 4.6 for the 76.0° and 63.4° cases at Mach 0.85. This 63.4° case will be used later to discuss how, through the modification of the flow physics, rear wall sloping is successful in the suppression of the pressure oscillations. Although Figure 4.6 shows that the 76.0° and 63.4° slopes for the CFD results are not as close to the experimental data as for the clean cavity, the data does compare reasonably well. The overall reduction for the experimental and CFD results tends to be of the same magnitude for both cases. The CFD results over-predict the SPL levels near the centre of the cavity, however the troughs in the CFD results agree with the experimental values (locations X/L=0.25 and X/L=0.75). Arguably the most important location in the cavity is where the acoustic load is at a maximum, where the oscillating shear layer impinges on the aft wall. The experiments show that the reduction experienced on the aft wall in moving from the clean cavity to a 63.4° slope is 5 dB. The CFD results show almost an identical reduction. At the location X/L=0.25 the CFD results show a reduction of 10 dB which is similar to the reduction predicted by experiment. In practice it is desired to use CFD as a tool to predict whether certain suppression devices are successful. If the CFD results show consistency then it is reasonable to use then as a tool for the investigation of sloping of the rear wall. The comparisons shown here suggest the desired consistency for the current cases.

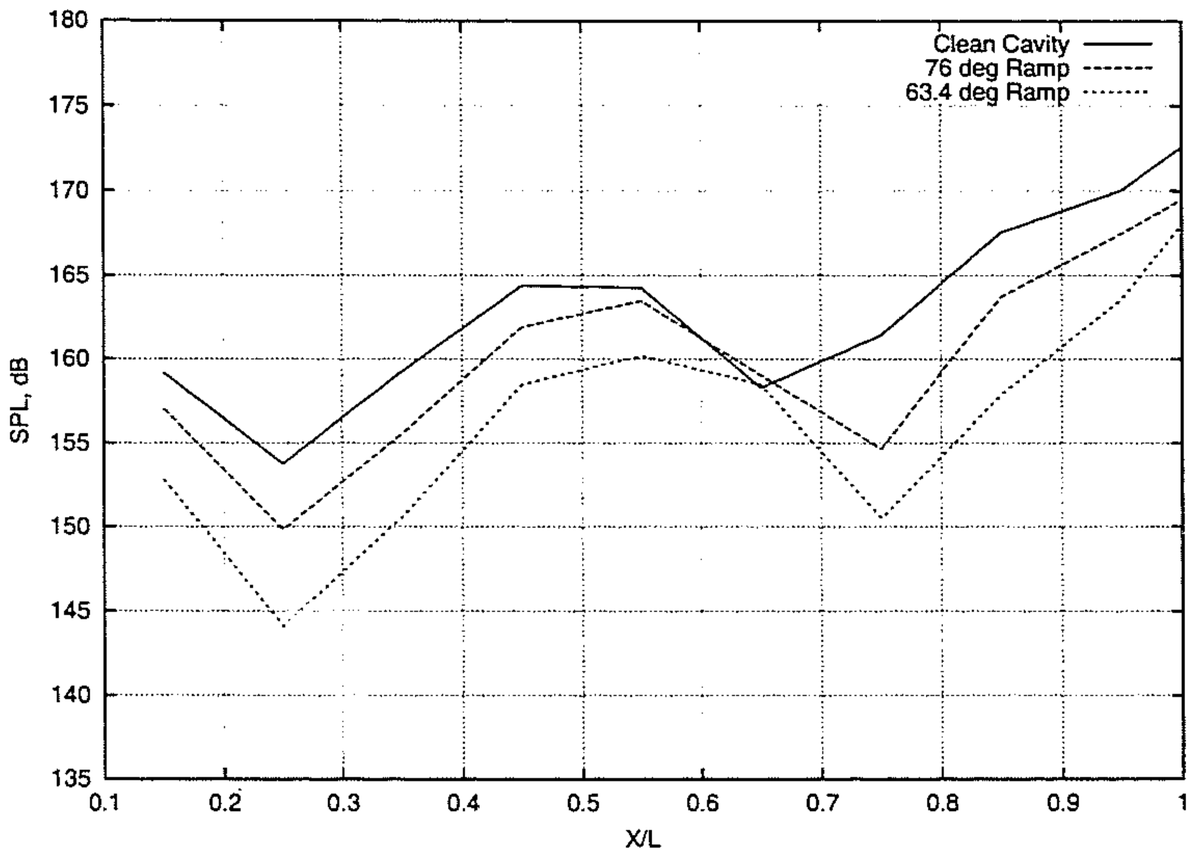

Figure 4.5: Effect of Rear Wall Sloping on Unsteady Pressure Level along Cavity Floor - Pmb2d

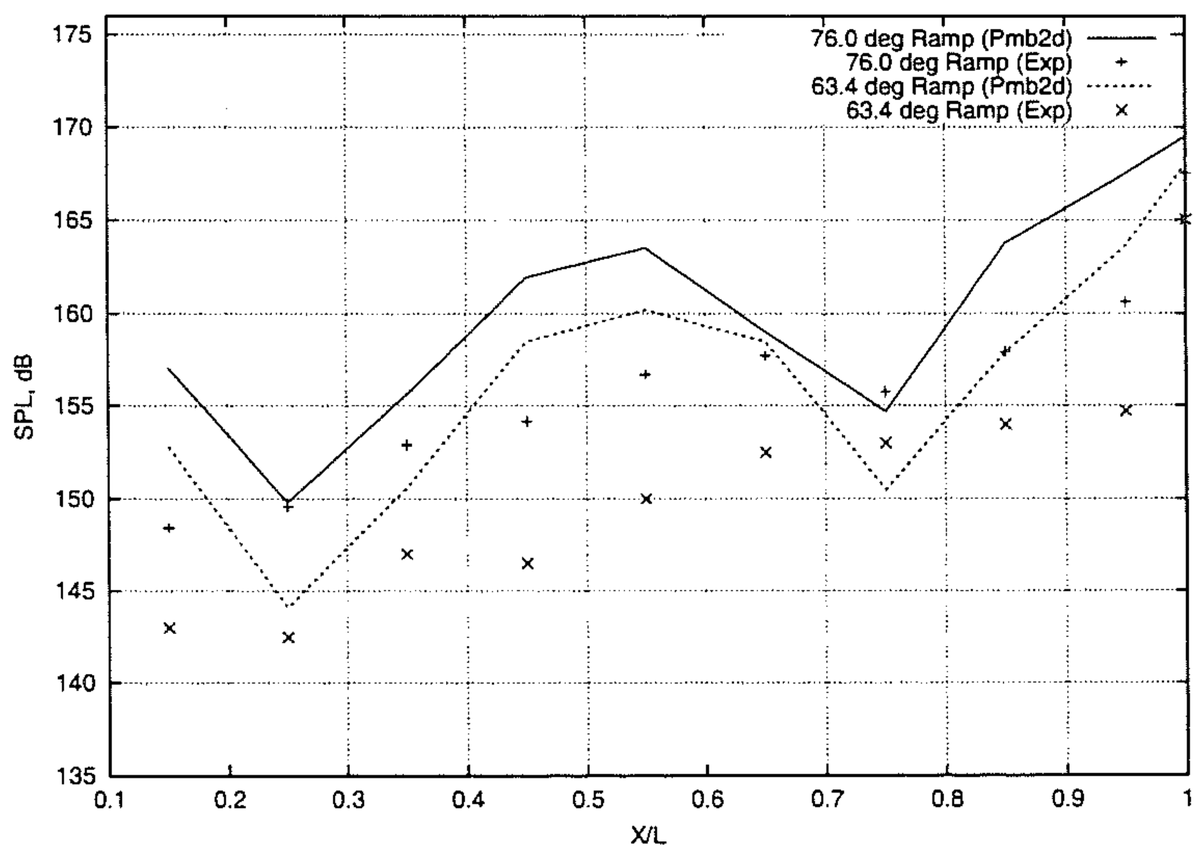

Figure 4.6: Effect of Rear Wall Sloping on Unsteady Pressure Level along Cavity Floor: Comparison of CFD with Experiment

4.5 Analysis

In the previous section it was suggested that a slope angle will exist where the flow makes the transition from the type corresponding to *clean* flow to that which is representative of *suppressed* flow. The behaviour of the curves in Figure 4.3 suggests that the flow environment for the clean and 76.0° slope cavities is very similar across the Mach range 0.8 to 1.19. This flow is distinctly different from that for

the 63.4° slope, as is evident from the different behaviour of the SPL levels over the same Mach range. It is easier to investigate the behaviour of the various flows for the Mach range 0.98 to 1.1 since a hypothetical region may exist, as suggested in Figure 4.4. It is reasonable to assume that this hypothesis is applicable across the full range between Mach 0.8 and 1.19 since the behaviour of the curves is similar.

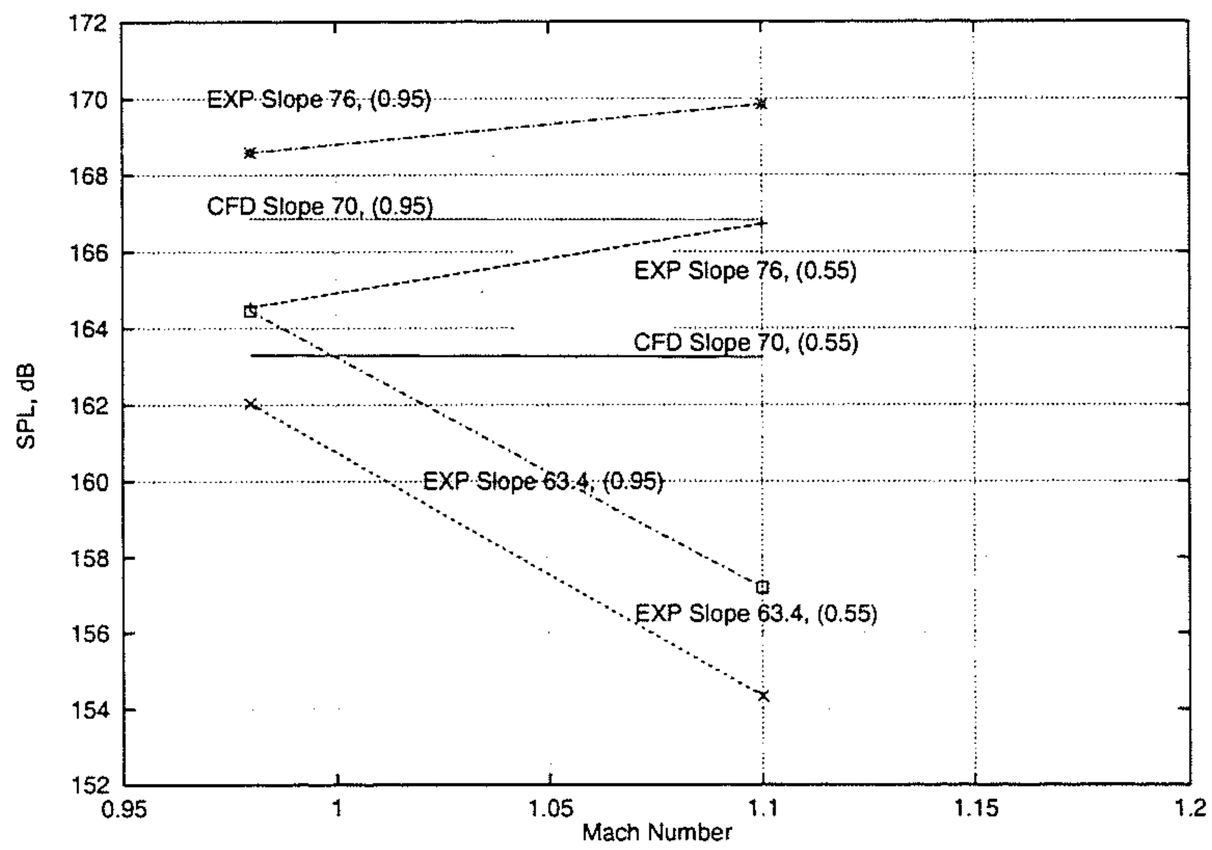

Figure 4.7: Effect of Rear Wall Sloping: Transition Region

Mach 0.98 and Mach 1.1 flow over cavities with various rear wall slopes between 76.0° and 63.4° was simulated. Figure 4.7 shows the predicted SPL values for the 70.0° slope at probe locations of X/L=0.55 and X/L=0.95. Also shown are the experimental results for slopes on either side of the CFD predictions, for 76.0° and 63.4° (which, from experiment, produces the minimum SPL of all the slopes tested).

The CFD simulations show that a rear wall slope of 70° results in negligible SPL variation between Mach 0.98 and Mach 1.1. In Figure 4.7 it is seen that as the slope of the rear wall is increased from 76° to 63.4° the variation in the gradient of the SPL vs Mach number curve is seen to be a smooth transition. This fact is very important and will be recalled in the following section. From the simulations performed for a slope of 70° the variation is very small between Mach 0.98 and Mach 1.1. Also indicated is that the basic trends of the SPL values are independent of the

probe position in the cavity.

4.6 Suppression of Oscillations

Shown in Figure 4.8 are comparisons between the pressure history traces for the clean case and 63.4° slope cavity. The effectiveness of the sloped cavity can be seen with the reduction in the amplitudes of the oscillations. In Figure 4.9 are the acoustic spectra for the sloped 63.4° cavity. This should be compared to Figure 2.4 in Chapter 2 which shows the similar spectra for the clean cavity. The reductions observed in unsteady pressure levels arise through the removal from the acoustic spectrum of the predominant and dominant tone. It is seen that the tonal frequencies present are slightly lower. This may be attributed to the fact that the cavity length is longer for the sloped case than for the clean case. Once again the broadband background is not predicted. For the sloping rear wall configuration the dominant second tone frequency at 390Hz has been massively reduced in amplitude. A reduction in the first tone is also evident most noticeably at X/L=0.25, 0.65 and 0.75. Overall it is seen that the reduction in the unsteady pressure levels arises from reduction of the second dominant tone. The physics of the flow will be investigated in the following sections.

4.7 Investigation of Flow Features

Heller and Bliss [41] attempted to explain theoretically why slanting of the trailing edge reduces pressure oscillations, for which a summary will follow. No experimental or CFD flow visualisations have been used to substantiate the theory. The current work will therefore be compared with the theoretical ideas of Heller and Bliss. The salient points will be highlighted and the reader is referred to the full work of Heller and Bliss for a more complete explanation.

Heller and Bliss argued that the stagnation streamline for a hypothetical steady flow would exist near the centre of the shear layer. They proposed a simplified model of the stagnation flow in a shear layer by making several assumptions. Previous shear

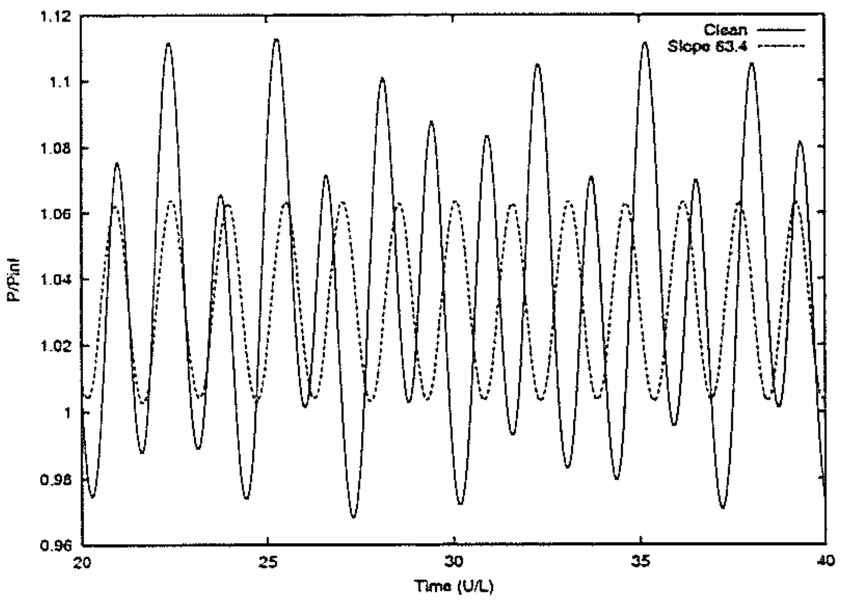

X/L=0.05

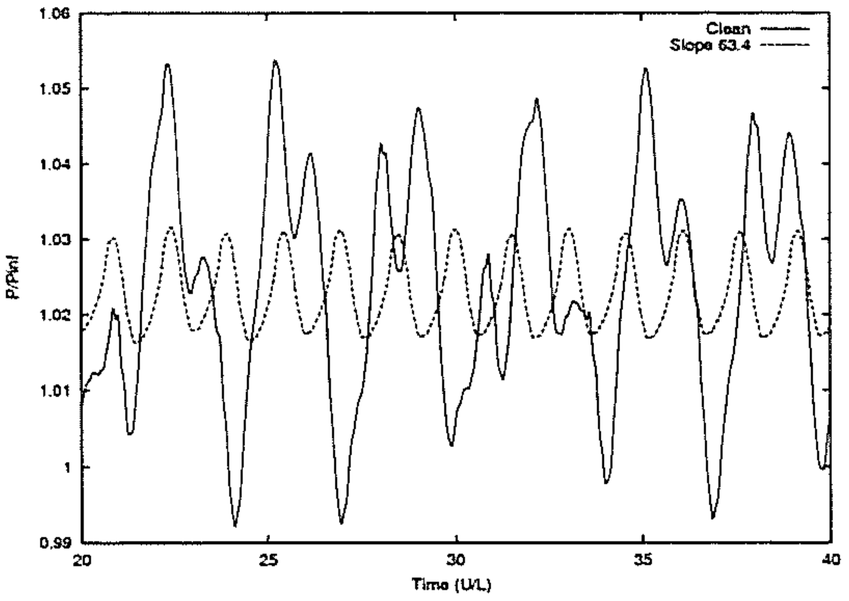

X/L=0.25

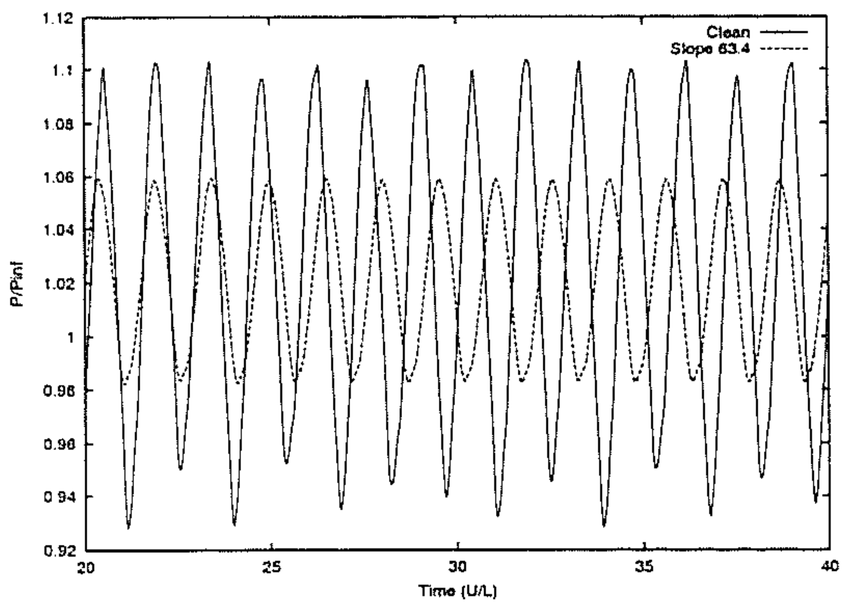

X/L=0.45

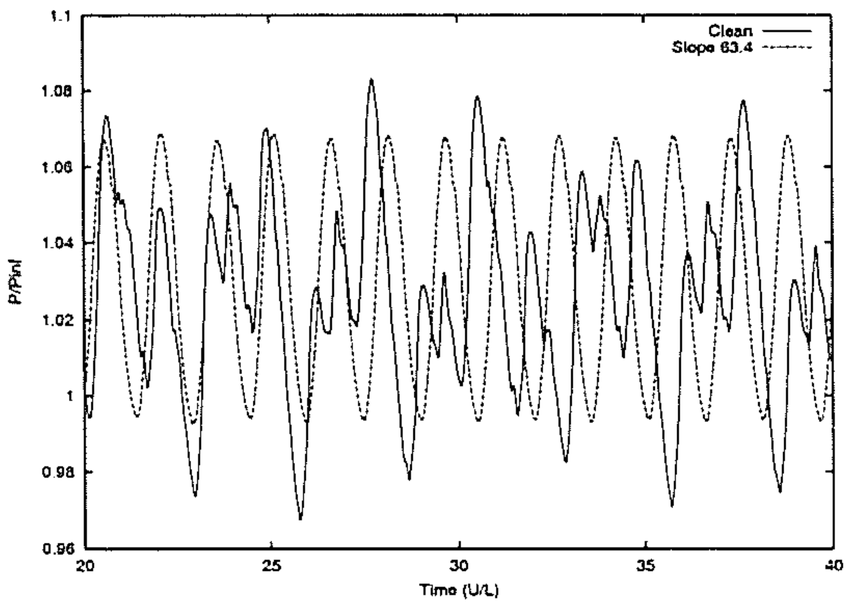

X/L=0.65

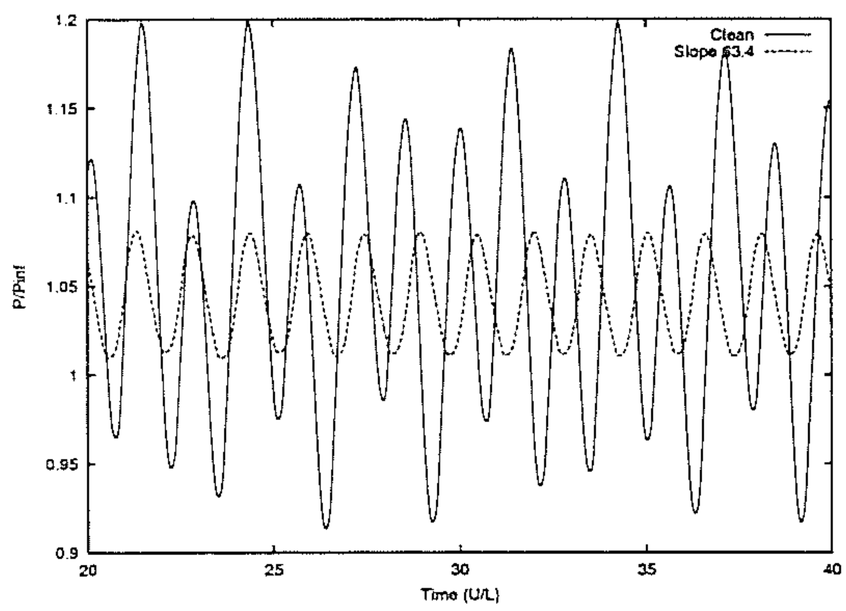

X/L=0.85

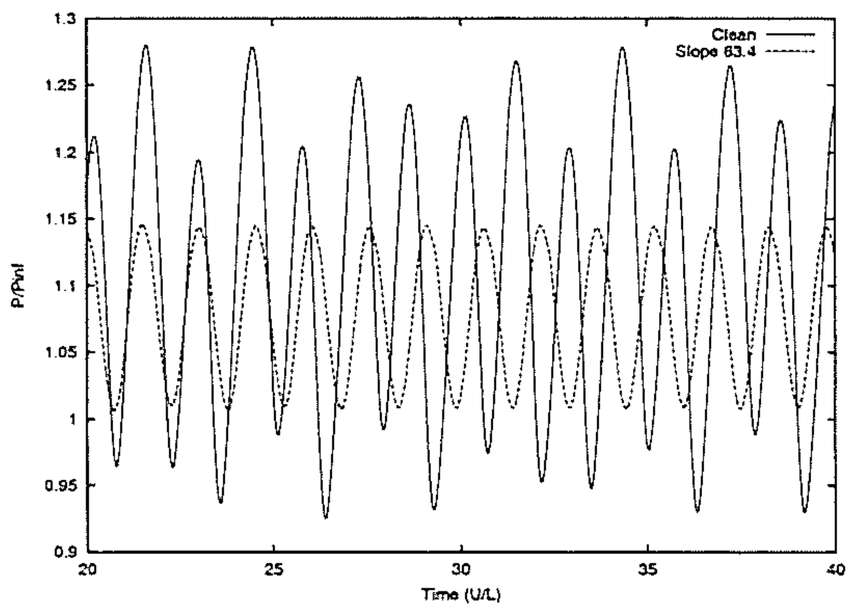

X/L=0.95

Figure 4.8: Pressure History Traces at Selected Locations on the Cavity Floor

layer solutions had shown that the shear is nearly constant in the middle region of the shear layer. Indeed the present computational solutions in Figure 4.16 show the

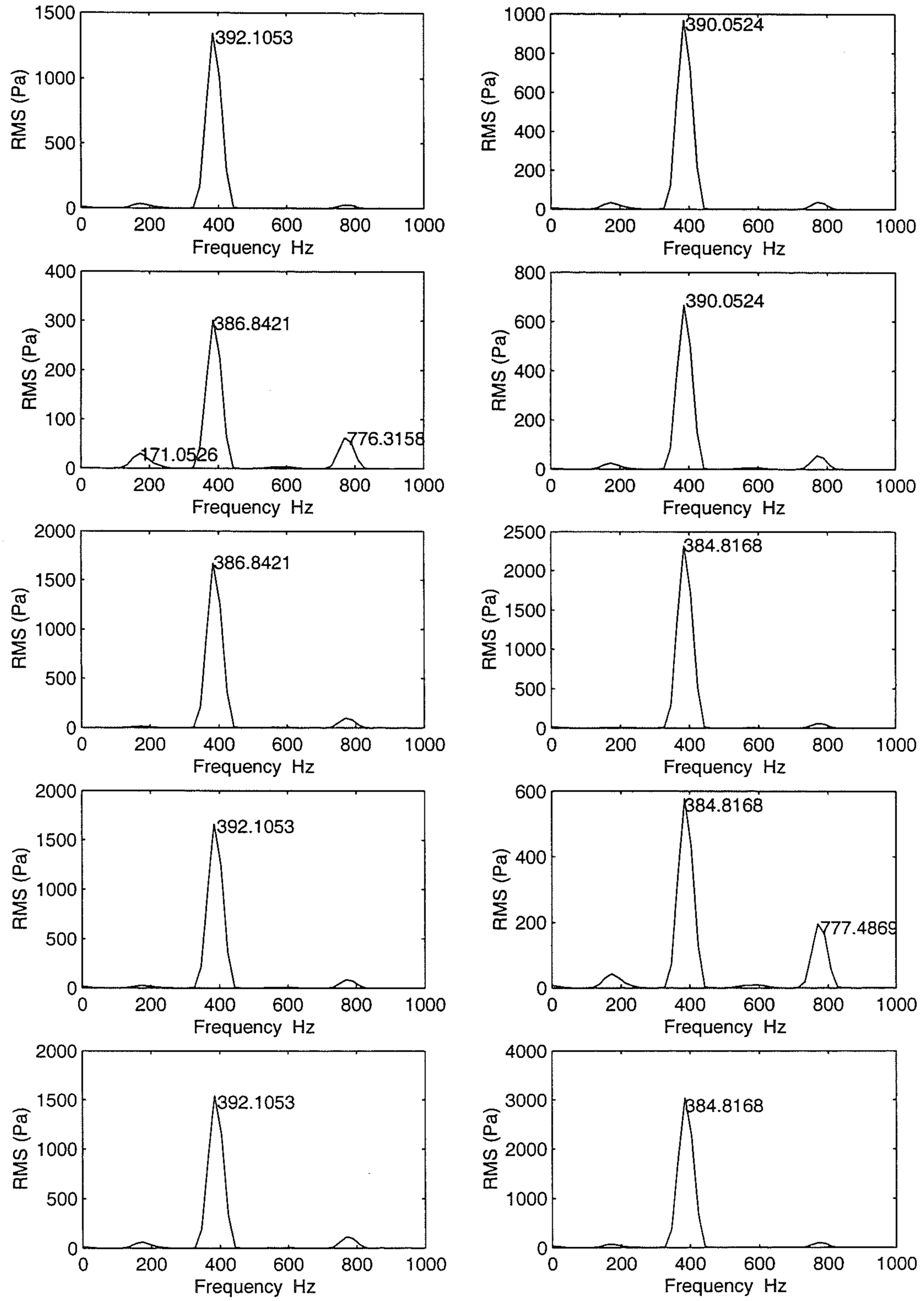

Figure 4.9: Experimental RMS Pressures along Cavity Floor. From left to right, top to bottom: X/L= 0.5, 0.15, 0.25, 0.35, 0.45, 0.55, 0.65, 0.75, 0.85, 0.95

vorticity not to vary significantly at this location (red part on the aft wall). Even the shed vorticity does not significantly alter the pattern on the aft wall. With the model being restricted to the local region around the stagnation point the flow is assumed to be *2 dimensional incompressible flow.* Heller and Bliss used potential flow theory to represent the flow and combined a shear flow with an irrotational stagnation point flow to depict the streamline patterns at the stagnation point. Normally such a combination is not allowed, however the assumed conditions permit it to be used so long as the region of application is restricted to around the local stagnation point.

A stream function $\psi(x, y)$ can be defined which satisfies Laplace's equation. For an irrotational stagnation point, of strength a, in a shear flow (strength b) of constant vorticity the stream function is defined by

$$\psi = axy + \frac{1}{2}by^2$$

The velocity components are

$$u = \frac{\partial \psi}{\partial y} = ax + by$$

$$v = -\frac{\partial \psi}{\partial x} = -ay$$

and the vorticity is

$$\zeta = \frac{\partial v}{\partial x} - \frac{\partial u}{\partial y} = -b$$

The streamline pattern, for values that give correct orientation of the shear flow, is shown in Figure 4.10. The horizontal axis is along the aft cavity wall while the vertical axis represents the spanwise direction in the cavity. The significant conclusion is that the *effect of the shear is responsible for the direction of the stagnation streamline.* As can be seen in Figure 4.10 this means that the shear layer impinges on the wall at an oblique angle. For the stagnation streamline - $\psi b/2 = 0$, the impingement angle is as sketched in Figure 4.10. The streamline for $\psi b/2 = -1$ represents the entrained flow while those for $\psi b/2 = 1$ and $\psi b/2 = 2$ are on the freestream side of the flow. Despite the simplifying assumptions the flow pattern is not too dis-similar to that shown for open flow in Chapter 3. Indeed the physical significance of the streamline pattern in Figure 4.10 can be recognised if the velocity gradients are considered. For the entrained fluid ($\psi b/2 \leq 0$) the streamlines are significantly curved as the flow has to move down the aft wall. Such curvature introduces centrifugal pressure forces. For a balance in pressure, necessary for steady flow, the velocities on the freestream side of the stagnation line are higher than those for the entrained flow as required. Thus the streamline pattern in Figure 4.10 is seen to have physical significance.

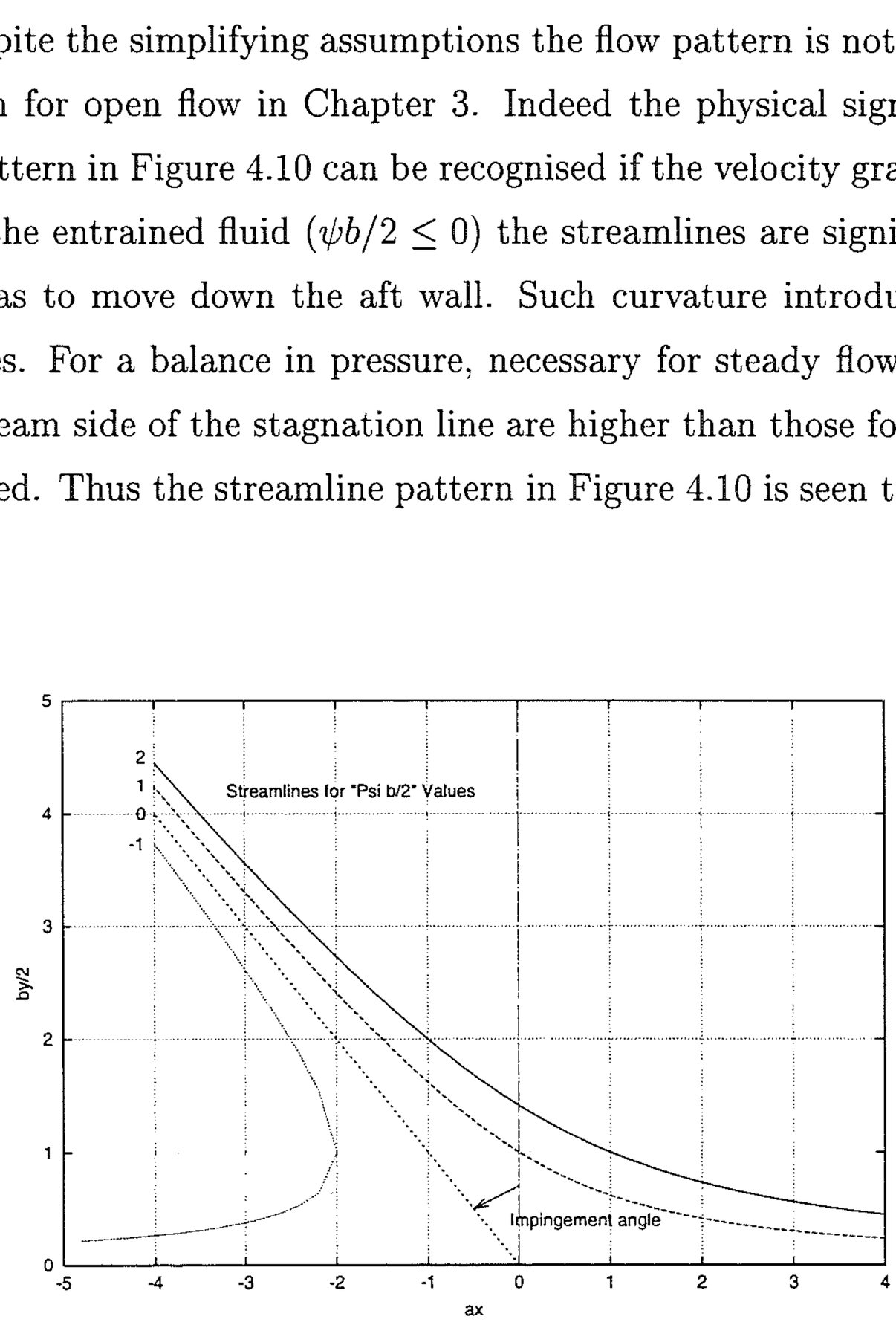

Figure 4.10: Aft Cavity wall Streamlines (fromPotential Flow Theory)

Heller and Bliss sketched how they envisaged the flow to be over the entire cavity, shown in Figure 4.11. To satisfy the impingement criteria on the aft wall the shear

layer is required to expand significantly into the cavity. The necessary curvature, due to the expansion fan at the leading edge, causes the freestream flow to produce static pressure variations. The pressure field within the cavity, for which the main influence is the presence of the vortices hence it will be relatively low, is unable to balance the external pressure variations and this ultimately leads to oscillation of the shear flow and an unsteady flow. To obtain a hypothetical steady flow an alternative flow configuration might be a shear layer which does not expand over the leading edge, thus allowing a balance of pressures and so not inducing oscillations in the shear layer. However such a flow convention does not satisfy the required impingement angle (Figure 4.10) which means that the flow on the aft wall will need to be unsteady. This indicates that it is very unlikely that steady flow is achievable for the clean open cavity flow problem.

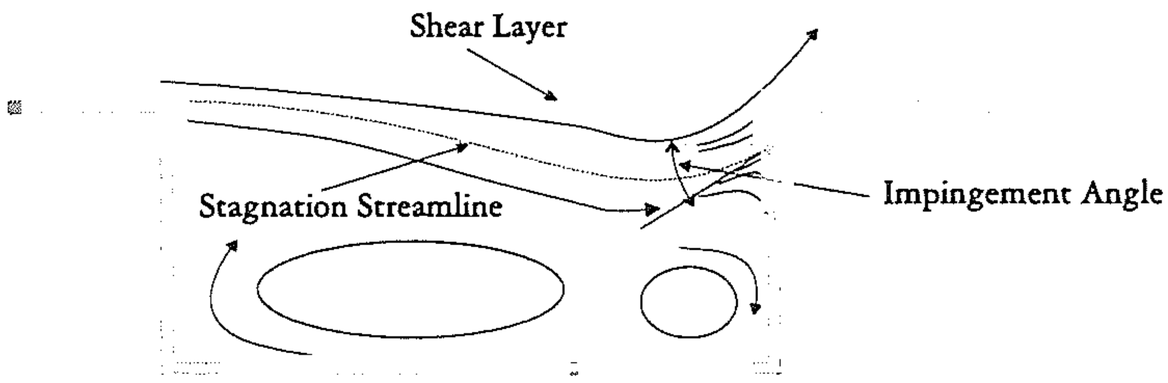

Figure 4.11: Flow Over a Clean Cavity

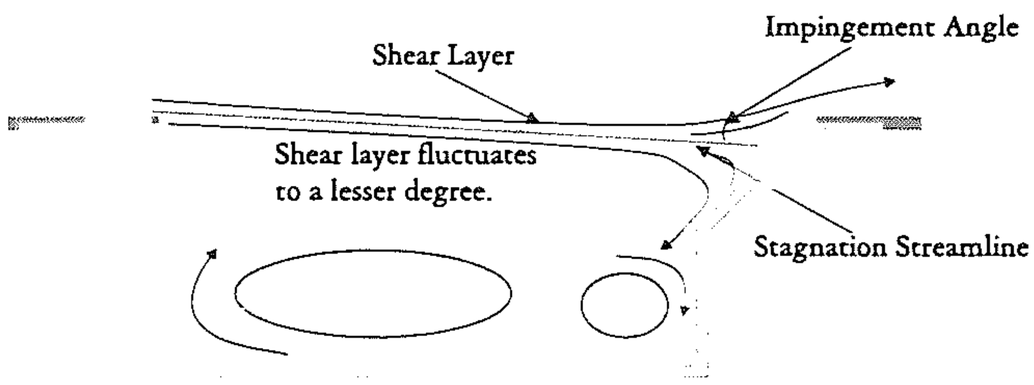

Figure 4.12: Flow Over a Sloped Trailing Edge Cavity

Heller and Bliss then considered a sloped cavity, applying the same line of reasoning to that used above. Once again the fundamental assumption is that a steady flow solution is achievable. Figure 4.12 shows the proposed flow pattern over a cavity with a sloped rear wall. It is seen that for an appropriate degree of sloping the stagnation line impinges on the aft cavity at an oblique angle. For this to occur the

flow does not need to expand into the cavity to the extent it does for a conventional cavity. In fact for an appropriate degree of sloping the shear layer can be effectively straight as it traverses the cavity opening. This requires no balancing of the pressures at the leading edge, which is required for the clean cavity and in effect induced the unsteady nature of the flow. The solution therefore indicates the possibility of achieving steady flow. Of course due to the assumptions made for the flow impingement pattern the real flow pattern will not be as simple. Consideration of the feedback mechanisms with the small disturbances that exist in the shear layer tend to suggest that a completely steady flow for a slanted rear wall is not achievable. Therefore the effect of the sloped rear wall is to produce a steady flow structure that is precluded by details of the real flow structure. The overall effect is a reduction in the pressure oscillations through a dampening of the level of unsteadiness. The work of the present thesis intends to firstly show the hypothetical solutions proposed by Heller and Bliss are possible. From this it will be demonstrated that the level of unsteady activity for a sloped cavity is noticeably lessened. It will be interesting to see how the solutions compare with those proposed by Heller and Bliss, an exercise not undertaken in any previous studies in the literature for suppression via rear wall sloping.

Heller and Bliss developed their models assuming steady flow but the present simulations (and experiments against which the results have been validated) show the flow to be highly unsteady. Levels of up to 167 dB were recorded for the 63.4° sloped wall. Therefore for comparisons with the models of Heller and Bliss (Figures 4.11 and 4.12) the time averaged solutions will be considered. These solutions are averaged over 10 oscillation cycles. The streamlines at the aft wall are shown in Figure 4.13 for the clean cavity configuration. At the aft cavity wall the streamline pattern is remarkably similar to that proposed by Heller using potential flow theory. The flow is seen to impinge at an oblique angle and the radii of curvature of the streamlines on the free-stream side are greater than those below the stagnation line. It is seen that the time averaged flow matches very well with the hypothetical flow proposed by Heller and Bliss. In Figure 4.15 (a) it is seen that the flow expands into the cavity at the leading edge, as proposed by Heller and Bliss. To balance the

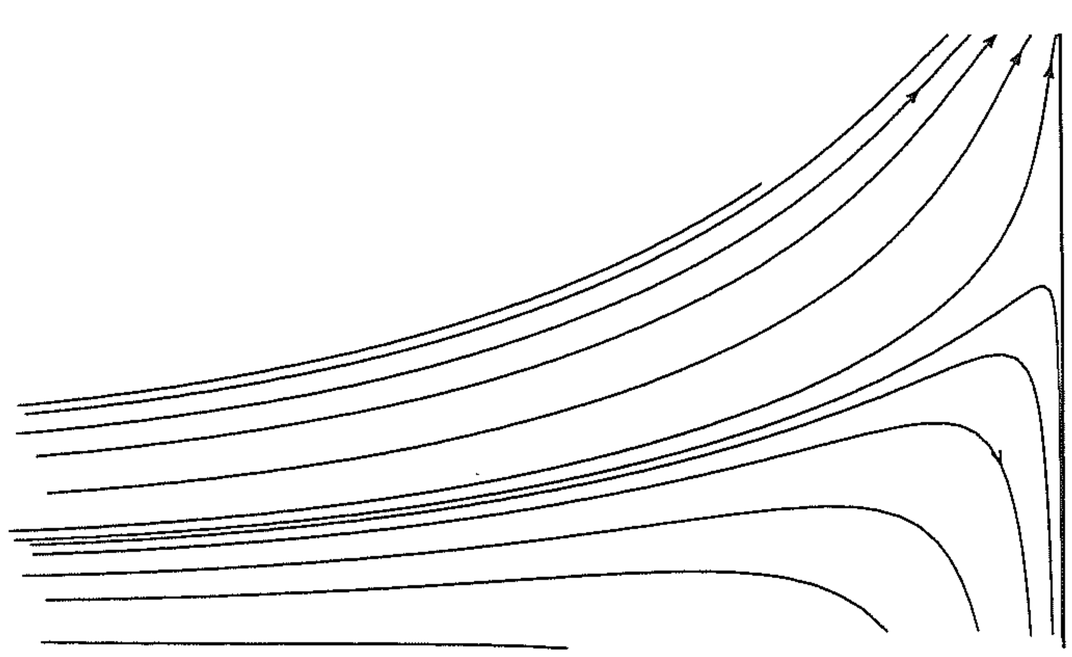

Figure 4.13: Shear layer at rear of clean cavity

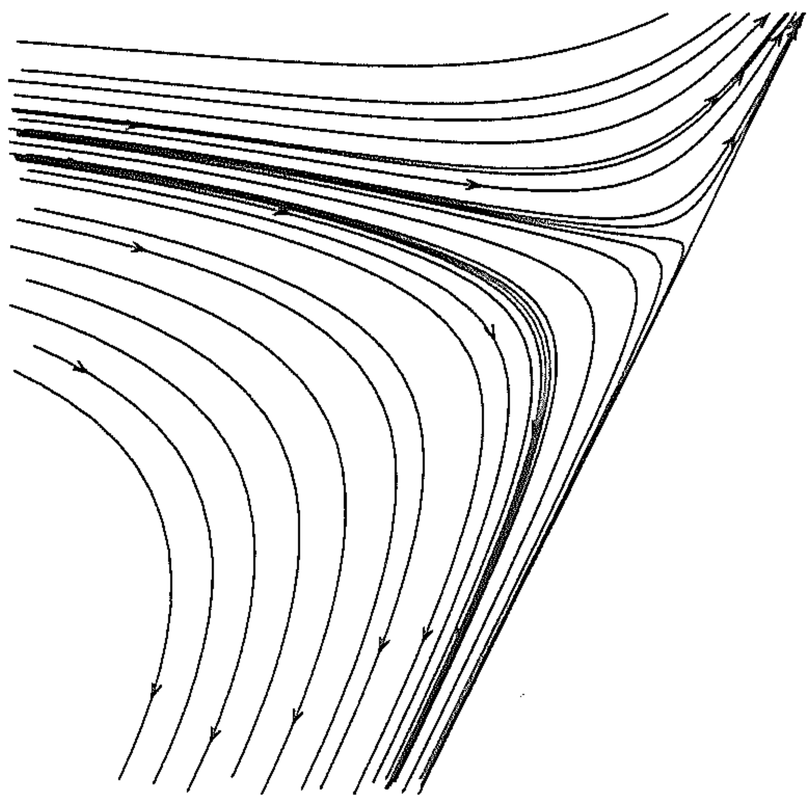

Figure 4.14: Shear layer at rear of 63.4° slope cavity

pressure variations the flow must be unsteady in nature, which is indeed the case. The computational clean case agrees very well with the Heller and Bliss model, so it is hoped a similar comparison for the sloped case will provide information regarding how suppression of the pressure oscillations occurs.

The streamlines over the 63.4° sloped case are shown in Figure 4.14. Once again they agree well with those proposed by Heller and Bliss. This has not been previously shown in any of the literature. The stagnation line impinges at an oblique angle and it can be seen that the radii of curvature of the streamlines on the cavity side are relatively larger than the corresponding ones for the clean case. This means that the centrifugal pressure forces will be less, thus reducing the strength of the pressure wave which forms at the aft wall and is fundamental to sustaining the feedback mechanism. However this, in the authors opinion, is not the significant factor in the suppression of the pressure oscillations for a sloped aft wall. Rather this may be attributable to the natural desire of the flow to tend towards a steady state. Looking at Figure 4.15 (b), the streamlines for the 63.4° sloped cavity show the shear layer still expands into the cavity at the leading edge but to a much lesser extent than for the clean case in Figure 4.15 (a). As discussed previously it does not need to since the flow impingement angle at the aft wall is more easily satisfied due to the sloping. The shear layer moves closer to what is essentially a straight shear layer and therefore steady flow. This is what Heller and Bliss proposed. The acoustic environment in the cavity is reduced as the flow moves away from a structure typical of highly unsteady flow. Nonetheless features inherent to clean cavity flow preclude a steady flow. The shear layer still expands (Figure 4.15 (b)) into the cavity at the leading edge and as such the static pressure variations induce an unsteady motion. However the extent of the oscillations need not be as great due to the impingement angle at the aft wall being satisfied. In summary the flow structure is tending towards a steady flow but it's unsteady nature dominates and the overall effect is a *less definable clean cavity flow.* The remainder of the section will aim to highlight the flow being *less unsteady* rather than attempt to show distinct differences occurring between the two cases.

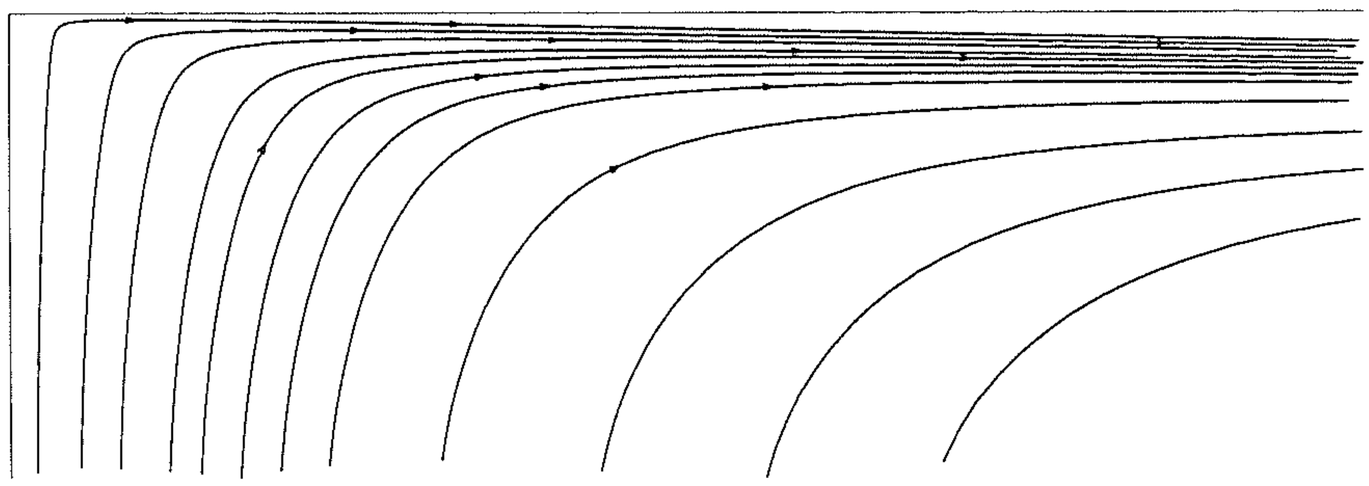

(a) Clean Cavity

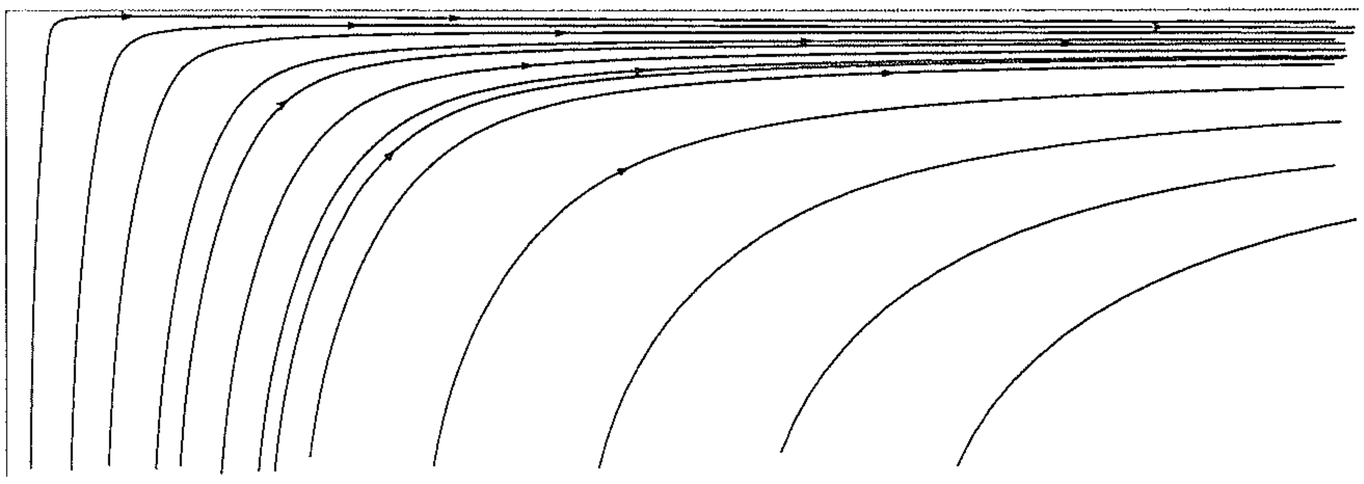

(b) 63.4° Slope Cavity

Figure 4.15: Shear layer at front of Cavity

Shown in Figure 4.16 are the instantaneous vorticity magnitude contours for the clean cavity and the slope of 63.4°, corresponding to the non-dimensional time interval 21.62 to 22.72, as in Figure 4.8 . The inherent unsteadiness in the shear layer, which sustains the periodic shedding of vorticity, is apparent in both cases. The shedding of the vorticity for the clean case compares well to that shown recently by Sinha and Arunajatesan [77] for LES simulations on a fine grid. As is discussed in earlier chapters the impingement of vortices on the aft cavity wall sustain the feed-

back mechanism. The upstream propagation of disturbances periodically lifts the shear layer at the leading edge, locking in the shedding of further vorticity. When animations of the two cases are compared, represented pictorially in Figure 4.16, differences are apparent in the level of unsteadiness. For the 63.4° slope the oscillation of the shear layer is significantly dampened as compared to the clean case. This indicates the tendency towards a straight shear layer and therefore steady flow. The heights of the peaks and troughs are smaller for the 63.4° case. Figure 4.16 (a) shows the 63.4° cavity at the same instant in time as the clean case. This represents the mass addition stage of the cycle, as can be seen by the pressure trace which is at a peak at X/L = 0.95. The trace shows that the magnitude of the oscillations for the 63.4° case is some 10 % less than that for the clean case and the less pronounced shear layer can be seen in Figure 4.16 (a). Notice how the trough approaching the aft wall for the clean case is considerably lower (almost in the cavity) when compared to the 63.4° cavity. The peak of the shear layer is also more pronounced for the clean cavity. It is seen that the higher peak and lower trough lead to a more definable shape for the clean case. It has a clearly distinguishable *comma* shape which in turn occupies a larger area. The 63.4° cavity is not as pronounced showing that the solution is tending more towards that which is representative of the flow structure proposed by Heller and Bliss. For the 63.4° slope the area of high vorticity is smaller and does not protrude into the cavity as much. This will obviously be significant when it approaches the aft wall. The lower vorticity levels (relative to the clean case) impinging on the aft wall will lessen the feedback mechanisms and in turn the overall process. Moving through Figures 4.16 (b), (c) and (d) it is seen that the shedding of the higher magnitude vorticity is more *elastic* for the 63.4° case. As it approaches the aft wall the high magnitude vorticity stretches out further before finally detaching and impinging on the aft wall. This observation tends to suggest the 63.4° cavity is closer to achieving steady flow. For such flow the shear layer will not oscillate as much and the vorticity will fluctuate less. The *elastic* effect indicates that the flow is moving towards a steady state scenario. Recall that in the model of Heller and Bliss the vorticity was assumed to be constant at the local region of the stagnation line. A similar effect is seen here for the 63.4° case. For the clean case the high vorticity breaks off as it approaches the aft wall. This shed vorticity

also occupies a larger area and is deeper in the cavity than for the 63.4° case. It will thus have a more significant impact on the aft wall and therefore the feedback mechanism. Sequence (e) in Figure 4.16, which is the start of the cycle again, shows how the disturbances that would have propagated upstream have affected the leading edge vorticity. The 63.4° slope is seen to suppress the *comma* shape, which is easily distinguishable as a feature of the clean case.

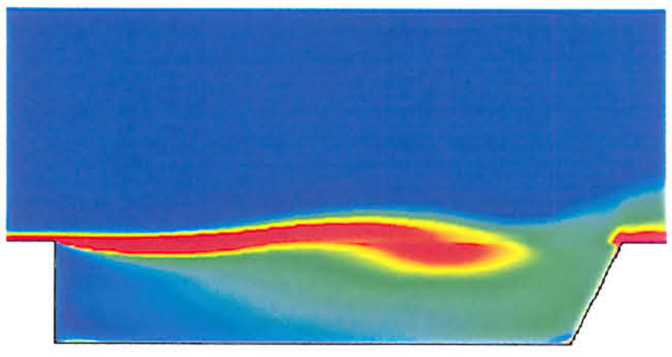

Time=21.52

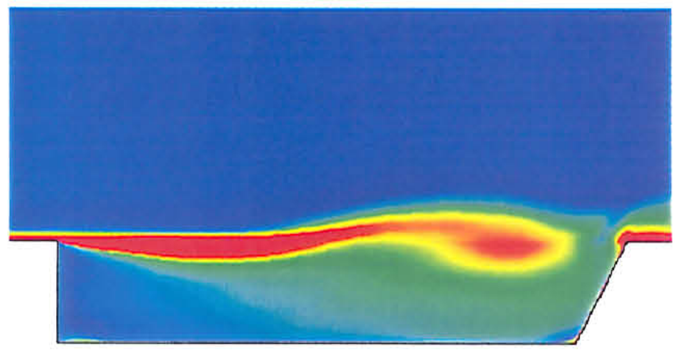

Time=21.82

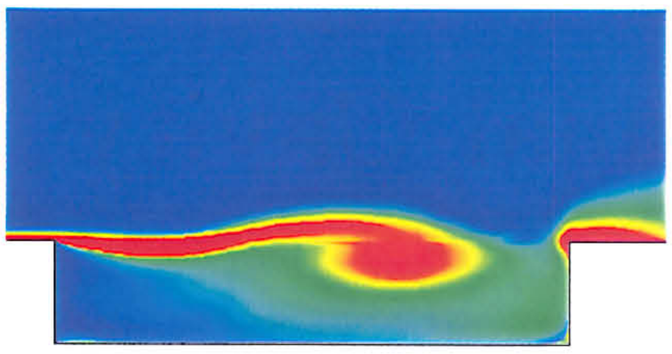

Time=22.02

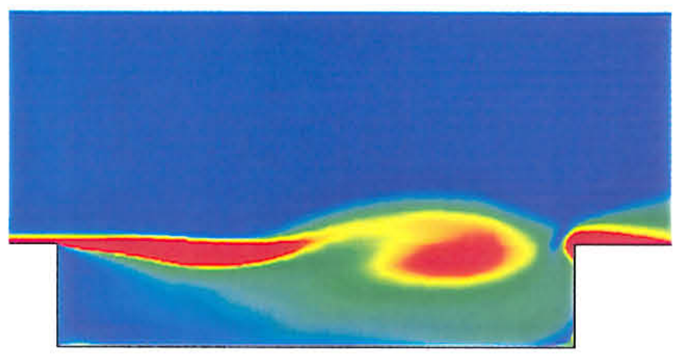

Time=22.22

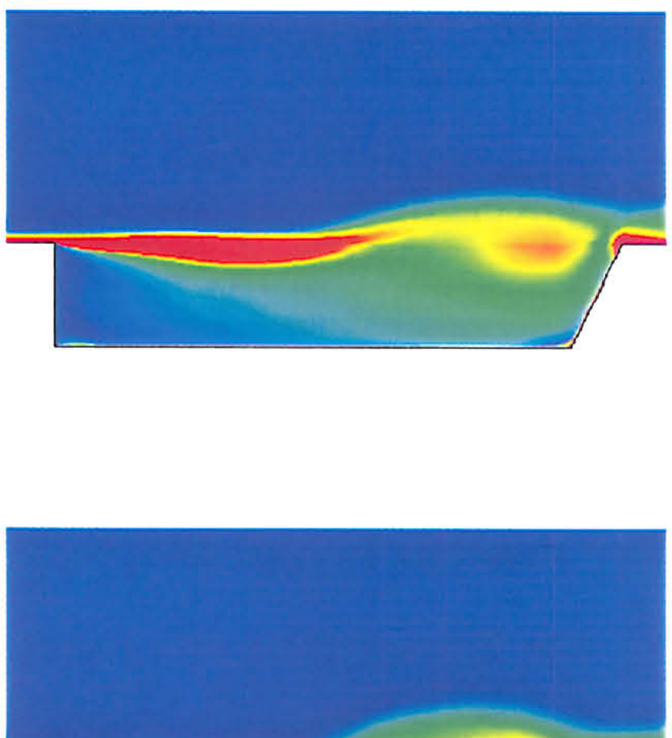

Time=22.62

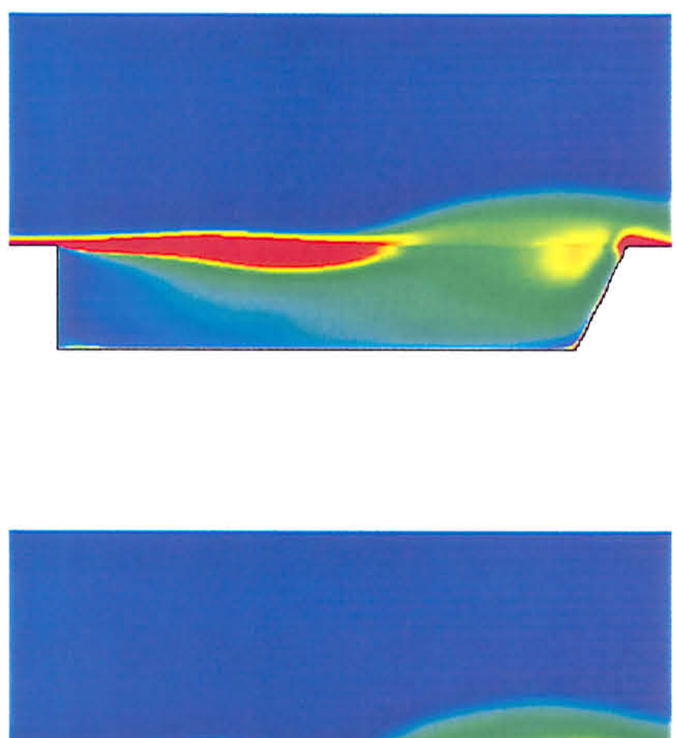

Time=22.62

Figure 4.16: Time Evolution of the Vorticity Contours Over one Oscillation Cycle for Clean and Sloped Cavity

Chapter 5

Supersonic Transitional Cavity flows

5.1 Introduction

At the store carriage integration and release conference, hosted by the Royal Aeronautical Society in 1990 [93], F J Wilcox presented a summary of the flow characteristics that were found to occur at supersonic speeds as determined from experiments conducted at the NASA Langley Research Centre. This section presents a discussion of these results which form a starting point for the analysis in this chapter.

Prior to the work of Stallings and Wilcox [80] it was known that open and closed cavity flow-fields at supersonic speeds existed for $L/D \leq 11$ and $L/D \geq 13$, respectively. Little was known about the intermediate flow-fields. Experiments were conducted over a variety of test conditions and for a range of cavity L/D ratios to determine where the change from open to closed flow occurs [80]. The cavity length was varied from 0.5 to 12 inches and the height from 0.5 to 2.5 inches, allowing $1 \leq L/D \geq 4.8$ and $1 \leq L/D \geq 24$ for heights of 2.5 and 0.5 inches respectively. A few configurations with modifications to the width were also tested. It was these tests that led to the definition of two further cavity flow-fields. Tests were conducted at Mach numbers of 1.5, 2.16 and 2.86 with a Reynolds number of 2×10^{-6} per foot, with the approaching boundary layer being of a turbulent nature. Wilcox presented Schlieren photographs for the Mach 2.86 case. The typical flowfields for

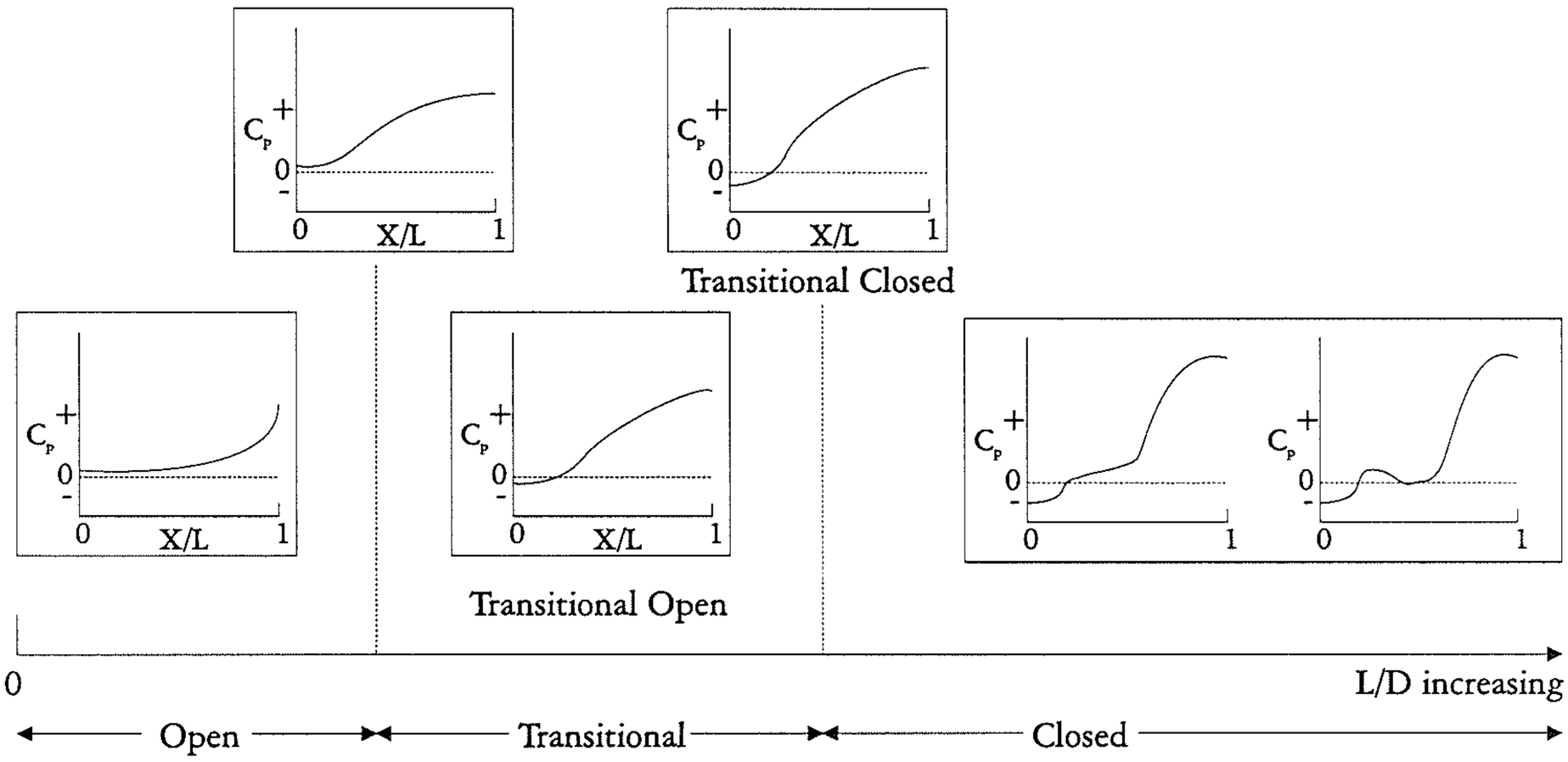

Figure 5.1: Cavity Flow Field Model: Closed Flow

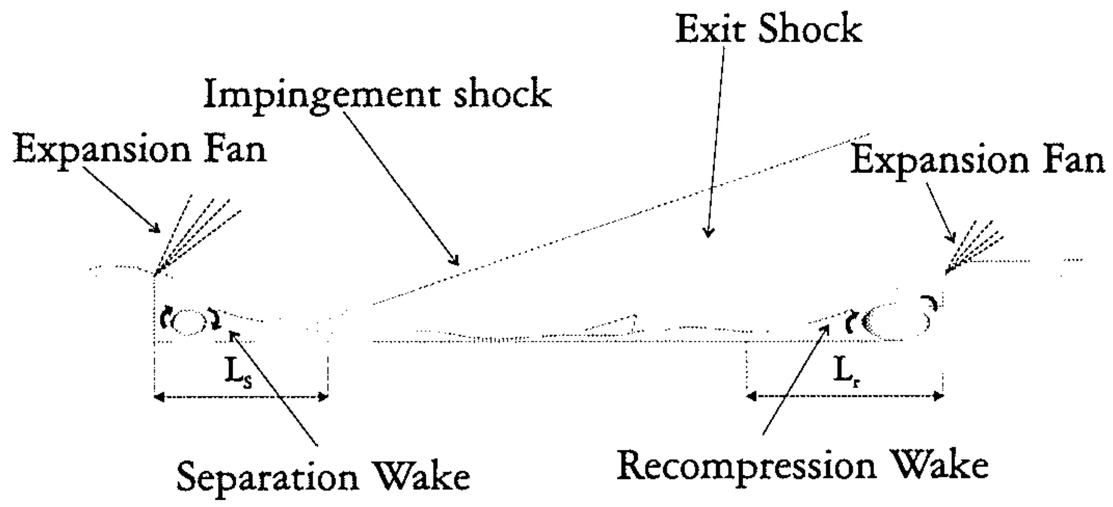

Figure 5.2: Cavity Flow Field Model: Closed Flow

closed, transitional-closed, and transitional-open open flow are shown in Figures 5.2, 5.3 and 5.4, respectively. The pressure distributions along the cavity floor for open and closed cavity flow are shown in figure 5.1. They are shown for comparison purposes only and will not be re-discussed. The pressure distributions found in the intermediate region (broadly defined by Wilcox as $11 \leq L/D \leq 13$) are also shown in figure 5.1. It is generally accepted that the pressure distributions are one of the best indicators of the type of flow occurring. The intermediate region is referred to as transitional cavity flow and can be sub classified as transitional-open flow and transitional-closed cavity flow, depending on which end of the spectrum it is closer to. For transitional-open flow the pressure distribution along the floor is similar to that for open flow. However the Cp at the front of the cavity is lower than for an open flow, given that the flow expands further into the cavity as L/D increases and

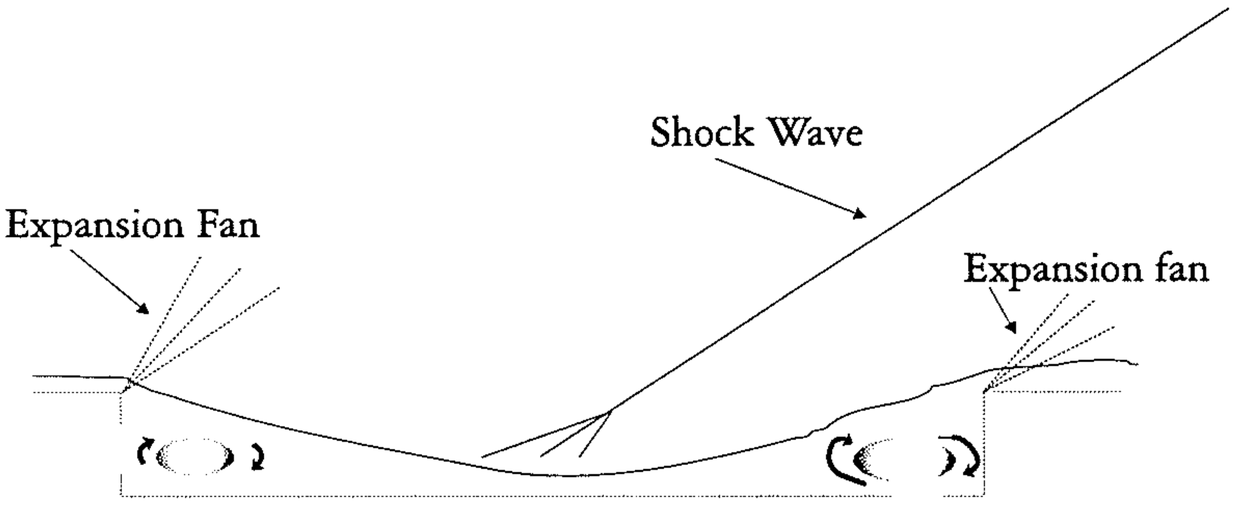

Figure 5.3: Cavity Flow Field Models: Transitional-Closed Flow

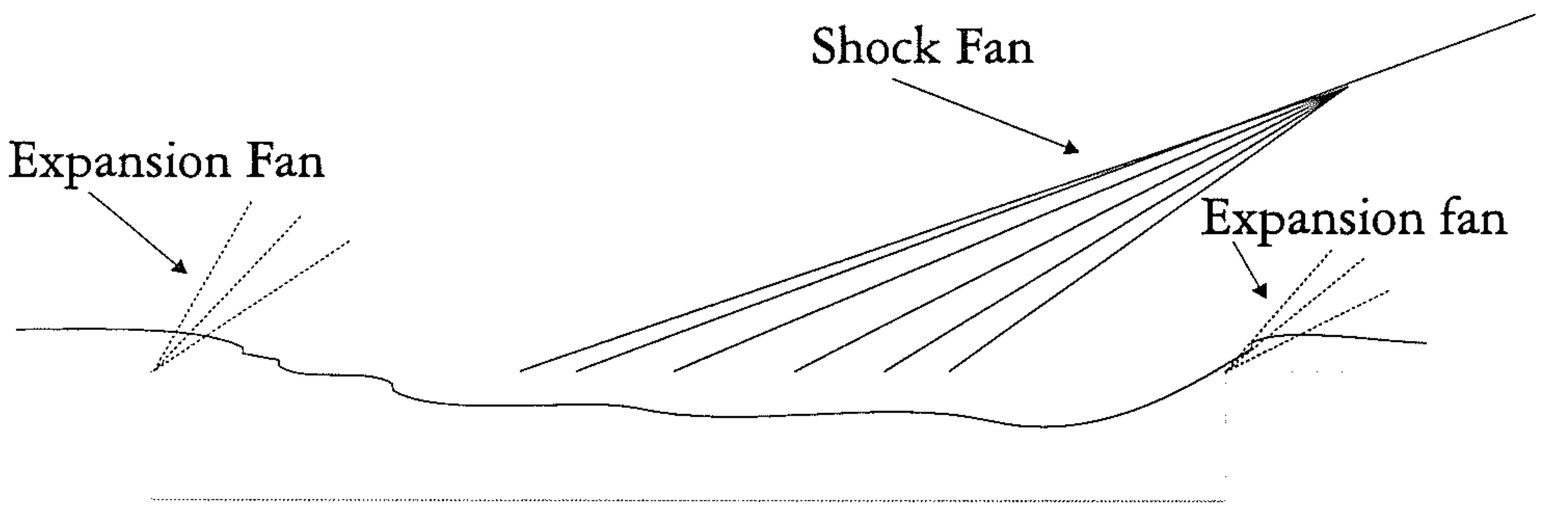

Figure 5.4: Cavity Flow Field Models: Transitional-Open Flow

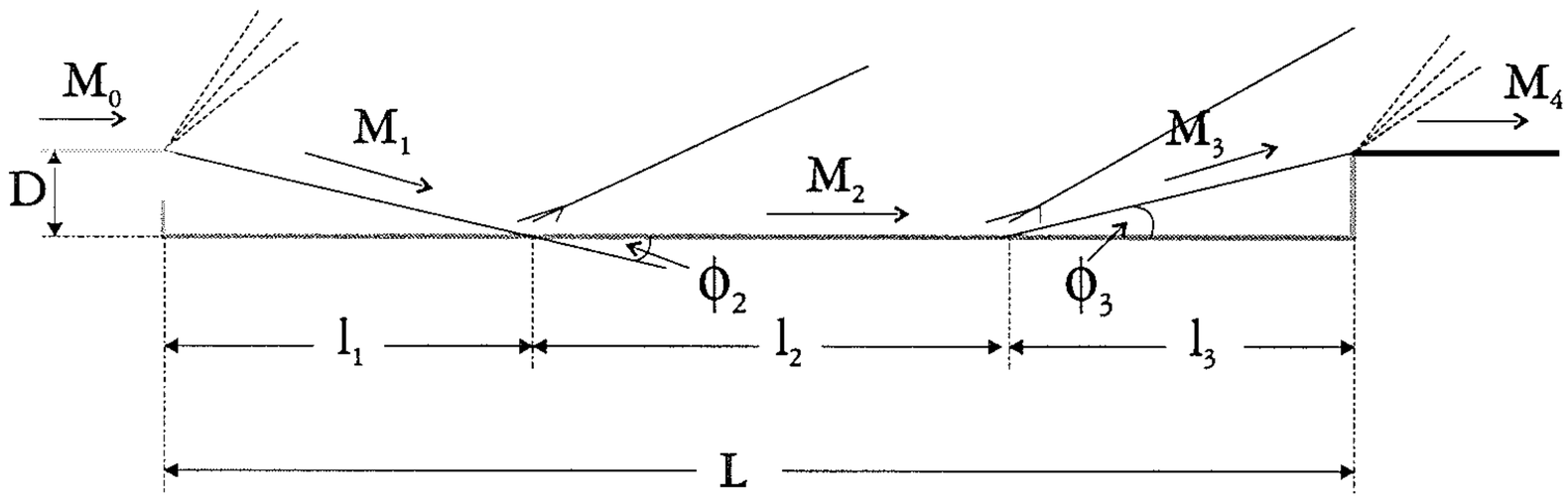

Figure 5.5: Simplified Model of the Flow

may in-fact give rise to a slight negative pressure coefficient. The pressure distribution then gently rises as the flow gradually turns away from the cavity resulting in a series of compression wavelets formed above the cavity, as shown in figure 5.4. The pressure at the rear of the cavity peaks at a value higher than that for open flow given the tendency of the flow to expand into the cavity more than it would for open flow. For open flow the fluctuating shear layer means the flow is not always impinging on the rear wall of the cavity but only does so during the mass addition stage of the cycle. For supersonic transitional cavity flow the behaviour is different. The flow for transitional open flow expands considerably at the trailing edge corner on leaving the cavity. Starting with closed cavity flow and decreasing the cavity length to depth ratio there comes a point where transitional closed flow is obtained. This occurs when the impingement and exit shocks collapse to form a single shock. The Cp distribution no longer has the plateau of closed flow (associated with the flow impinging on the cavity floor). It is similar in nature to the distribution for transitional-open flow, but with a greater difference in pressure between the front and aft of the cavity. Figures 5.4 and 5.3 are taken from Wilcox though it should be mentioned that the location of the flow field features as sketched is slightly misleading. For example, the compression waves shown for transitional open flow occur further downstream. From the Schlieren photographs the compression wavelets can be seen to form from X/L=0.5 until near the cavity exit [93]. The original experimental work was done in 1987 and recorded in reference [80]. This earlier reference raises some questions. There is confusion regarding the description of the transitional flows. The ensuing discussion will relate to figure 5.6, which is reproduced from the experimental work and appears in both of the above cited papers, albeit with different explanations. Numerous tests were conducted with the initial intention to determine the boundaries between open and closed flow. The critical L/D ratios from Mach 1.5 to 2.86 are shown in figure 5.6. From the diagram it is not apparent where the boundaries exist between transitional open and transitional closed flow. A point to note is that for Mach 1.5 the region for transitional flow is small.

In reference [80] L/D_{crit} is defined as the L/D ratio where the flow changes from open to closed or vice-versa. A hysteresis effect is found to occur. The cavity has a sliding block feature allowing the L/D ratio to be increased or decreased while the

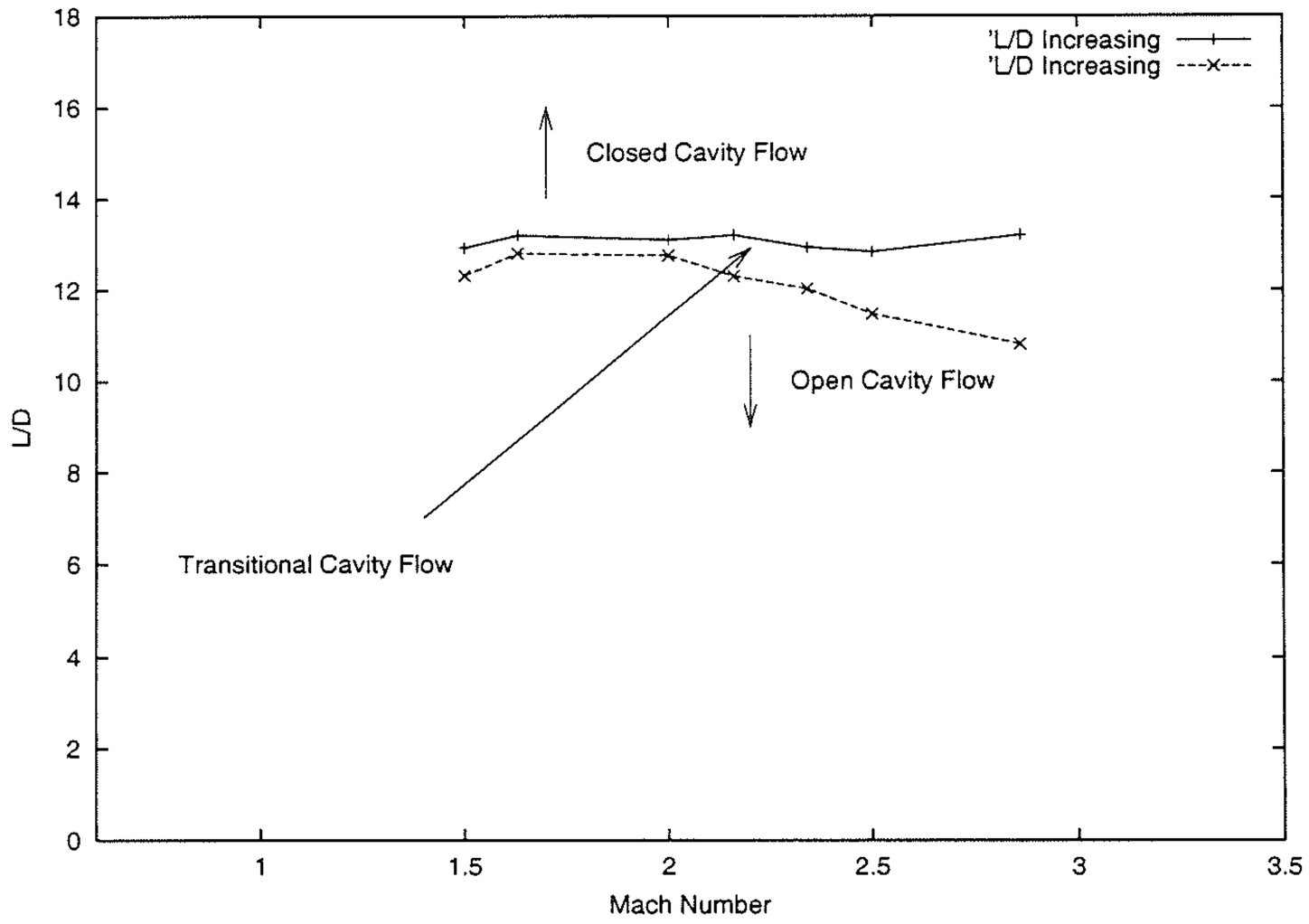

Figure 5.6: NASA Langley Tests: Variation of Critical L/D Ratio with Mach Number

flow is passing over it. In the experiments the flow field is initially of the closed type and the L/D ratio of the cavity is decreased until open flow is obtained. The change to open flow *is determined by the abrupt disappearance of the combined impingement/exit shock*(shown in Figure 5.3). Wilcox later states [93] that the combined impingement/exit shock is characteristic of transitional-closed flow. The critical L/D ratio for decreasing cavity length is represented by the lower line in figure 5.6. The opposite is then done, with the L/D ratio increasing as the flow passes over the cavity until closed cavity flow is obtained. The new flow regime *closed cavity flow is determined by the sudden reappearance of the combined impingement exit shock.* The critical L/D ratio for increasing length is shown by the upper line in figure 5.6. The critical L/D ratio (ie when the flow changes from open to closed or from closed to open) is higher for an increasing L/D ratio than for a decreasing one. The size of the hysteresis region increases with Mach number. Although there is no detailed discussion of transitional cavities, Stallings does mention in the introduction that for a cavity with a $L/D \approx 12$, the flow is on the verge of changing from closed to open flow. The impingement shock and exit shock that occur for larger L/D ratios (Figure 5.2) are no longer present but are replaced by a single wave (Figure 5.3).

The flow turns into the cavity before leaving with an exit angle that is close to the angle of flow impingement. This is termed transitional cavity flow.

In Wilcox's paper there is reference (though very broadly) to the work of A.F. Charwat, J.N. Roos, F.C Dewey Jr, and J.A. Hitz who published *An Investigation of Separated Flows- Part 1: The Pressure Field [21].* It is from this work, and previous references [47] [73] [58] [56], that an intermediate region is shown to exist.

Charwat mentions that the transition from an open cavity flow to the *intermediate length cavity is associated with the appearance of a weak oblique shock rooted in the shear layer.* This was noted by previous investigators, though without substantial comment. Charwat attributes the presence of the shock to the deflection of the external stream, which is part of the recompression mechanism. The existence of an intermediate flow is shown in the Schlieren photographs which clearly indicate three flow types occurring (open,transitional and closed cavity flow). Charwat shows the existence of a hysteresis region, which is as described above. Also described are the pressure distributions in the cavity whch are similar to those used today to identify open, transitional, and closed cavity flows. It is therefore reasonable to say that the work of Charwat was significant in the classification of intermediate cavity flow. He did however only define the existence of one intermediate type of flow, which Stallings later sub-classified into transitional open and transitional closed cavity flow.

Prior to the work of Charwat, R W McDearmon [56] published the technical note *Investigation of the Flow in a Rectangular Cavity in a Flat Plate.* The work, although concerned with cavities in the high supersonic regime (at a Mach Number of 3.55), highlighted the existence of the sub-classes later to be named by Stallings and Wilcox [80] as transitional-open and transitional-closed cavity flows. The study was remarkably similar to that of Stallings in that the main features investigated were those of the cavity L/D ratio and the span of the cavity. The results consisted of pressure distributions along the cavity floor and Schlieren photographs and shadowgraphs of the shock structure immediately above the cavity. McDearmon obtained

L/D Ratio	Classification
24	Closed
10.8	Transitional
6.8	Open
4.95	Open
3	Open
2.1	Open

Table 5.1: Summary of McDearmon [56] Test Cases

.

pressure distributions for a range of L/D ratios, which are shown in Table 5.1. The terminology used today to describe these flows, though not defined at that time, is shown in column 2 of the table 5.1. The classification of the flows from the work of McDearmon (though not stated at the time) can be interpreted from the behaviour of pressure distributions and investigation of the Schlieren photographs and shadowgraphs - the methods used to classify cavity flows today. The behaviour of the flows were as follows:

- For $L/D = 24$ the flow became attached to the cavity floor.
- For $L/D = 10.8$ the flow was detached from the cavity floor.
- For $L/D = 6.8$, 4.95, 3 and 2.1 the flow was also detached though the phenomena was different than was evident for L/D=10.8
- There is a noticeable difference in the pressure distributions for $L/D = 10.8$ and $L/D = 24$
- From $L/D = 10.8$ to $L/D = 6.8$ a change in the L/D ratio of the cavity causes a change in the pressure distribution.
- For $L/D = 4.95$ to 2.1 the pressure distributions were very similar.

McDearmon proposed that a critical L/D ratio existed between $L/D = 10.8$ and $L/D = 24.0$ such that the pressure distribution was very sensitive to depth changes

for $L/D \leq L/D_{crit}$ and insensitive for $L/D \geq L/D_{crit}$. With the knowledge of cavity flows available today it is obvious that this critical L/D is in the transitional region. From the Schlieren photographs McDearmon produced sketches of the flow though did not explicitly name them. These sketches were later named by Stallings and are as shown in figures 5.2, 5.3 and 5.4. McDearmon described them as closed cavity flow, a cavity flow with a *shock fan* above the cavity(for $L/D = 10.8$), a cavity flow with a single shock wave above the cavity(for $L/D = 10.8$), and open cavity flow. The features observed to occur are the same as those used by Stallings to define the 4 classes of cavity flow

Note that the two flows found to exist for $L/D = 10.8$ were for different L/W ratios. The cavity flow with the shock fan is transitional-open while the flow with the single shock wave above the cavity is transitional-closed flow. Transitional-open flow occurred for the lower L/W ratio and transitional-closed for the higher L/W ratio. This phenomenon is in accord with the later results of Stallings; *As the width, W is decreased* L/D_{crit} *decreases.* Therefore at the smaller L/W ratio transitional-open flow is more likely to occur than transitional-closed flow - as was the case at the L/D=10.8 ratio in the experiments of McDearmon. McDearmon never showed the two transitional flows to exist for the same L/W ratio though this may be attributed to the fact that not enough L/D ratios were investigated, especially close to L/D_{crit}. In summary it is clearly evident that the 4 types of cavity flows at supersonic speeds were discovered, though not classified, long before the work of Stallings. In addition McDearmon, after an extensive review of the literature, was the first investigator to look at the effects of upstream and downstream lip radii on the cavity flow.

It was not until Stallings considered the centreline pressure distributions and the effect of the L/D ratio of the cavity that there was any mention of transitional cavity flow from the findings of his own work. The pressure distributions along the cavity floor are presented for closed flow, *transitional flow prior to changing to open flow*, *transitional flow after changing to open flow* and open cavity flow. No descriptions of the pressure distributions are given but it is assumed that these four flows relate to those defined by Wilcox. It can therefore also be assumed that L/D_{crit} corresponds to when transitional-closed flow switches to transitional-open

flow, rather than from closed to open as described by Stallings. The identification of transitional-open flow from transitional-closed flow was achievable by consideration of the flow fields and pressure distributions, as described earlier. It is also intended that more information will be obtained about the flow field for transitional cavities at supersonic speeds since as recently as 1998 there was uncertainty about these types of flow. From experiments [70] a cavity with L/D=10 was found to exhibit all the aerodynamic features associated with closed cavity flow even though it is classified as being within the transitional boundaries. It is therefore seen that much is to be gained from accurate simulations.

5.2 Results and Discussions

The nature of the supersonic transitional flow field is investigated in this chapter by analysing the results from simulation. Five cases were investigated at Mach 1.35 and a Reynolds number of 7.348 million with L/D ratios of 10, 12, 14, 16 and 20. An additional case with L/D=8 showed all the features described in the chapter on open flow and will not be discussed in the current chapter. The pressure distributions for L/D=10, 12 , 14, 16 and 20 are shown in figure 5.7. These correspond to the pressure distributions defined by Wilcox (and shown in figure 5.1), for transitional-open, transitional-closed and closed cavity flow. The associated flow field images are shown in figures 5.8 to 5.12 which represent Mach number contours coupled with the streamlines of the flow.

For all the cases no discrete tones were generated and as these simulations do not include broadband noise the flows converge to a steady state. This is expected given that Stallings [80] detected no upstream propagation of disturbances in the cavity even with broad background noise. The Schlieren images show no unsteady features either. It will be shown in the following chapter that for subsonic transitional-open cavities the flow is unsteady. The reason that the supersonic transitional-open flow is steady may be attributed to two reasons. One is that when classifying transonic and supersonic flow it is easier to identify the flow type occurring by considering the features evident above the cavity. These are readily identifiable with features distinct from subsonic flows. Subsonic flow classification relies on the characteristic

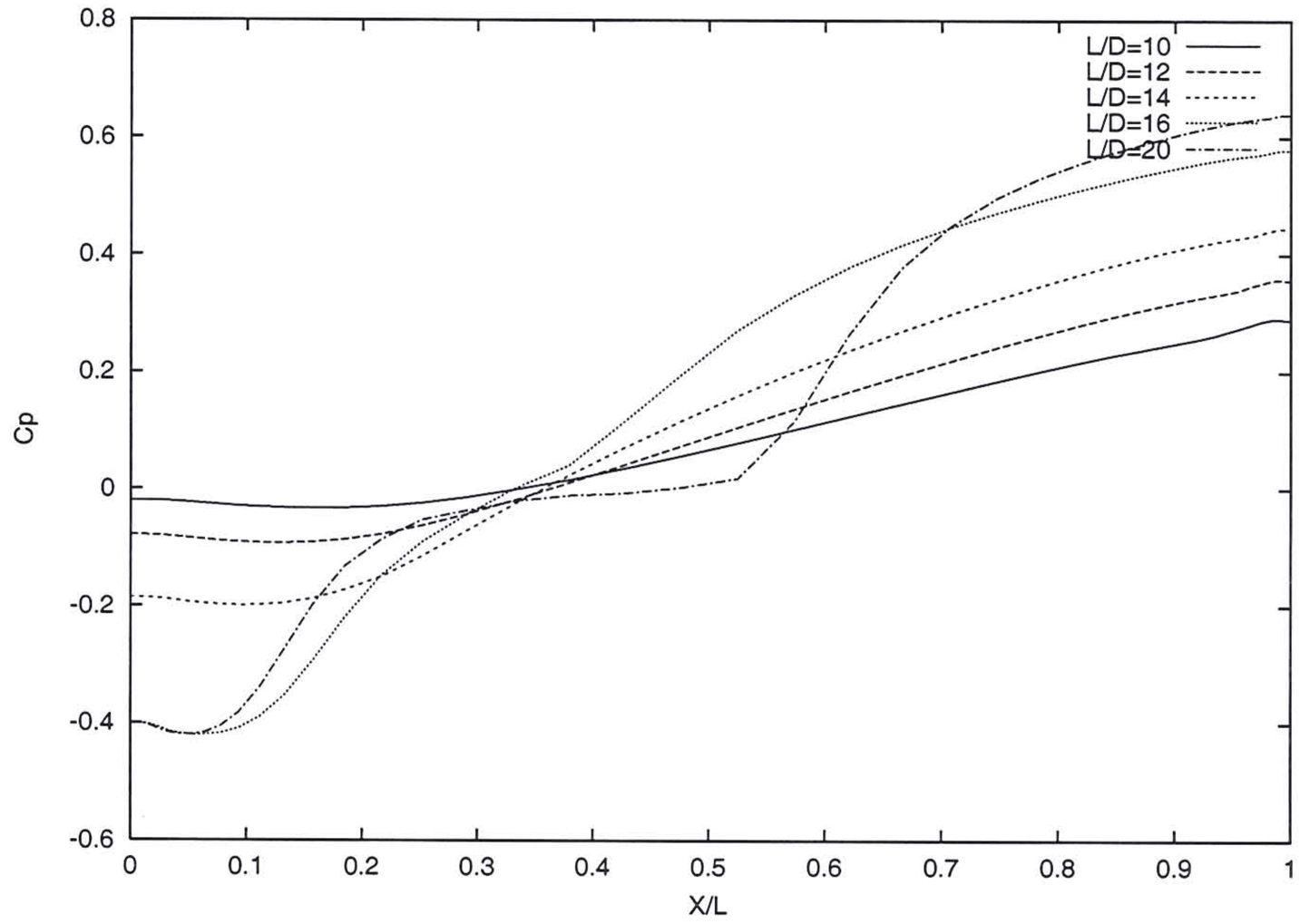

Figure 5.7: Pressure Distribution Along Cavity Floor: Mach 1.35

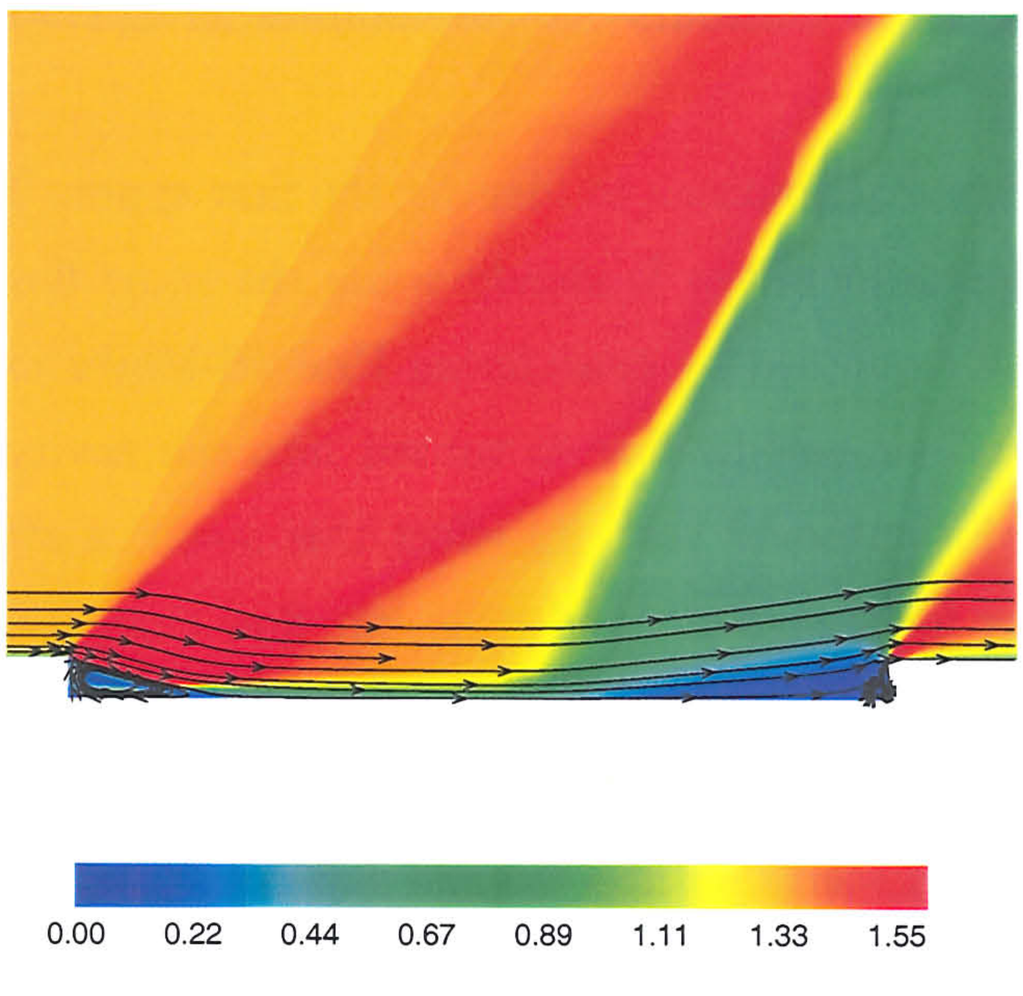

Figure 5.8: Mach Contours and Streamlines for L/D=20 Mach 1.35

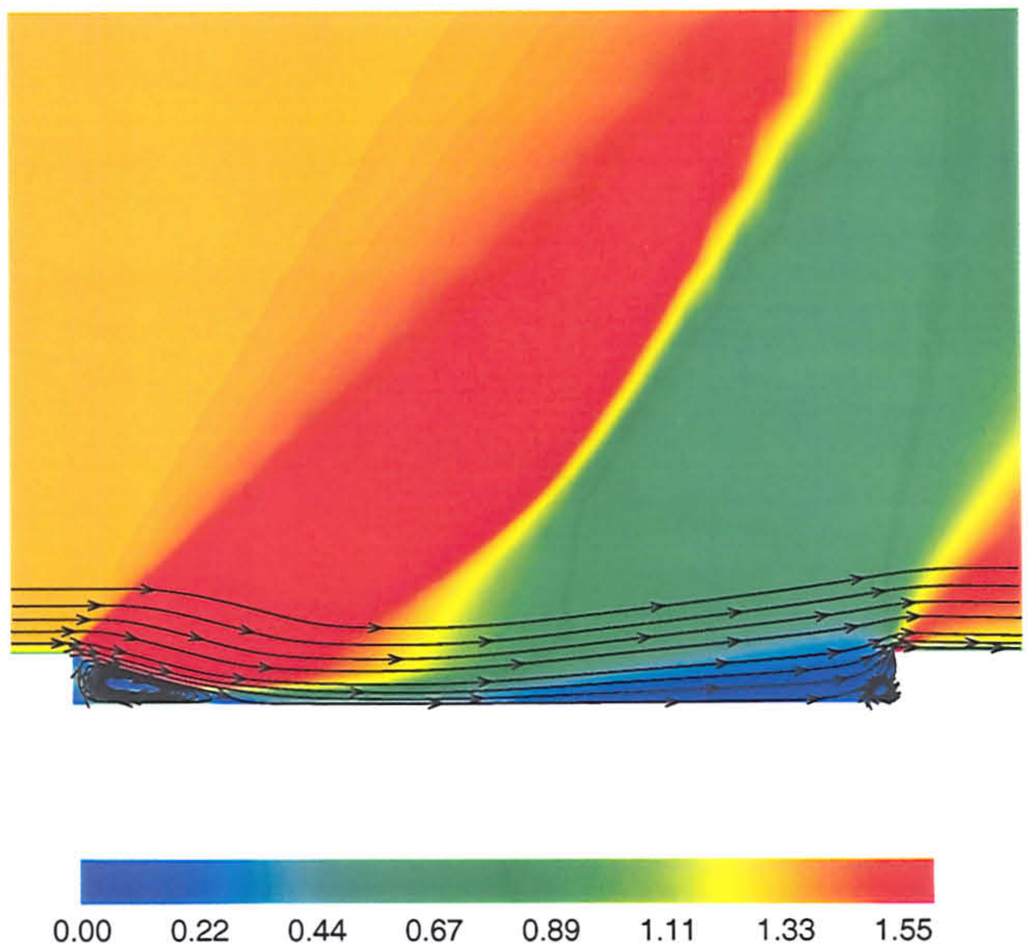

Figure 5.9: Mach Contours and Streamlines for L/D=16 Mach 1.35

cavity floor pressure distributions to identify the flow types. The main reason why transonic transitional-open flow is steady while the same flow at subsonic speeds is unsteady can be explained by considering Prandtl-Meyer expansion theory. For the same L/D ratio supersonic flow is turned into the cavity to a greater extent than it would be for subsonic flow. In effect this means a steady flow is likely to be obtained earlier for supersonic and transonic flow than for subsonic flow. Even though the flow is steady distinctive features above the cavity allow for classification of three types of supersonic flow - transitional-open, transitional-closed, and closed flow. Comparisons between the subsonic and supersonic results will be made in the following chapter and the above hypothesis shown to be correct.

Considering first the $L/D = 20$ and $L/D = 16$ cases the features evident in figures 5.8 and 5.9 indicate that closed cavity flow is occurring. An expansion fan, centred at the upstream lip, turns the flow into the cavity. Behind the upstream wall, which is essentially a downward facing step, there is a separation wake, which is clearly evident in the figures. Interestingly, the reattachment point of the wake

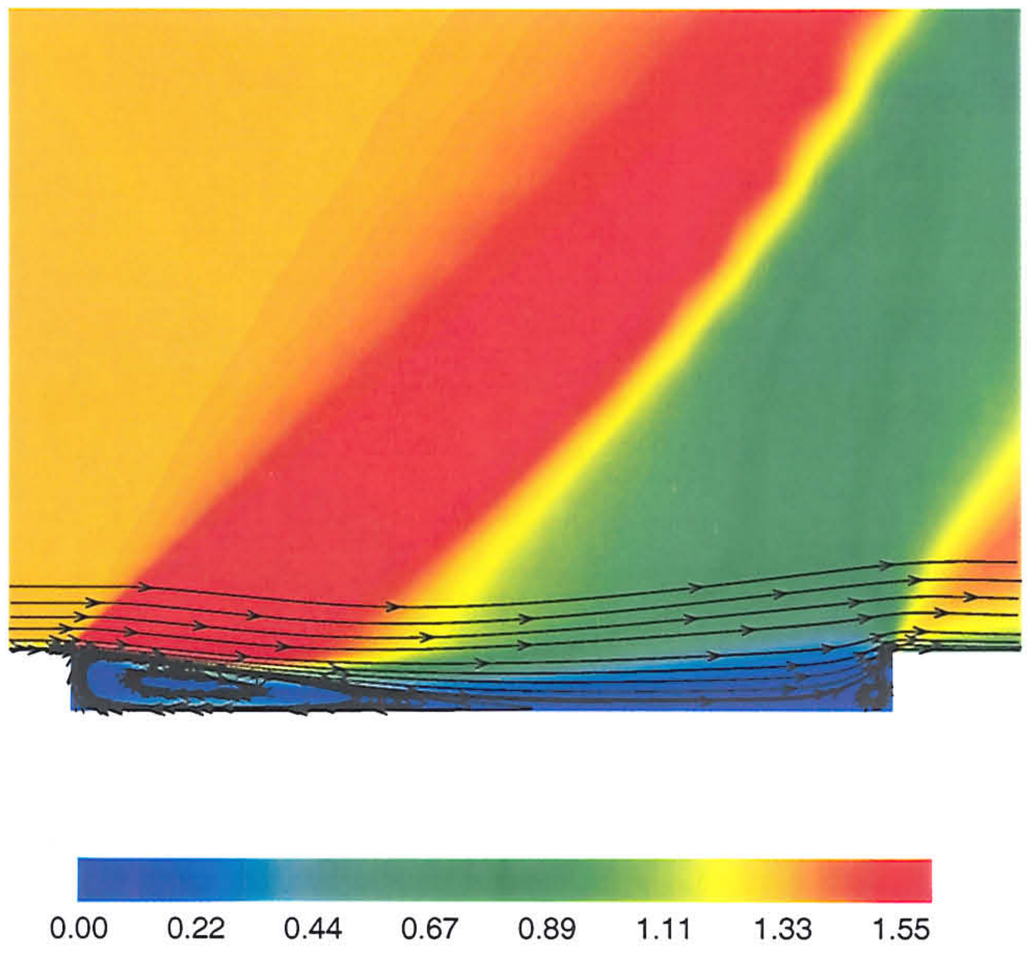

Figure 5.10: Mach Contours and Streamlines for L/D=14 Mach 1.35

for $L/D = 16$ is further downstream than that for $L/D = 20$. The parameter which determines this is the length of the separation wake to its height - L_s/D. For closed cavity flows it is possible to determine a value for this ratio by relating the base pressure of the wake to its L/D ratio by a Prandtl-Meyer expansion centred at the upstream lip. It has been shown [21] that L_s/D is very nearly constant with both Mach and Reynolds number. The ratios of L_s/D are shown in figure 5.14. The values obtained from the current calculations are $L_{s,16} = 3.428571424$ and $L_{s,20} = 3.428571420$. These values compare very well to those given in [33] and [62] for backward facing steps.

The pressure distribution along the cavity floor is shown in figure 5.7. It is seen that as the flow expands into the cavity the pressures behind the front face are low but increase with distance along the cavity floor. This is because there is greater momentum of the flow in the part of the separation bubble that is further upstream. The rise in pressure is gradual with increasing X/L. After the separation wake the flow impinges on the cavity floor - an impingement shock in clearly visible in

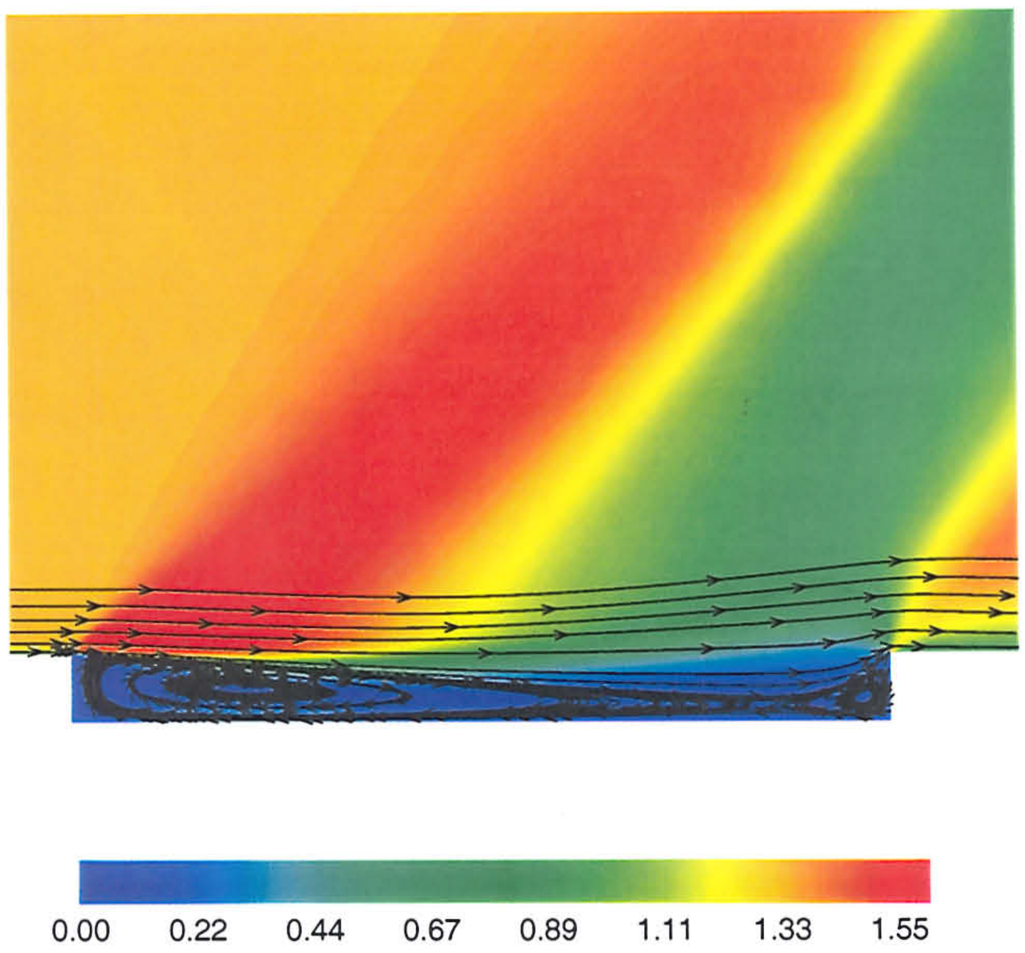

Figure 5.11: Mach Contours and Streamlines for L/D=12 Mach 1.35

figures 5.8 and 5.9. For the $L/D = 20$ cavity the flow impinges on the cavity floor from $X/L = 0.175$ and from here until separation there is a plateau in the pressure distribution. Eventually the shear layer separates from the floor prior to the aft wall and the flow will exit the cavity. A recompression wake is formed prior to the aft wall and the flow is essentially that over a forward facing step. An exit shock forms above the cavity as the flow turns to leave the cavity and as it does it encounters an expansion fan centred at the corner of the aft wall.

For closed cavity flows the separated regions are mutually independent. The flow stops being of the closed type when the L/D ratio decreases to the point where the vertices of the separation wake and recompression come together. From the flow visualisation the movement towards each other of the vertices for the $L/D = 20$ and $L/D = 16$ case is evident. As mentioned above, it has been shown by McDearmon [56] that as the L/D ratio of the cavity continues to decrease the pressure distribution along the cavity floor will vary noticeably. It is shown in figure 5.7 that the pressure distributions for $L/D = 16$ and $L/D = 14$ are distinctly different, indicating that

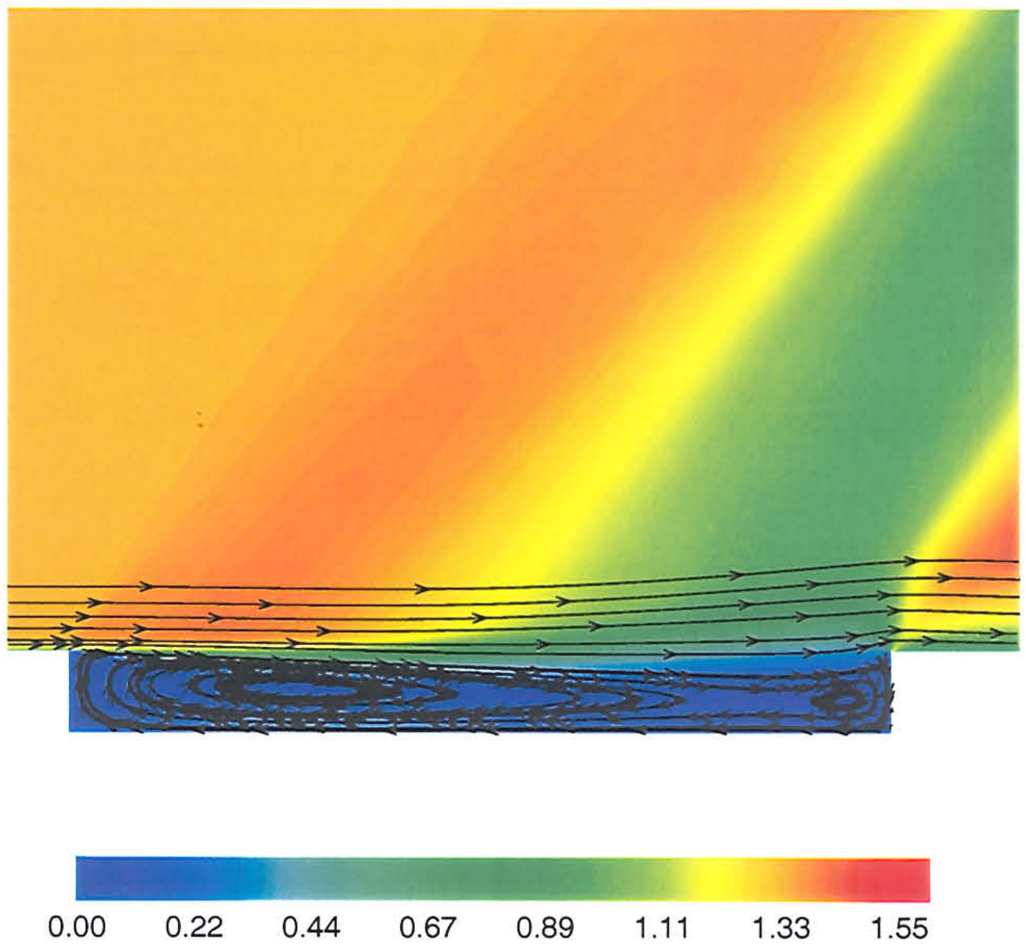

Figure 5.12: Mach Contours and Streamlines for L/D=10 Mach 1.35

that the flow changes from closed to transitional somewhere between these ratios. The pressure and streamline contours for $L/D = 14$ are shown in figure 5.10. From the figure it can be seen that the L/D ratio is just less than that required for transitional-closed flow since

- at $L/D = 14$ there is a stream of flow from vortex 1 (at the fore wall) to vortex 2 (residing at the aft wall)
- at $L/D = 16$ the vortices are mutually independent.

Between these ratios there will be a flowfield where the vertices of the two vortices come together. The flowfield for $L/D = 14$ corresponds well to figure 5.3 which was sketched from the shadowgraphs of McDearmon [56]. At the front lip there is an expansion fan turning the flow towards the cavity floor. Importantly the flow does not attach to the cavity floor. This result is evident from the skin-friction coefficients along the cavity floor (figure 5.13) and agrees with the observations of McDearmon. Rather than the flow attaching to the cavity floor it is deflected

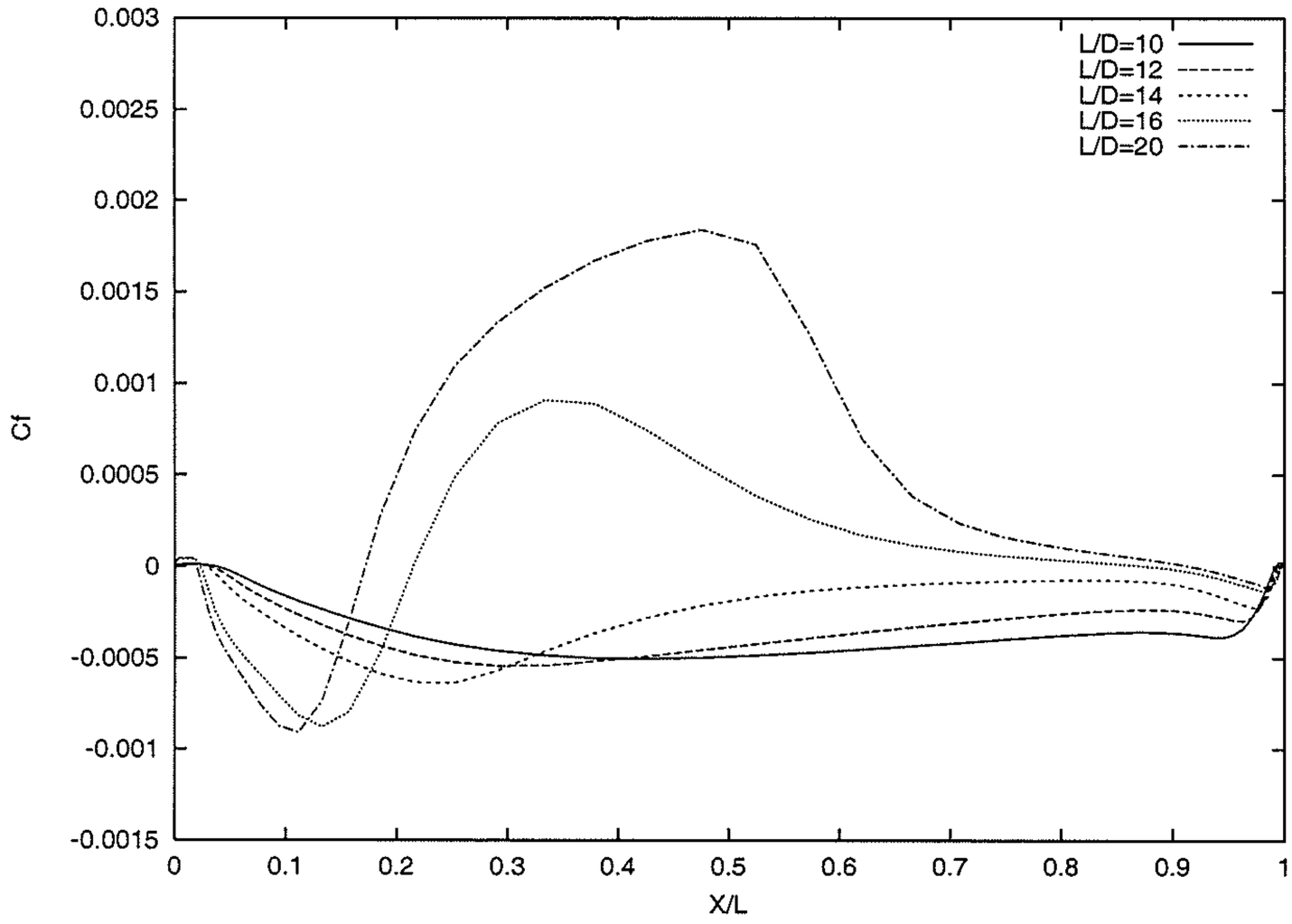

Figure 5.13: Skin Friction Distribution Along Cavity Floor: Mach 1.35

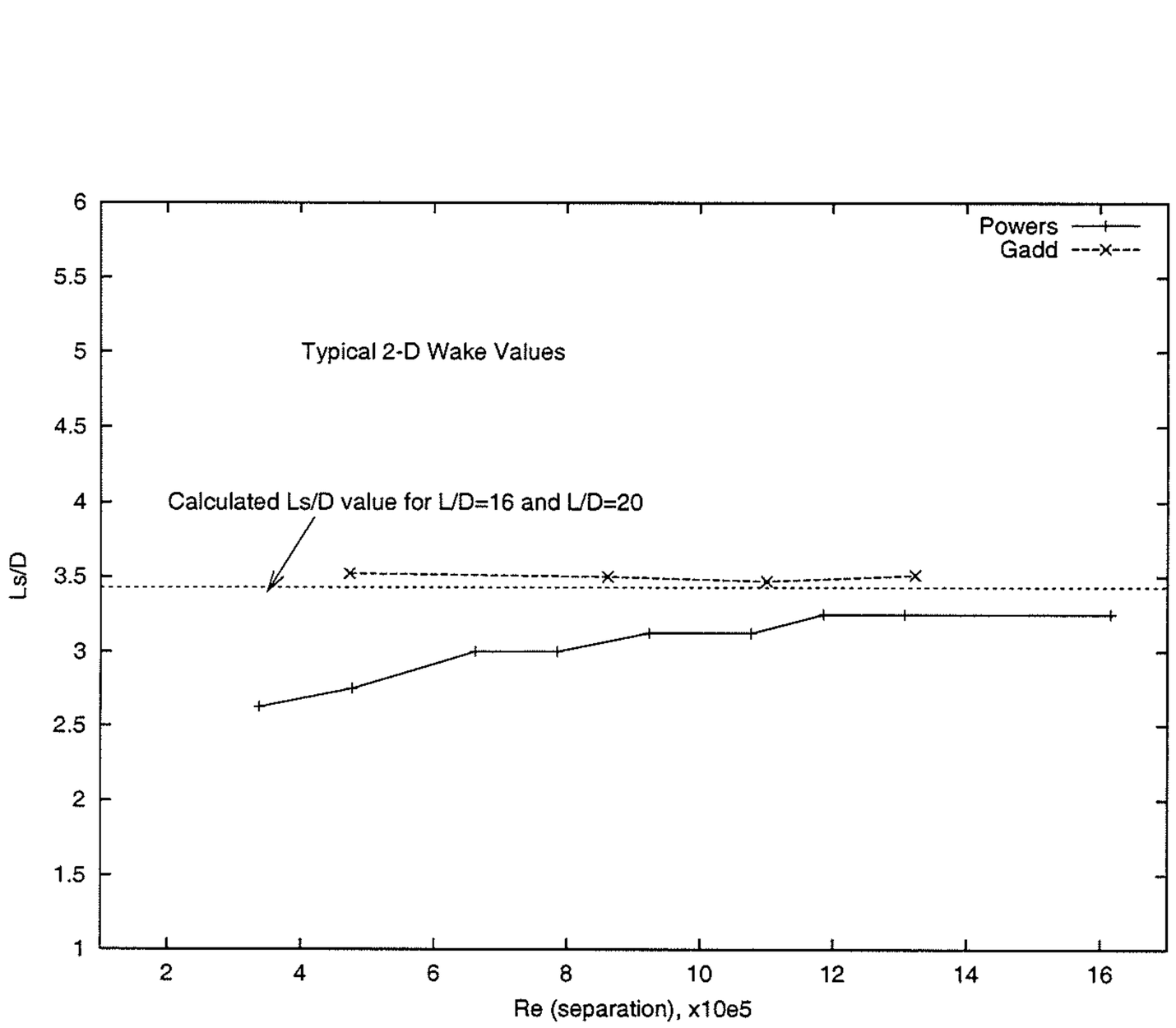

Figure 5.14: Length to Height Ratio of Separation Wake for Closed Flow

upward at approximately the same angle as the initial downward deflection. This is caused by the presence of a weak shock in the vicinity of the cavity centre. From the simulations L/D_{crit} occurs at approximately $L/D = 14$.

It is possible to analytically predict a value of L/D_{crit} by assuming supersonic flow over a 2D cavity [56]. The simplified model of the flow is shown in Appendix A Figure A.1. As the method considers Prandtl-Meyer expansions no account is taken of the boundary layer. The method and an example calculation for the prediction of L/D_{crit} is given in Appendix A. The variation of the predicted L/D_{crit} with upstream Mach number is shown in figure 5.15. For the present case of $M_0 = 1.35$ L/D_{crit} is predicted as 12.79. The discrepancy between this value and the one determined from the simulation ($L/D = 14$) can be explained since the Prandtl-Meyer expansions assume an abrupt turning of the flow as it enters the cavity, attaches to the floor and separates. In reality the turning motion is more gradual. Hence, the Prandtl-Meyer theory would be expected to under-predict the value of L/D_{crit}. McDearmon also found this when comparing his experimental results. Therefore the L/D_{crit} of 12.79 predicted by [56] compares very well to the $L/D_{crit} = 14$ from the simulations. Other L/D_{crit} values are shown for Mach numbers of 1.3, 1.4 and 1.5 and these too compare very well. They are seen to be almost an upward shift of the curve predicted by Prandtl-Meyer expansion theory.

Stallings [80] and McDearmon [56] both showed that as the L/D ratio was further decreased there would come a point where a series of compression wavelets form above the cavity. This represents transitional-open cavity flow. This type of flow is clearly seen in figures 5.11 and 5.12 for L/D ratios of 10 and 12 respectively. There is seen to be expansion of the flow into the cavity at the leading edge of the fore wall. The expansion is not as severe as at larger L/D ratios and the decrease in pressure is insufficient to allow flow attachment. The detached flow encounters a series of compression wavelets which gradually deflect the flow away from the cavity floor. A further expansion of the flow is encountered at the corner of the aft wall. The pressure contours in figures 5.11 and 5.12 agree well with the sketches reproduced in figure 5.4 obtained from Schlieren photographs.

In addition to capturing the flow trends exhibited experimentally the flow behaviour

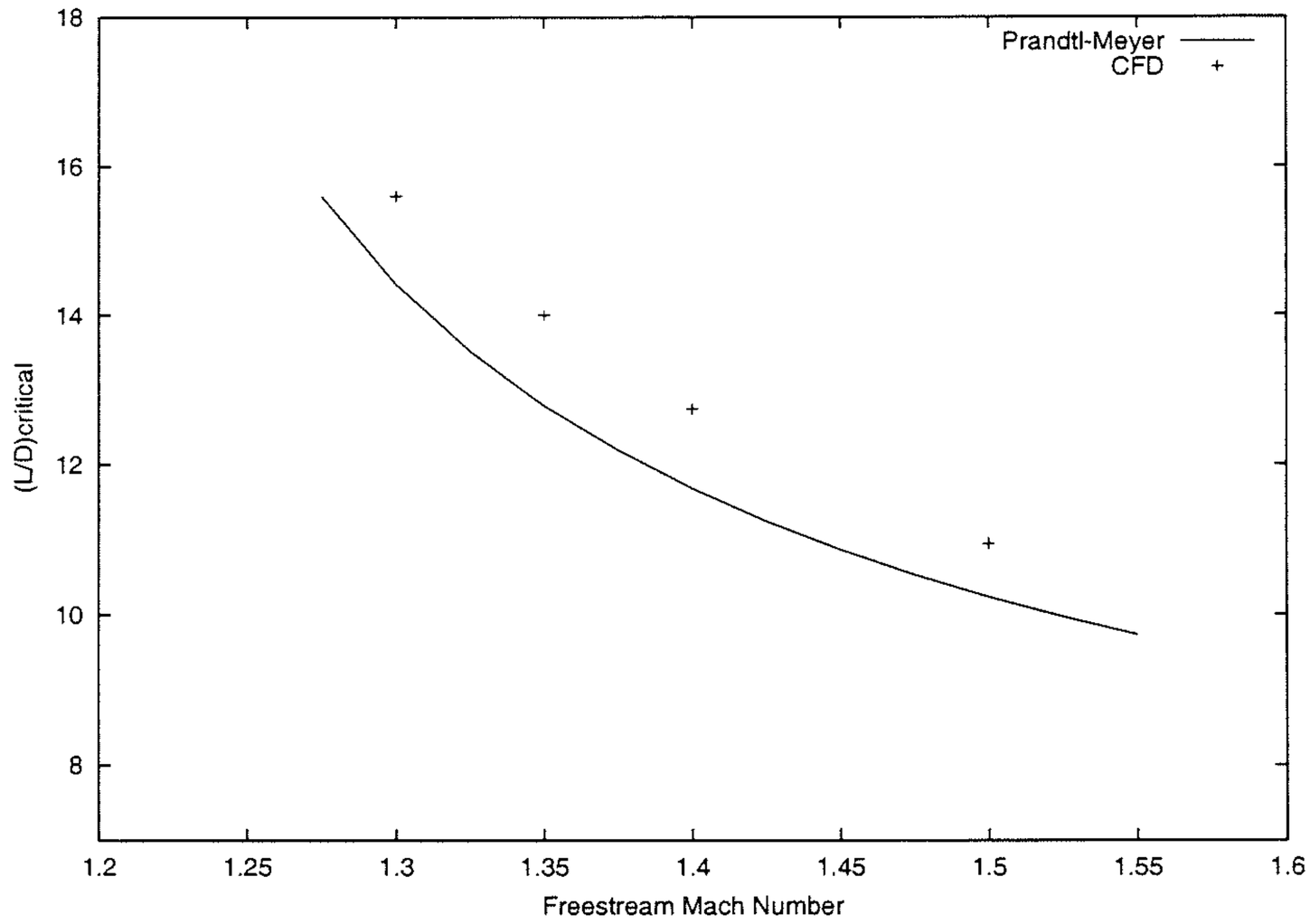

Figure 5.15: Prediction of (L/D)crit from Prandtl-Meyer Expansions

inside the cavity is evident. For transitional-open flow the flow is steady with two vortices resident in the cavity. The larger vortex, which lies under the separation wake, is seen to have a lobe which resides near the aft wall (essentially the recompression wake). The vortices do not oscillate in the cavity and so the flow is steady. This is a feature which has not been previously reported. When the L/D ratio is further descreased unsteady flow is obtained along the lines described in the chapter on open flow.

Chapter 6

Subsonic Transitional Cavity flows

6.1 Introduction

In the preceding chapters CFD has been used largely in conjunction with experimental results to reveal further features of cavity flows. While new ideas have been hypothesised care has been taken to compare them with the findings from previous research. In this chapter CFD will be used to advance the understanding of subsonic transitional cavity flows. A detailed literature review revealed that the flow features of subsonic transitional flow have not been mentioned despite a comprehensive experimental study revealing much about the flow characteristics [61]. It will also be shown that CFD can be used to highlight erroneous conclusions obtained from the experiments. An error in the conclusions derived from the experimental work will be highlighted.

In 1993 [61] Plentovich, Stallings and Tracey conducted one of the most comprehensive experimental investigations for subsonic and transonic cavity flows. These experiments were carried out to determine the characteristics of open, transitional and closed cavity flows. The location of the boundaries between these flow types received particular attention. Information about transitional cases at supersonic speeds was already available. However, at this time little was known about the subsonic case. Indeed, in 1992 [70] it was cited that a cavity with L/D=10 exhibited all the aerodynamic features associated with an aerodynamically shallow cavity. This

was at odds with the broad definition previously given, which would have defined this case as transitional. The continued development of aircraft requires that stores can be released over the entire flight envelope. The experiments, following on from the previous supersonic study [80], determined the flow characteristics at subsonic and transonic speeds and in particular defined the boundaries where cavity flow changes from open to transitional and from transitional to closed flow. It is worthwhile first to define the meaning of *flow characteristics* as used in the work of Plentovich et al. The flow was characterised by the static-pressure distributions obtained along the cavity floor. The pressure distributions that were used to classify the supersonic flow types are shown in figure 6.1. These were used as a reference in the subsequent classification of the subsonic flow types.

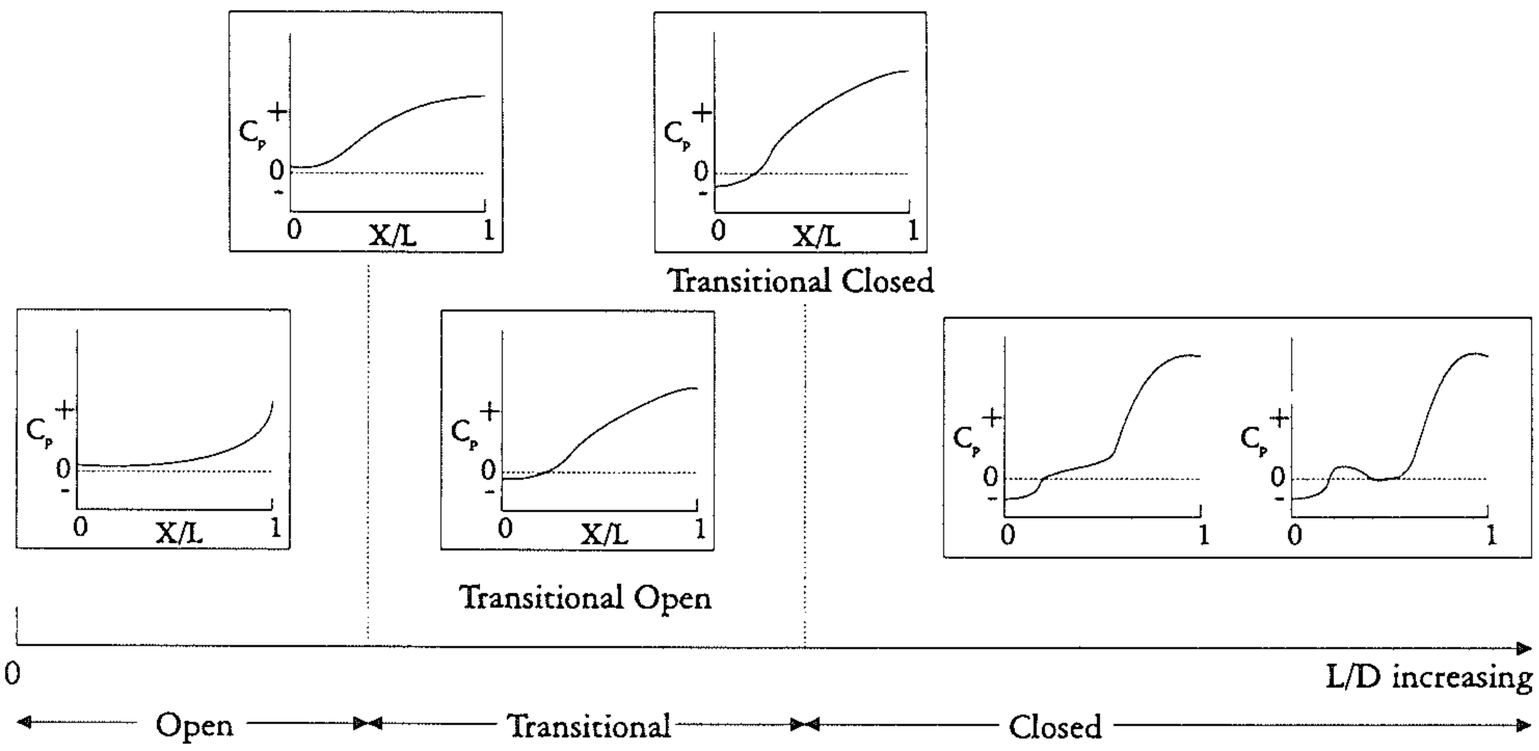

Figure 6.1: Measured Static Pressure Distribution for Supersonic Flow: Wilcox

For the supersonic investigation consideration was given to images of the flowfield, in addition to the static-pressure distributions. However for the subsonic and transonic investigation there was a lack of qualitative flow visualisation data. The Schlieren and vapour screen flow visualisation techniques used did not reveal any useful information. However Plentovich et al did obtain substantial information about the flowfields from the static-pressure results and these are discussed in the next section. In 1997 the unsteady pressure measurements [88] were presented by Tracy and Plentovich, though not with any significant discussion, to complete the data set. The current solutions will be used to provide insight into the flow features occurring for transitional cavity flows and also to enhance the existing knowledge of the flow

characteristics, as defined above.

6.1.1 Cavity floor pressure measurements

Plentovich conducted tests over a Mach number range of 0.2 to 0.95 at a unit Reynolds number of 3×10^6. The boundary layer approaching the cavity was turbulent. Length to depth ratios (L/D) of 1 to 17.5 for width to depth ratios of (W/D) of 1,4, 8 and 16 were investigated. Fluctuating and static pressure data in the cavity was obtained although it was the averaged static pressure data that was used when characterising the cavity flow. This was mainly due to the fact that in the previous supersonic investigation [80] the classification of the supersonic flowfields was made using the static pressure distributions. Typical pressure distributions are shown in figure 6.1 for supersonic flow. The acoustic fields for open and closed flow were known but were undetermined for transitional-open and transitional closed flow. This necessitated the use of the static pressure data to classify the flow types occurring and the characteristics of the supersonic flow types were used as a basis for comparison. For the subsonic regimes open, transitional, and closed cavity flow are found to occur.

Distributions measured from the experiments, representing these flow types, are shown in figure 6.2. The similarity to the supersonic distributions (shown in figure 6.1) is evident. Plentovich [61] gave an interpretation of the pressure distributions for defining the boundaries between open, transitional and closed flows at subsonic and transonic speeds:

- *Open Flow*

  C_p is uniform for $X/L \leq 0.6$ $(Cp \approx 0)$.

  At $X/L \geq 0.6$ the pressures increase with increasing X/L and the distribution has a *concave-up shape.*

- *Open/Transitional Flow Boundary*

  $C_p \approx 0$ over the forward portion of the cavity.

  The pressure distribution over the rearward portion of the cavity $(X/L \geq 0.6)$ changes from a *concave-up shape to a concave-down shape.*

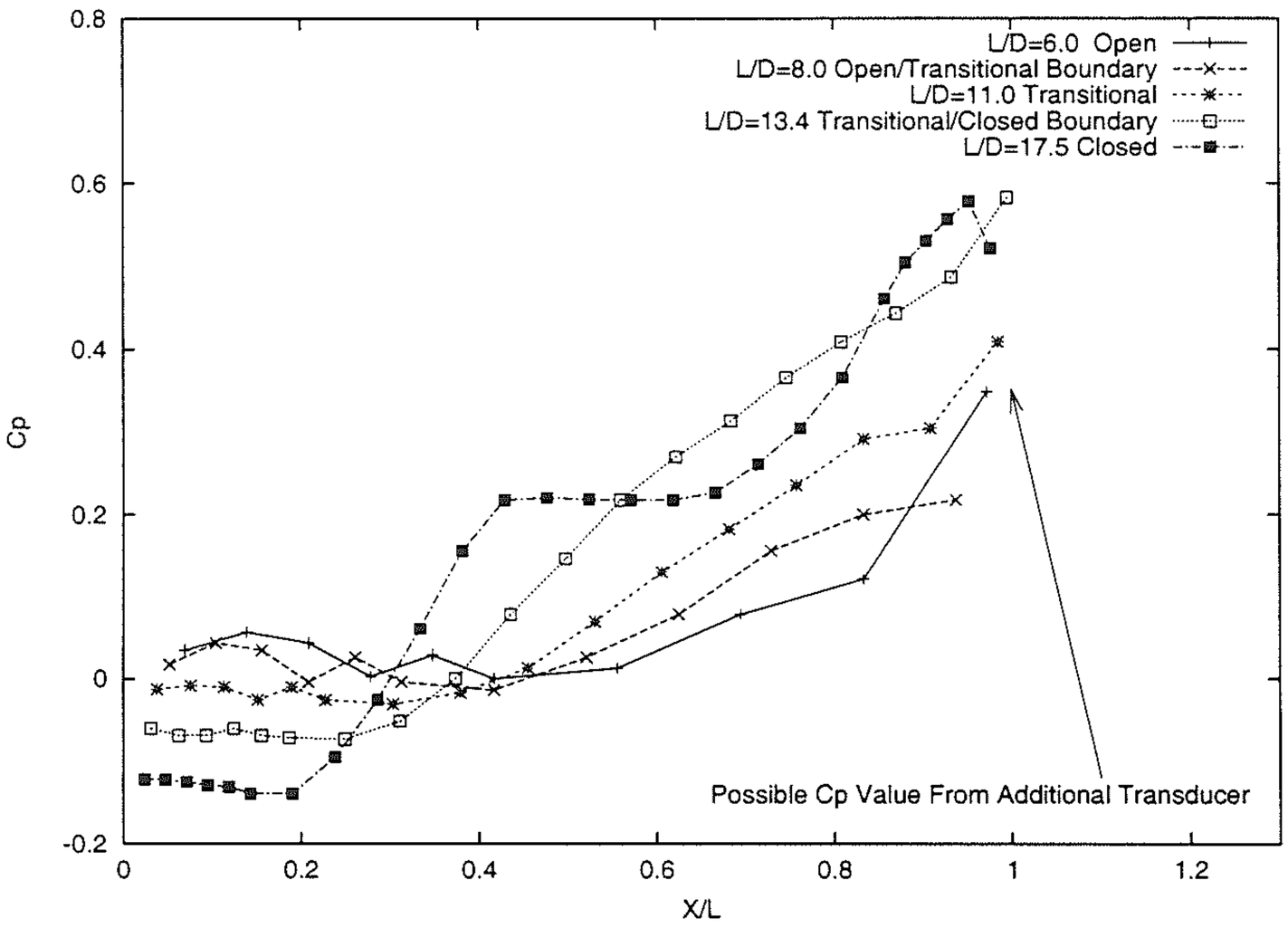

Figure 6.2: Measured Cavity Floor Distributions for each Flow Regime. M =0.95, taken from reference [61].

- *Transitional Flow*

  The C_p distribution increases gradually for $X/L \leq 0.6$.

  The pressure distribution from $X/L \geq 0.6$ is now concave-down.

- *Transitional/Closed Flow Boundary*

  Pressure coeffients increase uniformly from negative values in the vicinity of the front face to large positive values ahead of the rear face. The extreme values are of the same magnitude as those measured for closed cavity flow.

- *Closed Flow*

  The flow becomes closed when an inflection point occurs in the pressure distribution at $X/L \approx 0.5$.

  A further increase of the cavity L/D ratio causes the inflection point to form a plateau.

  A still further increase of the L/D ratio causes a decrease of pressure in the plateaued region.

  The maximum pressure at $X/L \approx 1$ is approximately the same value measured at the boundary of transitional flow.

It is important to note the way in which Plentovich characterises the cavity flows and the problems that may occur, as a result of experimental limitations, when analysing the results. In his analysis, Plentovich defines the boundary between open and transitional flow to occur when the *pressure distribution over the rearward portion of the cavity changes from a concave up shape to a concave down shape.* Investigation of the experimental data shows that the the measurement which determines the curve shape for $L/D = 8$ (Figures 6.2 and 6.3) is at $X/L = 0.9375$. It is possible that extra points closer to the rear wall would change the shape of the distribution and hence the classification. For example, a point at the location of the arrowhead in the figure makes the pressure distribution concave up. Employing the method of classification used by Plentovich et al this would indicate open flow rather than transitional. Figures 6.4 and 6.5 show that the last pressure transducer on the cavity floor for transitional flow is someway short of those for both open and closed flow. For both the transitional cases in the figures it is evident that a further point downstream could change the shape of the pressure distribution with the previously last value (now second last) effectively acting as an inflection point. Although Plentovich considers data for various widths and depths the conclusions relating to the classification tend to be the same. The data in figures 6.2, 6.4 and 6.5 is for $W/D = 4$. The length of the cavity is variable whilst the depth is 2.4 inches and the width 9.6 inches. With these numbers the reasons for the location of the pressure transducers and hence the analysis of the results can be seen. Figure 6.3 shows the location of selected pressure transducers from the experiment of Plentovich. The variable length of the cavity is shown for L=14.4, 19.2 and 26.4 inches, which gives L/D ratios of 6, 8 and 11, respectively (those corresponding to the data in figure 6.3). For L/D=6 the final transducer is at L=14 inches (X/L=0.97222) which is reasonably close to the cavity rear wall. However for L/D=8 the final transducer is at L=18 inches giving a location in terms of X/L of 0.9375. For L/D=11 the location is 26 inches which gives X/L=0.984848. It is therefore seen that the location of the transducer for the L/D=8 case does not allow direct comparisons to be made. It is clearly evident that the location of the pressure transducers close to the rear wall is critical in determining the characteristics of the flow. However this is also a limitation of the experimental setup used.

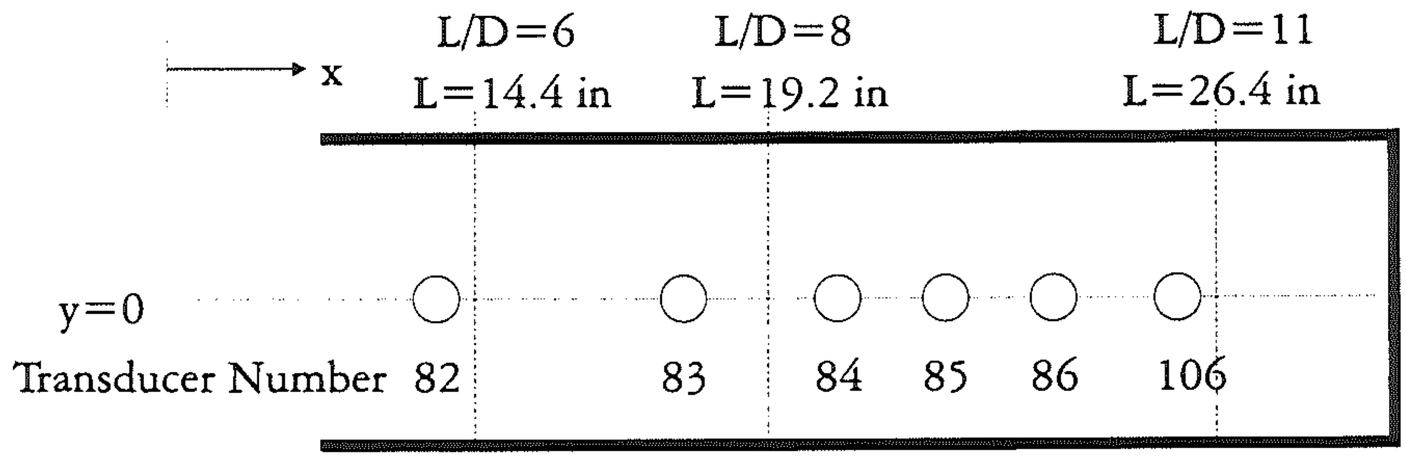

Transducer Number	Tansducer location (in)	X/L
82	14	0.97222 (L=14.4)
83	18	0.9375 (L=19.2)
84	20	
85	22	
86	24	
106	26	0.9848 (L=26.4)

Figure 6.3: Experimental setup of cavity and pressure transducers taken from reference [61].

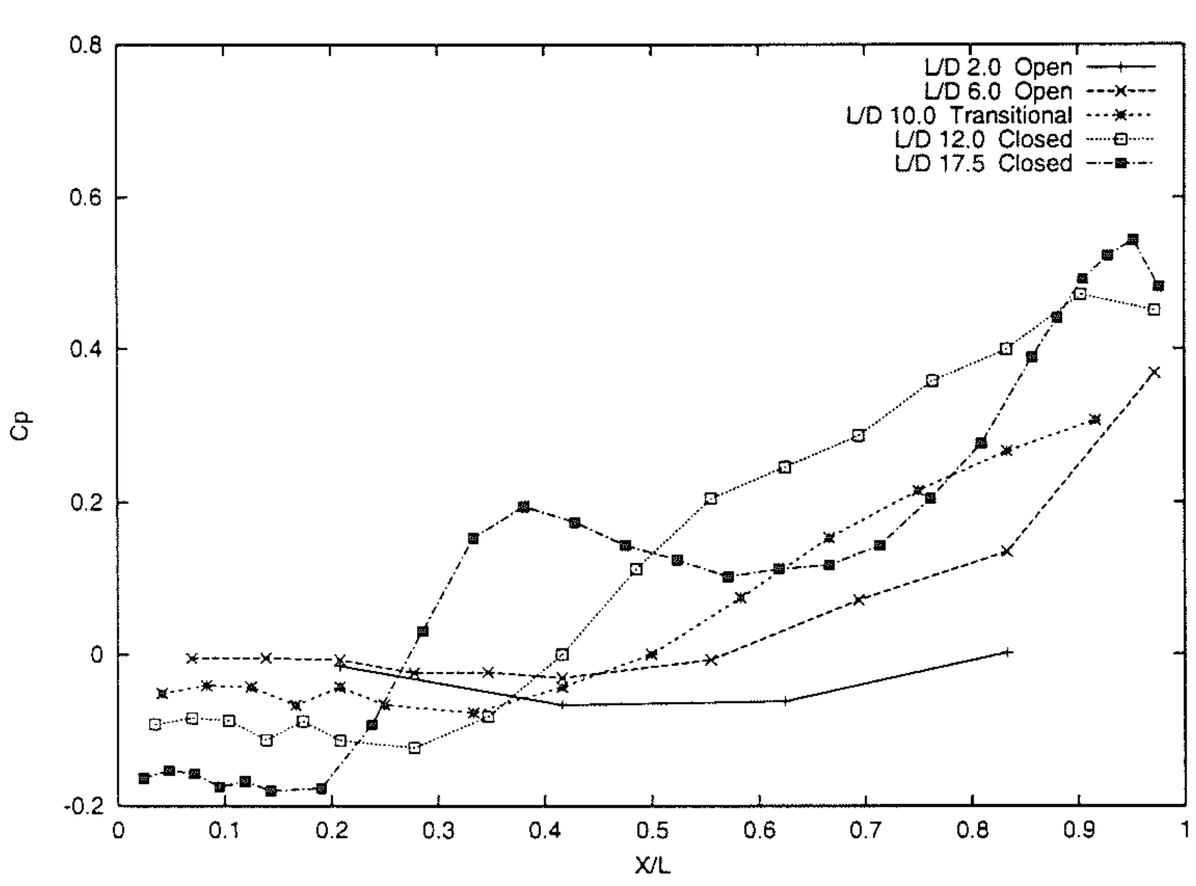

(a) Distribution along Cavity Floor

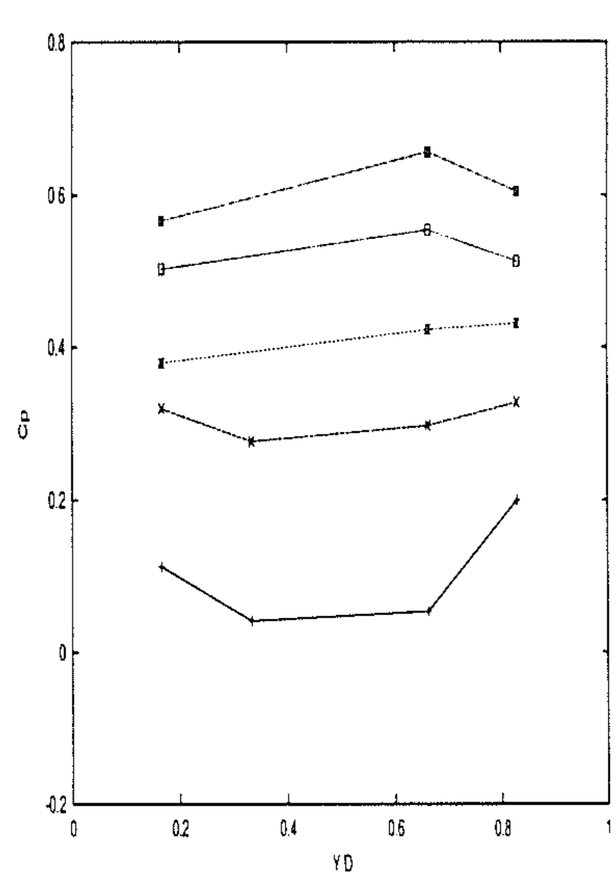

(b) Distribution along Aft Wall

Figure 6.4: Effect of variation in L/D ratio on pressure distribution, Mach 0.8, taken from reference [61]

Further investigation of figures 6.4 and 6.5 show that the pressures on the aft wall increase gradually as the L/D ratio of the cavity increases. The final value on the cavity floor should be close to the value at the bottom of the aft wall for all

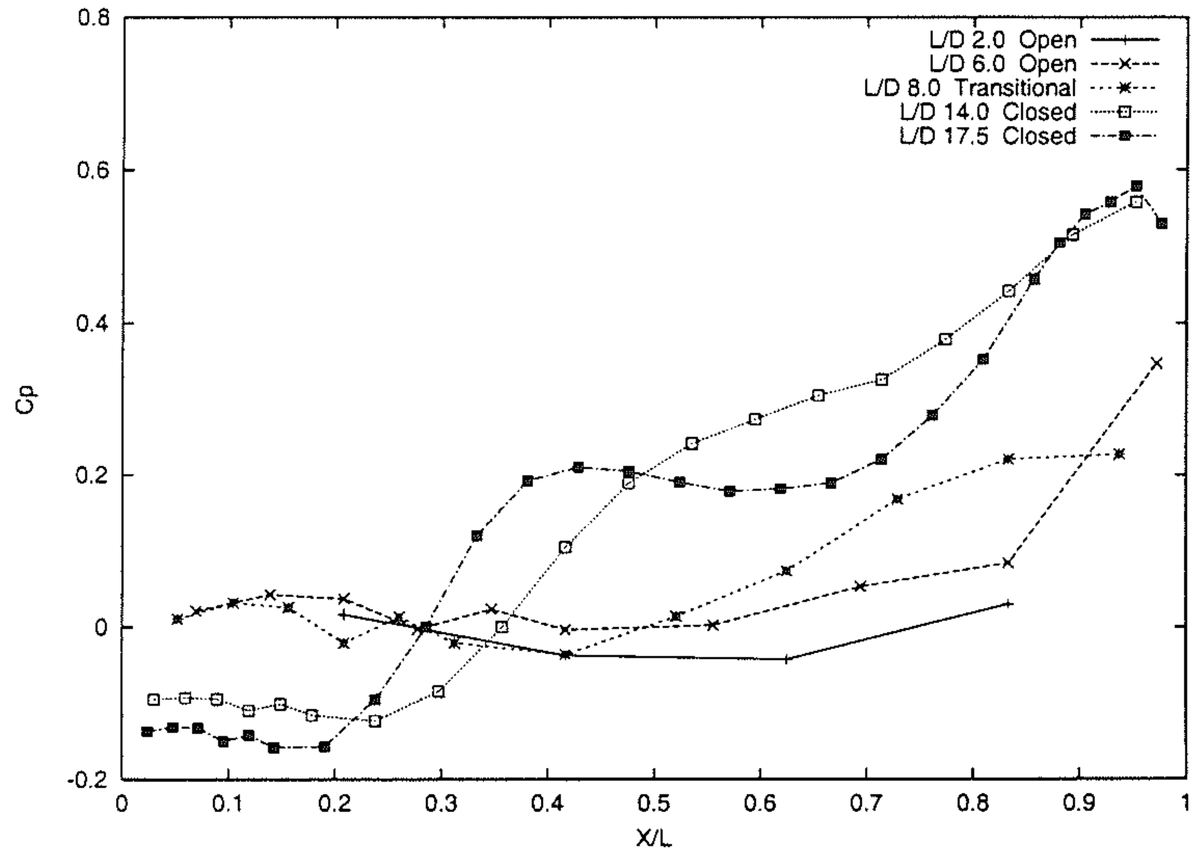

(a) Distribution along Cavity Floor

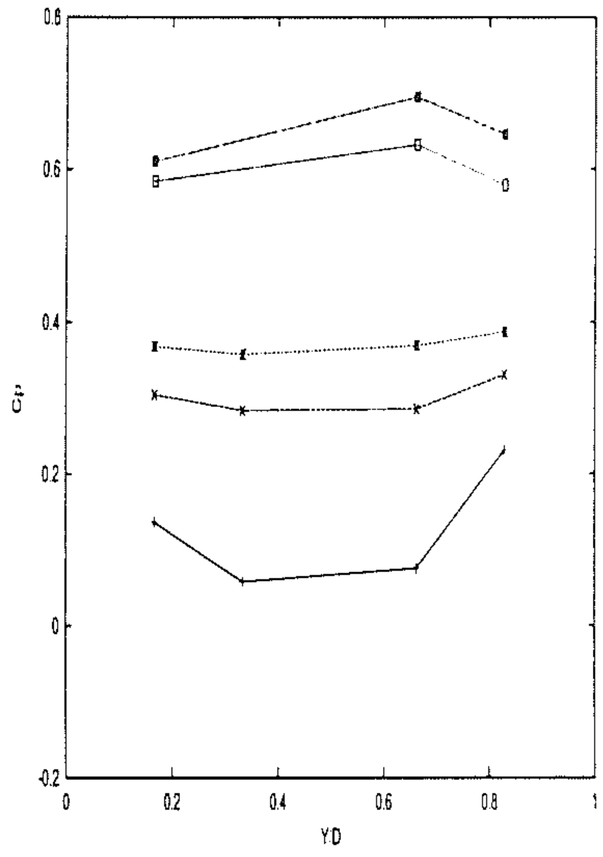

(b) Distribution along Aft Wall

Figure 6.5: Effect of variation in L/D ratio on pressure distribution, Mach 0.9, taken from reference [61]

flow types. This seems to be the case for most of the flows with the exception of transitional. The final pressure value on the floor of the cavity for transitional flow is less than for open flow. However the values on the aft wall are higher for transitional than for open flow. This would tend to suggest that more points on the floor of the cavity for transitional flow would show the final values to be higher. This would indeed change the shape of the distribution from concave down to concave up and so require redefinition of the method used by Plentovich to characterise subsonic cavity flow and frequently used as a benchmark by other investigators.

Plentovich noted that in some of the experimental test cases the *pressure distribution only approximately matched the generic distribution in figure 6.2 and that interpretation of the results was required.* Plentovich therefore stated that the boundaries presented could be estimated only. The fact that no qualitative flow visualisation data was available is cited as one of the reasons for this. The current work intends to address this issue by presenting a comprehensive analysis of the flow physics for transitional cavity flows based on the results of simulations.

6.1.2 Influence of Mach number and Cavity Width

The Mach number strongly influences the location of change from transitional to closed flow with L/D values between 9 and 15. For example, the change from transitional to closed flow occurred at L/D=9 for Mach 0.6 flow whereas it was at L/D=13 for Mach 0.9. From the data Plentovich was able to construct a diagram which approximately showed the boundaries for a range of Mach numbers. A similar diagram is sketched in figure 6.6. Plentovich plotted diagrams for W/D ratios of 8, 4 and 1. There was some variance in where the boundaries occurred but the trends for W/D ratios of 4 and 8 were quite similar. However, three dimensional effects did not seem to have a critical effect. Consideration of the effects of width and Mach number led to the conclusion that the onset of transitional flow occurs consistently for L/D in the range 7 to 9 and the value of the L/D ratio corresponding to closed cavity flow increases with increasing Mach number.

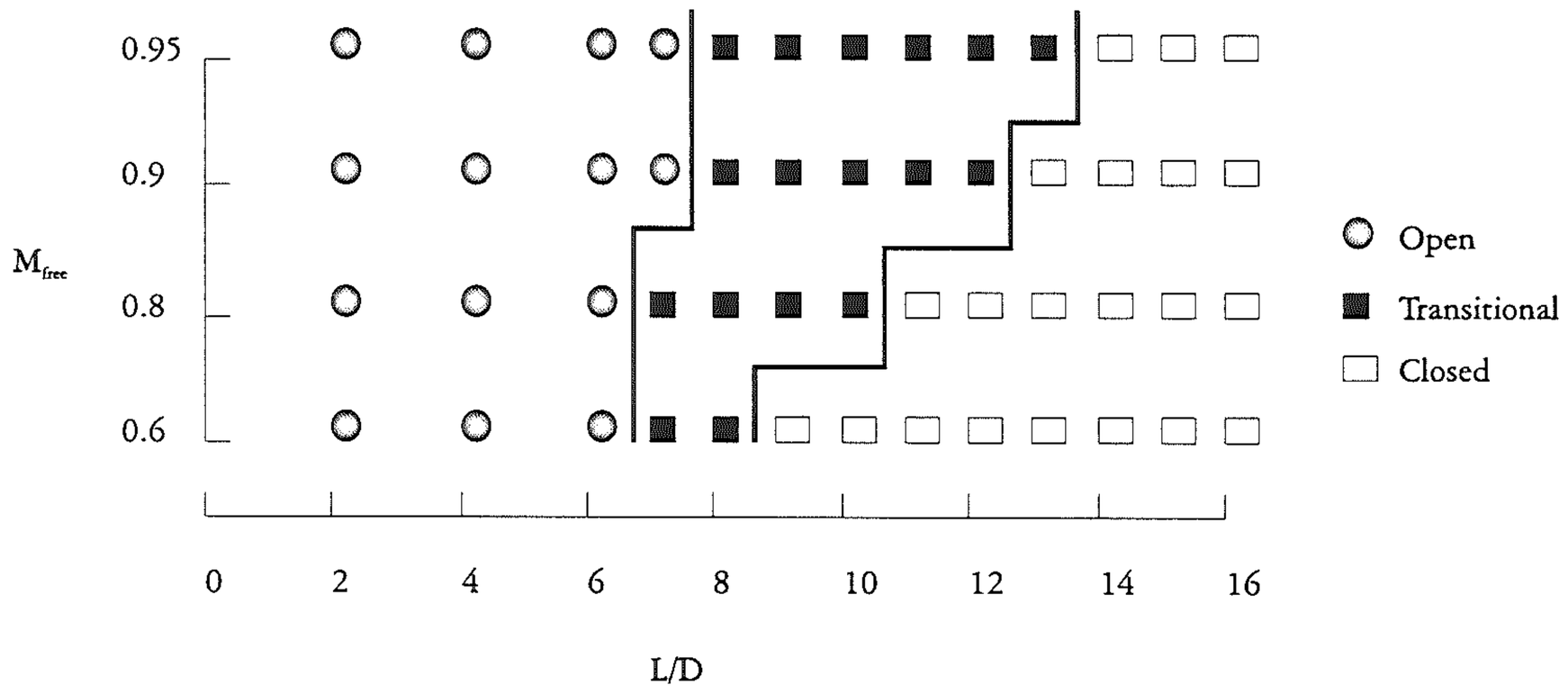

Figure 6.6: Boundaries between various flow types - Plentovich Experiment

6.1.3 Aft Wall Pressures

Plentovich's study revealed an interesting trend in the pressure distribution from data taken on the aft wall. Figures 6.4 and 6.5 show the aft wall pressure data where the Y/D value of 0 represents the bottom of the aft wall with Y/D = 1 representing the cavity edge. The data shows that for open flow the peak pressure measured on the aft cavity wall occurs at the pressure orifice located closest to

the cavity edge. As transitional cavity flow is approached it can be seen that the pressure measured at the penultimate orifice is close to that measured at the last. For closed cavity flow the peak pressure is found to occur at the penultimate orifice. The trend is for the *peak pressure to move from the cavity edge as the flow field changes from open to closed.* Plentovich assumed that this trend is associated with the *impingement point of the dividing streamline for the flow approaching the aft cavity wall.* This suggestion is illustrated in figures 6.7 and 6.8.

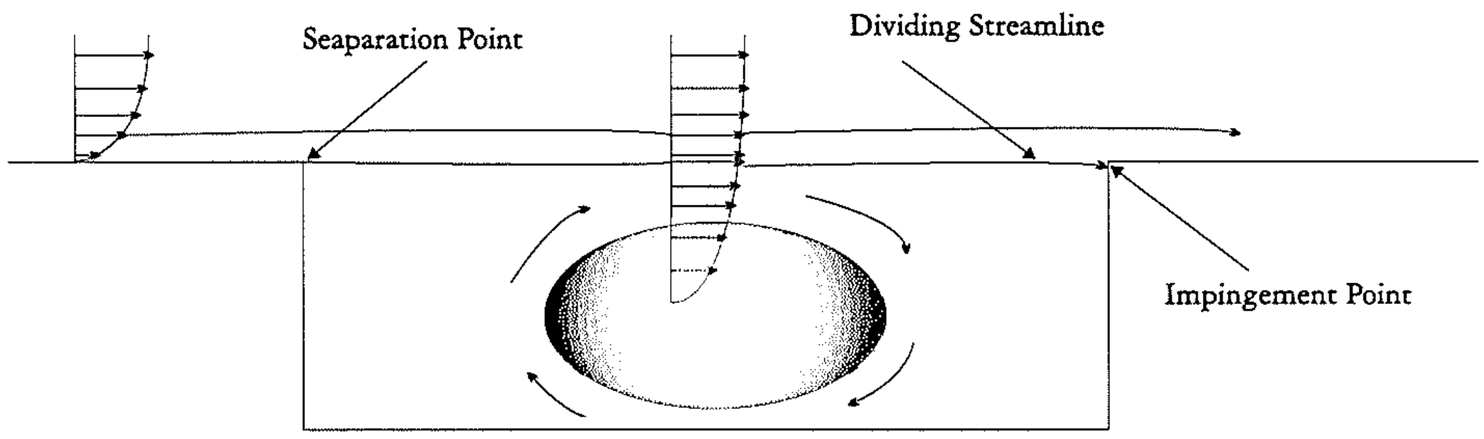

Figure 6.7: dividing Streamline Concept - Open Flow

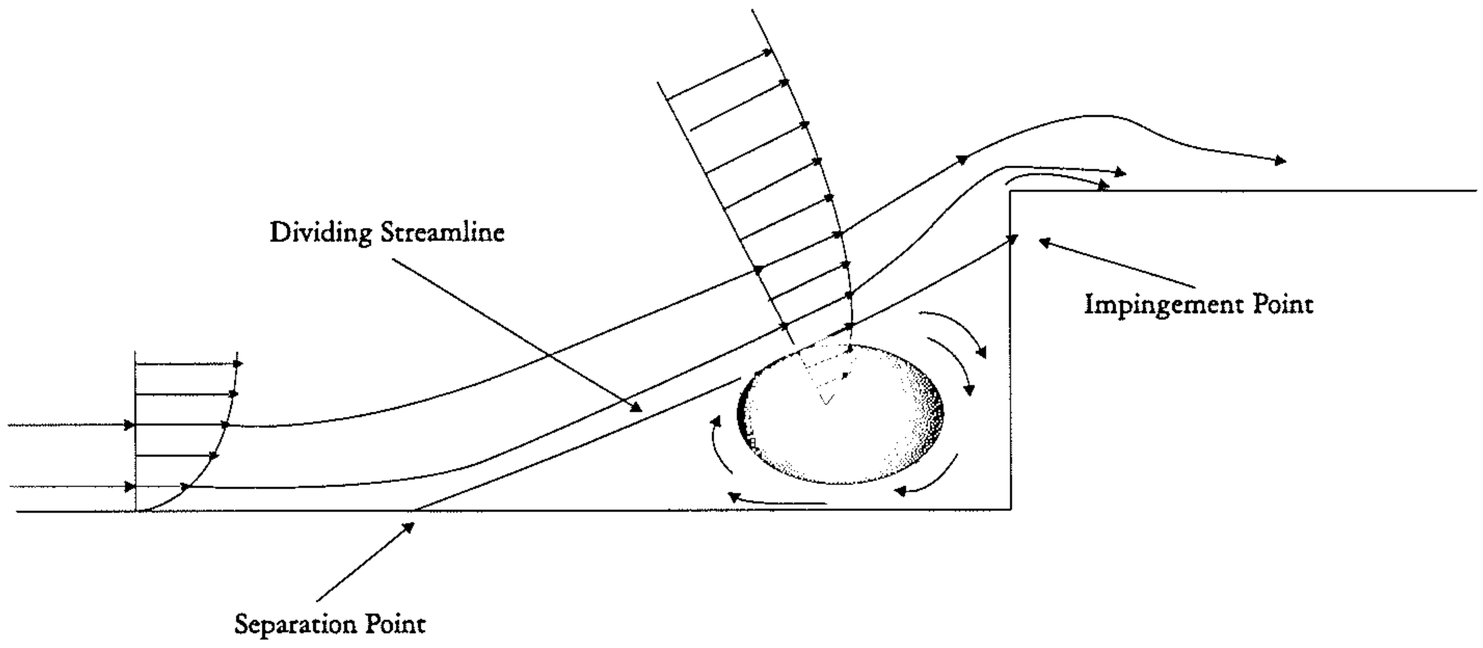

Figure 6.8: dividing Streamline Concept - Closed Flow

Open cavity flow is shown in figure 6.7 and indicates that the impingement point of the dividing streamline is close to the cavity edge. Obviously this is a simplified description of the flow given that previous chapters have show the shear layer to fluctuate. Nonetheless, the impingement point does not traverse too far down the aft wall. On the other hand, for the closed case, the flow separates from the cavity floor prior to impinging on the aft cavity wall. Hence, the impingement point for closed flow is much further down the cavity wall. This is shown in figure 6.8. As

transitional cavity flow will fluctuate between the flow-fields for the open and closed cases it is expected that the pressure trend will reflect this, as shown in figures 6.4 and 6.5. Plentovich believed that the pressure trends on the aft cavity wall could be used as an *indicator for defining the cavity flow field type occurring in the subsonic and transonic regimes.* Due to a lack of flow visualisation this work could only draw qualitative sketches. The present work intends to investigate the suggestions of Plentovich and determine the flow-fields for open, transitional and closed cavity flows.

6.2 Flow Characteristics

6.2.1 Test Cases

Two dimensional cavity flow simulations are presented in this section for subsonic and transonic speeds. The test cases selected represent an extension of previous simulations, given in chapter 3, performed for open cavity flow (L/D=5). A data base was built up covering a wide range of cavity configurations and conditions, as suggested by Ross [70]. The conditions for the calculations are shown in table 6.1.

	Mach Number	Re	L/D
Original Run	0.85	6.783e6	5
(A) Extension	0.85	As Above	4-16
(B) Validation [88]	0.9	4.96	8

Table 6.1: Summary of Test Cases

6.2.2 Floor pressure distributions

The pressure distributions along the cavity floor for Mach 0.85 flow are shown for L/D ratios of 4 to 16 in figure 6.9. The distributions cover the entire range of cavity flow from open to closed. Close inspection of the figure reveals the following trends;

1. For L/D=4 the flow is open. The C_p distribution is effectively uniform for $X/L \leq 0.6$. The pressure then decreases slightly before increasing to a maxi-

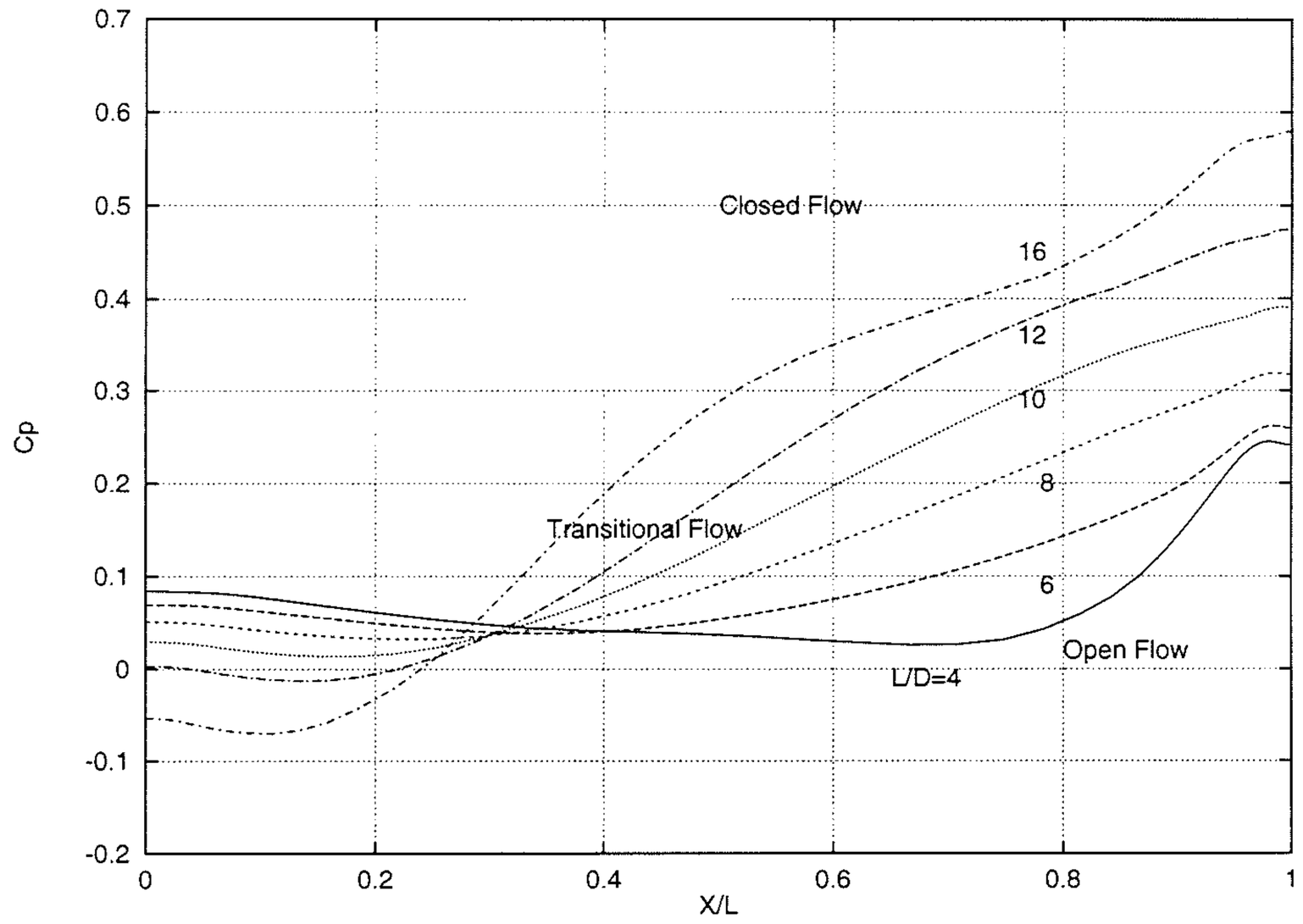

Figure 6.9: Variation of Mean Static Pressure Distribution Along Cavity Floor with L/D Ratio. CFD

mum at X/L=1 causing the existence of what Plentovich termed a concave-up shape. This seems ambiguous and relative to the following descriptions for transitional and closed flow will simply be referred to as concave.

2. As the L/D ratio increases the pressure at the front of the cavity gradually decreases. This effect is attributable to the flow expanding further into the cavity at the leading edge. With the flow turning more into the cavity the pressure at the aft of the cavity will also increase as is evident in figure 6.9. With the pressure gradient between the front and rear of the cavity increasing this has the effect of smoothing the concave shape associated with open flow. At L/D=6 the flow is still open though the concaveness of the distribution is less pronounced. At L/D=8 the curve is almost linear. This L/D ratio is well within the transitional bounds as classified by Plentovich and so it is reasonable to assume the present simulations are predicting a transitional flow. The difference in the flowfield will be discussed shortly.

3. A further increase in the L/D ratio causes the distribution to curve outwards.

The pressure distribution has a convex shape. The final distribution is shown for a closed cavity flow with L/D=16. Although a point of inflection or plateau region is not present the progression of the shapes that this would eventually occur.

Comparing these trends with those observed in the work of Plentovich, it is seen that they are very similar. The only real difference is in how the change from open to transitional cavity flow is interpreted. The influence of the location of pressure orifices in the experiments for the transitional could have influenced the interpretation of the results as discussed above. The computed pressure distributions show that for transitional flow the pressure at X/L=1.0 should be higher than that for open. This in turn causes a reduction of the concaveness of the pressure distribution as transitional flow is approached. Looking back at the experimental results of Plentovich (figure 6.2) it is seen that the characteristics of the pressure distributions are very similar. In the current work, at an L/D ratio of 8, the concaveness of the pressure distribution has been smoothed out to such an effect that it is almost linear. This effect is also seen at the other Mach numbers. Plentovich defined that for open flow the distribution would be concave up while for transitional flow the shape is concave down. In the present results, at the boundary of open and transitional flow, the distribution is neither concave nor convex.

6.2.3 Change from open to transitional flow

The time averaged pressure distribution for the L/D =8 Mach 0.85 case tested by DERA is almost identical to that of NASA test case, as shown in figure 6.10. The latter case will be used for the analysis of the flow features following the methodology previously applied to the open case. The trajectory of the vortex cores and pressure waves from the numerical computation for L/D=8 is shown in figure 6.11. The events are similar to those that occur in the open cavity, involving the interaction of vortices in the cavity as they feed off the leading edge vorticity before moving downstream in the cavity. Figures 6.14, 6.15 and 6.16 show the pressure contours, streamlines and

vorticity contours, respectively, for the L/D=8 cavity. Subtle differences from open cavity flow are evident. The intensity of the pressure oscillations for transitional flow, though still substantial, is reduced. Figure 6.12 shows the gradual reduction in the SPL on the cavity floor as L/D ratio increases. A notable trend is that at $X/L \approx 0.25$ the decrease in the SPL as L/D increases is quite substantial. Figure 6.11 indicates that this location is where a new vortex forms in the cycle and just downstream from this location is where the vortex encounters an upstream moving pressure wave.

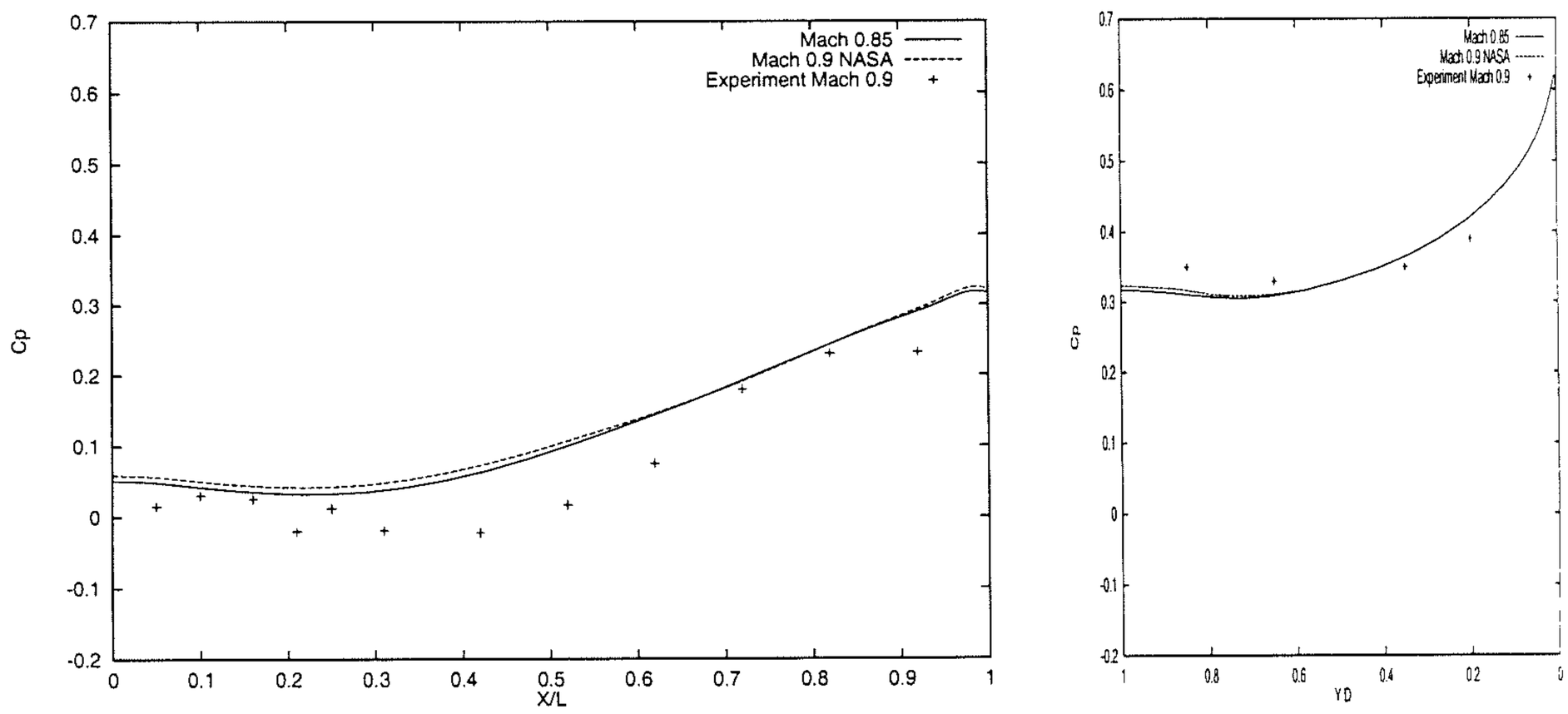

(a) Cavity Floor (b) Cavity Aft Wall

Figure 6.10: Comparison of Pressure Distribution for Transitional Cavity Flow, L/D=8

The pressure trace taken from the aft wall of the cavity is shown in figure 6.13 and, in accordance with figure 2.21, indicates that one mode is dominating. The flow is analysed between the non-dimensional times of 34.02 and 35.42, representing one complete period. At T=34.02 there are two vortices present in the cavity (figure 6.16(a)). The vortex that is at $X/L \approx 0.3$ has been formed recently, whilst the vortex further downstream is approaching the aft wall after feeding off vorticity that has convected downstream. The pressure trace is approaching a minimum signalling that the flow is at the end of the mass expulsion stage. A pressure wave that was formed at the mass addition stage has propagated upstream to a position X/L=0.45,

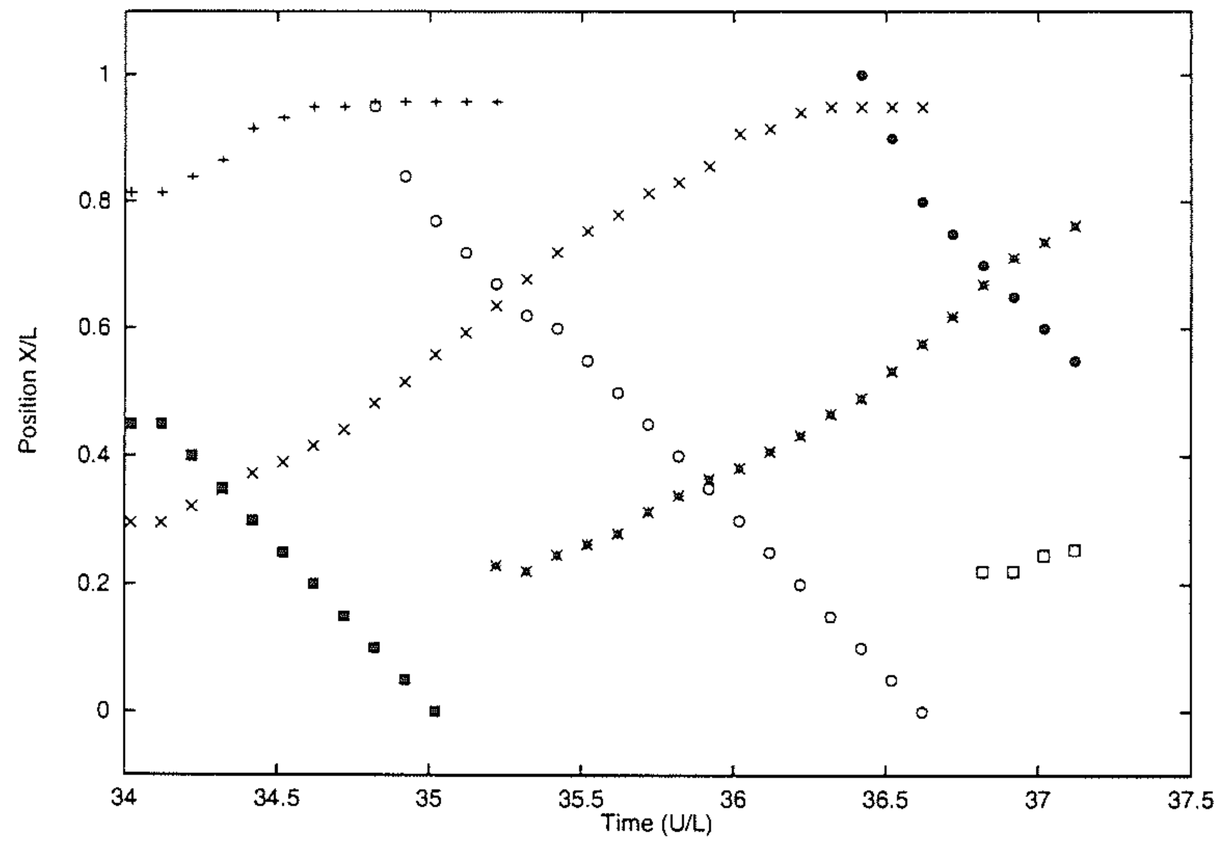

Figure 6.11: Horizontal Tracking of Vortices and Waves. Computation L/D=8

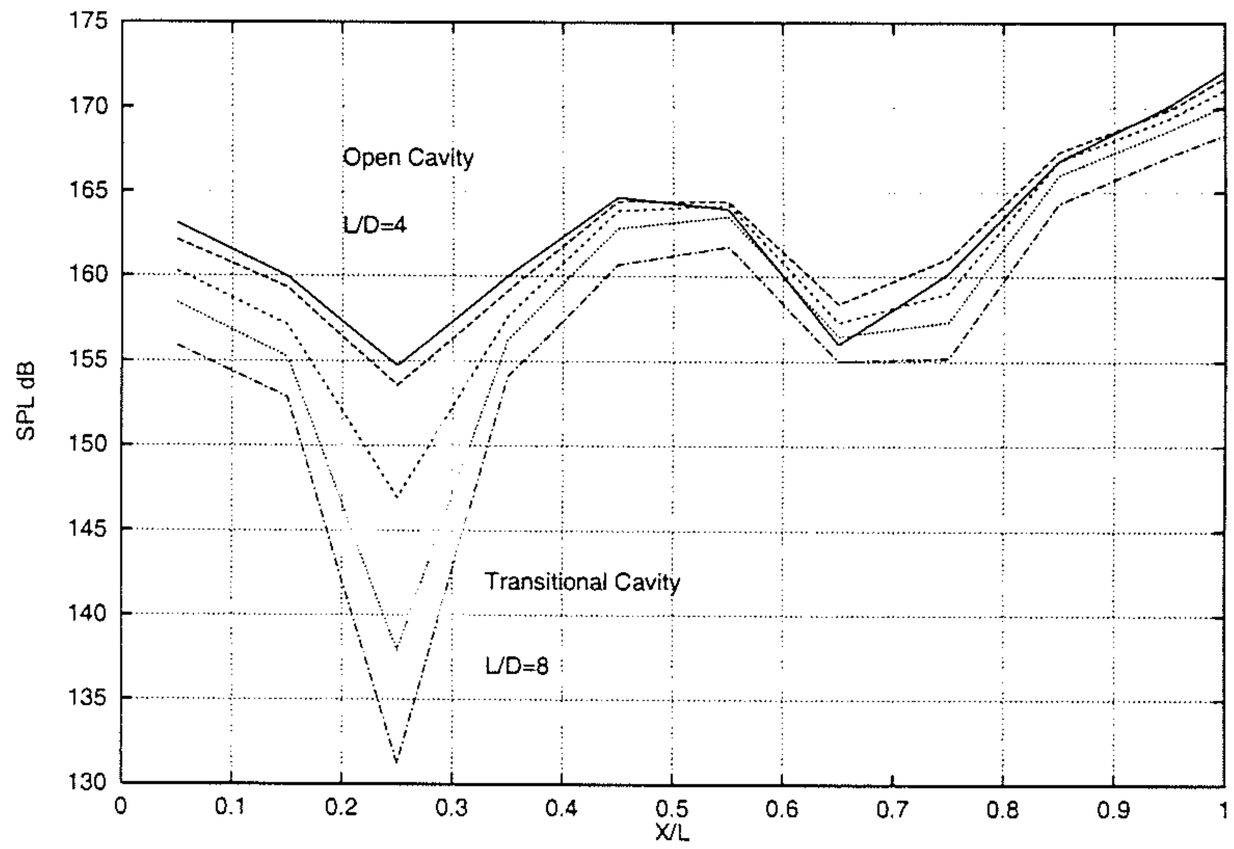

Figure 6.12: Variation of SPL along cavity with L/D ratio

as shown in figure 6.14 (a). The remains of a weaker pressure wave can be seen to be passing over the upstream edge of the cavity. Moving to the start of the mass addition stage ($T \approx 34.3$) it is seen, from figure 6.15 (c) at T=34.42, that the vorticity lobe previously present (figure 6.15 (a)) has apparently dissipated from the shear layer into the free stream. This lobe had formed from the downstream convection of vorticity from the leading edge. Looking at an entire cycle it is seen that the growth in vorticity from the leading edge and the subsequent lobe that is formed effectively controls the motion of the shear layer. The vorticity is strongest below the crest of

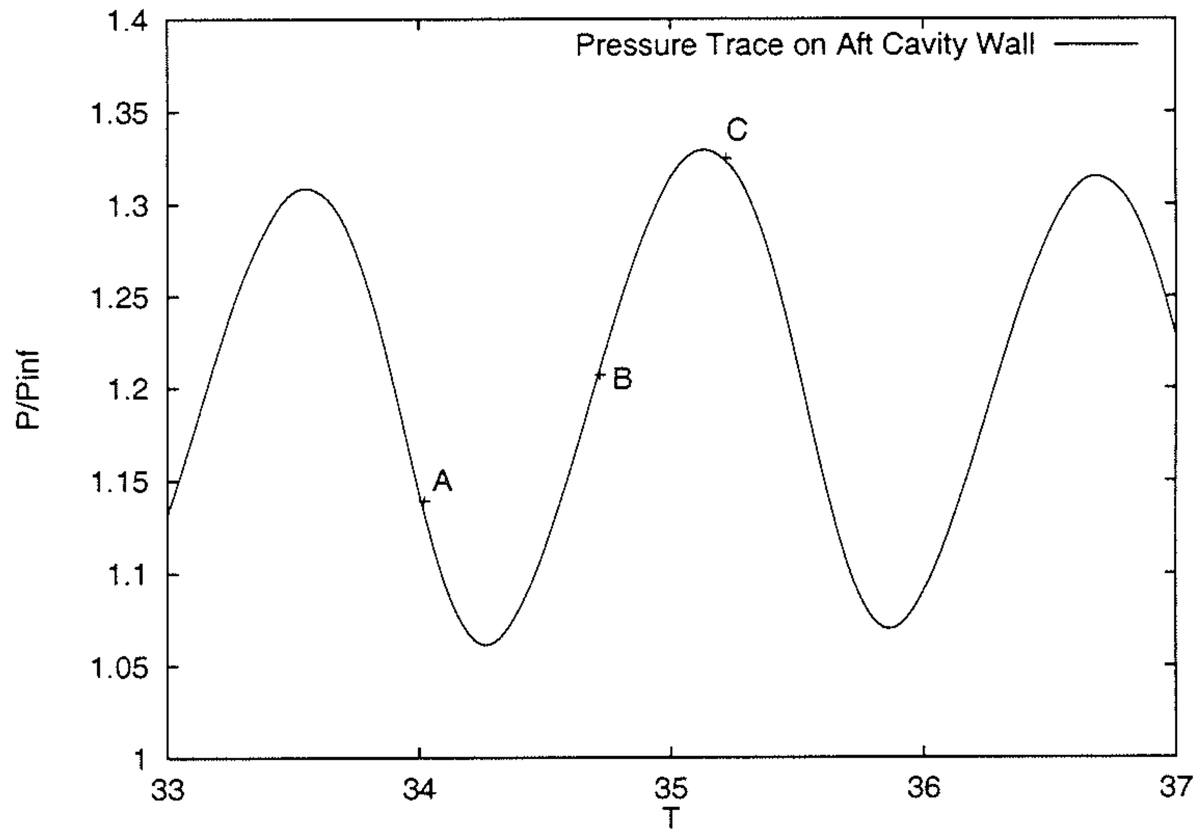

Figure 6.13: Pressure history on aft cavity wall, Mach 0.9 L/D=8

a shear layer wave while it is weakest between the troughs. In figure 6.15 (c) the vorticity is strong at $X/L \approx 0.45$ which can be seen to be to the front of the new vortex. While the vorticity is high here it is low further downstream where flow will now begin to enter the cavity. As it does so the trailing edge vortex, which has been weakened through the dissipation of vorticity, is pushed downwards in the cavity. The subsequent motion is similar to that witnessed for open cavity flow so will only be commented on briefly.

The vorticity is shown in figures 6.15 (c) to (e) representing the portion of the time trace from T=34.42 to T=34.82. The growth and downstream movement of the vorticity is clearly evident as it rides at the front of the shear layer crest driving flow into the cavity. The mass addition has forced the trailing edge vortex to the bottom of the cavity and it will soon be absorbed by the apporaching one. In addition to the inflow caused by the shear layer attaching to the rear wall a new pressure wave is formed, as can be seen in figure 6.14 (e), at the aft cavity wall. Meanwhile the previous pressure wave that has been propagating upstream is approaching the cavity leading edge. It is the pressure wave passing over the fore cavity wall that leads to the generation of further vorticity thus making the cycle self-sustaining. The pressure wave actually passes over the leading edge at T=35.02 as can be seen from figures 6.11 and 6.14(f). A growth in the vorticity can be seen to occur shortly

afterwards ($T = 35.22$ at $X/L \approx 0.3$, figure 6.15 (g)). This vorticity then forms a lobe similar to the one occurring further downstream at the same time ($T = 35.42$). The lobe then influences the movement of the shear layer thus closing the cycle.

Returning to the mass addition stage of the cycle the main difference between open and transitional flow becomes apparent when the streamlines in the cavity are considered. At $T = 34.82$ the weakened vortex at the trailing edge is soon to be absorbed. For open cavity flow the *absorbing* vortex is further downstream than it is here. The process of a new vortex forming at the leading edge from the elongation of the absorbing vortex for open cavity flow begins just as the trailing edge vortex is absorbed. For transitional cavity flow, because the cavity is longer, the formation of a new vortex begins sooner. The vortex is already substantially elongated towards the leading edge of the cavity in figure 6.16(f). By the time mass is being expelled from the cavity, T=35.22, there are effectively *three* vortices resident in the cavity. This does not occur for open cavity flow and is a feature that could be used to define transitional cavity flow. Eventually the weak trailing edge vortex is absorbed and the cycle is complete.

The time averaged flow field for a transitional cavity is shown in figure 6.17. The flow consists of a dominant vortex occupying the majority of the cavity with a lobe forming off it towards the aft cavity wall. Plentovich, while considering the location of the impingement point for the dividing streamline, suggested that the flowfield for transitional flow would be changing from open to closed flow. Strictly speaking this is not the case as it has been shown that transitional flow has unique characteristics. However the time averaged flowfield in figure 6.17 does show features common to both open and closed flow. For closed flow there is a separation and recompression wake and in figure 6.17 there is evidence of the initial formation of two vortices which would form such regions. However as the flow is not uniquely that representing closed cavity flow but has features of open flow, such as the elongation and downstream movement of the vortices, the separation and recompression regions (if they existed) are drawn together. This forms a dominant vortex with a lobe. Transitional flow is therefore a hybrid of open and closed cavity flow.

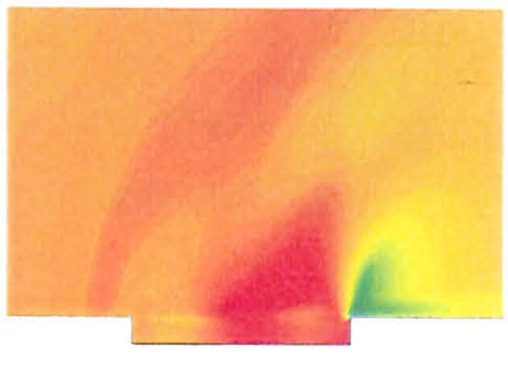

(a) Time=34.02

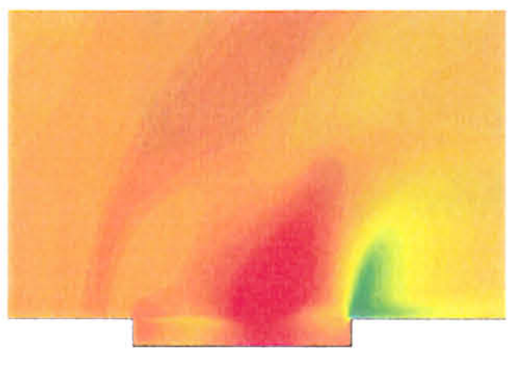

(b) Time=34.22

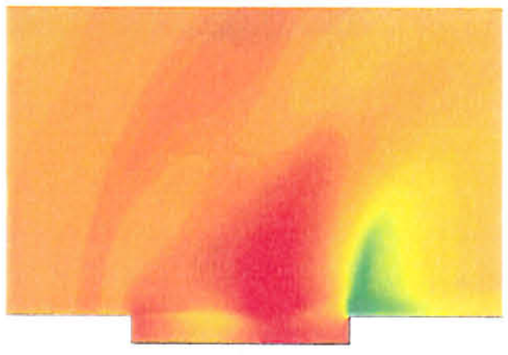

(c) Time=34.42

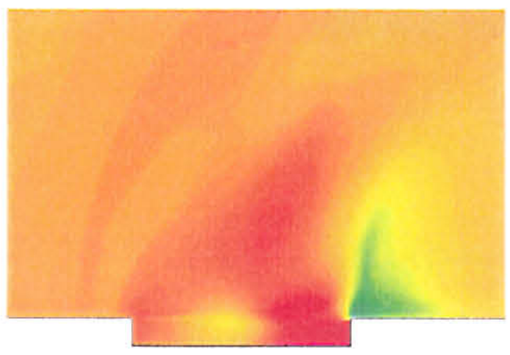

(d) Time=34.62

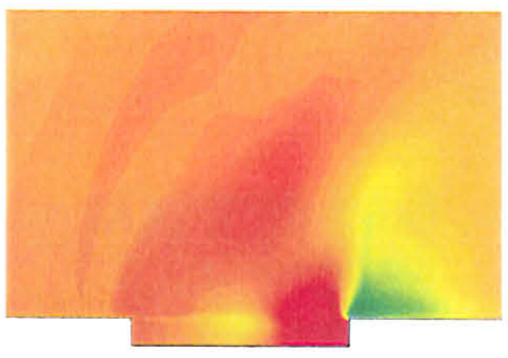

(e) Time=34.82

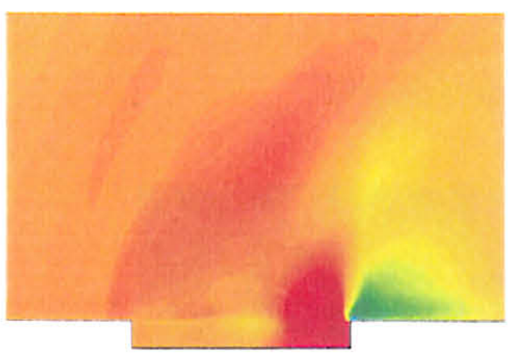

(f) Time=35.02

(g) Time=35.22

(h) Time=35.42

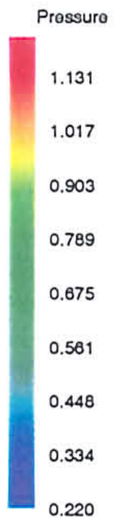

Figure 6.14: Pressure Contours for Mach 0.85, L/D=8

(a) Time=34.02

(b) Time=34.22

(c) Time=34.42

(d) Time=34.62

(e) Time=34.82

(f) Time=35.02

(g) Time=35.22

(h) Time=35.42

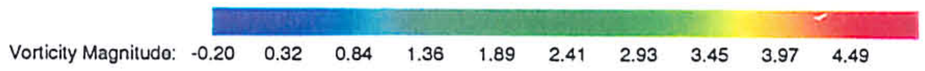

Figure 6.15: Vorticity Contours for Mach 0.85, L/D=8

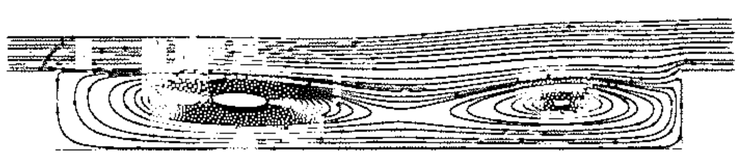

(a) Time=34.02

(b) Time=34.22

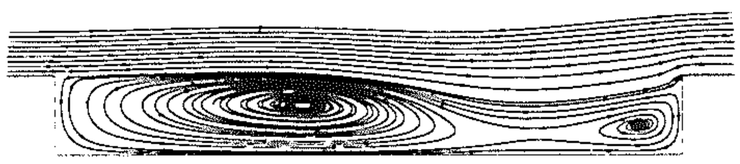

(c) Time=34.42

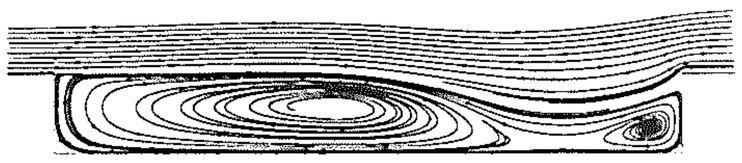

(d) Time=34.62

(e) Time=34.82

(f) Time=35.02

(g) Time=35.22

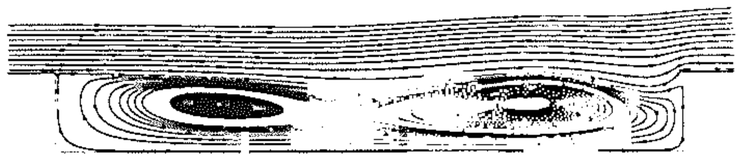

(h) Time=35.42

Figure 6.16: Streamlines for Mach 0.85, L/D=8

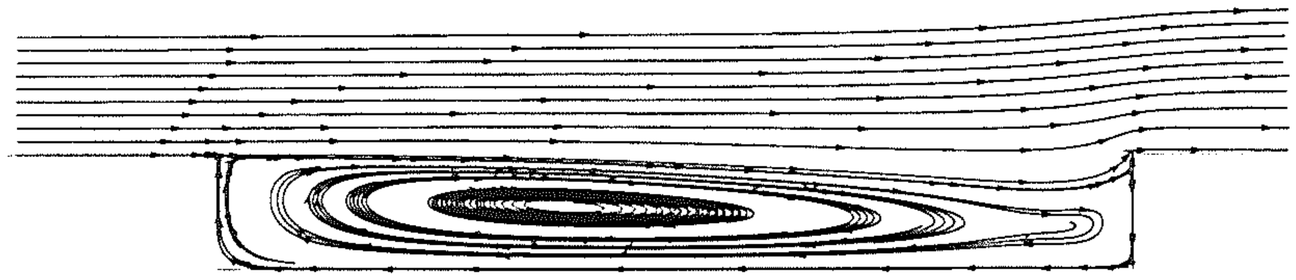

Figure 6.17: Time Averaged Streamline Contours: L/D=8 Mach=0.9

6.2.4 Transitional to Closed Flow

It is more difficult to define the boundary between transitional and closed flow by looking at the pressure distribution along the floor alone. Plentovich defined closed flow to occur *when an inflection occurs in the pressure distribution at X/L* ≈ 0.5. Looking at the present results for Mach 0.85 (shown in figure 6.9) this would suggest that closed flow does not occur until X/L=16. However the flow features suggest the change happens for lower values of L/D. For a cavity of L/D=12 the present simulation converges to a steady state. The results show the flowfield to be that of a closed cavity flow. This is shown in figure 6.18 and can be seen to be essentially the flow over a downstream facing step and ahead of an upstream facing step. The distinctive separation and recompression wakes associated with such a flow are clearly evident. The boundary between transitional and closed flow, shown in figure 6.6, occurs at $12 \leq L/D \leq 13$ for Mach 0.9, whilst it occurs at $10 \leq L/D \leq 11$ for Mach 0.8. These values are derived by considering the shape of the pressure distributions on the cavity floor, as discussed previously. The boundary for Mach 0.85 flow is consistent with these values. However, the pressure distribution for L/D=12 in figure 6.9 is remarkably similar to the distribution for a L/D=12 cavity from the study of Plentovich, and shown in figure 6.4. this tends to suggest that more than just the pressure distribution along the cavity floor should be considered in the classification of cavity flow types.

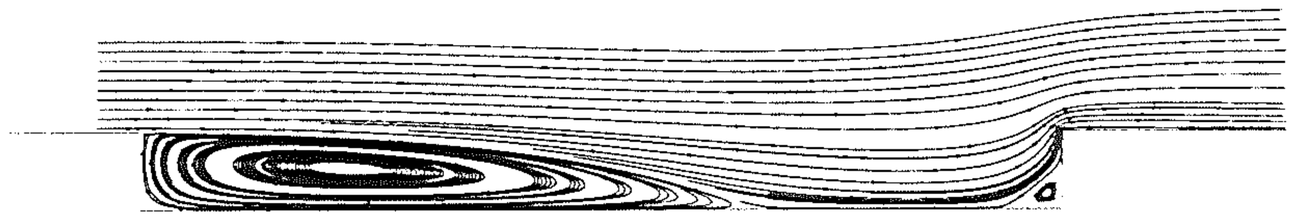

Figure 6.18: Streamline Contours: L/D=12, Mach=0.85

6.2.5 Aft Cavity Wall Pressure Distributions

Plentovich suggested that the aft wall pressure distributions could be used as an indicator for defining the cavity flow field types in the subsonic and transonic speed regimes. The time average pressure distributions are shown in figure 6.19 on the cavity aft wall for L/D ratios of 4 to 16. The class of flow was determined by consideration of the cavity pressure distributions along the cavity floor as well as the flow features. The current section investigates how the behaviour of the pressure distribution on the aft wall varies with L/D ratio and in particular the variation in the pressure distribution close to the top of the aft wall. In the work of Plentovich [61] important features reported concerning the cavity aft wall pressures for the three types of flow are as follows:

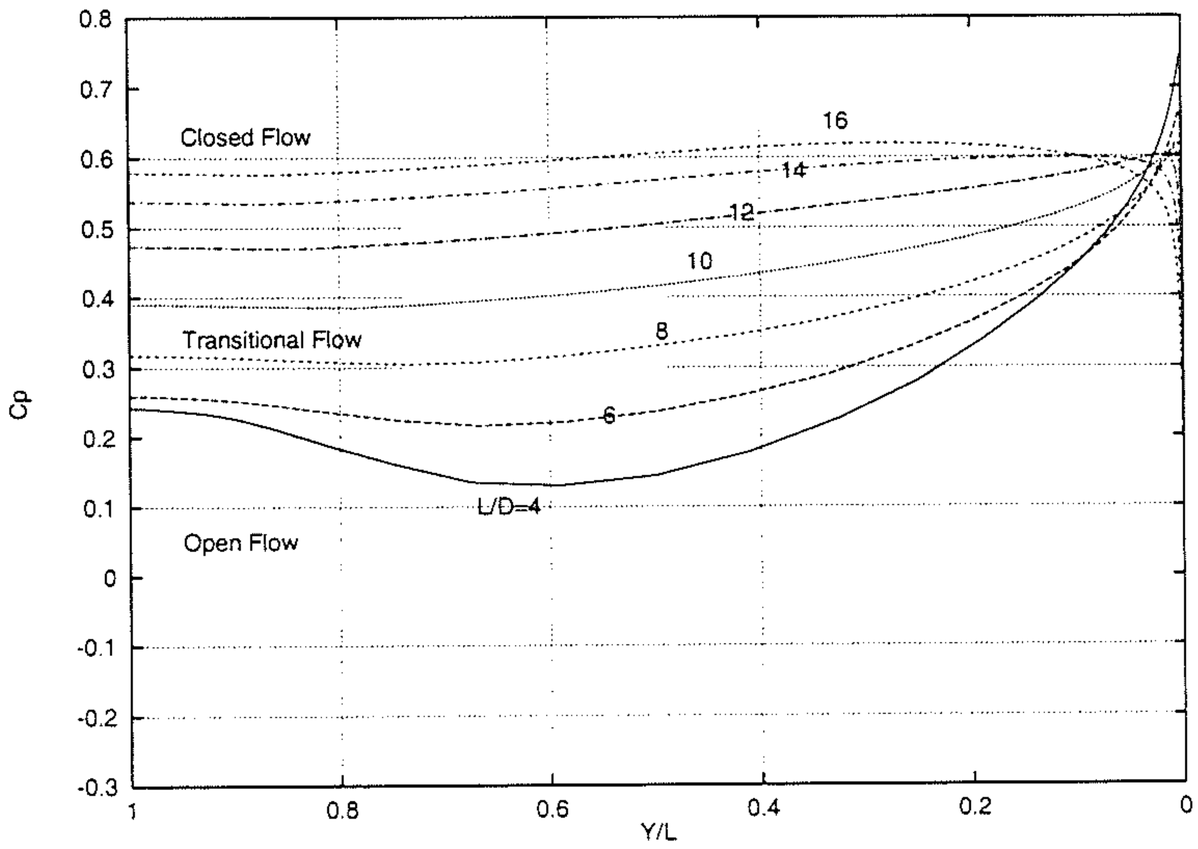

Figure 6.19: Variation of Mean Static Pressure Distribution Along Aft Wall with L/D ratio, Mach = 0.85. CFD

1. For open cavity flow, the peak pressure on the aft cavity wall occurs nearest

the edge of the cavity (Y/D = 0)

2. The peak pressure for closed cavity flow occurs a certain distance away from the top edge.

3. The peak pressure for the transitional cavity flow is relocated from the cavity edge (open flow characteristic) to a distance just off the top of the aft wall (similar to closed flow). It should be noted that this trend was not consistently exhibited, especially for wider cavities.

It is worth remembering that there were only 4 pressure orifices on the aft wall to record the static pressures. The present simulation has 51 points along the aft wall, which will provide a more detailed picture of the pressure distribution on the aft wall. The trends from the present simulations are now considered for the three types of cavity flow thought to exist at subsonic speeds. In figure 6.19 Y/D=1 corresponds to the cavity floor, whilst Y/D=0 represents the top of the cavity. For the three classes of flow the results of the simulation show:

1. For open cavity flow the pressure distribution on the aft wall is of a similar pattern to that along the cavity floor. Figure 6.19 shows that the time-averaged pressure decreases slightly into a valley forming a concave shape. As the top of the cavity wall is approached the pressure increases significantly, peaking at a value which is 3 times higher than the pressure at the bottom of the aft wall. The peak pressure is therefore nearest the edge of the cavity.

2. As transitional flow is approached (L/D 8 to 12) the concaveness in the pressure distribution occurring for open flow is gradually smoothed. This is caused by the pressure increasing at the bottom of the aft wall due to more of the freestream flow expanding into the cavity. Close inspection of the Cp value at the cavity edge (Y/D=0) reveals that the peak pressure is a short distance inside the cavity. This was suggested by Plentovich [61]. However, it was not previously reported (due to limitations in the number of measurement points) that the peak pressure is actually lower than that for open flow.

3. For closed cavity flow the Cp values further increase towards the bottom of the aft wall which is due to the flow fully expanding into the cavity. The time-

averaged pressure distribution is reasonably constant near the bottom of the aft cavity wall, rising moderately to a peak pressure some 20 percent before the cavity edge. The pressure then decreases slightly before dropping significantly near the cavity edge. Plentovich [61] showed the pressure to decrease after the peak pressure for closed cavity flow. However, again because of the lack of static pressure probes, it was not shown to what extent. The trend for increasing L/D ratio shows the pressure distribution changing from a concave shape to a convex one.

The pressure distributions only allow for a limited analysis of the flow to be performed, however by presenting the same data in a different format the understanding of the flow can be greatly enhanced. Figures 6.20 and 6.21 show the maximum time averaged C_p and its location along the aft wall, respectively, as the L/D ratio of the cavity is increased. Figure 6.20 indicates that as the L/D ratio of the cavity increases the maximum value of pressure occurring on the aft wall decreases. Figure 6.21 re-iterates the trend suggested by Plentovich and shown in the points above; as the L/D ratio of the cavity increase the location of the peak pressure moves further away from the cavity edge. It was inferred [61] that the peak pressure on the cavity aft wall is associated with the impingement point of the dividing streamline and figures 6.20 and 6.21 to help explain why. For open cavity flow the shear layer fluctuates at the trailing edge as mass addition and expulsion occurs. For open cavity flow the net effect on the time average of the flow is a slight expansion of flow *into* the cavity. The dividing streamline therefore occurs a slight distance into the cavity and the pressure will be closer to the freestream value. As the L/D ratio of the cavity increases the flow is more freely able to expand into the cavity at the leading edge. This has the effect of moving the impingement point of the dividing streamline further down the aft cavity wall. Figure 6.22 shows the time averaged streamlines at the aft wall for the L/D=8 transitional cavity. It can be seen that the dividing streamline impinges on the aft wall, as the flow is *leaving* the cavity. In addition the curvature of the streamline is greater that for open flow and so the pressure is lower. As closed cavity flow is approached the flow ultimately impinges on the cavity floor, shown in figure 6.18, before separating prior to the aft wall with the impingement point of the dividing streamline moving further down the aft cavity wall. However

an interesting feature from figure 6.20 indicates that there comes a point when the pressure stops decreasing and actually begins to increase again. In the present calculations this occurs from L/D=14. Figure 6.18 shows the streamlines within the L/D=12 cavity at Mach 0.85. The flow impinges on the cavity floor at X/L=0.7 and separates at X/L=0.94. The length of this attachment region is 0.24 and this value increases with increasing cavity L/D ratio. For L/D=14 the attachment length is 0.37 while for L/D=16 it is 0.48 The effect of the increasing cavity L/D ratio is that the flow within in the cavity becomes closer to resembling that experienced in the freestream. Essentially if the L/D ratio is large enough freestream values will be experienced within the cavity. This is why the maximum pressure on the aft wall can be seen to increase from L/D=14 onwards. Figure 6.21 shows the location of the maximum pressure moves considerably down the aft wall. Also on examination of figure 6.19, the distribution switches from a concave shape at L/D=12 to a convex shape at L/D=16, with L/D=14 being linear. Plentovich defined closed flow as occurring *when an inflection occurs in the pressure distribution at* $X/L \approx 0.5$. From figure 6.9 this does not occur at L/D=12 but is evident for L/D=16. When all of the above trends are considered it tends to suggest that there occurs a region of flow which might be classified as transitional-closed flow. In contrast with supersonic flow where transitional-closed flow is identified by the existence of a single shock in the flow structure, for subsonic flow several factors need to be considered. The above factors therefore tend to suggest that transitional closed flow occurs for $10 \leq L/D \leq 14$ at subsonic speeds.

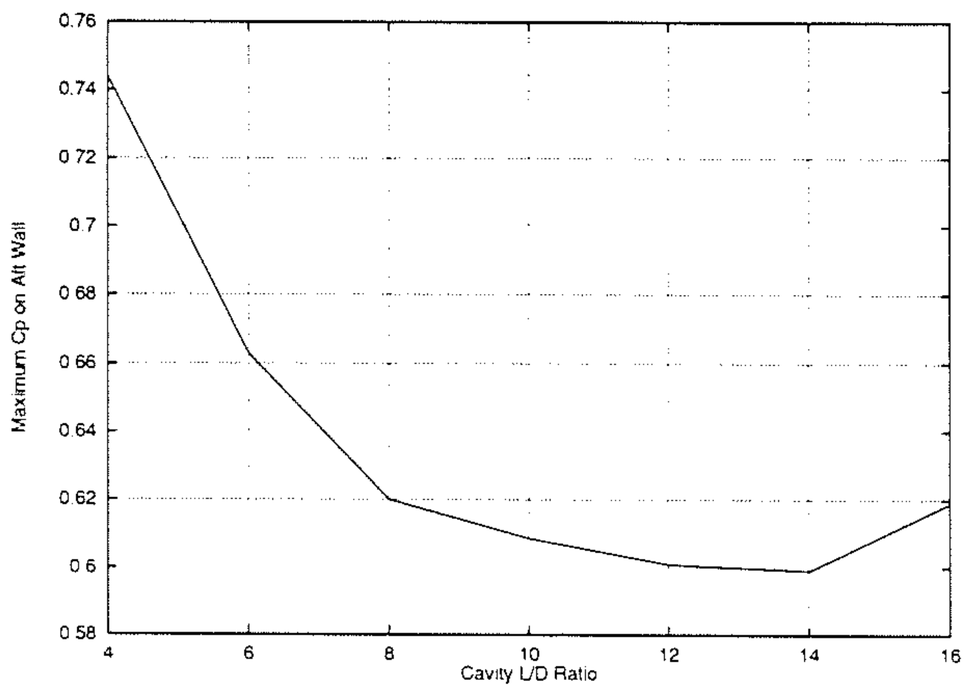

Figure 6.20: Variation of Maximum Pressure value with L/D Ratio, Mach = 0.85

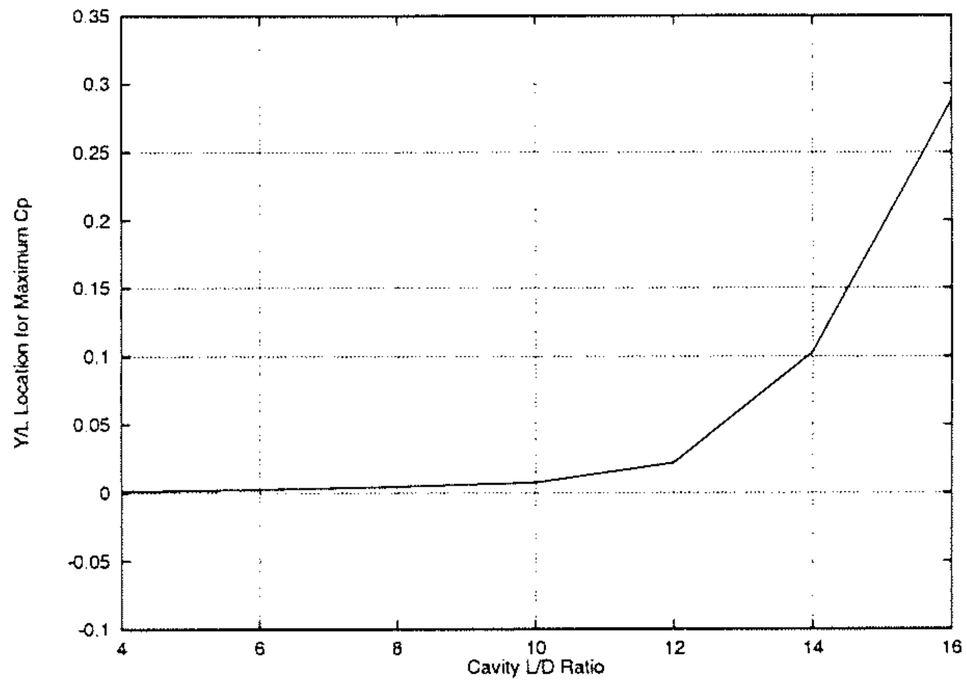

Figure 6.21: Variation of Maximum Pressure Location with L/D Ratio, Mach = 0.85

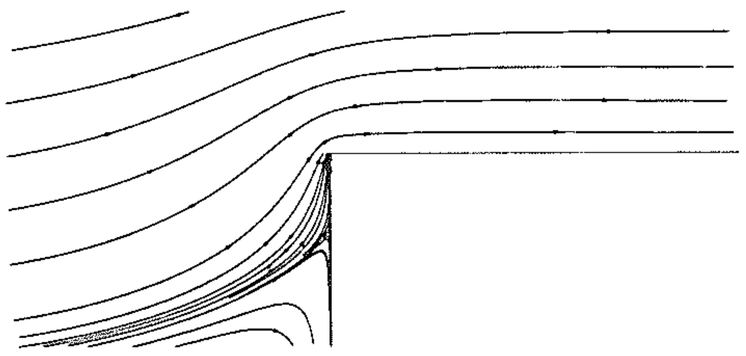

Figure 6.22: Streamline Contours on aft wall for L/D=8

6.3 Comparison with Supersonic results

Open flow is found to exhibit similar flow characteristics in the cavity for subsonic and supersonic speeds. Only the external flow features, where quasi-steady shocks appear, show differences. For closed cavity flow there are similar flow structures present, with impingement and exit shocks being additional features at supersonic speeds. The trends for the pressure distributions for open and closed flow at subsonic and supersonic speeds are also similar.

The transitional flow types occur at the L/D ratios shown in Figure 6.23. The experimental work of Plentovich shows the boundaries for transitional flow to shift with increasing Mach number - figure 6.6. For the present simulations a similar trend is evident: at Mach 1.35 the transitional flow type occurs at L/D=10 whilst for Mach 0.85 it occurs earlier at L/D=8.

For the subsonic cases it has been shown that the boundary between open and transitional flow may be estimated by considering the pressure distribution on the cavity floor. For open flow the distribution is concave down whilst for transitional it is convex. At the boundary itself the distribution is linear (figure 6.9). A similar description has not been made for supersonic flow. However, this also appears to be the case for L/D=10 in figure 5.7. This suggests that this behaviour is indicative of the boundary between open and transitional flow for both subsonic and supersonic speeds.

The boundaries are shown in figure 6.23. Plentovich showed the change in pressure distribution from open to transitional flow to be a smooth progression. A re-evaluation by Plentovich of the data of Stallings suggested a similar trend at supersonic speeds. The current results support this suggestion. When transitional flow is achieved there are differences between the flows observed at subsonic and supersonic speeds. At subsonic speeds transitional flow, as indicated by a convex pressure distribution, has a flow structure that is capable of supporting three vortices in the cavity. The general flow mechanisms are similar to those evident for open flow with the growth in vorticity from the leading edge and the subsequent lobe that is formed effectively controlling the motion of the shear layer. The formation of the vortices in the cavity and their role in the mass expulsion process is governed by the same mechanisms also. Results have shown that as the L/D ratio increases the flow features resemble those of a closed cavity (from L/D=10 to 13). However by the definition given by Plentovich for the pressure distribution of closed flow (that *when an inflection occurs in the pressure distribution at* $X/L \approx 0.5$) this would suggest that at L/D=12 the flow is not closed. Further investigation of the flow features (figure 6.21) has led to the definition of such flow as being *transitional-closed flow* with the boundary between this and closed flow occurring at L/D=14. This necessitates the re-classification of transitional flow to be transitional-open flow as shown in figure 6.23. It has been shown that for transonic speeds that the flow in the transitional region is steady in nature while for subsonic speeds transitional-open flow is unsteady. It was previously hypothesised that Prandtl-Meyer expansions cause steady

flow to be achieved earlier for transonic speeds. Figure 6.23 shows that transitional open flow occurs at L/D=8 for Mach 0.85 while it occurs at L/D=10 for Mach 1.35. For subsonic speeds the transitional-open flow was identified by internal cavity flow features as well as considering the characteristic pressure distributions. It is an unsteady flow and transitional-closed flow is found to occur when the flow converges to a steady state at L/D=12. This steady flow at subsonic speeds is at a higher L/D ratio than that of the L/D=10 ratio which produces steady flow at Mach 1.35. This agrees with the earlier hypothesis. As steady flow occurs earlier for transonic speeds than compared to subsonic speeds differences are going to occur when defining the boundaries since the methods of defining the flows are not homogeneous. However the methods used in the present thesis to identify the flows have strong foundations for their validity. In the process of using these methods features have been identified which significantly enhance the current understanding of transitional cavity flows.

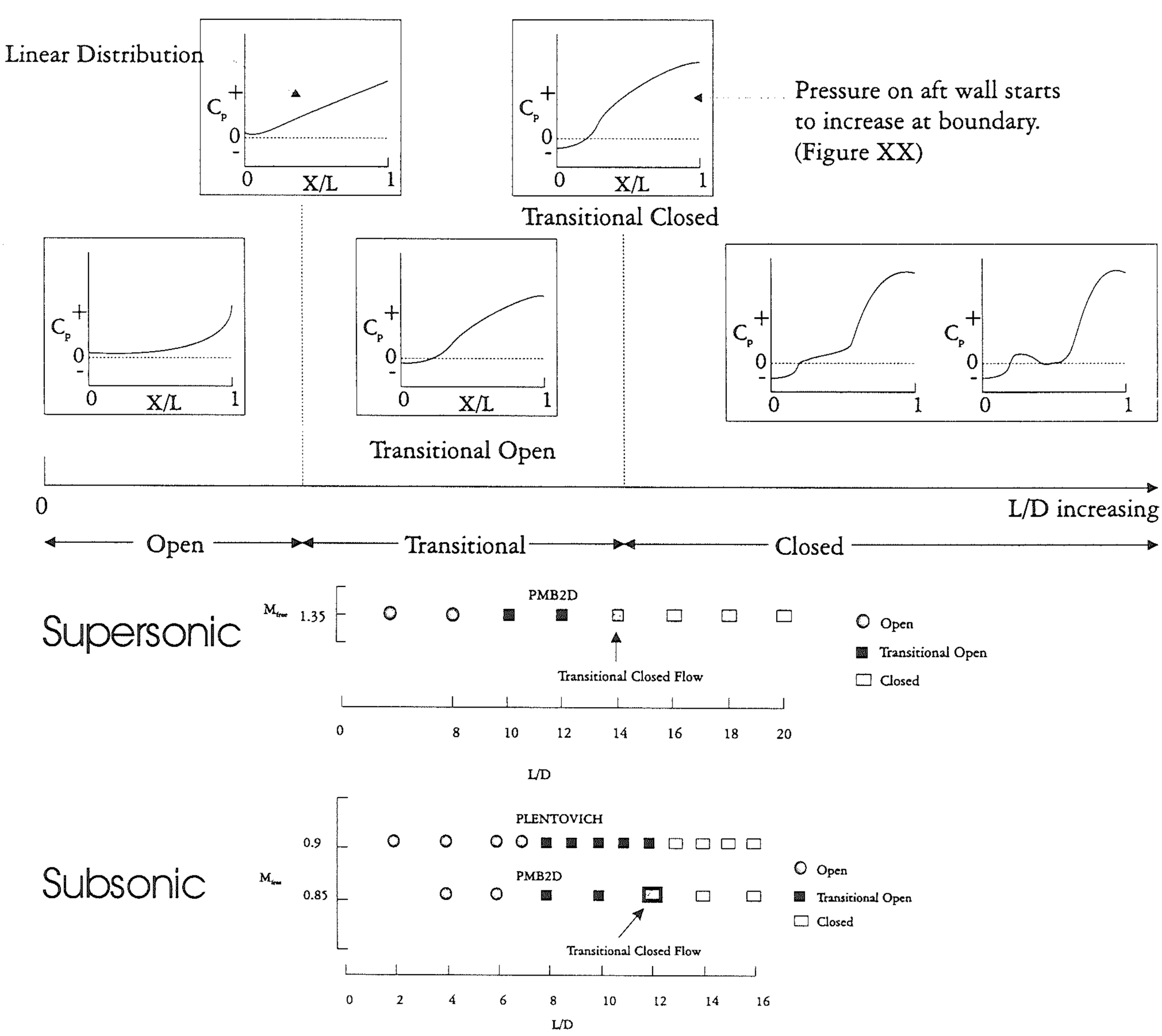

Figure 6.23: Summary of results for Transitional Cavities

Chapter 7

Conclusions

In this work the flow phenomena occurring in open, transitional-open, transitional-closed, and closed cavity flows were investigated using time accurate solutions of the Navier-Stokes equations. By relating the results to prior experimental and theoretical works the understanding of the flow physics were enhanced. It has also been shown that there are significant benefits to be obtained by using CFD synergistically with experimental studies.

In Chapter 2 of this work the validation and verification of the numerical approach was considered. The capability of the method to predict cavity flow was demonstrated. Simulation of the flow over open, transitional-open, transitional- closed, and closed cavity types from Mach 0.6 to Mach 1.35 was conducted. The following is a summary of the main points of the chapter:

- the RANS approach taken in the present work is used carefully in conjunction with the available experimental data since the applicability of using RANS is open to discussion.

- grid independent results are not obtained for the unsteady flows since the grid resolves eddies in addition to the turbulent k-w model. This is a form of double accounting. The correct level of modelling was achieved through careful selection of grid density.

- the 2D cavity simulations are representative of the experimental case of the

cavity with the bay doors at 90 degrees, as intuition suggests.

- for open cavity flows the acoustic spectra at positions along the cavity floor predict the experimental cavity tones. The RMS pressure levels are over-predicted by the CFD as compared with the experimental values. However the CFD results do not capture the background noise and this means that the SPL distribution along the cavity floor agrees excellently with experiment for Mach numbers of 0.85 and Mach 1.19. The pressure traces from the CFD results are compared with a section of those from experiment. Even for the locations in the cavity where the higher frequencies are more prevalent than at other positions the traces show reasonable agreement in phase and amplitude.

- for transitional-open flow at Mach 0.9 (an unsteady flow) the frequency content is predicted very well as is the time averaged pressure distributions on the cavity floor and aft walls.

- for the steady transitional and closed cavity flows grid independence is obtained. The problem of resolving frequencies was no longer an issue.

The chapter clearly demonstrates that the current approach produces good agreement with various experimental measurements for the range of cases investigated. The present method has a good basis to examine the physics occurring for open to closed cavity flow.

Chapter 3 presents a detailed analysis of the flow physics for open cavity flow at Mach 0.85 and Mach 1.19. The investigation uses CFD synergistically with experimental and theoretical methods to significantly enhance the understanding of the cavity flow physics. An innovative approach was implemented to track the positions of the upstream propagating pressure waves and the downstream moving vortices in the cavity. The detailed results from the CFD have enabled examination of the flow features inside the cavity which are not easily obtainable from experiments and reveal the following about the flow mechanisms:

- The 2nd cavity tone dominates at a frequency of 410 Hz. However it is noted that at the locations in the cavity where the pressure waves pass over the

vortices the 1st tone of 175 Hz increases in amplitude significantly. The reason for this was not investigated at the time and is an area suggested for future work

- At Mach 0.85 the flow is characterised by a series of vortices whose cores travel downstream forcing the shear layer motion. The shear layer impinges on the aft cavity wall inducing pressure waves that travel upstream. Meanwhile the main vortex in the cavity becomes stretched and a new vortex forms off a lobe at the leading edge. While this is occurring the pressure waves reach the front of the cavity and generate vorticity that helps with the inception of a new vortex.

- Despite a considerable rise in the unsteady pressure levels at Mach 1.19, the same flow mechanisms are prevalent inside the cavity. The findings of previous experiments, that seem at odds with each other with regards to explanation of the flow physics, are reviewed and comparisons are made with the the present simulations. Interpretation of the CFD results indicates that the experimental results are different perspectives of the same events:

  - The growth of a new vortex is responsible for the leading edge quasi-steady leading edge compression shock.

  - The new vortex appears after the upsteam moving pressure wave reflects off the front cavity wall.

  - The present case shows that a vortex from a previous cycle is responsible for the pressure wave which propagates upstream.

It is shown that the acoustic levels experienced in the cavity are substantially high. Chapter 4 investigates a passive control method to suppress the pressure oscillations. This involves sloping the aft cavity wall. The study follows experimental tests and provides an understanding of why sloping of the rear wall is successful in attenuating the pressure oscillations. The CFD results show consistency with those gathered experimentally and indicate that the decrease in the SPLs is gradual as the sloping of the aft wall is shallowed. A transtional region is shown to exist at 70° and little differences are noticed between the flowfield for a clean cavity and that for a slope

of 76°. The evidence gathered supports the earlier but unsubstantiated hypothesis of Heller and Bliss. The main points are:

- for clean cavity flow the impingement angle of the stagnation streamline on the aft wall requires the shear layer to expand into the cavity at the leading edge. This induces the highly unsteady nature of the shear layer.

- for a cavity with a sloped aft wall the stagnation streamline can impinge on the aft wall at an oblique angle. This means that the shear layer does not need to expand into the cavity as much hence suppressing the unsteady nature of the shear layer.

- the time averaged streamlines for a clean cavity and a 63.4° slope cavity agree remarkabley well with the pattern hypothesised by Heller and Bliss

- examination of the flow at the aft wall show the radii of curvature of the streamlines on the cavity side are larger for a sloped cavity wall than for a clean one. Specifically this means the centrifugal pressure forces will be less hence suppressing the amplitude of the oscillations

- it was found that a sloped cavity has a natural desire to approach a steady state. The shear layer tends towards having a straight stagnation line at its centre which reduces the unsteady environment in the cavity. However features inherent to clean cavity flow preclude a totally steady flow being obtained.

The success of CFD in indicating why the suppression method of rear wall sloping is successful strengthens the case for it to be more widely used. Cavity experiments are prohibitively expensive but if the potential of the current approach can be correctly harnessed then it offers a very useful avenue of investigation. The experiments also investigated the effect of leading edge spoilers for suppressing the cavity tones. It was suggested that CFD could be used to examine the effect that sloped rear walls and leading edge spoilers have on the cavity tones when used in tandem. This is obviously an area that future work can investigate.

Chapter 5 describes the flow features for transitional cavity flows at supersonic

speeds. A comprehensive review of the literature indicates that by applying the principles used to classify cavity flows today the work of McDearmon shows that 4 types of cavity flows exist at supersonic speeds. The 4 types of cavity flows found to exist are later credited as to being classified by Stallings. Two references by Stallings give conflicting statements about the change from transitional-closed to transitional-open flow although due to the experimental setup there is evident a hysteresis effect. The hysteresis effect evident in the experiments for the transitional region depending on whether the L/D ratio is gradually increased or decreased was not investigated by CFD and is an area suggested for future work. The main results of the study are:

- for supersonic flow Prandtl-Meyer theory predicts steady flow will be obtained at a lower L/D ratio than it will be for subsonic flow. The present simulations show transitional-open and transitional-closed flows at Mach 1.35 generate no discrete tones.

- closed cavity flow exists at L/D=16. The ratio of the separation wake length to cavity depth for L/D=20 and 16 is 3.4, which agrees well with experimental values. The separation wake and the re-attachment wake are mutually independent for open cavity flow.

- the flow changes to transitional closed flow when the vertices of the separation and recompression wakes merge. The impingement and exit shocks for closed flow collapse to form a single shock wave. This point is defined as L/D_{crit}. The values predicted from the simulations agree very well with experiment and those obtained by Prandtl Meyer expansion theory.

- it is more difficult to define an exact boundary between transitional-closed and transitional-open flow at supersonic speeds. The trailing edge vortex becomes a lobe of the large leading edge vortex. The impingement shock no longer exists and is replaced by a series of compression wavelets.

Chapter 6 examines a class of cavity flows for which little information about the flow features has been documented in the literature. At subsonic speeds experiments were conducted to provide information about the characteristic floor pressure

distributions. The current approach highlights a drawback of the experimental procedure and considers the erroneous conclusions derived from the work. The results of the chapter can be summarised as follows:

- the experimental results define 3 types of flow to exist: open, transitional and closed and these are identified by the floor pressure distributions.

- the experimental work is hindered by the amount of pressure tappings used in the cavity. Specifically this leaves the generic pressure distributions defined for transitional flow open to question.

- the present study shows that more than just the pressure distribution along the cavity floor should be considered when classifying cavity flows. Other characteristics of the flow field are identified that can be indicative of the type of cavity flow occurring. A particularly useful one is the pressure distributions on the aft cavity wall.

- The peak pressure on the aft wall decreases with increasing L/D ratio. The location of the maximum pressure measured moves closer to the top of the aft wall with decreasing L/D ratio (towards open flow). Inspection of the pressure distributions indicate that another type of cavity flow, not previously classified, exists - this is referred to as transitional-closed cavity flow. Four types of flow are shown to exist which is similar to supersonic flow.

- consideration of the pressure distributions along the cavity floor show the boundary between open and transitional-open flow is characterised by a linear pressure distribution.

The flow features for transitional-open flow are similar to those for open-flow with only subtle differences. The transitional-open flow also makes it easier to see features that are described for open-flow. A pressure wave passing over the leading edge is clearly seen to induce increased vorticity which forms a lobe and ultimately influences the shear layer motion. Up to 3 vortices can be seen to exist in the cavity at one time.

Much has been learned about cavity flow in the present thesis and it is apparent that the current approach has the potential to be of use in the future. In addition to those areas already suggested immediate future work that should be attempted is the following:

- insufficient spatial discretisations has been performed. It is suggested that the grid is refined further with up to 1 million points if necessary to understand the problems mentioned previously. Computing facilities available at the time to the author restricted such a study.

- The 2D cavity simulations are representative of the experimental case of the cavity with the bay doors at 90°. A 3D study of the cavity is an obvious extension of the work and is already underway.

Correctly harnessed the use of CFD, in conjunction with theory and measured data, has enhanced the understanding of cavity flow phenomena

Appendix A

Prediction of $(L/D)_{detached}$ for Transitional Cavities

A.1 Introduction

An attempt was made by McDearmon to predict the critical L/D ratio of the cavity for a range of Mach numbers [56]. A simplified version of supersonic flow over a two-dimensional cavity, as shown in Figure A.1, was considered. The following assumptions were made

- Effect of boundary layer is negligible.
- Flow turns abruptly upon attaching and separating from cavity bottom.

Therefore considering Figure A.1, $(L/D)_{detached}$ is the ratio at which $l_2 \rightarrow 0$

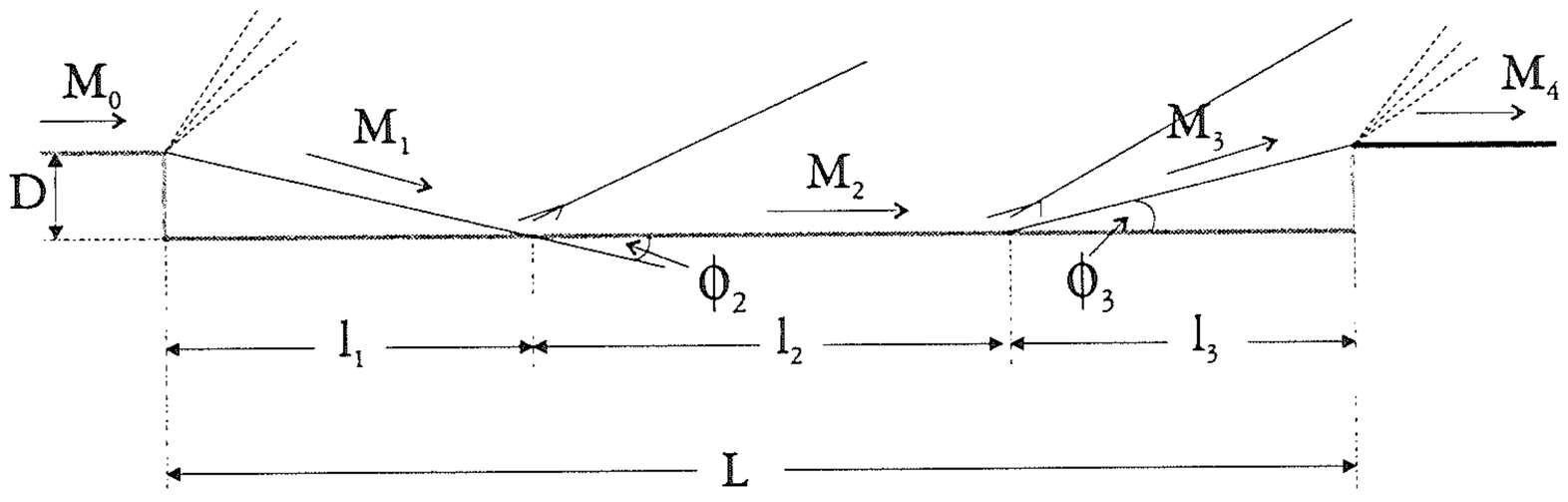

Figure A.1: Simplified Model of the Flow

For a shallow cavity with $L/D \geq (L/D)_{detached}$:

$$L = l_1 + l_2 + l_3 = D\cot\phi_2 + l_2 + D\cot\phi_3$$

Approaching the critical L/D ratio by decreasing the cavity length and with the condition that $l_2 \to 0$:

$$\left(\frac{L}{D}\right) = \cot\phi_2 + \frac{l_2}{D} + \cot\phi_3$$

$$\left(\frac{L}{D}\right)_{detached} = \cot\phi_2 + \cot\phi_3$$

It has previously been shown [55] that the flow phenomena for a two-dimensional base and a forward facing step are analogous. In the present case the area behind the rearward-facing step is referred to as region 1, and the area ahead of the forward facing step as region 2. There is the additional consideration of region 2 in the present case. This region will be represented by a flat plate and it is assumed this additional region will not alter the flow in region 1.

Love [54] defined empirically the peak pressure-rise coefficient associated with a turbulent boundary layer separating ahead of a forward-facing step, given by:

$$P = \frac{3.2}{8 + (M_\infty - 1)^2}$$

Effects of Reynolds number, boundary-layer thickness and step height are not accounted for. However Chapman [20] showed the equation gives a good prediction over the supersonic Mach number range.

Application of the above analogy across the oblique shock separating region 1 from region 2 gives :

$$P = \frac{P_2 - P_1}{q_1} = \frac{3.2}{8 + (M_\infty - 1)^2}$$

$$\Rightarrow \qquad \frac{P_2}{P_1} = \frac{q_1}{P_1}\frac{3.2}{8+(M_\infty-1)^2}+1$$

From compressible flow relations for a calorically perfect gas:

$$\frac{P_1}{q_1} = \frac{2}{\gamma M_1^2}$$

Hence the static pressure ratio across the oblique shock separating region 1 from region 2 is given by

$$\frac{P_2}{P_1} = 0.7M_1^2\frac{3.2}{8+(M_\infty-1)^2}+1$$

It is shown in [2] (for oblique as well as normal shocks) that the flow deflection angle for various upstream Mach numbers is

$$\phi_2 = \tan^{-1}\left\{\frac{5\left(\frac{P_2}{P_1}-1\right)}{7M_1^2-5\left(\frac{P_2}{P_1}-1\right)}\left[\frac{7M_1^2-\left(6\frac{P_2}{P_1}+1\right)}{6\frac{P_2}{P_1}+1}\right]^{\frac{1}{2}}\right\}$$

Substitution for P_2/P_1 gives[1]

$$\phi_2 = \tan^{-1}\left[\frac{1.6}{(M_1^2-2M_1+7.4)}\left(\frac{M_1^3-2M_1^3+6.08M_1^2+2M_1-9}{2.92M_1^2-2M_1+9}\right)^{\frac{1}{2}}\right]$$

Region 3 is then considered to be the area ahead of a forward-facing step and using the assumption that the flow phenomena behind a rearward-facing step are analogous to those ahead of a forward-facing step[2]

$$\phi_3 = \tan^{-1}\left[\frac{1.6}{(M_1^2-2M_1+7.4)}\left(\frac{M_1^3-2M_1^3+6.08M_1^2+2M_1-9}{2.92M_1^2-2M_1+9}\right)^{\frac{1}{2}}\right]$$

Values of M_2 can be obtained by assuming that M_2 is the flow over a wedge with a semivertex angle ϕ_3. M_2 is thus obtainable from normal shock relations [2].

[1] Note that the corresponding equation in [56] is in error.

[2] Note that again the corresponding equation in [56] is in error.

An example calculation is presented in the following section to demonstrate the process involved in determining $(L/D)_{detached}$ and also to calculate $(L/D)_{detached}$ for the present case of $M_0 = 1.35$.

A.2 Example Calculation

From the equations in the previous section it is now possible to predict the critical $\frac{L}{D}$ detachment ratio for a range of Mach numbers. An example calculation is presented for $M_0 = 1.35$, which is the case analysed in the simulations.

The value of ϕ_2 is a function of M_1 and these are calculated on a spreadsheet. In addition to calculating ϕ_2 it is possible to determine the Prandtl-Meyer angle $\nu(M_1)$ from

$$\nu = \sqrt{\frac{\gamma+1}{\gamma-1}}\tan^{-1}\sqrt{\frac{\gamma-1}{\gamma+1}(M^2-1)} - \tan^{-1}\sqrt{M^2-1}$$

Assuming a Prantl-Meyer expansion of the flow around the upstream wall of the cavity the angle $\nu(M_0)$ can be obtained from

$$\nu(M_0) = \nu(M_1) - \phi_2$$

So for a given M_0, $\nu(M_0)$ is obtainable from equation A.1 which in turn gives $\nu(M_1)$ from equation A.1. $\nu(M_0)$ is then located on the spreadsheet to give ϕ_2 and $\nu(M_1)$. The values for the present case of $M_0 = 1.35$ are highlighted in table A.1

For $M_0 = 1.35 \quad \Rightarrow \quad \nu(M_0) = 7.560724$

This gives $\quad M_1 \approx 1.75056253 \qquad \phi_2 \approx 11.72887$

$\nu(M_0)$	$\nu(M_1)$	M_1	ϕ_2
7.560004	19.28865	1.75053	11.72864
7.560225	19.28894	1.75054	11.72871
7.560446	19.28923	1.75055	11.72878
7.560668	19.28952	1.75056	11.72885
7.560889	19.28981	1.75057	11.72892
7.561110	19.29010	1.75058	11.72899
7.561331	19.29040	1.75059	11.72906
7.561552	19.29069	1.75060	11.72913

Table A.1: Values of ϕ_2 for a chosen $\nu(M_0)$.

With the knowledge of M_1 and ϕ_2 it is now possible to obtain M_2. which is considered to be the flow past a wedge with a semi-vertex angle ϕ_2.

With $M_1 \approx 1.75056253$ and $\phi_2 \approx 11.72887 = \delta$ the shock defelection angle, θ is obtained from oblique shock relations.

Therefore $\theta = 47.90172$

The remainder of the calculation will incur some error since θ was read from a chart.

Hence $M_{n,1} = 1.75056 \sin 47.90172 = 1.2989$

From normal shock relations $M_{n,2} = 0.7784 \quad \Rightarrow \quad \mathrm{M}_2 = 1.31882$

Replacing $M_2 = 1.31882$ in the equation $\Rightarrow \quad \phi_3 = 7.144795$

With both ϕ_2 and ϕ_3 now known $(L/D)_{detached}$ is calculated as:

$$\left(\frac{L}{D}\right)_{detached} = \cot\phi_2 + \cot\phi_3 = 4.8166 + 7.9776 = 12.7942$$

Appendix B

Theory Guide to pmb2d

B.1 Introduction

This document gives technical background to the two-dimensional parallel multi-block flow solver called Pmb2D developed at the University of Glasgow. Reference is made to the open literature for full details of the theory.

B.2 Mean Flow Models

The two-dimensional (planar) and axisymmetric Navier-Stokes equations are presented in various forms. The code solves the following versions of these equations

- Laminar Navier-Stokes Equations in non-dimensional and curvilinear form
- Reynolds-Averaged Navier-Stokes Equations in non-dimensional and curvilinear form
- Euler equations (setting viscosity and thermal conductivity to zero) in non-dimensional and curvilinear form

B.2.1 Non-dimensional form

The derivation of the Navier-Stokes equations is included in most fluid dynamics texts, for example [3]. In a two-dimensional Cartesian frame they can be written as

$$\frac{\partial \mathbf{W}}{\partial t} + \frac{\partial (\mathbf{F}^i - \mathbf{F}^v)}{\partial x} + \frac{\partial (\mathbf{G}^i - \mathbf{G}^v)}{\partial y} = 0 \tag{B.1}$$

The vector $\mathbf{W}$ is the vector of conserved variables:

$$\mathbf{W} = \begin{pmatrix} \rho \\ \rho u \\ \rho v \\ \rho E \end{pmatrix} \tag{B.2}$$

where ρ is the density, $\mathbf{V} = (u, v)$ is the Cartesian velocity vector and E is the total energy per unit mass. The flux vectors $\mathbf{F}$ and $\mathbf{G}$ consist of inviscid (^{i}) and ($^\nu$) viscous diffusive parts. These are written in full as :

$$\mathbf{F}^i = \begin{pmatrix} \rho u \\ \rho u^2 + p \\ \rho uv \\ \rho uH \end{pmatrix}$$

$$\mathbf{G}^i = \begin{pmatrix} \rho v \\ \rho uv \\ \rho v^2 + p \\ \rho vH \end{pmatrix} \tag{B.3}$$

$$\mathbf{F}^\nu = \frac{1}{Re} \begin{pmatrix} 0 \\ \tau_{xx} \\ \tau_{xy} \\ u\tau_{xx} + v\tau_{xy} + q_x \end{pmatrix}$$

$$\mathbf{G}^\nu = \frac{1}{Re} \begin{pmatrix} 0 \\ \tau_{xy} \\ \tau_{yy} \\ u\tau_{xy} + v\tau_{yy} + q_y \end{pmatrix} \tag{B.4}$$

The stress tensor and of the heat flux vector components are written as:

$$
\begin{aligned}
\tau_{xx} &= -\mu\left(2\frac{\partial u}{\partial x} - \frac{2}{3}\left(\frac{\partial u}{\partial x} + \frac{\partial v}{\partial y}\right)\right) \\
\tau_{yy} &= -\mu\left(2\frac{\partial v}{\partial y} - \frac{2}{3}\left(\frac{\partial u}{\partial x} + \frac{\partial v}{\partial y}\right)\right) \\
\tau_{xy} &= -\mu\left(\frac{\partial u}{\partial y} + \frac{\partial v}{\partial x}\right) \\
q_x &= -\frac{1}{(\gamma-1)M_\infty^2}\frac{\mu}{Pr}\frac{\partial T}{\partial x} \\
q_y &= -\frac{1}{(\gamma-1)M_\infty^2}\frac{\mu}{Pr}\frac{\partial T}{\partial y}
\end{aligned}
\tag{B.5}
$$

Here γ is the specific heat ratio, Pr is the laminar Prandtl number, T is the static temperature and M_∞ and Re are the freestream Mach number and Reynolds number, respectively. The various flow quantities are related to each other by the perfect gas relations:

$$
\begin{aligned}
H &= E + \frac{p}{\rho} \\
E &= e + \frac{1}{2}\left(u^2 + v^2\right) \\
p &= (\gamma - 1)\,\rho e \\
\frac{p}{\rho} &= \frac{T}{\gamma M_\infty^2}
\end{aligned}
\tag{B.6}
$$

Finally, the laminar viscosity μ is evaluated using Sutherland's law:

$$
\frac{\mu}{\mu_0} = \left(\frac{T}{T_0}\right)^{3/2}\frac{T_0 + 110}{T + 110} \tag{B.7}
$$

where μ_0 is a reference viscosity at a reference temperature T_0. These can be taken as $\mu_0 = 1.7894\text{x}10^{-5}$ kg/(m.s) with $T_0 = 288.16$ K. The non-dimensionalisation used is as follows:

$$
x = \frac{x^*}{L^*}, \qquad y = \frac{y^*}{L^*}, \qquad t = \frac{t^*}{L^*/V_\infty^*},
$$

$$u = \frac{u^*}{V_\infty^*}, \qquad v = \frac{v^*}{V_\infty^*}, \qquad \mu = \frac{\mu^*}{\mu_\infty^*},$$

$$\rho = \frac{\rho^*}{\rho_\infty^*}, \qquad p = \frac{p^*}{p_\infty^* V_\infty^{*2}}, \qquad T = \frac{T^*}{T_\infty^*}, \qquad e = \frac{e^*}{V_\infty^{*2}} \tag{B.8}$$

where * denotes dimensional quantities and $_\infty$ denotes free-stream values.

B.2.2 Reynolds-averaged form

The Reynolds-averaged form of the Navier-Stokes equations permits turbulent flow to be considered. The development is not presented here. It is merely noted that fundamental to this approach is the consideration of the flow variables as consisting of two components, a time averaged component and a turbulent fluctuation component. For example, density and velocity components are decomposed as

$$u = \bar{u} + u', \qquad v = \bar{v} + v', \qquad \rho = \bar{\rho} + \rho'$$

The quantities k (the turbulent kinetic energy), μ_T (the turbulent viscosity) and Pr_T (the turbulent Prandtl number) are introduced via the important Boussinesq assumption in an attempt to model the fluctuating-variable stress terms arising from the Reynolds averaging. For a complete discussion of this subject see [3]. The Reynolds-averaged form of the Navier-Stokes equations are identical to those presented in Section B.2.1, except for the stress tensor and heat flux vector components shown below. The variables should be considered as mean flow quantities (superscripts are dropped for clarity). The turbulent nature of the flow is modelled via μ_T and k and a closure hypothesis or turbulence model, for example the $k - \omega$ model,

Section B.3.

$$
\begin{aligned}
\tau_{xx} &= -(\mu+\mu_T)\left(2\frac{\partial u}{\partial x}-\frac{2}{3}\left(\frac{\partial u}{\partial x}+\frac{\partial v}{\partial y}\right)\right)+\frac{2}{3}\rho k \\
\tau_{yy} &= -(\mu+\mu_T)\left(2\frac{\partial v}{\partial y}-\frac{2}{3}\left(\frac{\partial u}{\partial x}+\frac{\partial v}{\partial y}\right)\right)+\frac{2}{3}\rho k \\
\tau_{xy} &= -(\mu+\mu_T)\left(\frac{\partial u}{\partial y}+\frac{\partial v}{\partial x}\right)
\end{aligned}
\tag{B.9}
$$

$$
\begin{aligned}
q_x &= -\frac{1}{(\gamma-1)M_\infty^2}\left(\frac{\mu}{Pr}+\frac{\mu_T}{Pr_T}\right)\frac{\partial T}{\partial x} \\
q_y &= -\frac{1}{(\gamma-1)M_\infty^2}\left(\frac{\mu}{Pr}+\frac{\mu_T}{Pr_T}\right)\frac{\partial T}{\partial y}
\end{aligned}
\tag{B.10}
$$

B.2.3 General Curvilinear form

The equations are written in curvilinear (ξ,η) form to facilitate use on curvilinear grids of arbitrary local orientation and density. A space transformation from the Cartesian coordinate system to the local coordinate system must then be introduced:

$$
\begin{aligned}
\xi &= \xi(x,y) \\
\eta &= \eta(x,y) \\
t &= t
\end{aligned}
$$

The Jacobian matrix of the transformation is given by

$$
J = \frac{\partial(\xi,\eta)}{\partial(x,y)}
$$

The equations (B.1) can then be written as

$$
\frac{\partial \hat{\mathbf{W}}}{\partial t}+\frac{\partial(\hat{\mathbf{F}}^i-\hat{\mathbf{F}}^v)}{\partial \xi}+\frac{\partial(\hat{\mathbf{G}}^i-\hat{\mathbf{G}}^v)}{\partial \eta}=0 \tag{B.11}
$$

where

$$\begin{aligned}
\hat{\mathbf{W}} &= \frac{\mathbf{W}}{J} \\
\hat{\mathbf{F}}^i &= \frac{1}{J}\left(\xi_x \mathbf{F}^i + \xi_y \mathbf{G}^i\right) \\
\hat{\mathbf{G}}^i &= \frac{1}{J}\left(\eta_x \mathbf{F}^i + \eta_y \mathbf{G}^i\right) \\
\hat{\mathbf{F}}^v &= \frac{1}{J}\left(\xi_x \mathbf{F}^v + \xi_y \mathbf{G}^v\right) \\
\hat{\mathbf{G}}^v &= \frac{1}{J}\left(\eta_x \mathbf{F}^v + \eta_y \mathbf{G}^v\right)
\end{aligned} \tag{B.12}$$

The expressions for the inviscid fluxes can be simplified somewhat by defining

$$\begin{aligned}
U &= \xi_x u + \xi_y v \\
V &= \eta_x u + \eta_y v
\end{aligned} \tag{B.13}$$

The inviscid fluxes can then be written as

$$\begin{aligned}
\hat{\mathbf{F}}^i &= \begin{pmatrix} \rho U \\ \rho u U + \xi_x p \\ \rho v U + \xi_y p \\ \rho U H \end{pmatrix} \\
\hat{\mathbf{G}}^i &= \begin{pmatrix} \rho V \\ \rho u V + \eta_x p \\ \rho v V + \eta_y p \\ \rho V H \end{pmatrix}
\end{aligned} \tag{B.14}$$

The derivative terms found in the viscous fluxes are evaluated using the chain rule, for example

$$\frac{\partial u}{\partial x} = \xi_x \frac{\partial u}{\partial \xi} + \eta_x \frac{\partial u}{\partial \eta}$$

The evaluation of the metrics of the transformation is clearly important, and is described in full in [3].

B.2.4 Axisymmetric Form

The code allows the solution of the Reynolds-Averaged Navier-Stokes equations for axisymmetric flow (i.e. cylindrical coordinates with symmetry in the azimuthal direction). The equations are written in the form

Mass continuity

$$\frac{\partial \rho}{\partial t} + \frac{\partial}{\partial r}\left(\rho v_r\right) + \frac{\partial}{\partial z}\left(\rho v_z\right) = -\frac{\rho v_r}{r} \tag{B.15}$$

Momentum

$$\begin{aligned}
&\frac{\partial}{\partial t}\left(\rho v_r\right) + \frac{\partial}{\partial r}\left(\rho v_r^2 + p\right) - \frac{\partial}{\partial r}\left[\frac{\mu + \mu_T}{Re}\left(2\frac{\partial v_r}{\partial r} - \frac{2}{3}\left(\frac{\partial v_z}{\partial z} + \frac{\partial v_r}{\partial r}\right) + \frac{2}{3}\rho k\right)\right] \\
&\quad + \frac{\partial}{\partial z}\left(\rho v_r v_z\right) - \frac{\partial}{\partial z}\left[\frac{\mu + \mu_T}{Re}\left(\frac{\partial v_z}{\partial r} + \frac{\partial v_r}{\partial z}\right)\right] = -\frac{\rho v_r^2}{r} + \frac{4\left(\mu + \mu_T\right)}{3Re}\left(\frac{1}{r}\frac{\partial v_r}{\partial r} - \frac{v_r}{r^2}\right)
\end{aligned} \tag{B.16}$$

$$\begin{aligned}
&\frac{\partial}{\partial t}\left(\rho v_z\right) + \frac{\partial}{\partial r}\left(\rho v_r v_z\right) - \frac{\partial}{\partial r}\left[\frac{\mu + \mu_T}{Re}\left(\frac{\partial v_z}{\partial r} + \frac{\partial v_r}{\partial z}\right)\right] + \frac{\partial}{\partial z}\left(\rho v_z^2 + p\right) \\
&- \frac{\partial}{\partial z}\left[\frac{\mu + \mu_T}{Re}\left(2\frac{\partial v_z}{\partial z} - \frac{2}{3}\left(\frac{\partial v_z}{\partial z} + \frac{\partial v_r}{\partial r}\right) + \frac{2}{3}\rho k\right)\right] = -\frac{\rho v_r v_z}{r} + \frac{\mu + \mu_T}{rRe}\left(\frac{1}{3}\frac{\partial v_r}{\partial z} + \frac{\partial v_z}{\partial r}\right)
\end{aligned} \tag{B.17}$$

Energy

$$\begin{aligned}
&\frac{\partial E_t}{\partial t} + \frac{\partial}{\partial r}\left(v_r\left(E_t + p\right)\right) + \frac{\partial}{\partial z}\left(v_z\left(E_t + p\right)\right) \\
&\quad - \frac{\partial}{\partial r}\left\{v_r\left[\frac{\mu + \mu_T}{Re}\left(2\frac{\partial u_r}{\partial r} - \frac{2}{3}\left(\frac{\partial u_r}{\partial r} + \frac{\partial u_z}{\partial z}\right) + \frac{2}{3}\rho k\right)\right] + v_z\left[\frac{\mu + \mu_T}{Re}\left(\frac{\partial u_r}{\partial z} + \frac{\partial u_z}{\partial r}\right)\right]\right\} \\
&\quad - \frac{\partial}{\partial z}\left\{v_z\left[\frac{\mu + \mu_T}{Re}\left(2\frac{\partial u_z}{\partial z} - \frac{2}{3}\left(\frac{\partial u_r}{\partial r} + \frac{\partial u_z}{\partial z}\right) + \frac{2}{3}\rho k\right)\right] + v_r\left[\frac{\mu + \mu_T}{Re}\left(\frac{\partial u_r}{\partial z} + \frac{\partial u_z}{\partial r}\right)\right]\right\} \\
&\quad - \frac{\partial}{\partial r}\left\{\frac{1}{\left(\gamma - 1\right)M_\infty^2}\left(\frac{\mu}{Pr} + \frac{\mu_T}{Pr_T}\right)\frac{\partial T}{\partial r}\right\} - \frac{\partial}{\partial z}\left\{\frac{1}{\left(\gamma - 1\right)M_\infty^2}\left(\frac{\mu}{Pr} + \frac{\mu_T}{Pr_T}\right)\frac{\partial T}{\partial z}\right\} \\
&\quad = \frac{1}{r}\left[-v_r\left(E_t + p\right) + \frac{\mu + \mu_T}{Re}\left(v_z\frac{\partial u_z}{\partial r} + \frac{v_z}{3}\frac{\partial u_r}{\partial z} - \frac{4v_r}{3}\frac{\partial u_z}{\partial z} + \frac{2v_r}{3}\rho k\right)\right. \\
&\quad \left. + \frac{1}{\left(\gamma - 1\right)M_\infty^2}\left(\frac{\mu}{Pr} + \frac{\mu_T}{Pr_T}\right)\frac{\partial T}{\partial r}\right]
\end{aligned} \tag{B.18}$$

Note that these equations are non-dimensional, see Section B.2.1. The curvilinear form is obtained using the space transformation described in Section B.2.3. For these equations written in full see [38].

B.3 Turbulence Model

The turbulence model available in the code is the two-equation $k-\omega$ turbulence model.

B.3.1 Non-dimensional form

The $k-\omega$ turbulence model of Wilcox [92] in non-dimensional form can be written as follows:

Eddy Viscosity

$$\mu_T = \rho k/\omega \tag{B.19}$$

Turbulence Kinetic Energy

$$\rho\frac{\partial k}{\partial t} + \rho\mathbf{V}.\nabla k - \frac{1}{Re}\nabla.\left[\left(\mu + \sigma^*\mu_T\right)\nabla k\right] = \mu_T P - \frac{2}{3}\rho k S - \beta^*\rho k\omega \tag{B.20}$$

Specific Dissipation Rate

$$\rho\frac{\partial \rho\omega}{\partial t} + \rho\mathbf{V}.\nabla\omega - \frac{1}{Re}\nabla.\left[\left(\mu + \sigma\mu_T\right)\nabla\omega\right] = \alpha\frac{\omega}{k}\left[\mu_T P - \frac{2}{3}\rho k S\right] - \beta\rho\omega^2 \tag{B.21}$$

Closure Coefficients

$$\alpha = 5/9, \qquad \beta = 3/40, \qquad \beta^* = 9/100, \qquad \sigma = 1/2, \qquad \sigma^* = 1/2 \tag{B.22}$$

In the above relations,

$$\begin{aligned} P &= \left[\left(\nabla\mathbf{V} + \nabla\mathbf{V}^T\right) : \nabla\mathbf{V} - \frac{2}{3}\left(\nabla.\mathbf{V}\right)^2\right] \\ S &= \nabla.\mathbf{V} \end{aligned}$$

The equations as shown above use the same non-dimensional quantities as in Section B.2.1, with the addition of

$$k = \frac{k^* Re}{V_\infty^{*2}}, \qquad \omega = \frac{\omega^* L^*}{V_\infty^*}, \qquad \mu_T = \frac{\mu_T^*}{\mu_\infty^*}$$

B.3.2 General Curvilinear form

The equations for k and ω can be written in a curvilinear form analogous to that used for the mean flow equations in Section B.2.3 . Written in full, the two-dimensional Cartesian form of equations (B.21) and (B.22) become

$$\frac{\partial \mathbf{q}}{\partial t} + \frac{\partial (\hat{\mathbf{F}}_T^i - \hat{\mathbf{F}}_T^v)}{\partial \xi} + \frac{\partial (\hat{\mathbf{G}}_T^i - \hat{\mathbf{G}}_T^v)}{\partial \eta} = \frac{\hat{\mathbf{S}}_T}{J} \tag{B.23}$$

where the vectors of conserved variables, convective and diffusive fluxes are respectively

$$\mathbf{q} = \frac{1}{J} \begin{pmatrix} \rho k \\ \rho \omega \end{pmatrix} \qquad \hat{\mathbf{F}}_T^i = \frac{1}{J} \begin{pmatrix} \rho k U \\ \rho \omega U \end{pmatrix} \qquad \hat{\mathbf{G}}_T^i = \frac{1}{J} \begin{pmatrix} \rho k V \\ \rho \omega V \end{pmatrix}$$

$$\hat{\mathbf{F}}_T^v = \frac{1}{J} \left(\xi_x \hat{\mathbf{M}} + \xi_y \hat{\mathbf{N}} \right) \qquad \hat{\mathbf{G}}_T^v = \frac{1}{J} \left(\eta_x \hat{\mathbf{M}} + \eta_y \hat{\mathbf{N}} \right)$$

where the tensors M and N are equal to

$$\hat{\mathbf{M}} = \frac{1}{Re} \begin{pmatrix} (\mu + \sigma^* \mu_T) (\xi_x k_\xi + \eta_x k_\eta) \\ (\mu + \sigma \mu_T) (\xi_x \omega_\xi + \eta_x \omega_\eta) \end{pmatrix}$$

$$\hat{\mathbf{N}} = \frac{1}{Re} \begin{pmatrix} (\mu + \sigma^* \mu_T) (\xi_y k_\xi + \eta_y k_\eta) \\ (\mu + \sigma \mu_T) (\xi_y \omega_\xi + \eta_y \omega_\eta) \end{pmatrix}$$

Finally, the source term is written as

$$\hat{\mathbf{S}}_T = \begin{pmatrix} \hat{\mathbf{P}}_k - \hat{\mathbf{D}}_k \\ \hat{\mathbf{P}}_\omega - \hat{\mathbf{D}}_\omega \end{pmatrix}$$

with the components

$$\hat{\mathbf{P}}_k = \mu_T \left\{ \left(\frac{\partial u}{\partial y} + \frac{\partial v}{\partial x} \right)^2 + 2 \left[\left(\frac{\partial u}{\partial x} \right)^2 + \left(\frac{\partial v}{\partial y} \right)^2 \right] - \frac{2}{3} \left(\frac{\partial u}{\partial x} + \frac{\partial v}{\partial y} \right)^2 \right\} - \frac{2}{3} \rho k \left(\frac{\partial u}{\partial x} + \frac{\partial v}{\partial y} \right)$$

$$\hat{\mathbf{D}}_k = \beta^* \rho \omega k$$

$$\hat{\mathbf{P}}_\omega = \alpha \frac{\omega}{k} \hat{\mathbf{P}}_k$$

$$\hat{\mathbf{D}}_\omega = \beta \rho \omega^2$$

Again the velocity derivative terms are evaluated in (ξ,η) space via the chain rule, as mentioned in Section B.2.3, but remain unexpanded in the source term components above for brevity.

B.3.3 Axisymmetric Form

In cylindrical coordinates, for axisymmetric flow with no azimuthal dependence, the two equation turbulence model becomes

Turbulence Kinetic Energy

$$\begin{aligned} \frac{\partial}{\partial t}(\rho k) + \frac{\partial}{\partial r}(\rho k v_r) + \frac{\partial}{\partial z}(\rho k v_z) - \frac{1}{Re} \left\{ \frac{\partial}{\partial r} \left[(\mu + \sigma^* \mu_T) \frac{\partial k}{\partial r} \right] + \frac{\partial}{\partial z} \left[(\mu + \sigma^* \mu_T) \frac{\partial k}{\partial z} \right] \right\} \\ = \mu_T P - \frac{2}{3} \rho k S - \beta^* \rho k \omega - \frac{\rho k v_r}{r} + \frac{1}{Re} \left\{ \frac{1}{r} \left[(\mu + \sigma^* \mu_T) \frac{\partial k}{\partial r} \right] \right\} \end{aligned} \tag{B.24}$$

Specific Dissipation Rate

$$\frac{\partial}{\partial t}(\rho\omega) + \frac{\partial}{\partial r}(\rho\omega v_r) + \frac{\partial}{\partial z}(\rho\omega v_z) - \frac{1}{Re}\left\{\frac{\partial}{\partial r}\left[(\mu + \sigma\mu_T)\frac{\partial \omega}{\partial r}\right] + \frac{\partial}{\partial z}\left[(\mu + \sigma\mu_T)\frac{\partial \omega}{\partial z}\right]\right\}$$
$$= \alpha\frac{\omega}{k}\left[\mu_T P - \frac{2}{3}\rho k S\right] - \beta\rho\omega^2 - \frac{\rho\omega v_r}{r} + \frac{1}{Re}\left\{\frac{1}{r}\left[(\mu + \sigma\mu_T)\frac{\partial \omega}{\partial r}\right]\right\} \tag{B.25}$$

In the above relations,

$$P = \left(\frac{\partial v_z}{\partial r} + \frac{\partial v_r}{\partial z}\right)^2 + 2\left[\left(\frac{\partial v_r}{\partial r}\right)^2 + \left(\frac{\partial v_z}{\partial z}\right)^2 + \left(\frac{v_r}{r}\right)^2\right] - \frac{2}{3}\left(\frac{\partial v_r}{\partial r} + \frac{\partial v_z}{\partial z} + \frac{v_r}{r}\right)^2$$

$$S = \frac{\partial v_r}{\partial r} + \frac{\partial v_z}{\partial z} + \frac{v_r}{r}$$

The curvilinear form is obtained using the space transformation described in Section B.2.3. For these equations written in full see [38].

B.4 Spatial Discretisation for Mean Flow Equations

The Navier-Stokes equations are discretised using a cell-centred finite volume approach. The computational domain is divided into a finite number of non-overlapping control-volumes, and the governing equations are applied to each cell in turn. Also, the Navier-Stokes equations are re-written in a curvilinear coordinate system which simplifies the formulation of the discretised terms since body-conforming grids are adopted here. The spatial discretisation of equation (B.11) leads to a set of ordinary differential equations in time:

$$\frac{d\mathbf{W}_{i,j}}{dt} = -\mathbf{R}_{i,j} \tag{B.26}$$

where $\mathbf{W}$ and $\mathbf{R}$ are the vectors of cell conserved variables and residuals respectively. The convective terms are discretised in the present work using Osher's upwind scheme [59] for its robustness, accuracy and stability properties. In addition, a MUSCL interpolation [90] is used to provide third-order accuracy and the Anderson [4] or van Albada limiter [89] prevents spurious oscillations from occurring

around shock waves. The discretisation of the viscous terms requires the value of the velocity components and their derivatives, as well as the derivatives of the static temperature, at the edges of each cell. Cell-edge values of the velocity components are approximated by the average of the two adjacent cell-centre values, as shown below:

$$u_{i+\frac{1}{2},j} = \frac{1}{2}\left(u_{i,j} + u_{i+1,j}\right) \tag{B.27}$$

Cell-edge values of the derivatives are obtained using Green's formula applied to an auxiliary cell surrounding the considered edge, for example:

$$\begin{aligned} \frac{\partial u}{\partial x} &= \frac{1}{h_{aux}} \oint_{\Omega_{saux}} u dy \\ \frac{\partial u}{\partial y} &= \frac{-1}{h_{aux}} \oint_{\Omega_{saux}} u dx \end{aligned} \tag{B.28}$$

where h_{aux} is the area of the auxiliary cell. The values at the four points a, b, c, d are obtained using the neighbouring cell-centre values:

$$\begin{aligned} u_a &= u_{i,j} \\ u_b &= \frac{u_{i,j-1} + u_{i,j} + u_{i+1,j-1} + u_{i+1,j}}{4} \\ u_c &= u_{i+1,j} \\ u_d &= \frac{u_{i,j} + u_{i,j+1} + u_{i+1,j} + u_{i+1,j+1}}{4} \end{aligned} \tag{B.29}$$

The choice of the auxiliary cell is guided by the need to avoid odd-even point decoupling and to minimise the amount of numerical viscosity introduced in the discretised equations.

The boundary conditions are set by using two rows of halo cells. Values are set in the halo according to interior values and boundary values. Once halo values are set then all interior cells are treated in an identical fashion. The extrapolations used are shown in table B.1. The subscript 1 denotes values in the interior cell adjacent to the boundary, 2 the next interior cell, b1 the first halo cell and b2 the second halo cell and file denotes values read from a file. ϕ_e denotes the value $\phi_e = 2\phi_1 - \phi_2$, $u_t = n_y(1.5u_1 - u_2) - n_x(1.5v_1 - v_2)$ where n_x and n_y are the boundary normal components, u_w,v_w and t_w are the boundary velocity components and temperature, $val = 1.0 - 0.5(\gamma - 1)u_1^2$ and $s = \gamma M_\infty^2$. Values ϕ_{vc} are calculated using the compressible vortex correction of [86].

Boundary Type	First Halo Cell	Second Halo Cell
Far Field (no vortex correction)	$\rho_{b1} = 1.0$ $u_{b1} = u_\infty$ $v_{b1} = v_\infty$ $p_{b1} = p_\infty$	$\rho_{b2} = \rho_{b1}$ $u_{b2} = u_{b1}$ $v_{b2} = v_{b1}$ $p_{b2} = p_{b1}$
Far Field (vortex correction)	$\rho_{b1} = \rho_{vc}$ $u_{b1} = u_{vc}$ $v_{b1} = v_{vc}$ $p_{b1} = p_{vc}$	$\rho_{b2} = \rho_{b1}$ $u_{b2} = u_{b1}$ $v_{b2} = v_{b1}$ $p_{b2} = p_{b1}$
Wall (inviscid)	$\rho_{b1} = \rho_e$ $u_{b1} = 2(u_w + u_t n_y) - u_1$ $v_{b1} = 2(v_w - v_t n_x) - v_1$ $p_{b1} = p_e$	$\rho_{b2} = 2\rho_{b1} - \rho_1$ $u_{b1} = 2(u_w + u_t n_y) - u_2$ $v_{b1} = 2(v_w - v_t n_x) - v_2$ $p_{b2} = 2p_{b1} - p_1$
Wall (viscous adiabatic)	$\rho_{b1} = \rho_1$ $u_{b1} = 2u_w - u_1$ $v_{b1} = 2v_w - v_1$ $p_{b1} = p_1$	$\rho_{b2} = \rho_{b1}$ $u_{b2} = 2u_w - u_2$ $v_{b2} = 2v_w - v_2$ $p_{b2} = p_{b1}$
Wall (viscous isothermal)	$\rho_{b1} = 2s * p_{b1}/t_w - \rho_1$ $u_{b1} = 2u_w - u_1$ $v_{b1} = 2v_w - v_1$ $p_{b1} = p_1$	$\rho_{b1} = 2s * p_{b1}/t_w - \rho_2$ $u_{b2} = 2u_w - u_2$ $v_{b2} = 2v_w - v_2$ $p_{b2} = p_{b1}$
0th extrapolation	$\rho_{b1} = \rho_1$ $u_{b1} = u_1$ $v_{b1} = v_1$ $p_{b1} = p_1$	$\rho_{b2} = \rho_1$ $u_{b2} = u_1$ $v_{b2} = v_1$ $p_{b2} = p_1$
1st extrapolation (pext¡0)	$\rho_{b1} = \rho_e$ $u_{b1} = u_e$ $v_{b1} = v_e$ $p_{b1} = p_e$	$\rho_{b2} = 2\rho_{b1} - \rho_1$ $u_{b2} = 2u_{b1} - u_1$ $v_{b2} = 2v_{b1} - v_1$ $p_{b2} = 2p_{b1} - p_1$
1st extrapolation (pext¿0)	$\rho_{b1} = \rho_e$ $u_{b1} = u_e$ $v_{b1} = v_e$ $p_{b1} = pext$	$\rho_{b2} = 2\rho_{b1} - \rho_1$ $u_{b2} = 2u_{b1} - u_1$ $v_{b2} = 2v_{b1} - v_1$ $p_{b2} = pext$
1st extrapolation (pext¡0)	$\rho_{b1} = \rho_{file}$ $u_{b1} = u_{file}$ $v_{b1} = v_{file}$	$\rho_{b2} = \rho_{b1}$ $u_{b2} = u_{b1}$ $v_{b2} = v_{b1}$

Boundary Type	First Halo Cell	Second Halo Cell
Far Field	$k_{b1} = k_\infty$	$k_{b1} = k_\infty$
	$\omega_{b1} = \omega_\infty$	$\omega_{b2} = \omega_{b1}$
reservoir	$k_{b1} = k_\infty$	$k_{b1} = k_\infty$
	$\omega_{b1} = \omega_\infty$	$\omega_{b2} = \omega_{b1}$
Wall	$k_{b1} = -k_1$	$k_{b2} = -k_2$
	$\omega_{b1} = 2\omega_w - \omega_1$	$\omega_{b2} = 2\omega_w - \omega_2$
0th extrapolation	$k_{b1} = k_1$	$k_{b1} = k_{b1}$
	$\omega_{b1} = \omega_1$	$\omega_{b2} = \omega_{b1}$
1st extrapolation	$k_{b1} = k_1$	$k_{b2} = k_{b1} - k_1$
	$\omega_{b1} = \omega_1$	$\omega_{b2} = 2\omega_{b1} - \omega_1$
symmetry	$k_{b1} = k_1$	$k_{b2} = k_2$
	$\omega_{b1} = \omega_1$	$\omega_{b2} = \omega_2$

Table B.2: Boundary conditions for the turbulent flow equations

B.5 Spatial Discretisation for Turbulent Flow Equations

The semi-discrete form of the $k - \omega$ turbulence model is given by

$$\frac{d\mathbf{q}_{i,j}}{dt} = -\mathbf{Q}_{i,j}. \tag{B.30}$$

Here $\mathbf{Q}_{i,j}$ denotes the discretisation of the spatial and source terms. The convective terms are discretised by the Engquist-Osher method [27], considering the k and ω equations as decoupled scalar equations with a prescribed velocity field. The spatial discretisation is either first or third order accurate using MUSCL interpolation and the limiters as described for the mean flow equations. The viscous diffusion terms are discretised in an identical fashion to those in the mean flow equations. The source term is evaluated at the cell centre, using the approach described above for the evaluation of derivatives in equation (B.28).

The turbulent boundary conditions are implemented as for the mean flow values.

The halo values are given in table B.2 where

$$\omega_w = \frac{60\mu_{wall}}{\beta_1 * \rho_w * Re * d^2} \tag{B.31}$$

where d is the normal distance from the wall interface centre to the centre of the first interior cell.

B.6 Steady State Solver for Inviscid and Laminar Cases

The integration in time of equation (B.26) to a steady-state solution is performed using an implicit time-marching scheme:

$$\frac{\mathbf{W}^{n+1} - \mathbf{W}^n}{\Delta t} = -\mathbf{R}^{n+1} \tag{B.32}$$

where subscripts (i, j) are neglected for clarity. The above equation represents a system of non-linear algebraic equations and to simplify the solution procedure, the flux residual $\mathbf{R}^{n+1}$ is linearised in time as follows:

$$\begin{aligned} \mathbf{R}^{n+1} &= \mathbf{R}^n + \frac{\partial \mathbf{R}}{\partial t}\Delta t + O(\Delta t^2) \\ &\approx \mathbf{R}^n + \frac{\partial \mathbf{R}}{\partial \mathbf{W}}\frac{\partial \mathbf{W}}{\partial t}\Delta t \\ &\approx \mathbf{R}^n + \frac{\partial \mathbf{R}}{\partial \mathbf{W}}\Delta W \end{aligned} \tag{B.33}$$

where $\Delta\mathbf{W} = \mathbf{W}^{n+1} - \mathbf{W}^n$. Equation (B.32) now becomes the following linear system:

$$\left(\frac{I}{\Delta t} + \frac{\partial \mathbf{R}}{\partial \mathbf{W}}\right)\Delta\mathbf{W} = -\mathbf{R}^n \tag{B.34}$$

The complexity of a direct method to compute a linear system is of the order of $\mathcal{N}^3$, which becomes prohibitive when the total number of equations $\mathcal{N}$ becomes large. On the other hand, iterative techniques such as Conjugate Gradient (CG) methods are capable of solving large systems of equations more efficiently in terms of time and memory. CG methods find an approximation to the solution of a linear system by minimising a suitable residual error function in a finite-dimensional space of potential solution vectors. Several algorithms, such as BiCG, CGSTAB, CGS and

GMRES, have been tested in [7] and it was concluded that the choice of method is not as crucial as the preconditioning. The current results use a Generalised Conjugate Gradient method [5].

The preconditioning strategy is based on a Block Incomplete Lower-Upper factorisation [5] since it appears to be the most promising. The sparsity pattern of the Lower and Upper matrices is defined with respect to the sparsity of the unfactored matrix for simplicity.

Implicit schemes require particular treatment during the early stages of the iterative procedure. The usual approach in starting the method is to take a small CFL number and to increase it later on. However, it was found that smoothing out the initial flow doing some explicit iterations, and then switching to the implicit algorithm was equally efficient. In the present method, a specified number of forward Euler iterations are executed before switching to the implicit scheme.

The inviscid fluxes are calculated using an upwind scheme. Hence, the numerical flux across an edge depends on the values of the flow variables on either side of the edge. For example, for the interface between cell (i, j) and cell $(i+1, j)$:

$$\mathbf{F}_{i+\frac{1}{2},j} = \mathbf{F}\left(\mathbf{W}^{+}_{i+\frac{1}{2},j}, \mathbf{W}^{-}_{i+\frac{1}{2},j}\right) \tag{B.35}$$

where the left and right states are extrapolated using a MUSCL interpolation, leading to the following relations:

$$\begin{aligned} \mathbf{W}^{-}_{i+\frac{1}{2},j} &= \mathcal{F}\left(\mathbf{W}_{i-1,j}, \mathbf{W}_{i,j}, \mathbf{W}_{i+1,j}, \mathbf{W}_{i+2,j}\right) \\ \mathbf{W}^{+}_{i+\frac{1}{2},j} &= \mathcal{G}\left(\mathbf{W}_{i-1,j}, \mathbf{W}_{i,j}, \mathbf{W}_{i+1,j}, \mathbf{W}_{i+2,j}\right) \end{aligned} \tag{B.36}$$

As a result, the flux residual for cell (i, j) is a function of nine points:

$$\mathbf{R}_{i,j} = \mathbf{R}\left(\mathbf{W}_{i-2,j}, \mathbf{W}_{i-1,j}, \mathbf{W}_{i,j}, \mathbf{W}_{i+1,j}, \mathbf{W}_{i+2,j}, \mathbf{W}_{i,j-2}, \mathbf{W}_{i,j-1}, \mathbf{W}_{i,j+1}, \mathbf{W}_{i,j+2}\right)$$

The above formulation for $\mathbf{R}_{i,j}$ leads to a Jacobian matrix $\partial\mathbf{R}/\partial\mathbf{W}$ which has nine non-zero entries per row. However, trying to reduce the number of non-zero blocks would have several advantages. Firstly, the memory requirements are lowered. Secondly, the resolution of the linear system by the CG method is faster in terms of CPU-time since all the matrix-vector multiplications involved require less operation counts. Finally, the linear system is easier to solve since the approximate Jacobian

matrix is more diagonally dominant. A full discussion of the approximate Jacobian formulation is given in [18].

An approximation to the exact Jacobian arises from neglecting the influence of the MUSCL interpolation:

$$\begin{aligned} \mathbf{W}^{-}_{i+\frac{1}{2},j} &= \mathcal{F}'\left(\mathbf{W}_{i,j}\right) \\ \mathbf{W}^{+}_{i+\frac{1}{2},j} &= \mathcal{G}'\left(\mathbf{W}_{i+1,j}\right) \end{aligned} \tag{B.38}$$

The flux residual now becomes a function of only five points:

$$\mathbf{R}_{i,j} = \mathbf{R}'\left(\mathbf{W}_{i-1,j}, \mathbf{W}_{i,j}, \mathbf{W}_{i+1,j}, \mathbf{W}_{i,j-1}, \mathbf{W}_{i,j+1}\right) \tag{B.39}$$

This approximation, which is applied only for the derivation of the Jacobian terms, reduces memory requirements and matrix-vector multiplication operation counts to 5/9 of the values using the exact Jacobians.

The discretisation of the viscous terms leads to a viscous flux residual which is a function of the following nine points: $\mathbf{W}_{i-1,j-1}$, $\mathbf{W}_{i,j-1}$, $\mathbf{W}_{i+1,j-1}$, $\mathbf{W}_{i-1,j}$, $\mathbf{W}_{i,j}$, $\mathbf{W}_{i+1,j}$, $\mathbf{W}_{i-1,j+1}$, $\mathbf{W}_{i,j+1}$ and $\mathbf{W}_{i+1,j+1}$. An exact derivation of the inviscid and viscous Jacobians together would involve four more terms in addition to the nine above: $\mathbf{W}_{i-2,j}$, $\mathbf{W}_{i+2,j}$, $\mathbf{W}_{i,j-2}$ and $\mathbf{W}_{i,j+2}$.

However, in view of the computational results presented in the previous section, it seems more interesting from a storage and CPU-time point of view to derive an approximate formulation for the viscous Jacobians based on equation (B.39). Indeed, such an approach would give savings of 8/13 for the memory requirements and any matrix-vector multiplication operation counts. A simple approximation results from taking into account only the influence of the two points situated either side of the considered edge during the calculation of the viscous flux across a cell interface. For example, the contributions of $\mathbf{W}_{i,j-1}$, $\mathbf{W}_{i,j+1}$, $\mathbf{W}_{i+1,j-1}$ and $\mathbf{W}_{i+1,j+1}$ are neglected and only the terms arising from $\mathbf{W}_{i,j}$ and $\mathbf{W}_{i+1,j}$ are kept. This amounts to making a thin layer approximation for the derivation of the viscous Jacobians in the direction normal to the edge.

B.7 Steady State Solver for Turbulent Case

The integration in time of equation (B.30) to a steady-state solution is performed using an implicit time-marching scheme:

$$\frac{\mathbf{q}^{n+1} - \mathbf{q}^n}{\Delta t} = -\mathbf{Q}^{n+1}. \tag{B.40}$$

This nonlinear system of equations is formulated and solved in an identical manner to that described above for the mean flow. Equations (B.32) and (B.40) are solved in sequence, i.e. the eddy-viscosity is regarded calculated from the latest values of k and ω and is used to advance the mean flow solution and then this new solution is used to update the turbulence solution, freezing the mean flow values.

An approximate Jacobian is used for the source term by only taking into account the contribution of the dissipation terms $\hat{\mathbf{D}}_k$ and $\hat{\mathbf{D}}_\omega$ i.e. no account of the production terms is taken on the left hand side of (B.40). This approach has a stability advantage as described in [92].

B.8 Unsteady Flow Solver

The formulation is described for the turbulent case. The laminar and inviscid cases represent a simplification of this.

Following the pseudo-time formulation [45], the updated mean flow solution is calculated by solving the steady state problems

$$\mathbf{R}^*_{i,j} = \frac{3\mathbf{w}^{n+1}_{i,j} - 4\mathbf{w}^n_{i,j} + \mathbf{w}^{n-1}_{i,j}}{2\Delta t} + \mathbf{R}_{i,j}(\tilde{\mathbf{w}}^{k_m}_{i,j}, \tilde{\mathbf{q}}^{k_t}_{i,j}) = 0 \tag{B.41}$$

$$\mathbf{Q}^*_{i,j} = \frac{3\mathbf{q}^{n+1}_{i,j} - 4\mathbf{q}^n_{i,j} + \mathbf{q}^{n-1}_{i,j}}{2\Delta t} + \mathbf{Q}_{i,j}(\tilde{\mathbf{w}}^{l_m}_{i,j}, \tilde{\mathbf{q}}^{l_t}_{i,j}) = 0. \tag{B.42}$$

Here k_m, k_t, l_m and l_t give the time level of the variables used in the spatial discretisation. Note that for the problems of this paper the grid is moved rigidly but if grid deformation was required then time varying areas would be required [24] in the expression for the real time derivative in equations (B.41) and (B.42). If $k_m = k_t = l_m = l_t = n + 1$ then the mean and turbulent quantities are advanced in real time in a fully coupled manner. However, if $k_m = l_m = l_t = n + 1$ and

$k_t = n$ then the equations are advanced in sequence in real time, i.e. the mean flow is updated using frozen turbulence values and then the turbulent values are updated using the latest mean flow solution. This has the advantage that the only modification, when compared with the laminar case, to the discretisation of the mean flow equations is the addition of the eddy viscosity from the previous time step. The turbulence model only influences the mean flow solution through the eddy viscosity and so any two equation model can be used without modifying the mean flow solver. Hence, the implementation is simplified by using a sequenced solution in real time. However, the uncoupling could adversely effect the stability and accuracy of the real time stepping, with the likely consequence of limiting the size of the real time step that can be used.

Equations (B.41) and (B.42) represent a coupled nonlinear system of equations. These can be solved by introducing an iteration through *pseudo time* τ to the steady state, as given by

$$\frac{\mathbf{w}_{i,j}^{n+1,m+1} - \mathbf{w}_{i,j}^{n+1,m}}{\Delta\tau} + \frac{3\mathbf{w}_{i,j}^{k_m} - 4\mathbf{w}_{i,j}^{n} + \mathbf{w}_{i,j}^{n-1}}{2\Delta t} + \mathbf{R}_{i,j}(\tilde{\mathbf{w}}_{i,j}^{k_m}, \tilde{\mathbf{q}}_{i,j}^{k_t}) = 0 \qquad \text{(B.43)}$$

$$\frac{\mathbf{q}_{i,j}^{n+1,m+1} - \mathbf{q}_{i,j}^{n+1,m}}{\Delta\tau} + \frac{3\mathbf{q}_{i,j}^{l_t} - 4\mathbf{q}_{i,j}^{n} + \mathbf{q}_{i,j}^{n-1}}{2\Delta t} + \mathbf{Q}_{i,j}(\tilde{\mathbf{w}}_{i,j}^{l_m}, \tilde{\mathbf{q}}_{i,j}^{l_t}) = 0. \qquad \text{(B.44)}$$

where the $m-th$ pseudo-time iterate at the $n+1th$ real time step are denoted by $\mathbf{w}^{n+1,m}$ and $\mathbf{q}^{n+1,m}$ respectively. The iteration scheme used only effects the efficiency of the method and hence we can sequence the solution in pseudo time without compromising accuracy. Examples of For example, using explicit time stepping we can calculate $\mathbf{w}^{n+1,m+1}$ using $k_m = n+1, m$ and $k_t = n+1, m$ and $\mathbf{q}^{n+1,m+1}$ using $l_m = n+1, m+1$ and $l_t = n+1, m$. For implicit time stepping in pseudo time we can use $k_m = l_m = l_t = n+1, m+1$ and $k_t = n+1, m$. In both of these cases the solution of the equations is decoupled by freezing values but at convergence the real time stepping procedes with no sequencing error. It is easy to recover a solution which is sequenced in real time from this formulation by setting $k_t = n$ throughout the calculation of the pseudo steady state. This facilitates a comparison of the current pseudo time sequencing with the more common real time sequencing. In the code the pseudo steady-state problems are solved using the implicit steady state solver described above.

B.9 Mesh Treatment

There are two mesh movement methods available in the code. The simplest involves rigid mesh rotation and translation in the y-direction. The second involves a more flexible regeneration method by transfinite interpolation of displacements. The mesh velocities and boundary velocities are calculated from the difference formula

$$\frac{dx}{dt} \approx \frac{3\mathbf{x}_{i,j}^{n+1} - 4\mathbf{x}_{i,j}^{n} + \mathbf{x}_{i,j}^{n-1}}{2\Delta t}. \tag{B.45}$$

The cell areas are either calculated algebraically from the vertex locations using a cross product or are obtained from the Global Conservation Law.

When computing the flow on a moving grid, the cell areas vary in time and it is therefore important to discretise the time-dependent metrics carefully in order to maintain the conservative properties of the scheme. If the cell areas are calculated analytically in terms of the grid node positions, numerical errors will be introduced in the calculated solution which increase with time. To avoid such numerical errors, the cell areas must be integrated forward in time by using the same method as used to solve the flow conservation laws [87]. This is achieved by introducing a Geometric Conservation Law (GCL) which can be derived from the continuity conservation law written in integral form by assuming a uniform flow field. This yields,

$$\frac{\partial}{\partial t}\int_{\Omega} dV - \oint_{\partial\Sigma} \mathbf{v}\cdot\mathbf{n}d\Sigma = 0 \tag{B.46}$$

where V is the cell area, $\mathbf{v}$ is the grid speed, $\mathbf{n}$ is the normal area vector and $\partial\Sigma$ is the boundary surface of the control volume Ω. Using the same second-order time discretisation as for the flow equations [24], equation (B.46) becomes

$$\frac{3V_{i,j}^{n+1} - 4V_{i,j}^{n} + V_{i,j}^{n-1}}{2\Delta t} - \oint_{\partial\Sigma} \mathbf{v}\cdot\mathbf{n}d\Sigma = 0 \tag{B.47}$$

This law states that the change in area of each control volume between t^n and t^{n+1} must be equal to the area swept by the cell boundary during $\Delta t = t^{n+1} - t^n$. The volume $V_{i,j}^{n+1}$ at the new time step can then be computed by

$$V_{i,j}^{n+1} = \frac{4V_{i,j}^{n}}{3} - \frac{V_{i,j}^{n-1}}{3} + \frac{2\Delta t}{3}\oint_{\partial\Sigma} \mathbf{v}\cdot\mathbf{n}d\Sigma \tag{B.48}$$

where

$$\oint_{\partial\Sigma} \mathbf{v}\cdot\mathbf{n}d\Sigma = (\xi_t)_{i+1/2,j} - (\xi_t)_{i-1/2,j} + (\eta_t)_{i,j+1/2} - (\eta_t)_{i,j-1/2}$$

and

$$\xi_t = -(\xi_x x_t + \xi_y y_t), \qquad \eta_t = -(\eta_x x_t + \eta_y y_t)$$

Note that this is an explicit equation for $V_{i,j}^{n+1}$ since the terms ξ_t and η_t are prescribed from the node values. Using the GCL to calculate the volumes numerically rather than analytically yields a self-consistent solution for the effective volume elements. In other words, it ensures that errors arising from the computation of the geometric quantities are consistent with those arising from the integration of the flow equations. The importance of the GCL for flow computations on moving grids has been described in [87] [1] [34] [53] [91]. The GCL needs to be evaluated once at every global time step to calculate the new cell areas.

The mesh regeneration is achieved through the transfinite interpolation (TFI) of displacements within the multiblock method.

We first need to determine the displacements of the four block corners (or block vertices). In order to identify a moving block from a fixed block, we introduce a new parameter MOVE in the grid file which is set to one for each moving block and to zero for all fixed blocks. For each block corner, a search is made over its neighbours, and if at least one of the neighbouring blocks surrounding this corner point (i.e., all blocks having this point as a vertex) is fixed (i.e., block flagged with MOVE=0), then no displacement is allowed for this point. Otherwise, the corner point is moved according to the motion of the solid surface. The displacement of all points lying on a moving surface is assumed to be known. In the present work, we consider only rigid motions for oscillating pitching aerofoils and oscillating flaps, but the application of the method can be easily extended to more complex configurations and more general deformations.

The displacements of the four corner points are then used to interpolate the displacement of all the points along the block boundary. We denote by bfx and $dbfx$ the position vector and displacement vector respectively associated with the

grid points of the mesh,

$$bfx = \begin{bmatrix} x(\xi,\eta) \\ y(\xi,\eta) \end{bmatrix}, dbfx = \begin{bmatrix} dx(\xi,\eta) \\ dy(\xi,\eta) \end{bmatrix}$$

Let A and B be the two end-points of a block face with respective displacements denoted by $dbfx_A$and $dbfx_B$ respectively. The displacement $dbfx$ of any point P along this boundary can then be obtained by the weighted formula

$$dbfx = \left(1 - \frac{a}{c}\right) dbfx_A + \left(1 - \frac{b}{c}\right) dbfx_B$$

where $a = ||\vec{AP}||$, $b = ||\vec{BP}||$ and $c = ||\vec{AB}||$. Here, the distances are calculated from the previous grid point coordinates. If both end-points are fixed (i.e., zero displacement), then the whole block face remains fixed.

Following the original formulation of the TFI algorithm described by Gordon and Hall [35], the general transfinite interpolation method results in a recursive algorithm which is here applied to the grid point displacements :

$$\begin{aligned} dbfx(\xi,\eta) = bff_1(\xi,\eta) &+ \phi_1^0(\eta)\left[dbfx_{b1}(\xi) - bff_1(\xi,0)\right] \\ &+ \phi_2^0(\eta)\left[dbfx_{b3}(\xi) - bff_1(\xi,1)\right] \end{aligned}$$

where

$$bff_1(\xi,\eta) = \psi_1^0(\xi) dbfx_{b4}(\eta) + \psi_2^0(\xi) dbfx_{b2}(\eta)$$

and $dbfx_{b1}$,$dbfx_{b2}$,$dbfx_{b3}$,and $dbfx_{b4}$ are the interpolated displacements along the four block faces. The functions ψ and ϕ are the blending functions in the ξ and η directions respectively. These functions are given by the grid point distributions along each block face as

$$\begin{aligned} \psi_1^0(\xi) &= 1 - s_1(\xi) \\ \psi_2^0(\xi) &= s_3(\xi) \\ \phi_1^0(\eta) &= 1 - s_4(\eta) \\ \phi_2^0(\eta) &= s_2(\eta) \end{aligned}$$

where $s_1(\xi)$ is the stretching function on the block face $\eta = 0$, $s_2(\eta)$ on the block face $\xi = 1$, $s_3(\xi)$ on the block face $\eta = 1$, $s_4(\eta)$ on the block face $\xi = 0$. The coordinates of the new grid points are then simply obtained by

$$bfx(\xi, \eta) = bfx_0(\xi, \eta) + dbfx(\xi, \eta)$$

where $dbfx$ is the interpolated displacement and bfx_0 is the vector position for the initial undisturbed grid.

B.10 Pitch-Plunge Solver

The structural model available in the code assumes that the aerofoil responds to the flow by moving in pitch and plunge, with a linear restoring force being exerted by the rest of the wing. Following the formulation of [51], the equations describing this are

$$\frac{d\mathbf{q}}{dt} = \mathbf{F}(\mathbf{q}, \mathbf{w}) \tag{B.49}$$

where $\mathbf{q} = (\alpha, h, d\alpha/dt, dh/dt)^T$, α is the aerofoil incidence and h is the vertical displacement non dimensionalised by the semi-chord, measured positive downwards. The vector on the right hand side is $\mathbf{F}(\mathbf{q}, \mathbf{w}) = (q_3, q_4, F_3, F_4)^T$ where, denoting $\tilde{\mathbf{q}} = (q_1, q_2)^T$, $\tilde{\mathbf{F}} = (F_3, F_4)^T$ is given by

$$\tilde{\mathbf{F}} = \mathbf{F}_a(\mathbf{w}) - M^{-1}K\tilde{\mathbf{q}}$$

where

$$\mathbf{M} = \begin{bmatrix} 1 & x_\alpha \\ x_\alpha & r_\alpha^2 \end{bmatrix}$$

$$\mathbf{K} = \begin{bmatrix} \omega_R^2 & 0 \\ 0 & r_\alpha^2 \end{bmatrix}, \mathbf{F}_a = \begin{bmatrix} -C_L/\beta \\ 2C_M/\beta \end{bmatrix}$$

and $\beta = 4\overline{U}/(\pi\mu\omega_\alpha^R)$. The notation and values used here are

- C_L and C_M are the lift and moment coefficients obtained from the flow solution
- M and K are the mass and stiffness matrices respectively

- x_α is the offset between the centre of gravity and the point about which the pitching motion takes place (called the elastic axis) , measured negative for the centre of gravity aft of the elastic axis
- r_α^2 is the radius of gyration, representing the effect of the moment of inertia about the elastic axis
- ω_R^2 is the square of the ratio of the natural frequencies of plunging ω_h to pitching ω_α
- μ is the ratio of the aerofoil to fluid mass
- $\overline{U} = 4b/(U_\infty \omega_\alpha)$ is called the reduced velocity of the problem where U_∞ is the freestream fluid velocity and b is the aerofoil chord length. Increasing values of the reduced velocity indicate an increasingly flexible structure.

Note that the non-dimensionalisation of time for the structural model is with respect to $U_\infty/2b$. The values of plunge and time are converted by the factors 0.5 and $2.0/\overline{U}$ when going from the flow solver to the structural solver and the reciprocal of these when going from the structural solver to the flow solver.

The structural equations are solved using the standard fourth order Runge-Kutta method. When using Using the solution of equation (B.49), the geometry for the flow problem can now be denoted $\Gamma = \Gamma(\alpha, h)$, and hence depends on the structural solution. In return, the structural solution depends on the flow solution through the the lift and moment coefficients. Following the pseudo-time approach of Jameson for the flow solution and using a Runge Kutta solution for the structural solution, the updated flow and structural solutions at time n+1 are calculated from the nonlinear system of algebraic equations

$$\mathbf{R}^*_{i,j} = \frac{3\mathbf{w}^{n+1}_{i,j} - 4\mathbf{w}^{n}_{i,j} + \mathbf{w}^{n-1}_{i,j}}{2\Delta t} + \mathbf{R}_{i,j}(\mathbf{w}^{n+1}_{i,j}) = 0 \tag{B.50}$$

for $\Gamma = \Gamma(\alpha^{n+1}, h^{n+1})$ and

$$\mathbf{q}^{n+1} = \mathbf{G}(\mathbf{q}^n, C_L^n, C_M^n, C_L^{n+1}, C_M^{n+1}) \tag{B.51}$$

where $\mathbf{G}$ indicates the Runge-Kutta solution. If an uncoupled solution is used then lift and moment values at time levels n-1 and n are used to extrapolate for the

values at n+1. The updated structural solution is then used to update the flow solution. However, the mismatch between the lift and moment values associated with the flow solution and the extrapolated values used to update the flow solution introduces a source of error into the calculation which is potentially serious since it is associated with the transfer of energy between the fluid and structure which is the crucial feature of the problem. We refer to this method as being sequenced in real time.

This phasing error was removed in [15] by using the same Runge Kutta method to update the flow instead of equation (B.50). However, using an explicit method to update the flow values incurs a stability restriction on the size of the time step. Using equation (B.50) is preferable from this point of view since the time step can be chosen on the basis of time accuracy alone. Equation (B.50) is solved by introducing an iteration $\mathbf{w}_{i,j}^{n+1,m}$ through pseudo time which converges to the updated flow solution. The method used to solve the pseudo time problem is discussed in detail in [18], [24] and [9] and involves implicit time stepping and a Krylov type linear solver. Multigrid is an attractive alternative for solving the pseudo steady state problem. An iteration for the structural solution can be introduced so that the latest approximation to the updated lift and moment values is used to calculate a better approximation to the updated pitch and plunge, i.e.

$$\mathbf{q}^{n+1,m+1} = \mathbf{G}(\mathbf{q}^n, C_L^n, C_M^n, C_L^{n+1,m+1}, C_M^{n+1,m+1}).$$

The $m+1$th flow iterate is calculated for the geometry $\Gamma = \Gamma(\alpha^{n+1,m}, h^{n+1,m})$. The mesh velocities required for the transformation are calculated from the mesh locations at time n and pseudo time iterate n+1,m. At convergence the structural solution has been updated using the the correct moment and lift values. The solution is sequenced in pseudo time, with the solution being coupled in real time.

B.11 Axisymmetric Code

B.11.1 Mean flow equations

In the present method, the equations for axisymmetric flow are formulated to look like the planar flow equations except for a non-zero right-hand side which is treated

as a source term. The fluxes on the left-hand side are treated as in the two-dimensional (planar) case, see Section B.4. The inviscid part of the source term is treated implicitly, but the viscous part is treated explicitly. Numerical experiments have shown that it is necessary to have an implicit treatment for the axisymmetric inviscid terms if a tight restriction on the allowable time step is to be avoided. The explicit treatment of the axisymmetric viscous terms does not have a deleterious effect on stability or limit the allowable time step, on comparison with the original planar code, so an implicit treatment was not attempted. The modified linear system for the axisymmetric case is then written as :

$$\left(\frac{I}{\Delta t} + \frac{\partial\left(\mathbf{R} - \mathbf{H}_i\right)}{\partial \mathbf{W}}\right) \Delta \mathbf{W} \;=\; -\mathbf{R}^n + \mathbf{H}_i^n + \mathbf{H}_v^n \tag{B.52}$$

where $\mathbf{H}_i$ and $\mathbf{H}_v$ are the inviscid and viscous parts respectively of the discretised source term. System (B.52) is solved using an identical scheme as used for (B.34). The inviscid source term Jacobian is evaluated as

$$\frac{\partial \mathbf{H}_i}{\partial \mathbf{W}} \;=\; -\frac{1}{r}\begin{bmatrix} v_r & 0 & \rho & 0 \\ v_r v_z & \rho v_r & \rho v_z & 0 \\ v_r^2 & 0 & 2\rho v_r & 0 \\ v_r \frac{|\vec{V}|^2}{2} & \rho v_r v_z & \frac{\gamma}{\gamma-1}p + \rho\frac{|\vec{V}|^2}{2} + \rho v_r^2 & \frac{\gamma}{\gamma-1}v_r \end{bmatrix} \tag{B.53}$$

where $|\vec{V}|^2 = v_r^2 + v_z^2$.

B.11.2 Turbulent flow equations

For the turbulent flow equations the modification of the linear system to include the additional axisymmetric source terms is performed in an analogous manner:

the 'inviscid' parts of the additional source term $\mathbf{H}_T$ are treated implicitly, and the 'viscous' parts explicitly. The Jacobian of the additional axisymmetric source term is then written as

$$\frac{\partial \mathbf{H}_T}{\partial \mathbf{q}} = -\frac{1}{r}\begin{bmatrix} \frac{5}{3}\rho v_r & 0 \\ 0 & \left(1+\frac{2}{3}\alpha\right)\rho v_r \end{bmatrix} \tag{B.54}$$

For full details see [38].

B.12 Test Cases

The following is a list of reports and publications associated with Pmb2d.

B.13 Further assistance

Contact the CFD group, Aerospace Engineering Department, University of Glasgow, for further assistance.

Any comments or suggestions are welcomed and should be addressed to Ken Badcock at the University of Glasgow (gnaa36@aero.gla.ac.uk).

Reference	Year	Main Points
[6]	1995	steady multiblock test cases single aerofoil tests on preconditioning
[36]	1996	steady multiblock test cases two aerofoil configurations Williams aerofoil
[24]	1997	unsteady Euler test cases single and multi-element aerofoil configurations pseudo time method - mesh deformation
[18]	1997	steady N-S test cases single aerofoil configurations approximate Jacobians
[8]	1997	laminar cavity test cases cavity configurations
[9]	1997	unsteady turbulent test cases single aerofoil configurations sequencing of turbulence model
[38]	1998	axisymmetric test cases ogive and afterbody configurations axisymmetric treatment
[26]	1998	unsteady mesh treatment single and multi-element aerofoil configurations mesh deformation and GCL
[37]	1998	underexpanded jet study shock wave reflection
[29]	1999	supersonic flow over cylinders
[30]	1999	supersonic flow over spiked bodies
[43]	1999	cavity flow

Appendix C

Animations CD-ROM

A CD-ROM containing the animations of the analysed cavity flows has been enclosed to aid the undersatnding of the flow features. The film of aircraft and stores compatibility testing by Charles Epstein has also been included.

Movies are provided for the clean cavity case, sloped 63.4° cavity and the transitonal cavity flow: the movies show the pressure contours, streamlines and vorticity contours. Each animation is provided in .rm format and accompanied by the executable framer.exe to enable their visualisation on a pc. To view either use the mouse to move forward frames in the movie or hit 'L' on the keyboard for the movie to loop. The full contents of the CD-ROM is given in Table C.1.

Case	Pressure Contours movie filename	Streamlines movie filename	Vorticity Magnitude contours movie filename
Mach 0.85 L/D=5 Clean	pres.rm	stre.rm	vort.rm
Mach 0.85 L/D=5 Slope 63.4°	pres.rm	stre.rm	vort.rm
Mach 0.9 L/D=8	pres.rm	stre.rm	vort.rm

Table C.1: Contents of the CD-ROM of animations.

Bibliography

[1] Allen, C.B. Central-difference and upwind-biased schemes for steady and unsteady Euler aerofoil computations. *Aeronautical Journal*, 52–62, 1995.

[2] Ames Research Staff. Equations, Tables, and Charts for Compressible Flow. *NACA Rep 1135*, 1953.

[3] Anderson, D.A., Tannehill, J.C., and Pletcher, R.H. Computational Fluid Mechanics and Heat Transfer. *Series in Computational Methods in Mechanics and Thermal Sciences*, 1984.

[4] Anderson, W.K., Thomas, J.L., and Van leer, B. Comparison of finite volume flux vector splittings for the Euler equations. *AIAA Journal*, 24, 1453–1460, 1986.

[5] Axelsson, O. Iterative Solution Methods. *Cambridge University Press*, 1994.

[6] Badcock, K.J., Porter, S., andRichards, B.E. Unfactored multiblock methods:Part I initial method development. *Aerospace Engineering Report 11, Glasgow University, Glasgow, UK*, 1995.

[7] Badcock, K.J., Xu, X., Dubuc, L., and Richards, B.E. Preconditioners for high speed flows in aerospace engineering. *Numerical Methods for Fluid Dynamics V*, pp. 287–294, 1996.

[8] Badcock, K.J., Gribben, B.J., Dubuc, L., Cantariti,F., Woodgate, M.A. and Richards, B.E. Demonstration of PMB for Cavity Calculations. *University of Glasgow, Aerospace Engineering report 9712*, 1997.

[9] Badcock, K.J., Goura, G.S.L., and Richards, B.E. Investigation of sequencing effects on the simulation of fluid-structure interaction. *Aerospace Engineering Report, 13, Glasgow University, Glasgow, UK*, 1997.

[10] Badcock, K.J. Review of Cavity GAP modelling study. *BAE SYSTEMS report BAE-WAE-RP-GEN-001041*, 2000.

[11] Badcock, K.J., Richards, B.E. and Woodgate, M.A. Elements of Computational Fluid Dynamics on block structured grids using implicit solvers. *Progress in Aerospace Sciences*, 36, pp 351-392, 2000.

[12] Badcock, K.J., Cantariti, F., Hawkins, I., Woodgate, M., Dubuc, L. and Richards, B.E. Simulation of Unsteady Turbulent Flows around Moving Aerofoils using the Pseudo time method. *Int J Num Meth in Fluids*, 2000.

[13] Batten, P., Goldberg, U. and Chakravarthy, S. Sub-grid turbulence modeling for unsteady flow with acoustic resonance. *AIAA-00-0473*, 2000.

[14] Baysal, O., Yen, G-W, Fouladi, K. Navier-Stokes Computations of cavity aeroacoustics with suppression devices. *Journal of Vibration and acoustics*, 11:102–112, 1994.

[15] Bendiksen, O.O. A new approach to computational aeroelasticity', in 32nd Structures. *Structural Dynamics and Materials Conference*, AIAA, 1991.

[16] Bilanin, A.J., and Covert, E.E. Estimation of Possible Excitation Frequencies for Shallow Cavities. *AIAA Journal*, 11, 1973.

[17] Block, P.J.W. and Tam, C.K.W. On the Tones and Pressure Oscillations Induced by the Flow over Rectangular Cavities. *Journal of Fluid Mechanics*, pp 373-399, 1978.

[18] Cantariti, F., Dubuc, L., Gribben, B., Woodgate, M., Badcock, K.J., and Richards, B.E. Approximate Jacobians for the solution of the Euler and Navier-Stokes equations. *Aerospace Engineering Report, 5*, Glasgow University, Glasgow, UK, 1997.

[19] Ceruzzi, P.E. Beyond the Limits. *National Air and Space Museum, The MIT Press*, 1999.

[20] Chapman, D.R., Kuen, D.M., and Larson, H.K. Investigation of Separated Flows in Supersonic and Subsonic Streams with Emphasis on the Effect of Transition. *NACA Rep 1356*, 1958.

[21] Charwat, A.F., Roos, R.N., Dewey Jr, F.C., and Hitz, J.A. An Investigation of Separated Flows- Part 1: The Pressure Field. *Journal of the Aerospace Sciences, Vol 28, Pt. 1, pp 457-470*, 1961.

[22] Clark, R.L. Evaluation of F-111 Weapon Bay Aero-Acoustic and Weapon Separation Improvement Techniques. *AFFDL-TR-79-3003*, February, 1979.

[23] Dorr, R.F. Washington watch. *Aerospace America*, August, 2001.

[24] Dubuc, L., Cantariti, F., Woodgate, M., Gribben, B., Badcock, K.J., and Richards, B.E. Solution of the Euler unsteady equations using deforming grids. *to appear in AIAA J.*

[25] Dubuc, L., Cantariti F., Woodgate, M., Gribben, B., Badcock, K.J. and Richards, B.E. Solution of the unsteady Euler equations using an implicit dual time method. *AIAA J*, 36, 1417-1424, 1998.

[26] Dubuc, L., Cantariti, F., Woodgate, M., Gribben, B., Badcock, K.J., and Richards, B.E. A grid deformation technique for unsteady flow computations. *Int J Num Meth Fluids*, 32, pp. 285-311, 2000.

[27] Enquist, B. and Osher, S. One–sided difference approximations for nonlinear conservation laws. *Math. Comp.*, 36 154, 321–351, 1981.

[28] Epstein, C. Aircraft/Stores Compatibility Testing. *CD-Rom included with thesis.*

[29] Feszty, D. Badcock, K.J. and Richards, B.E. Numerical Simulation of steady supersonic and hypersonic flows over simple bodies of revolution. *Glasgow University, Glasgow, UK*, Aerospace Engineering Report, 1999.

[30] Feszty, D. Badcock, K.J. and Richards, B.E. Numerical Simulation of High-speed unsteady flows over axisymmetric spiked bodies. *Glasgow University, Glasgow, UK*, Aerospace Engineering Report, 1999.

[31] Ffowcs-Williams. Aeroacoustics. *Annual Review of Fluid Mechanics*, Vol 9:447–468, 1977.

[32] Franke, M.E., and Carr, D.L. Effects of Geometry on Open Cavity Flow-Induced Pressure Oscillations. *AIAA Paper 75-492*, March, 1975.

[33] Gadd, G.E., Holder, D.W., and Regan, J.D. Base Pressures in Supersonic Flow. *ARC TR CP 271*, 1955.

[34] Gaitonde, A.L. A dual-time method for the solution of the unsteady Euler equations. *Aeronautical Journal*, 10, 1994.

[35] Gordon, W.J., and Hal, C.A. Construction of curvilinear coordinate systems and applications of mesh generation. *Int J Num Meth in Engineering*, 7, 461–477, 1973.

[36] Gribben, B.J. Progress report: Application of the multiblock method in computational aerodynamics. *Aerospace Engineering Report, 21, Glasgow University, Glasgow, UK*, 1996.

[37] Gribben, B.J, Badcock, K.J., and Richards, B.E. Shock reflection hysteresis in an underexpanded jet: a CFD study. *Glasgow University, Glasgow, UK.*

[38] Gribben, B.J. Application of the multiblock method in computational aerodynamics. *PhD thesis*, University of Glasgow, 1999.

[39] Gribben, B.J., Badcock, K.J. and Richards, B.E. Numerical Study of Shock Reflection Hysteresis in an Underexpanded Jet. *AIAA J*, Vol 38, 2000.

[40] Heller, H.H., Holmes, D.G., and Covert, E.E. Flow Induced Pressure Fluctuations in Shallow Cavities. *Journal of Sound and Vibration*, vol 18, 1971.

[41] Heller, H.H., and Bliss, D.B. The Physical Mechanism of Flow Induced Pressure Fluctuations in Cavities and Concepts for their Supression. *AIAA Paper 75-491*, 1975.

[42] Heller, H.H. and Delfs. J. Cavity Pressure Oscillations: The Generating Mechanism Visualised. *Journal of Sound and Vibration*, 196, 1996.

[43] Henderson, J., Badcock, K.J. and Richards, B.E. Closed, Transitional and Open Supersonic Cavity flow Simulations using Pmb2d. *Glasgow University, Glasgow, UK*, Aerospace Engineering Report, 1999.

[44] Henderson, J., Badcock, K.J, and Richards, B.E. Understanding Subsonic and Transonic Open Cavity Flows and Supression of Cavity Tones. *AIAA Paper*, AIAA 2000-0658, January 2000.

[45] Jameson, A. Time dependent calculations using multigrid, with applications to unsteady flows past airfoils and wings. *Technical report*, AIAA 91-1596, 1991.

[46] Jeng, Y.N and Wu, T-J. Numerical Study on a supersonic open cavity flow with geometric modification on aft bulkhead. *AIAA-92-2627-CP*, 1992.

[47] Johannesaen, N.H. Experiments on Supersonic Flow Past Bodies of Revolution with Annular Gaps of Rectangular Section. *Phil. Mag. [7], Vol 46, No 372, pp31-39*, 1955.

[48] Kaufman, L.G., Maciulaitis, A., and Clark, R.L. Mach 0.6 to 3.0 Flows over Rectangular Cavities. *Flight Dynamics Lab, Wright Patterson AFB, AFWAL-TR-82-3112, May*, 1983.

[49] Kim, I. Numerical Investigation of Unsteady Supersonic Flowfield with Passive Control. *PhD Thesis*, North Carolina State University, 1991.

[50] Kim, I and Chokani, N. Navier-Stokes study of supersonic cavity flowfield with passive control. *J Aircraft*, 29:217–223, 1992.

[51] Kousen, K.A. and Bendiksen, O.O. Nonlinear aspects of the transonic aeroelastic stability problem. *29th Structures, Structural Dynamics and Materials Conference*, AIAA, 1988.

[52] Krishnamurty, K. Acoustic Radiation from Two-Dimensional Rectangular Cut-Outs in Aerodynamic Surfaces. *NACA Report*, TN-3487, 1955.

[53] Lesoinne, M. and Farhat, C. Geometric conservation laws for aeroelastic computations using unstructured dynamic meshes. *12th AIAA CFD conference, San Diego*, AIAA, 1995.

[54] Love, E.S. Pressure Rise Associated with Shock-Induced Boundary-Layer Separation. *NACA TN 3601*, 1955.

[55] Love, E.S. Base Pressure at Supersonic Speeds on Two-Dimensional Airfoils and on Bodies of Revolution with and without Fins having Turbulent Boundary Layers. *NACA TN 3819*, 1957.

[56] McDearmon, R.W. Investigation of the Flow in a Rectangular Cavity in a Flat Plate at a Mach Number of 3.55. *NASA TN D-523*, 1960.

[57] McGraw-Hill. Encyclopedia of Science and Technology. *McGraw-Hill Book Company*, Vol 12 p583, 1977.

[58] Morozov, G.M. Interaction Between a Supersonic Stream and a Rectangular Depression on a Flat Plate. *Soviet Physics, Tech. Physics, Vol 3 No 1, pp. 144-149*, 1958.

[59] Osher, S., and Chakravarthy, S.R. Upwind schemes and boundary conditions with applications to Euler equations in general coordinates. *Journal Computational Physics*, 50, 447–481, 1983.

[60] Pereira, J.C.F., and Sousa, J.M. Influence of Impingement Edge Geometry on Cavity Flow Oscillations. *AIAA Journal*, Vol. 32, NO. 8, 1737-1740, 1994.

[61] Plentovich, E.B., Stallings, R.L.Jnr. and Tracy, M.B. Experimental Cavity Pressure Measurements at Subsonic and Transonic Speeds' Static Pressure Reults. *NASA TP-3358*, 1993.

[62] Powers, W.F., Stetson, K.F., and Adams, M.C. A Shock Tube Investigation of Heat Transfer in the Wake of a Hemisphere-Cylinder with Application to Hypersonic Flight. *AVCO Research Report No. 30*, 1958.

[63] Raman, G. and Raghu, S. Cavity Resonance Suppression using Minature Fluidic Oscillators. *5th AIAA/CEAS Aeroacoustics Conference*, AIAA 1999-1900, 1999.

[64] Rizzetta, D.P. Numerical Simulation of Supersonic Flow over a three-dimensional cavity. *AIAA J*, 26:799–807, 1988.

[65] Rockwell, D. and Naudascher, E. Review-Self Sustaining Oscillations of Flow Past Cavities. *Journal of Fluids Engineering*, 100, 1978.

[66] Rockwell, D. and Knisely, C. The Organised Nature of Flow impingement Upon a Corner. *Journal of Fluid Mechanics, Vol 93, Pt. 3, pp 413-432*, 1979.

[67] Rona, A. and Dieudonne, W. A Flow Resonant Model of Transonic Laminar Open Cavity Flow. *AIAA Paper*, AIAA 2000-1967, June 2000.

[68] Roshko, A. Some Measurements of Flow in a Rectangular Cutout. *NACA Report*, TN-3488, 1955.

[69] Rossiter, J.E. Wind Tunnel Experiments on the Flow over Rectangular Cavities at Subsonic and Transonic Speeds. *Ministry of Aviation, Aeronautical Research Council*, R&M 3438, 1964.

[70] Ross, J.A. and Peto, J.W. The Unsteady Environment Within an Internal Weapons Bay or Cavity. *DERA Bedford, Internal Report*, 1992.

[71] Ross, J. and Peto, J.W. The effect of cavity shaping, front spoilers and ceiling bleed on loads acting on stores, and on the unsteady environment within weapons bays. *DERA/AS/HWA/Cr 97010/1*, 1997.

[72] Ross, J. Dera internal report, uk restricted. *MSSA CR980744/1.0*, 1998.

[73] Sandahl, A.C. and Maxime, A.F. Similitude Relations for Free-Model Wind-Tunnel Studies of Store Dropping Problems. *NASA TN-3907*, 1957.

[74] Shaw, L. High Speed Applications of Active Flow Control for Cavity Aeroacoustics . *6th AIAA/CEAS Aeroacoustics Conference*, AIAA 2000-1926, 2000.

[75] Shaw, L. and Northcraft, S. Closed Loop Active Control for Cavity Aeroacoustics . *5th AIAA/CEAS Aeroacoustics Conference*, AIAA 1999-1902, 1999.

[76] Shih, S.H., Hamed, A. and Yeuan, J.J. Unsteady supersonic cavity flow simulations using coupled $k-\epsilon$ and Navier-Stokes equations. *AIAA J*, 32:2015–2021, 1994.

[77] Sinha, N. and Arunajatesan, S. High Fidelity Simulation of Weapons Bay Aeroacoustics and Active Control. AIAA Paper 2000-1968, 2000.

[78] Sinha, N., York, B.J., Dash, S.M., Chidambaram, N. and Findlay,D. A perspective on the simulation of cavity aeroacoustics. *AIAA 98-0286*, 1998.

[79] Smith, D.L. Prediction of the Pressure Oscillations in Cavities Exposed to Aerodynamic flow. *AFFDL AD-A018 518*, Oct 1975.

[80] Stallings, R.L.Jnr. and Wilcox, F.J.Jnr. Experimental Cavity Pressure Distribution at Supersonic Speeds. *NASA TP-2683*, 1987.

[81] Stallings, R.L.Jnr. and Wilcox, F.J.Jnr . Experimental Investigation of Porous-Floor Effects on Cavity Flow Fields at Supersonic Speeds. *NASA TP-3032*, 1990.

[82] Stallings, R.L.Jnr. Store Separation form Cavities at Supersonic Flight Speeds. *Journal of Spacecraft and Rockets, Vol 20, No2 pp 129-132*, 1987.

[83] Stanek, M.J., Raman, R., Kibens, V., Ross, J.A., Odera, J. and Peto, J.W. Control of Cavity Resonance Through Very High Frequency Forcing. *6th AIAA/CEAS Aeroacoustics Conference*, AIAA 2000-1905, 2000.

[84] Tam, C., Orkwis, P.D. and Disimile, P.J. Supersonic Open Cavity Flow Physics Ascertained from Algebraic Turbulence Model SImulations. *AIAA Paper 96-0075*, 1996.

[85] Tam, C,, Orkwis, P.D. and Disimile, P.J. Comparison of Baldwin-Lomax Turbulence Models for Two-Dimensional open cavity computations. *AIAA J*, Vol 34:629–631, 1996.

[86] Thomas, J.L. and Salas, M.D. Far-field boundary conditions for transonic lifting solutions to the Euler equations. *AIAA Journal*, 24, 1074–1080, 1986.

[87] Thomas, P.D., and Lombard, C.K. Geometric conservation law and its application to flow computations on moving grids. *AIAA J*, 17, 1030–1037, 1979.

[88] Tracy, M.B., and Plentovich, E.B. Cavity Unsteady Pressure Measurements at Subsonic and Transonic Speeds. *NASA TP-3669*, 1997.

[89] Van Albada, G.D., Van Leer, B., and Roberts, W.W. A comparative study of computational methods in cosmic gas dynamics. *Astronomy and Astrophysics*, 108, 1982.

[90] Van Leer, B. Towards the ultimate conservative difference scheme. V:a second–order sequel to Godunov's method. *J. Comput. Phys.*, 32, 101–136, 1979.

[91] Venkatakrishnan, V. and Mavriplis, D.J. Implicit method for the computation of unsteady flows on unstructured grids. *12th AIAA Computational Fluid Dynamics Conference*, AIAA, 1995.

[92] Wilcox, D.C. Turbulence Modelling for CFD. *DCW Industries, Inc.*, California, 1993.

[93] Wilcox, F.J. Jnr. Experimental Measurements of Internal Store Separation Characteristics at Supersonic Speeds. *Store Carriage, Integration and Release. The Royal Aeronautical Society*, Three Day Conference, April, 1990.

[94] Williams, D.R., Fabris, D., Iwanski, K. and Morgan, J. Closed Loop Control in Cavities with Unsteady Bleed Forcing. AIAA Paper 2000-0470, 2000.

[95] Xhang, X and Edwards, J.A. Computational analysis of unsteady supersonic flows driven by thick shear layers. *Aeronautical Journal*, pages 365–374, November, 1988.

[96] Zhang, X., Rona, A., and Edwards, J.A. The Effect of Trailing edge Geometry on Cavity Flow Oscillation Driven by a Supersonic Shear Layer.

[97] Zhang, X., Cheng, X.X., Rona, A. and Edwards, J.A. Attenuation of Cavity Flow Oscillation Through Leading Edge Flow Control. *Journal of Sound and Vibration*, Vol 221, 1999.

[98] Zhang, X. Compressible cavity flow oscillation due to shear layer instabilities and pressure feedback. *AIAA J*, 33:1404–1411, 1995.